Braunschweiger Schriften zur Mechanik Nr. 63-2008

Seismic Risk Analysis of Buried Lifelines

von

Robert Borsutzky

Institut für Angewandte Mechanik

Technische Universität Braunschweig

Herausgegeben vom Mechanik-Zentrum der
Technischen Universität Braunschweig

Schriftleiter: Prof. Dr. rer. nat. H. Antes
Institut für Angewandte Mechanik
Postfach 3329
38023 Braunschweig

Von der Fakultät Architektur, Bauingenieurwesen und Umweltwissenschaften
der Technischen Universität Carolo-Wilhelmina zu Braunschweig
zur Erlangung des Grades eines Doktor-Ingenieur (Dr.-Ing.)
genehmigte Dissertation

Eingereicht am 10. Oktober 2007
Mündliche Prüfung am 23. November 2007

Berichterstatter

Prof. Dr. rer. nat. H. Antes
Prof. Dr. Ing. T. Crespellani

BSM 63-2008
ISBN 978-3-920395-62-3

Seismic Risk Analysis of Buried Lifelines

Dissertation

submitted to and approved by the

Faculty of Architecture, Civil Engineering and Environmental Sciences
University of Braunschweig – Institute of Technology

and the

Faculty of Engineering
University of Florence

in candidacy for the degree of a
Doktor-Ingenieur (Dr.-Ing.) /
Dottore di Ricerca in Risk Management on the Built Environment *)

by
Robert Borsutzky
from Hamburg, Germany

Submitted on	10 October 2007
Oral examination on	23 November 2007
Professorial advisors	Prof. Heinz Antes
	Prof. Teresa Crespellani

2008

*) Either the German or the Italian form of the title may be used.

The dissertation is published in an electronic form by
the Braunschweig university library at the address

http://www.biblio.tu-bs.de/ediss/data/

Abstract

In seismic-prone areas, the earthquake resistance of lifelines plays a role of particular importance for civilisation. Seismically caused failure of lifelines can result in disastrous events. Due to the grave consequences of those failures in past earthquakes, the need for reliable models examining the dynamic response of lifelines under earthquake excitation grows.

In this thesis, a methodology is developed to analyse the damage risk of buried lifelines exposed to seismic wave propagation. This risk analysis covers the probabilities of hazard occurrence, exposure and vulnerability. In order to reach this aim, a three-dimensional numerical model is developed to analyse the dynamic response of pipelines embedded in soil. Thereby, the emphasis is placed on three topics: the incorporation of dynamic soil-structure interaction enabling wave radiation to infinity, the advanced modelling of seismic excitation, and the over-all consideration of uncertainties.

A hybrid finite element-scaled boundary finite element method is presented to examine soil-structure interaction. Whereas the finite element method enables a detailed modelling of the near-field, i.e., the domain containing pipe and soil, the scaled boundary finite element method fulfils the wave radiation condition at infinity. In the latter method, increase of efficiency is achieved by reducing the non-locality in space and time along with employing substructuring techniques without losses of accuracy.

For modelling seismic wave propagation in the near-field, a novel procedure based on the domain reduction method is introduced which includes two steps. In the first step, a large scale simulation of the earthquake is performed by means of numerical Green's functions. The earthquake source is modelled as finite fault with a complex slip distribution. From this first step, forces equivalent to the seismic source are determined and applied to the hybrid model, described above. Thus, realistic seismic wave propagation inside the near-field can be modelled.

Thereupon, an integrated probabilistic analysis is performed, which includes parameters of the entire seismic wave propagation path, starting from the earthquake source, through the earth crust and the soil and ending up at the buried lifeline. For this process a point estimate method is employed which enables an efficient and reliable determination of the failure probability of the pipeline. Another advantage is the compatibility to deterministic finite element methods.

The applicability of the present methodology is demonstrated by a simulation of a real earthquake and the application to parts of a lifeline network of a municipality in Emilia-Romagna, Italy. Furthermore, an extended parameter study is performed to exhibit the effects of computational aspects as well as of seismic parameters, of pipe design and of construction details.

The present work introduces a sophisticated tool for an integrated analysis of the damage seismic risk of underground lifelines. Nevertheless, the present methodology is not only applicable to buried lifelines but to any other structure or region of interest under seismic wave excitation.

Zusammenfassung

In seismisch gefährdeten Gebieten ist die Widerstandsfähigkeit von Versorgungsleitungen - so genannten Lifelines - gegen Erdbeben von zentraler Bedeutung für die Zivilisation. Das seismisch bedingte Versagen von Lifelines und dessen desaströse Folgen offenbaren die Notwendigkeit von verlässlichen Modellen, die das dynamische Antwortverhalten dieser unterirdischen Strukturen unter Erdbebeneinwirkung realistisch abbilden können.

In der vorliegenden Arbeit wird eine Methode entwickelt, durch welche das Schadensrisiko von unterirdischen Versorgungsleitungen infolge von seismischen Wellenausbreitungseffekten analysiert werden kann. Diese Risikoanalyse umfasst die Wahrscheinlichkeiten des Auftretens der Gefährdung, der Aussetzung sowie der Verwundbarkeit. Zur Durchführung der Analyse wird ein dreidimensionales numerisches Modell entwickelt, welches das dynamische Verhalten von erdverlegten Rohrleitungen beschreibt. Bei der Entwicklung wurden drei Schwerpunkte gesetzt: die detaillierte Modellierung der dynamischen Boden-Bauwerk-Wechselwirkung unter Berücksichtigung der Wellenabstrahlung ins Unendliche, die realistische Modellierung der seismischen Anregung sowie die globale Berücksichtigung von Unsicherheiten.

Zur Untersuchung der Boden-Bauwerk-Wechselwirkung wird eine hybride Finite Element-Scaled Boundary Finite Element Methode verwendet, wobei die Finite Element Methode eine genaue Abbildung des Nahfeldes (Boden und Rohrleitung) ermöglicht und die Scaled Boundary Finite Element Methode die Wellenabstrahlung ins Unendliche. In letztgenannter Methode können Effizienzsteigerungen ohne Genauigkeitsverluste durch die Reduzierung der Nichtlokalitäten in Raum und Zeit als auch durch den Einsatz von Substrukturmethoden erreicht werden.

Zur Modellierung der seismischen Wellenausbreitung im Nahfeld wird eine neuartige Prozedur basierend auf der Domain Reduction Method vorgestellt, welche zwei Schritte beinhaltet. Im ersten Schritt wird eine großmaßstäbliche Simulation des Erdbebens mit Hilfe von numerischen Green'schen Funktionen durchführt, bei welcher die Erdbebenquelle als komplexe, endliche Verwerfung modelliert wird. Aus diesem ersten Schritt werden Kräfte äquivalent zur Erdbebenquelle ermittelt und im zweiten Schritt auf das oben beschriebene hybride Modell aufgebracht. Diese Methode ermöglicht die Modellierung einer realistischen seismischen Wellenausbreitung innerhalb des Nahfeldes.

Darauf aufbauend wird eine ganzheitliche probabilistische Analyse durchgeführt, welche Parameter des kompletten Ausbreitungspfades der seismischen Wellen - angefangen bei der Erdbebenquelle, durch die Erdkruste, bis hin zur unterirdischen Versorgungsleitung - einbindet. Für dieses Verfahren wird ein Punktschätzverfahren eingesetzt, welches einerseits eine effiziente und verlässliche Bestimmung der Versagenswahrscheinlichkeit einer Rohrleitung ermöglicht und andererseits kompatibel zu deterministischen Finite Element Methoden ist.

Die Anwendbarkeit der vorgestellten Methode wird anhand der Simulation eines realen Erdbebens und der Analyse von Teilen eines Lifeline-Netzwerks in einer Gemeinde in der Emilia-Romagna, Italien, demonstriert. Darüber hinaus wird eine umfassende Parameterstudie durchgeführt, um die Einflüsse von numerischen Aspekten als auch von seismischen Parametern und von Konstruktionsdetails aufzuzeigen.

Die vorliegende Arbeit stellt damit ein Werkzeug zur ganzheitlichen Analyse des seismischen Schadensrisikos von unterirdischen Versorgungsleitungen zur Verfügung. Der Einsatz der vorgestellten Methode ist nicht nur auf unterirdische Versorgungsleitungen beschränkt, sondern erstreckt sich auch auf jede andere Struktur oder Region, welche einer seismischen Wellenbelastung ausgesetzt ist.

Acknowledgments

This thesis originates from my research work at the universities of Braunschweig and Florence during the years 2003 to 2007.

Initially, I thank Prof. Dr. Heinz Antes who gave me the opportunity to do research at the *Institut für Angewandte Mechanik* of the *Technische Universität Braunschweig* and who attended the progress of the work with enduring interest. My particular gratitude goes to PD Dr. Lutz Lehmann for his permanent openness to scientific discussions, his extensive review of this dissertation and his amicable counsel which definitely enriched this work.

I thank my Italian tutors Prof. Dr. Teresa Crespellani und Prof. Dr. Giovanni Vannucchi from the *Università degli Studi di Firenze* for their professional suggestions, their constant willingness for technical discussions and their cordial hospitality. I address the same gratitude to Dr. Johann Facciorusso.

For their very helpful support concerning the seismological aspects of this thesis and their beneficial remarks and suggestions, I have to express my gratefulness to Dr. Enrico Priolo und Dr. Peter Klin of the *Centro di Ricerche Sismologiche* in Trieste.

I have to thank all colleagues of the *Institut für Angewandte Mechanik* for their friendly collegiality, their help and for the likeable atmosphere in the institute.

For the chance to prepare this work within the International Doctoral Course "Risk Management of Natural and Civilization Hazards on Buildings and Infrastructure" of the *Deutsche Forschungsgemeinschaft*, I thank Prof. Dr. Udo Peil und Prof. Dr. Claudio Borri. In the same way, I like to thank all the colleagues from the Italian and from the German side of this course for their friendly companionship and their passionate endeavour in the intercultural exchange.

Robert Borsutzky

To my family and Katharina

Contents

1 Introduction

Underground pipeline systems are commonly used to carry materials essential to the support of life such as water, sewage, gas, or liquid fuels. For this reason, they are often referred to as lifelines. In seismic-prone areas, the earthquake resistance of lifelines plays a role of particular importance for civilisation. Therefore, it is especially necessary to design lifelines under consideration of the consequences that their failure might have.

1.1 Buried lifelines subject to earthquakes

To address the behaviour and the dangerous consequences that the failure of underground lifelines has, it is at first necessary to clarify the terms of what is a lifeline and which of those are subject of this work.

Terminology: Lifelines are the arteries and veins of modern life and civilisation. They transport all resources essential to support life - or at least civilised life - to their place of destination. Therefore, the term *lifeline* comprises a great amount of structures with wide spread intended purposes of usage.

Usually, lifelines are sorted into categories depending on the medium that they transport. Following this definition, a lifeline can be a water pipeline or a high voltage cable as well as a bridge or a rail track. Mainly, six categories can be distinguished depending on the media:

1) potable water	2) sewage	3) gas and liquid fuels
4) electric power	5) telecommunication	6) traffic and transportation.

In contrast to the categories 4) to 6), the lifelines belonging to the categories 1) to 3) are used for the transportation of gases or liquids. All gases and the predominant part of liquids are transported in closed systems, like pipelines. In fact, pipelines are one of the widest spread forms of lifelines. Whereas global pipeline infra-structure systems, like inter-continental gas pipelines, are mostly situated over ground, local pipeline systems, e.g., for the supply of cities, are mainly installed under ground. This work is exclusively focused on the concern of underground pipelines.

Importance of lifelines: Special importance is attached to lifelines after the occurrence of a disastrous event, e.g., an earthquake, a flood, or a terror attack. In those cases, lifelines are needed for the supply of key institutions that have a central importance, e.g., hospitals, emergency accommodations, or schools. Thus, the maintenance of essential goods is vitally important to be preserved. In consideration of this importance, damaged pipelines represent a source of danger in double sense. Firstly, they imperil its local surroundings by the instantaneous effects of their failure as, e.g., fires or explosions. Secondly, they endanger collaterally by the non-support of vitally important necessities as, e.g., potable water.

Examples for disastrous consequences: The failure of buried pipelines caused by seismic events can result in several forms of disastrous consequences. Examples for those consequences are destructive fires (1906 San Francisco, 1995 Kobe), breakdown of water supply (1985 Mexico City, 1999 Taiwan), epidemics (2001 El Salvador) or even political destabilisation of a country (1972 Managua) [O'Rourke

and Liu, 1999; Ayala *et al.*, 1990; Eidinger and Avila, 1999; Tsai *et al.*, 2000; Takada *et al.*, 2002]. Especially momentous is the failure of water distribution systems, which dangerously impacts people's health in two ways: the fire-extinction is strongly hindered, and the cutoff of potable water may lead to epidemics.

Failure modes: In most cases, structures with large extensions, like pipelines, are more resistant to earthquakes the more flexible they are, since energy can be transformed into deformation. Generally, pipelines behave stiffest in their longitudinal direction, whereas they are very flexible perpendicular to this direction. Hence, in the majority of cases, damages of underground pipelines are caused by ground motions in longitudinal pipe direction in which the highest stresses are induced.

Pipelines are classified into two general types: continuous and segmented pipelines. According to those types, different seismic failure modes can be observed. For continuous pipelines (e.g., made of welded steel) seismic failure is most often due to local compressions buckling, i.e., wrinkling, and tensile rupture [O'Rourke, 1995]. Another reason for damage is beam buckling which depends on the burial depths and on the soil density. Failure modes of segmented pipelines (e.g., made of cast iron), especially of those with large diameters and thick walls, are mostly due to joint overloading. Examples are axial pull-out, crushing of joints, circumferential flexural failure and joint rotation [O'Rourke and Liu, 1999].

(a) Joint failure of a concrete pipeline.

(b) Failure of a steel pipeline.

Figure 1.1: Seismically damaged underground pipelines during the 1985 Michoacan earthquake (from [Flores-Berrones and Liu, 2003]).

Seismic hazards: Generally, the seismic hazards that lead to damages of buried lifelines are classified into three categories [O'Rourke, 1995]. Those causing hazards are *transient wave propagation*, *permanent ground deformation* and *active fault crossing*. Typically, failure of underground pipelines due to transient seismic wave propagation is spread over a large spatial scale. It affects wide parts of the lifeline network with relatively low damage rates. Contrariwise, damages caused by active fault crossing or permanent ground deformation, like lateral spreading due to liquefaction or landsliding, occur in isolated areas with high damage rates.

During a seismic event, usually combinations of those damage modes occur. An example is the 1906 San Francisco earthquake. 52% of all pipeline breaks occured due to permanent ground deformation in one single city block [O'Rourke *et al.*, 1985]. The remaining 48% of the pipeline damage is presumed by [O'Rourke and Liu, 1999] to be attributed to transient wave propagation. Nevertheless, there are examples of pure wave propagation hazards, like the 1985 Michoacan earthquake [Ayala *et al.*, 1990]. In this earthquake, the failure of the lifeline network of Mexico City was solely caused by seismic wave propagation. Other examples for lifeline damages only induced by seismic wave propagation are the earthquakes of 1964 Puget Sound, 1969 Santa Rosa and 1983 Coalinga [O'Rourke and Liu, 1999]. This work is concerned with the hazardous effects of seismic wave propagation characterised by transient strain and curvature.

1.2 State of research on underground pipelines

The analyses of buried pipelines have attracted a great number of researches. General methods of design and structural mechanics of buried pipes including all types of loadings are summarised in [Moser, 2001] and [Watkins and Anderson, 2000]. Whereas those books are mainly concentrated on construction and operation of the pipelines and include considerations of dynamic loadings only to a basic limit, many research works are exclusively concerned with the analysis of buried pipelines under earthquake conditions.

Those works studying the seismic behaviour of buried pipelines and their components are recapitulated in several state-of-the-art reviews, e.g., [O'Rourke *et al.*, 1985; O'Rourke, 1995; O'Rourke and Liu, 1999; Flores-Berrones and Liu, 2003]. The reviews include considerations of all three seismic hazards and the corresponding failure criteria of both two types of pipelines. Reviews which are only concerned with one of this types are, e.g., for segmented lifelines [Rucker and Dowding, 2000], or for continuous [O'Rourke and Shinozuka, 1995]. The results of the several research works went down in seismic design standards, e.g., [European Committee for Standarization (CEN), 1998], or in standard-like guidelines such as [American Lifelines Alliance, 2001a,b,c] or [Eidinger and Avila, 1999]. Other recapitulative works stating design criteria for underground pipelines are [Hall and Newmark, 1978; Ballantyne, 1995; Eidinger *et al.*, 2001].

The seismic risk of underground lifelines was subject of many researches of diversified approaches. A general overview of those works can be found in [Eguchi, 2003]. [Hashash *et al.*, 2001] divides the seismic hazard assessments for the design of underground structures in deterministic and probabilistic methods. The redundancy of lifelines for mitigation measures against seismic risk was performed by [Hoshiya *et al.*, 2004] using a deterministic approach, whereas the reliability measures for buried flexible pipes from [Sivakumar Babu and Rao, 2005] belong to the probabilistic methods. Concerning the hazard of permanent ground deformation, analyses were performed by, e.g., [Crespellani *et al.*, 1992, 1997]. Based on such hazard analyses, seismic zonations of lifelines were executed by [O'Rourke and Jeon, 2000] estimating losses and consequences. A complete risk analysis of a lifeline system subject to permanent ground deformations was executed by [Crespellani *et al.*, 2006]. The reliability of lifeline networks under the hazard of transient ground deformation was examined by [Selcuk and Yücemen, 2000], whereas the earthquake damage to buried lifelines due to this hazard was estimated by [Toprak and Taskin, 2007].

The thesis at hand focuses on the transient ground deformation hazard. Therefore, a state-of-the-art review is given subsequently, which deals with the methods of analysing buried pipelines under transient seismic wave propagation effects. The wave propagation analyses of underground pipelines and similar structures include experimental studies as well as analytical and numerical computational methods. An extended review of methods for analysing underground and lifeline structures exposed to seismic wave propagation considering *soil-structure interaction* (SSI) can be found in [Manolis and Beskos, 1997]. A web-based tool which incorporates many of those methods from quasi-static approaches to the pure finite element method was designed by [Kuhlmann, 2004].

Experimental methods can be classified into three categories. Firstly, shaking table tests with scaled models were performed to investigate the dynamic response of tunnels, e.g., by [Kuribayashi and Iwasaki, 1974], and buried pipelines, e.g., by [Simonis and Nash, 1984]. Secondly, observations and real site measurements of underground structures were executed by, e.g., [Sakurai and Takahasi, 1969; Davis and Bardet, 2000]. Thirdly, blast tests were performed by [Nash *et al.*, 1984] for elucidating the potential damage mechanisms of underground piping mechanisms.

Quasi-static methods which neglect the effects of SSI conservatively assume that the underground pipeline takes the same displacement configuration as the ground. Hence, an upper bound for the axial strain in a straight continuous pipeline is given. Such an approach for tunnels and pipelines was sug-

gested by [Newmark, 1971; Sakurai and Takahasi, 1969; Shah and Chu, 1974]. Quasi-static methods not considering SSI were used when phenomena in the inner of the pipeline are studied, like the interaction of the pipe and the transported liquid under seismic loading [Kisliakov, 1990].

Quasi-static methods which consider the effects of SSI are applicable to stiff structures in soft soil. The pipeline is modelled as a simple beam on an elastic foundation [Aoki and Hayashi, 1973; Constantopoulos *et al.*, 1979; Navarro and Samartin, 1988; Navarro, 1992]. In the quasi-static approach of [Penzien *et al.*, 1992], all basic components of the problem are examined, i.e., generation of free-field motion, calculation of the global response of a tunnel including SSI, and evaluation of separation effects at the joints. An extension to bends and branches of underground pipelines of the approach of [Newmark, 1971] which originally neglected SSI was suggested by [Shah and Chu, 1974]. Additionally, the consideration of local discontinuities as anchor blocks was implemented by [Varandega and Luciani, 1986]. Those quasi-static methods were, e.g., used to analyse the occurrence of transverse buckling of underground pipelines [Davis and Bardet, 1998; Mavridis and Pitilakis, 1995].

Lumped parameter models are an extension of the quasi-static concept where the pipeline is modelled as beam on an elastic foundation. Thereby, the pipeline is discretised by connected mass points or modelled as continuous whereas the soil is modelled by springs, dashpots and lumped masses, e.g., in [Dawkins, 1969; Yuan and Walker, 1970]. [Hindy and Novak, 1979] studied the influences on pipelines of two vertically separated soils and found out that axial stresses predominate over bending stresses for harmonic ground motion. The lumped parameter model was improved by [O'Rourke and Elhmadi, 1988; Elhmadi and O'Rourke, 1988, 1989, 1990] by introducing frictional slip in the soil spring elements as well as axial spring elements. The consideration of axial, bending and torsional effects was achieved by [Takada and Tanabe, 1987], whereas [Deans and Tang, 1979] presented a stiffness matrix approach for pipeline networks. Further studies with lumped parameter models were performed for normal fault movement [Vougiouskas and Carydis, 1995; Hahn and Sritharan, 1994] as well as for random seismic input [Mashaly and Datta, 1987; Selvadurai *et al.*, 1990; Lin *et al.*, 1990].

Analytical methods examine the buried structure as a discontinuity in a homogeneous full- or half-space which is excited by time-harmonic or transient waves. Early works of [Baron and Matthews, 1961] analysed the dynamic displacements and stresses around a circular cavity in a infinite medium under plane strain conditions caused by a *P*-wave. This approach was extended to half-spaces with a horizontal traction-free surface under anti-plane strain conditions excited by horizontally polarised *SH*-waves [Lee and Trifunac, 1979]. On this basis, the response of cylindrical shells due to Rayleigh waves was addressed by [El-Akily and Datta, 1981]. Several analyses of buried pipelines modelled as shell have been approached in full- or half-spaces in two dimensions [Datta *et al.*, 1984b], in axisymmetric coordinates [Datta *et al.*, 1982] and in three dimensions [Datta *et al.*, 1985; Wong *et al.*, 1986]. In a statistical approach, [Koike *et al.*, 2007] estimated the damaging ground strains for lifelines caused by *SH*-, Rayleigh and Love waves.

Semi-analytical methods are combinations of analytical and numerical methods which are usually restricted to the very specific problems for which they were developed. Eigenfunctions were conjuncted with the finite element method [Wong *et al.*, 1985; Datta *et al.*, 1984a] to study the response of infinitely long buried tunnels considering plane strain and excitations of *P*-, *SV*- and Rayleigh waves. Further works focused on the determination of equivalent spring stiffnesses [O'Leary and Datta, 1985; Chin *et al.*, 1987; Liu *et al.*, 1991] and on the combination of the cylindrical shell model with this equivalent spring model [Muleski *et al.*, 1979; Muleski and Ariman, 1985].

Numerical methods are widely used for the seismic analysis of underground structures. Early works approached the problem by incorporating only a single numerical method. Nowadays, combinations of several numerical methods have been proved to be more effective and better tailored to the requirements.

The *finite element method* generally enables the analysis of arbitrary structural geometry, medium inhomogeneities and complex material behaviour. Nevertheless, its incorporation requires the usage of non-reflecting boundary conditions [Mathews and Geers, 1985, 1987; Roesset and Ettouney, 1977]. By using the finite element method, the dynamic response of tunnels [Valliappan *et al.*, 1979; Schwartz, 1980; Gardien and Stuit, 2003] or conduits [Krauthammer and Chen, 1986] under plane strain conditions was studied. More complex free-field motion simulations for SSI analyses were performed by [Krauthammer and Chen, 1988; Ang and Newmark, 1963]. Since the usage of only one numerical method is simpler as employing hybrid methods, they are often employed for risk analyses as, e.g., by [Nedjar *et al.*, 2007].

The *finite difference method* is used by [Ang and Newmark, 1963] to study the response of underground structures exposed to blasts.

The *boundary element method* is very suitable for SSI analyses since it enables the wave radiation to infinity implicitly. [Kobayashi and Nishimura, 1983; Manolis and Beskos, 1983] performed two-dimensional studies of tunnel cross sections under plane strain conditions excited by *P*- and *S*-waves. The incorporation of a traction-free surface was done by, e.g., [Kontoni *et al.*, 1987]. Lined tunnels in a three-dimensional half-space were examined by [Stamos and Beskos, 1992, 1995] in frequency-domain.

Hybrid numerical methods combine the respective numerical methods such that each is optimally adopted. This is achieved by the later introduced substructure method which divides the entire domain into a near-field and a far-field. Usually, the near-field comprising the underground structure and the local soil is mapped by the finite element method.

The representation of the far-field is performed by several methods. The most common is the boundary element method which was, e.g., used by [von Estorff and Kausel, 1989; von Estorff and Antes, 1991; von Estorff *et al.*, 1991; von Estorff and Firuziaan, 2000] to simulate the dynamic response of tunnels. Three-dimensional analyses of buried pipeline segments were performed by [Manolis *et al.*, 1994, 1995], whereas the seismic response of subway tunnels was examined by [Shen and Wang, 1994; Wang, 1995] in frequency-domain and by [Liolios *et al.*, 2002] in time-domain.

Apart from the boundary element method, other methods were used to map the far-field such as the finite difference method for simulating non-linear SSI problems of buried reinforced concrete boxes [Nelson and Isenberg, 1976; Chen and Krauthammer, 1992]. Also analytical methods were coupled to the finite element method as eigenfunctions [Wong *et al.*, 1985] or trial functions [Wang and Takemiya, 1994].

The method used in this work is the *scaled boundary finite element method*. This method was incorporated to study the seismic response of structures with underground storeys [Naggar, 2003] or of buried pipelines [Borsutzky and Lehmann, 2006a].

1.3 Scope of this work

In this work, a methodology is developed to analyse the damage risk, i.e., the probability of failure, of buried lifelines exposed to seismic wave propagation. This risk analysis covers the probabilities of hazard occurrence, exposure and vulnerability, whereas consequences are excluded. In order to reach this aim, a three-dimensional numerical model is developed to analyse the dynamic response of pipelines embedded in soil. Thereby, the emphasis is placed on three topics: the incorporation of dynamic soil-structure interaction enabling wave radiation to infinity, the advanced modelling of seismic excitation and the over-all consideration of uncertainties.

1.3.1 Risk context

For analysing the seismic risk of buried lifelines correctly, it is necessary to gain a clear definition of the term risk. The *International Organization for Standardization* states risk as the "combination of the probability of an event and its consequences" [ISO, 2002]. Hence, risk R can be defined as the product of failure probability P_f and expected value of a given damage D:

$$R = P_f \cdot E(D). \tag{1.1}$$

From this definition it is evident that the evaluation of risk quantification has to be divided into two general steps. The first step is a probabilistic and parametric analysis, the second is a loss potential analysis. When examining the first step of the risk analysis more closely, the factor P_f can be subdivided into three components: the probability of hazard P_H, of exposure P_{Ex} and of vulnerability P_V. Thus, the total risk R can be derived from

$$R = \underbrace{P_H \cdot P_{Ex} \cdot P_V}_{\text{damage risk } R_d (=P_f)} \cdot E(D). \tag{1.2}$$

Even though, the product of the first three components is actually the probability of failure P_f, it is often referred to as *damage risk* R_d, e.g., in [Augusti *et al.*, 2001; Augusti, 2006]. This work focuses on on the analysis of all three components of this damage risk R_d of buried lifelines excited by seismic waves.

1.3.2 Objectives and outlines

The objective of this work is the development of a methodology which facilitates the determination of the damage risk of seismically excited underground pipelines. Therefore, a multi-method approach for the three-dimensional simulation of the dynamic response behaviour of the buried structure and its surrounding soil due to seismic wave propagation effects in time-domain is developed.

The developed methodology profitably combines multiple numerical methods in two main steps of simulation. The first step is a large scale earthquake simulation, whereas the second step is a simulation of the local domain containing the buried pipeline and the surrounding soil. Fig. 1.2 shows the entire analysed process of the addressed problem. The analysis begins at the origin of the earthquake, i.e., at the seismic source which is modelled as extended fault. Starting from there, the complete propagation of all seismic wave types to the local domain of interest is simulated. From the output of this large scale earthquake simulation, an equivalent seismic excitation for the local domain is derived. Thus, the dynamic response of the seismically excited local domain and of the contained pipeline can be computed.

In this procedure of analysing the damage risk of buried lifelines three questions are central to this work:

1) How to model the dynamic response in the local domain without disturbances caused by reflecting waves due to the modelling?

2) How to model the seismic wave excitation of the local domain realistically?

3) How to cope with uncertainties in the process?

The solutions presented in this work are specified subsequently.

1) Avoidance of wave reflections: A hybrid finite element-scaled boundary finite element method (FE-SBFEM) is presented to examine the soil-structure interaction problem in the local domain. The finite element method (FEM) enables the detailed modelling of the near-field, i.e., of the local domain containing pipeline and soil. The scaled boundary finite element method (SBFEM) [Wolf and Song, 1996; Wolf, 2003] is incorporated to model the dynamic response of the far-field at the near-field/far-field interface. Since the SBFEM fulfils the wave radiation condition at infinity, it is highly suitable

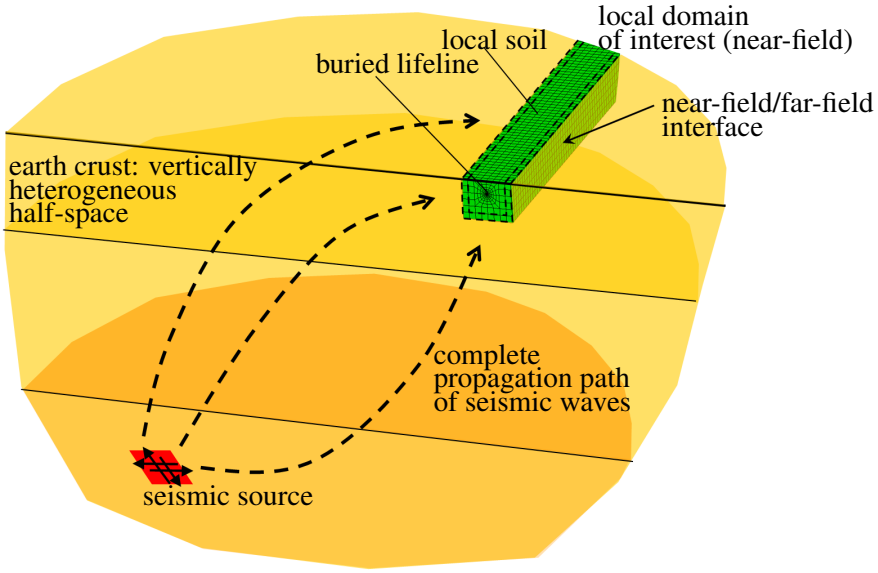

Figure 1.2: Sketch of the entire simulation which is subdivided into two steps. The first step simulates the origin of the earthquake at the source and the propagation of the complete seismic wave field to the local domain. In the second step, the dynamic response of this local domain containing the buried lifeline and the surrounding soil is analysed. The local domain is excited by equivalent seismic forces derived from the first step. The wave transmission through the artificial boundary (near-field/far-field interface) of the local domain is guaranteed.

to avoid wave reflections at the mentioned interface. An increase in efficiency is achieved within the SBFEM by reducing the non-locality in space and time along with employing sub-structuring techniques without losses of accuracy.

2) Seismic wave excitation: For the reliable modelling of seismic wave propagation in the near-field, a novel procedure on basis of the domain reduction method (DRM) [Bielak *et al.*, 2003] is introduced. This method includes the above mentioned two steps. In the first step, a large scale simulation of the earthquake is performed by means of numerical Green's functions derived from the discrete wavenumber finite element method (DWFEM) [Olson *et al.*, 1984]. The earthquake source is modelled as finite fault with a complex slip distribution determined by the deterministic stochastic k^{-2}-model [Herrero and Bernard, 1994]. From this first step, forces equivalent to the seismic source are determined and applied to the hybrid model, described before. Thus, realistic seismic wave propagation inside the near-field can be modelled.

3) Consideration of uncertainties: The uncertainties attached to the input-parameters of the entire simulation are considered by an integrated probabilistic analysis. This analysis employs the deterministic simulation procedure and includes parameters of the whole seismic wave propagation path, starting from the earthquake source, through the earth crust and the soil and ending at the buried lifeline. Further, a semi-probabilistic seismic hazard assessment is supplied. For the probabilistic treatment, a point estimate method (PEM) [Rosenblueth, 1975] is incorporated which enables an efficient and reliable determination of the failure probability, i.e., of the damage risk of the buried pipeline. Another advantage is the compatibility to deterministic finite element methods.

Risk analysis: Thus, solving the three central questions by incorporating the respective methods, this approach provides an advanced tool to determine the damage risk of buried pipelines endangered by transient seismic waves. With this tool, the specific components of the damage risk given in Eq. (1.2)

can be analysed. For example, the probability of hazard P_H can be derived by including considerations of the seismic fault, the earthquake occurrence, the size of the original seismic excitation, the depth of hypocentre, and the rupture type. The probability of exposure P_{Ex} embraces factors like the epicentral distance of the local domain, the profile of the earth and of the soil. Factors influencing the probability of vulnerability P_V are the pipeline design, type (continuous or segmented), building material and its cross section as well as construction details as the burial depth, the slippage between pipe and soil or a possible backfill.

The present work introduces a sophisticated tool for an integrated analysis of the damage seismic risk of underground lifelines. Nevertheless, the present methodology is not only applicable to buried lifelines but to any other structure or region of interest under seismic wave excitation.

1.3.3 Structure of the thesis

The thesis is structured into three parts. In Part I, the principles are addressed which form the basis of the developed methodology. The development of the methodology and the elaboration of the constituent methods are attended in Part II. In Part III, the applicability of the developed methodology is proved.

Part I: Basic principles: Initially, the derivation of elastodynamic waves is recapitulated in Chap. 2, where the basic equations of body waves and surface waves are explained. Hereafter, the topic of dynamic soil-structure interaction with emphasis on the wave radiation is discussed in Chap. 3. In doing so, methods of rigorous and approximative modelling are explicated with special reference to the boundary element method. Concluding the basic principles, the fundamentals of seismology are supplied in Chap. 4. The seismic process, i.e., the occurrence of earthquakes and seismic waves, is outlined, and quantitative representations are addressed followed by descriptions of ground motions.

Part II: Methodology: The developed methodology for analysing the damage risk of underground lifelines comprises several numerical methods. Those methods are schematically sketched in Fig. 1.3. The region of interest, i.e., the near-field, is simulated using the FEM (addressed in Chap. 5) and permits a detailed mapping of pipeline and local soil. It is aimed to model the effects of the seismic wave propagation as exact as possible in this FE domain that is locally truncated. Thus, firstly, wave reflections have to be avoided at those truncation boundaries. This is accomplished by the SBFEM (attended in Chap. 6) and which enables the wave transmission into the infinite half-space. Secondly, ways need to be found to introduce the seismic wave excitation into the local domain. Therefore, in Chap. 7, a special method on basis of the DRM is developed which synthesises the seismic ground motion from a large scale earthquake simulation. In this method, the extended seismic fault is assigned a complex slip distribution by the k^{-2}-model whereas the wave propagation through the earth crust is simulated by means of numerical Green's functions derived from the DWFEM. In order to examine the damage risk of an underground lifeline, the probability of failure needs to be determined. The procedure of this determination by means of the PEM is described in Chap. 8.

Part III: Application: The applicability of the present methodology is demonstrated by a simulation of a real earthquake and by studying computational aspects (in Chap. 9). The application to an existing lifeline network of a municipality in Emilia-Romagna, Italy is demonstrated in Chap. 10. Furthermore, an extended parameter study is performed to exhibit the influences of seismic parameters, pipe design, and construction details. Finally, the derivation of the damage risk, as described above, is exemplified.

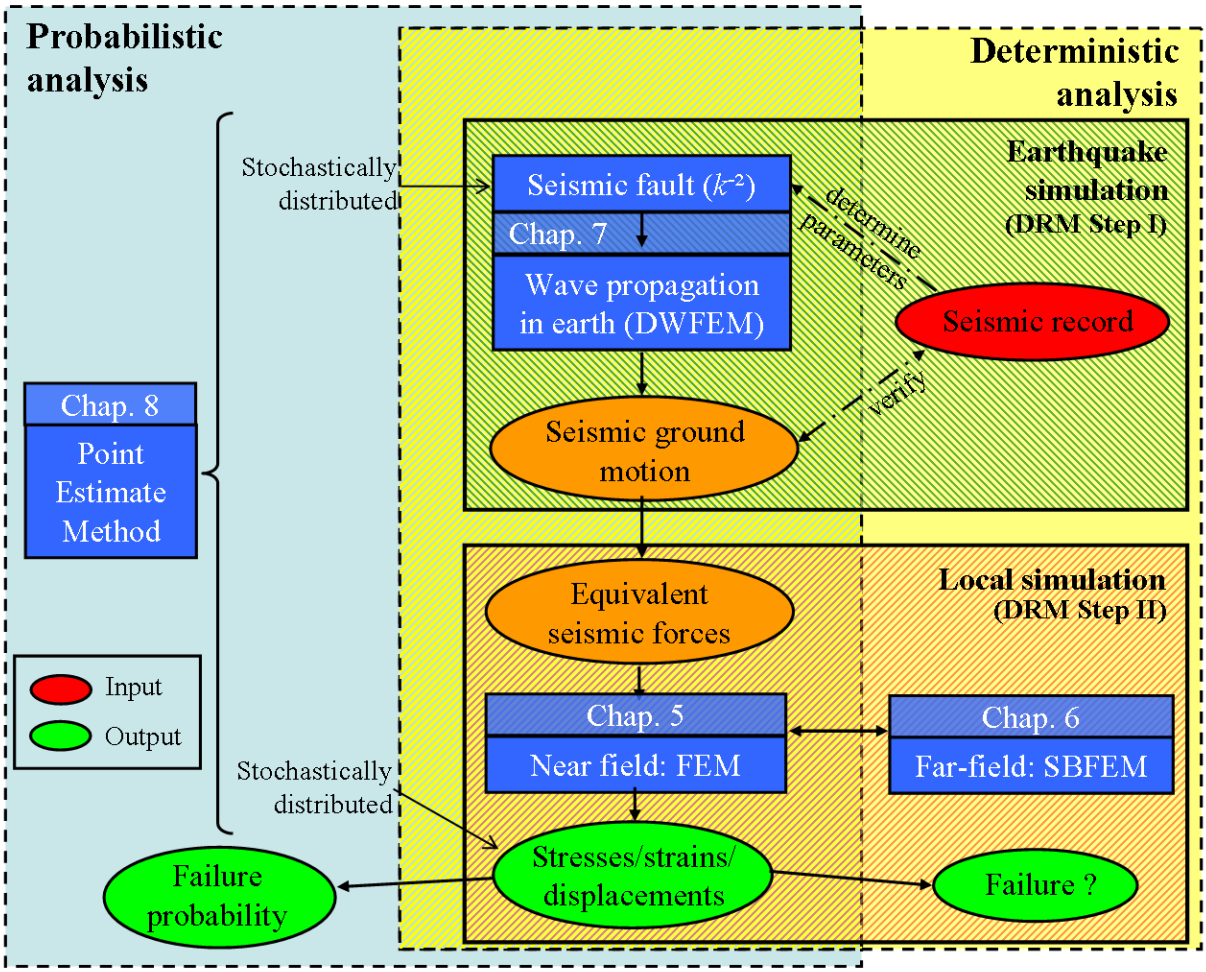

Figure 1.3: Schematic sketch of the developed methodology for analysing the seismic damage risk, i.e., the failure probability of buried pipelines. The development of the methodology is addressed in Part II of this work.

Part I

Basic principles

2 Elastodynamic waves

Understanding the behaviour of waves is of elementary importance in earthquake analyses. This chapter gives a review on elastodynamic waves that occur in solids. Thereby, the derivation of body and surface waves based on the theory of linear elasticity will be addressed followed by the discussion of the properties of those waves.

2.1 Equations of linear elasticity

The theory of linear elasticity is explained in, e.g., [Gould, 1994], or [Eringen and Suhubi, 1975], in detail. Hence, this section only quotes the most important equations.

According to Newton, for an arbitrary elastic body the *principle of linear momentum* applies. This principle states that the sum of the integrated tractions $\mathbf{t}$ and body forces $\mathbf{b}$ is equal to the acting acceleration forces:

$$\int_{\Gamma} t_i(\mathbf{x},t)d\Gamma + \int_{\Omega} b_i(\mathbf{x},t)d\Omega = \int_{\Omega} \rho\ddot{u}_i(\mathbf{x},t)d\Omega \,, \tag{2.1}$$

In Eq. (2.1), the arguments $\mathbf{x}$ and t are the position vector and the time, respectively. The domain of the body is indicated as Ω, whereas Γ denotes its boundary. For homogeneous distributed material, the constant mass density is described by ρ, and $\ddot{\mathbf{u}}$ is the displacement field differentiated twice with respect to time, i.e., the acceleration field.

Writing the traction vector $\mathbf{t}(\mathbf{x},t)$ with *Cauchy's theorem* as product of the symmetric stress tensor $\boldsymbol{\sigma}$ and the outward directed normal vector $\mathbf{n}$

$$t_i(\mathbf{x},t) = \sigma_{ik}(\mathbf{x},t)n_k(\mathbf{x}) \,, \tag{2.2}$$

the boundary integral in Eq. (2.1) can be converted via a Gauß transform into a domain integral:

$$\int_{\Gamma} t_i(\mathbf{x},t)d\Gamma_x = \int_{\Omega} \sigma_{ik,k}(\mathbf{x},t)d\Omega \,. \tag{2.3}$$

Dynamic equilibrium: Considering that equilibrium has to be satisfied for an arbitrary infinitesimal element, Eqs. (2.1) and (2.3) lead to *Cauchy's equation of motion* (or *balance of linear momentum*)

$$\sigma_{ik,k}(\mathbf{x},t) + b_i(\mathbf{x},t) = \rho\ddot{u}_i(\mathbf{x},t) \,. \tag{2.4}$$

Constitutive equation: For a general non-linear hyperelastic material, stresses σ_{ik} and strains ε_{ik} are related via

$$\sigma_{ik}(\mathbf{x},t) = \frac{\partial W}{\partial \varepsilon_{ik}(\mathbf{x},t)} \tag{2.5}$$

where W is the strain-energy density function of the considered material [Zienkiewicz and Taylor, 2005]. The strain-energy for linear elastic material is given by the quadratic form

$$W = \frac{1}{2}\varepsilon_{ik}C_{ikjl}\varepsilon_{jl} \tag{2.6}$$

where C_{ikjl} is the elastic stiffness tensor. Therewith, the constitutive relation for linear elastic material is represented by the *generalised Hooke's law*

$$\sigma_{ik}(\mathbf{x},t) = C_{ikjl}\varepsilon_{jl}(\mathbf{x},t) \tag{2.7}$$

which simplifies for an isotropic medium with *Lamé's constants* μ and λ to

$$\sigma_{ik}(\mathbf{x},t) = 2\mu\varepsilon_{ik}(\mathbf{x},t) + \lambda\delta_{ik}\varepsilon_{jj}(\mathbf{x},t)\ . \tag{2.8}$$

Strain-displacement relationship: In linear theory, the strains $\boldsymbol{\varepsilon}$ can be computed from the displacements $\mathbf{u}$ with

$$\varepsilon_{ik}(\mathbf{x},t) = \frac{1}{2}\Big(u_{i,k}(\mathbf{x},t) + u_{k,i}(\mathbf{x},t)\Big)\ . \tag{2.9}$$

Equation of motion: Inserting Eqs. (2.8) and (2.9) in Eq. (2.4), yields *Navier's equation of motion* for elastodynamic states

$$\mu u_{i,jj}(\mathbf{x},t) + (\mu+\lambda)u_{j,ij}(\mathbf{x},t) + b_i(\mathbf{x},t) = \rho\ddot{u}_i(\mathbf{x},t)\ . \tag{2.10}$$

The same equation, with omitted arguments $\mathbf{x}$ and t, reads in vector notation

$$(2\mu+\lambda)\nabla\nabla\mathbf{u} - \mu\nabla\times\nabla\times\mathbf{u} + \mathbf{b} = \rho\ddot{\mathbf{u}}\ . \tag{2.11}$$

The containing Lamé's constants μ and λ can be defined for an isotropic solid by means of the material constants, namely by Young's modulus E, shear modulus G, and Poisson's ratio ν:

$$\mu = G = \frac{E}{2(1+\nu)}\ , \tag{2.12}$$

$$\lambda = \frac{\nu E}{(1-2\nu)(1+\nu)}\ . \tag{2.13}$$

For an inhomogeneous material, Lamé's constants depend on the position $\mathbf{x}$. Then, Navier's equation reads with $\mu(\mathbf{x})$ and $\lambda(\mathbf{x})$

$$(2\mu+\lambda)\nabla\nabla\mathbf{u} - \mu\nabla\times\nabla\times\mathbf{u} + \nabla\lambda(\nabla\cdot\mathbf{u}) + 2\nabla\mu\frac{1}{2}[\nabla\mathbf{u} + (\nabla\mathbf{u})^T] + \mathbf{b} = \rho\ddot{\mathbf{u}}\ . \tag{2.14}$$

Boundary conditions: For a mixed initial boundary value problem, Dirichlet and Neumann boundary conditions have to be set:

$$u_i = \bar{u}_i \quad \text{on } \Gamma_u \quad \text{(Dirichlet) and} \tag{2.15}$$

$$t_i = \bar{t}_i \quad \text{on } \Gamma_t \quad \text{(Neumann)}\ . \tag{2.16}$$

The boundary parts Γ_u and Γ_t have to satisfy the conditions $\Gamma_u \cup \Gamma_t = \Gamma$ and $\Gamma_u \cap \Gamma_t = \emptyset$. In other words, the description on the boundary has to be complete and unique.

Initial conditions: Adopting finally the initial conditions

$$u_i(\mathbf{x},0) = u_{0i}(\mathbf{x}) \quad \text{and} \tag{2.17}$$

$$\dot{u}_i(\mathbf{x},0) = v_{0i}(\mathbf{x})\ , \tag{2.18}$$

results in a complete definition of the elastodynamic problem in the domain Ω.

2.2 Solutions of the equation of motion: body waves

The equation of motion, expressed by Eqs. (2.10) or (2.11), respectively, generally has two solutions, see, e.g., [Shearer, 1999], [Antes, 2002], or [Aki and Richards, 2002]. Those two solutions are the wave equations for two wave types, called primary (*P*-)waves and secondary (*S*-)waves. The characteristics of those waves, which are summarised under the term *body waves*, can be revealed from those equations.

For the derivation of the body wave equation, it is convenient to state the displacement vector $\mathbf{u}$ as superposition of the two wave types. Using the Helmholtz decomposition theorem, gives

$$\mathbf{u} = \mathbf{u}_P + \mathbf{u}_S = \nabla\varphi + \nabla \times \boldsymbol{\Psi} \,. \tag{2.19}$$

The displacement addend $\mathbf{u}_P = \nabla\varphi$ describes the divergence, whereas $\mathbf{u}_S = \nabla \times \boldsymbol{\Psi}$ represents the curl of the equation of motion. Thereby, φ and $\boldsymbol{\Psi} = [\Psi_x \Psi_y \Psi_z]^T$ are the so-called scalar and vector potentials, respectively. From the definitions of divergence Eq. (A.12) and curl Eq. (A.13), it can be recognised that $\nabla\varphi$ describes irrotational, volume-changing strains, whereas $\nabla \times \boldsymbol{\Psi}$ describes rotational, equivoluminal strains. Furthermore, assuming that the body force vector $\mathbf{b}$ can be decomposed in the same way into a divergence and a curl part, leads to the representation

$$\mathbf{b} = \nabla b + \nabla \times \mathbf{B} \,. \tag{2.20}$$

2.2.1 *P*-waves

The first type of body waves can be derived by analysing the irrotational properties of the equation of motion. Taking for that purpose the divergence of Eq. (2.11), using the vector identity $\nabla(\nabla \times \boldsymbol{\Psi}) = 0$ and recalling Eq. (2.19), yields the first wave equation

$$\frac{2\mu + \lambda}{\rho} \nabla^2 \mathbf{u}_P - \frac{\partial^2 \mathbf{u}_P}{\partial t^2} = \frac{1}{\rho} \nabla b \,. \tag{2.21}$$

Using the potential form of Eq. (2.19) and rearranging Eq. (2.21), the first wave equation can also be stated as

$$\frac{\partial^2 \varphi}{\partial t^2} = c_P^2 \nabla^2 \varphi + b \,, \tag{2.22}$$

where

$$c_P = \sqrt{\frac{2\mu + \lambda}{\rho}} \tag{2.23}$$

is the velocity at which the first kind of waves, called *P*-waves, propagate through a body. Using Eqs. (2.12) and (2.13) and introducing the bulk modulus $K = \lambda + 2\mu/3$, the *P*-wave velocity can also be expressed in terms of the material parameters G, K, ν and ρ:

$$c_P = \sqrt{\frac{G(2-2\nu)}{\rho(1-2\nu)}} = \sqrt{\frac{\frac{4}{3}G + K}{\rho}} \,. \tag{2.24}$$

Since the curl of divergence vanishes, i.e., $\nabla \times \mathbf{u} = \nabla \times \nabla\varphi = 0$, the motion of *P*-waves is curl-free or irrotational. In other words, the deformations due to this kind of wave do not have shearing or rotational components and only introduce volume changes in the material. That is why *P*-waves are also called *compressional* or *dilatational* waves. However, it should be noted that *P*-waves involve shearing as well as compression This can be seen in Eq. (2.24) in which both bulk and shear moduli G and K are contained.

The displacements occurring from a plane *P*-wave are shown in Fig. 2.1(a). The wave induced compressions and dilatations in propagation direction can be realised (*P*-waves are also called *longitudinal* waves). Since solids behave stiffest under volume-changing deformation *P*-waves have, compared to other wave types, the highest propagation velocity. This explains why they are called *P*-, i.e., *primary*, waves.

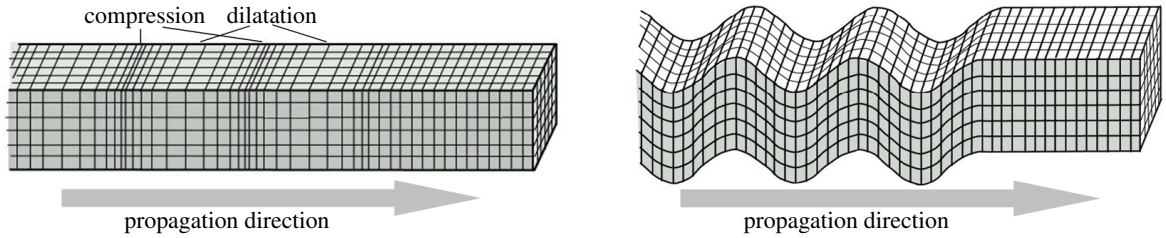

(a) P-wave: Displacements occurring from a plane *P*-wave, where the particle motion into propagation direction produces compression and dilatation zones.

(b) S-wave: Displacements occurring from a plane *S*-wave, where the particle motion perpendicular to the propagation direction produces equivoluminal shear deformations.

Figure 2.1: Displacements occurring from body waves (after [Department of Earth Science, 2007]) .

2.2.2 *S*-waves

The second type of body waves can be obtained by taking the curl of the equation of motion Eq. (2.11):

$$\frac{\partial^2(\nabla\times\mathbf{u})}{\partial t^2} = -\frac{\mu}{\rho}\nabla\times\nabla\times(\nabla\times\mathbf{u}) + \frac{1}{\rho}\nabla\times\mathbf{B} \tag{2.25}$$

Using the vector identities $\nabla\times\nabla\times\mathbf{u} = \nabla\nabla\mathbf{u} - \nabla^2\mathbf{u}$ and $\nabla(\nabla\times\mathbf{u}) = 0$, this equation becomes with Eq. (2.19)

$$\frac{\mu}{\rho}\nabla^2\mathbf{u}_S - \frac{\partial^2\mathbf{u}_S}{\partial t^2} = \frac{1}{\rho}\nabla\times\mathbf{B}\,. \tag{2.26}$$

Again, the potential form of this wave equation can be deduced by rearranging:

$$\frac{\partial^2\boldsymbol{\Psi}}{\partial t^2} = c_S^2\nabla^2\boldsymbol{\Psi} + \mathbf{B}\,, \tag{2.27}$$

where this time the wave velocity is

$$c_S = \sqrt{\frac{\mu}{\rho}} \quad \text{or} \quad c_S = \sqrt{\frac{G}{\rho}}\,. \tag{2.28}$$

The waves described by Eq. (2.27) are called *S*-waves, where the *S* stands for *secondary* or *shear*. Like the latter name implies, the motion of *S*-waves induces pure shear without any volume changes. Therefore, *S*-waves are also called *equivoluminal* or *distortional* waves. The reason for the pure shear motion is that divergence vanishes in Eq. (2.27), because of $\nabla\mathbf{u} = \nabla(\nabla\times\boldsymbol{\Psi}) = 0$. This behaviour can also be recognised when looking at the *S*-wave velocity in Eq. (2.28), which only contains the shear modulus *G*.

The displacements due to a plane *S*-wave are shown in Fig. 2.1(b). The medium's particles are moving perpendicular to the wave propagation direction. Therefore *S*-waves are also called *transversal* waves. Since the perpendicular particle motion has horizontal and vertical components with respect to the propagation direction, the *S*-wave is often divided into these two components: the horizontal *SH*-wave and the vertical *SV*-wave.

For the *S*-wave velocity is proportional to the shear modulus *G* (see Eq. (2.28)), this kind of wave can only occur in solids and never in Newtonian fluids or gases, where no shear resistance exists. *S*-waves are slower than *P*-waves, but still faster than surface waves which will be addressed later.

2.2.3 Equation of motion in terms of body wave velocities

For completeness reasons, it should be stated that Navier's equations of motion given in Eqs. (2.10) or (2.11) can also be expressed by means of the two body wave velocities from Eqs. (2.23) and (2.28)

instead of Lamé's constants. This is in index notation (compare Eq. (2.10))

$$c_S^2 u_{i,jj} + (c_P^2 - c_S^2) u_{j,ij} + \frac{b_i}{\rho} = \ddot{u}_i \tag{2.29}$$

or in vector form (compare Eq. (2.11))

$$c_P^2 \nabla\nabla\mathbf{u} - c_S^2 \nabla \times \nabla \times \mathbf{u} + \frac{\mathbf{b}}{\rho} = \ddot{\mathbf{u}} \,. \tag{2.30}$$

2.3 Solutions of the equation of motion in finite bodies: surface waves

So far, the treatment was limited to body waves, i.e., to waves that occur in a full-space. Considering a finite space, like the earth, other solutions of the equation of motion, Eq. (2.10), as the two discussed above (*P*- and *S*-waves), become available. The waves described by those additional solutions are called *surface waves*.

At a teleseismic distance, surface waves are generally the strongest recorded waves during an earthquake. Compared to body waves, surface waves propagate slower, their amplitude decay with range is generally much less, and they travel at strongly frequency-dependent velocities.

Although, there exists a number of surface waves, especially for higher-modes, there are basically two types of those waves which are important for seismic analyses, because they are travelling along the earth's surface. The first type of waves are called *Rayleigh waves*. For lateral homogeneous media those waves are radially polarised waves, i.e., they arise from interfering *P*- and *SV*-waves and exist at any free surfaces. The second type of waves, named *Love waves*, are transversely polarised waves, i.e., they are generated from interferences between reflected *SH*-waves. Hence, Love waves require a velocity increase with depth or a spherical body geometry.

This section gives an overview of the derivation of the constituting equations and describes the characteristics for the two important surface waves for seismic considerations, the Rayleigh waves and Love waves.

2.3.1 Rayleigh waves

As already discussed, Rayleigh waves occur from interferences between *P*- and *SV*-waves at the surface. Even though incident and reflected body waves do not sum up for this case constructively to produce surface waves, a solution for inhomogeneous waves trapped at the interface is possible.

Assume a homogeneous body with a surface described by the *x*-*y*-plane of a Cartesian coordinate system and the *z*-coordinate pointing downward into the body. In order to start with the examination of the phenomenon of the *P*- and *SV*-waves interaction with a free surface, the horizontal and vertical slowness p and η, respectively, will be defined as

$$p = c^{-1} = k/\omega \quad \text{and} \tag{2.31}$$

$$\eta = \sqrt{(c^{-2} - p^2)} \,, \tag{2.32}$$

with c being the wave velocity, k the wavenumber, and ω the angular frequency. Therewith, the displacements $\mathbf{u}$ for harmonic plane waves propagating in positive x-direction in a lateral homogeneous medium can be stated as

$$\mathbf{u} = \mathbf{A} e^{-i\omega(t - px - \eta z)} \,. \tag{2.33}$$

Recall that the displacements $\mathbf{u}$ can be expressed by the *P*-wave scalar potential φ and the *S*-wave vector potential $\mathbf{\Psi} = [\Psi_x \Psi_y \Psi_z]^T$, namely $\mathbf{u} = \nabla\varphi + \nabla \times \mathbf{\Psi}$ (Eq. (2.19)). Then, the plane wave solutions for φ

and Ψ_y (the only component of $\boldsymbol{\Psi}$ that produces *SV* motion for plane wave propagation in *x*-direction) are

$$\varphi = Ae^{-i\omega(t-px-\eta_P z)} \quad \text{and} \tag{2.34}$$

$$\Psi_y = Be^{-i\omega(t-px-\eta_S z)} , \tag{2.35}$$

where A and B are the amplitudes of the *P*- and *SV*-waves, respectively. Analogously to Eq. (2.32), the vertical slownesses are given here by $\eta_P = \sqrt{c_P^{-2} - p^2}$ and $\eta_S = \sqrt{c_S^{-2} - p^2}$.

Assuming that *P*- and *SV*-waves have the same horizontal slowness $p = const$ and noting that u_y and all derivatives in *y*-direction are zero for a plane *P*/*SV*-wave, the displacements of *P*- and *SV*-waves in *x*- and *z*-direction can be written by using Eqs. (2.34) and (2.35) as

$$u_x^P = \varphi_{,x} = pAi\omega e^{-i\omega(t-px-\eta_P z)} , \tag{2.36}$$

$$u_z^P = \varphi_{,z} = \eta_P Ai\omega e^{-i\omega(t-px-\eta_P z)} , \tag{2.37}$$

$$u_x^S = \psi_{y,z} = \eta_S Bi\omega e^{-i\omega(t-px-\eta_S z)} \quad \text{and} \tag{2.38}$$

$$u_z^S = -\psi_{y,x} = -pBi\omega e^{-i\omega(t-px-\eta_S z)} . \tag{2.39}$$

Considering now the stresses $\sigma_{xz} = \mu(u_{x,z} + u_{z,x})$ and $\sigma_{zz} = \lambda(u_{x,x} + u_{z,z}) + 2\mu u_{z,z}$, which can be derived from Eqs. (2.8) and (2.9), those equations can be rewritten by substituting the displacements from Eqs. (2.36) to (2.39) as

$$\sigma_{xz}^P = -A(2\mu p\eta_P)\omega^2 e^{-i\omega(t-px-\eta_P z)} , \tag{2.40}$$

$$\sigma_{zz}^P = -A\left[(\lambda+2\mu)\eta_P^2 + \lambda p^2\right]\omega^2 e^{-i\omega(t-px-\eta_P z)} , \tag{2.41}$$

$$\sigma_{xz}^S = B\mu\left(p^2 - \eta_S^2\right)\omega^2 e^{-i\omega(t-px-\eta_S z)} \quad \text{and} \tag{2.42}$$

$$\sigma_{zz}^S = B(2\mu\eta_S p)\omega^2 e^{-i\omega(t-px-\eta_S z)} . \tag{2.43}$$

At the stress free surface $z = 0$, the stress components are $\sigma_{xz} = \sigma_{xz}^P + \sigma_{xz}^S = 0$ and $\sigma_{zz} = \sigma_{zz}^P + \sigma_{zz}^S = 0$. Applying those boundary conditions to Eqs. (2.40) to (2.43) yields

$$A\left[2p\eta_P\right] - B\left[p^2 - \eta_S^2\right] = 0 \quad \text{and} \tag{2.44}$$

$$A\left[(\lambda+2\mu)\eta_P + \lambda p^2\right] - B\left[2\mu\eta_S p\right] = 0 . \tag{2.45}$$

With Eqs. (2.23) and (2.28), Eq. (2.45) can be written as

$$A\left[c_P^2(\eta_P^2 + p^2) - 2c_S^2 p^2\right] - B\left[2c_S^2\eta_S p\right] = 0 . \tag{2.46}$$

Eqs. (2.44) and (2.46) describe the free surface boundary conditions for *P*- and *SV*-waves with the horizontal slowness p.

Consider now the case where the analysed wave is slower than the body waves, i.e., the case for which $p > c_S^{-1} > c_P^{-1}$ is valid. Then, according to Eq. (2.32), both η_P and η_S are imaginary. By factoring out the depth dependence in Eq. (2.33), the displacements for harmonic plane waves can be expressed as

$$\mathbf{u} = \mathbf{A}e^{i\omega\eta z}e^{-i\omega(t-px)} . \tag{2.47}$$

Here, it can be realised that an imaginary value of η will result in a real value in the exponent. That means that the amplitudes of waves described by this equation grow or decay exponentially as a function of depth. When choosing the sign of η to give the decaying solution, the linear system of equations (2.44) and (2.46) has a non-trivial solution for single imaginary values of η_P and η_S only when the determinant vanishes. That is, when

$$(p^2 - \eta_S^2)\left[c_P^2(\eta_P^2 + p^2) - 2c_S^2 p^2\right] - 4c_S^2 p^2\eta_P\eta_S = 0 . \tag{2.48}$$

This equation can be expressed entirely in terms of p, c_P and c_S by substituting the vertical slownesses η_P and η_S and recalling that $p > c_S^{-1} > c_P^{-1}$ is valid:

$$\left(2p^2 - \frac{1}{c_S^2}\right)^2 - 4p^2\sqrt{p^2 - \frac{1}{c_P^2}}\sqrt{p^2 - \frac{1}{c_S^2}} = 0\,. \tag{2.49}$$

This equation is called *Rayleigh function* and has a single solution with an exact value of p which is depending on the body wave velocities c_P and c_S. The corresponding wave velocity $c_R = 1/p$, the Rayleigh wave velocity, is slightly smaller than the shear wave velocity c_S and lies within the range $0.8741 \leq c_R/c_S \leq 0.9554$. By deriving the function Eq. (2.49), [Rayleigh, 1885] proved for the first time the possibility of a surface wave consisting of coupled *P*- and *SV*-waves which is travelling on a stress free surface.

From the intermediate results of the derivation of the Rayleigh function, the horizontal and vertical displacements u_x and u_z can be determined. Those expressions depend besides the wave amplitude on the body wave velocities c_P and c_S, i.e., the material properties, and the Rayleigh wave length $\lambda_R = 2\pi c_R/\omega$. The qualitative development of the two components of the amplitude in dependency of depth over wave length z/λ_R is shown in Fig. 2.2(a) for varying Poisson's ratios ν. It can be recognised that the strongest motion of Rayleigh waves occurs in vicinity to the surface and decays rapidly with depth to about not more than a fifth of the surface amplitude at a depth of $z = 1.3\lambda_R$. Note also that the vertical component of the amplitude is maximal at a depth of $z = 0.1 \div 0.2\lambda_R$ and not at the surface. This fact is very important for the seismic analysis of buried pipelines whose burial depths lie in the same range as the maximal vertical displacement amplitude of Rayleigh waves.

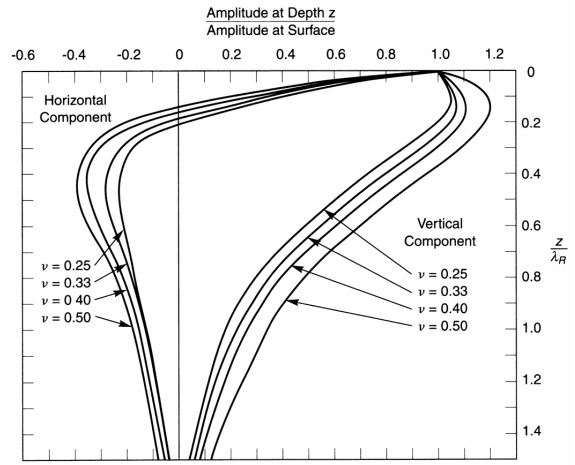

(a) Rayleigh-wave amplitude components in vertical and horizontal direction in dependency of depth z over wave length λ_R for varying Poisson ratio ν (from [Kramer, 1996] after [Richart *et al.*, 1970]).

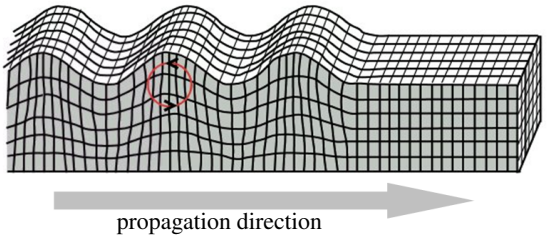

(b) Displacements occurring from a Rayleigh wave, where the particles are moving in a retrograde ellipse with respect to the propagation direction and the motion decays exponentially with depth (after [Department of Earth Science, 2007]) .

Figure 2.2: Rayleigh wave properties.

The graphs of Fig. 2.2(a) supply also information about the particle motion of Rayleigh waves. Since the horizontal displacements will be about zero when the vertical displacements reach their extreme value, the particles move in a retrograde ellipse as is shown in Fig. 2.2(b), where the general motion of Rayleigh waves is illustrated. In seismology, the minimum epicentral distance at which Rayleigh waves occur in a homogeneous medium in dependency on the focal depth $\hat{h}$, the *P*- and Rayleigh wave velocities c_P and

c_R, respectively, is given by [Ewing *et al.*, 1957] as

$$R = \frac{\hat{h}}{\sqrt{(c_P/c_R)^2 - 1}} \,. \tag{2.50}$$

2.3.2 Love waves

Love waves [Love, 1927] are transversely polarised waves which arise from constructive interfering *SH*-waves reflected at interfaces between layers with different material properties. Because of this constructive interference it is possible to model those surface-waves as a sum of body waves.

An elementary case in which Love waves occur is used here to demonstrate their origin and their basic dispersion properties. In this case, a plane wave is propagating in a half-space consisting of a single homogeneous layer overlying a homogeneous half-space (Fig. 2.3(a)). Let the rigidies and densities be μ_1 and ρ_1 for the surficial layer and μ_2 and ρ_2 for the half-space. Assume again Cartesian coordinates where the z-coordinate is pointing downward with $z = 0$ at the surface of the half-space and $z = h$ at the layer interface.

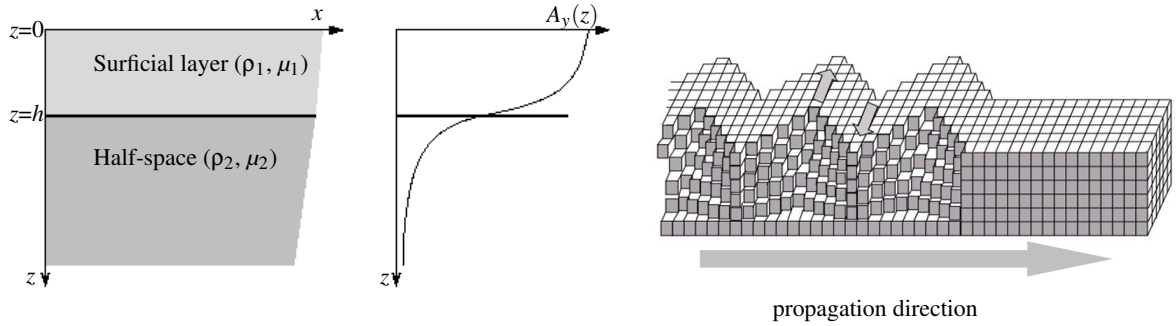

(a) Half-space consisting of a homogeneous surficial layer and an underlying homogeneous half-space with different material properties.

(b) Depth dependency of particle displacement amplitude A_y for Love waves.

(c) Displacements occurring from a Love wave, where the particles are moving horizontally perpendicular to the propagation direction and the motion decays sinusoidally in the surficial layer and exponentially in underlying half-space (after [Department of Earth Science, 2007]) .

Figure 2.3: Love wave properties.

A horizontal wave is examined which propagates in x-direction with a particle motion parallel to the surface and perpendicular to the propagation direction. This wave is a *SH*-wave which has only displacements in the y-direction u_y. The scalar homogeneous equations of motion for this one-dimensional problem are

$$\ddot{u}_{y1} = c_{S1}^2 \nabla^2 u_{y1} = c_{S1}^2 \left(u_{y1,xx} + u_{y1,zz}\right) \quad \text{for the surface-layer } 0 \le z \le h \text{ and} \tag{2.51}$$

$$\ddot{u}_{y2} = c_{S2}^2 \nabla^2 u_{y2} = c_{S2}^2 \left(u_{y2,xx} + u_{y2,zz}\right) \quad \text{for the half-space } h \le z. \tag{2.52}$$

A solution for those differential equations can be obtained by using the approach from Eq. (2.47), where the vertical dependence is factored out. Hence, the displacements for the two media can be described by the representations

$$u_{y1} = \left[\grave{S}_1 e^{-i\omega\eta_{S1}} + \acute{S}_1 e^{i\omega\eta_{S1}}\right] e^{-i\omega(t-px)} \quad \text{for } 0 \le z \le h \text{ and} \tag{2.53}$$

$$u_{y2} = \left[\grave{S}_2 e^{-i\omega\eta_{S2}} + \acute{S}_2 e^{i\omega\eta_{S2}}\right] e^{-i\omega(t-px)} \quad \text{for } h \le z, \tag{2.54}$$

where η_{S1} and η_{S2} are the vertical slownesses from Eq. (2.32) and p is the horizontal slowness from Eq. (2.31). Now, a representation is sought where the properties of the wave are expressed by terms of

the horizontal slowness $p = k/\omega$ or by its reciprocal value, the phase velocity. Then, the only remaining unknowns are the constant amplitudes $\grave{S}_1$, $\acute{S}_1$, $\grave{S}_2$ and $\acute{S}_2$ which solely depend on z.

Assume that the velocity in the overlying layer is lower than the one in the half-space, i.e., $c_{S1} < c_{S2}$. Because there is no energy supply at infinity $z \to \infty$, i.e., no upcoming waves can be produced there, the amplitude $\acute{S}_2$ vanishes. From the boundary condition $u_{y,z} = 0$ at the stress free surface $z = 0$ follows $\grave{S}_1 = \acute{S}_1$. $\grave{S}_1$ and $\grave{S}_2$ can be determined by the continuity conditions of displacements ($u_{y1} = u_{y2}$) and stresses ($\mu_1 u_{y1,z} = \mu_2 u_{y2,z}$) across the layer/half-space-interface $z = h$. Inserting Eqs. (2.53) and (2.54) into these conditions yields

$$2\grave{S}_1 \cos(-\omega \eta_{S1} h) = \grave{S}_2 e^{-i\omega\eta_{S2}h}\,, \tag{2.55}$$

$$-2\mu_1\,\omega\eta_{S1}\,\grave{S}_1 \sin(-\omega\eta_{S1}h) = \mu_2\, i\,\omega\eta_{S2}\,\grave{S}_2\, e^{-i\omega\eta_{S2}h}\,, \tag{2.56}$$

or combined in one equation

$$\grave{S}_2 = \frac{2\cos(-\omega\eta_{S1}h)}{e^{-i\omega\eta_{S2}h}}\grave{S}_1 = \frac{-2\mu_1\,\eta_{S1}\sin(-\omega\eta_{S1}h)}{\mu_2\, i\,\eta_{S2}\; e^{-i\omega\eta_{S2}h}}\grave{S}_1\,. \tag{2.57}$$

Substituting this term in Eqs. (2.53) and (2.54) gives the displacements u_y occurring from a Love wave:

$$u_{y1}(x,z,t) = 2\grave{S}_1 \cos(\omega\eta_{S1}z)\, e^{-i\omega(t-px)} \quad \text{for } 0 \le z \le h \text{ and} \tag{2.58}$$

$$u_{y2}(x,z,t) = 2\grave{S}_1 \cos(\omega\eta_{S1}z)\, e^{-i\omega\eta_{S2}(z-h)} e^{-i\omega(t-px)} \quad \text{for } h \le z. \tag{2.59}$$

Those equations show that the displacement amplitude varies sinusoidally in the surficial layer and decays exponentially with depth in the underlying half-space (see Fig. 2.3(b)). That is the reason why Love waves are often described as *SH*-waves trapped in a surficial layer. The general behaviour of Love waves is shown in Fig. 2.3(c). Next to the particle motion perpendicular to the propagation direction, the rapid decay of amplitude with depth can be recognised.

When the rearranged Eq. (2.57) is set to zero, the phase velocity eigenvalues of the Love wave $c_L = 1/p$ can be determined as the solution of

$$\tan\left(\omega h\sqrt{c_{S1}^{-2} - c_L^{-2}}\right) = \frac{\mu_2\sqrt{c_L^{-2} - c_{S2}^{-2}}}{\mu_1\sqrt{c_{S1}^{-2} - c_L^{-2}}}\,. \tag{2.60}$$

This equation defines the dispersion curves for Love waves within the layer. Because of the periodicity of the tangent function in Eq. (2.60), multiple values of ω exist for every value of c_L. This indicates that the Love wave velocity c_L ranges between the two *S*-wave velocities c_{S1} of the surficial layer (for high frequencies ω) and c_{S2} of half-space (for low frequencies ω). The values of the Love wave velocity $c_L(\omega)$ have to be determined numerically, since an analytical solution of Eq. (2.60) does not exists.

3 Dynamic soil-structure interaction

In many fields of engineering, problems are addressed where a bounded structure is present with an unbounded medium. The task in such problems is to determine the response of the bounded medium interacting with the unbounded one due to time-varying loads. An emphasis of this thesis is placed on the subject of *dynamic soil-structure interaction*. This term covers all types of problems where the time-dependent behaviour of structures in or on the soil is described. In those problems, the soil is assumed to be an unbounded, i.e., an infinite or semi-infinite medium. Other examples for the general problem in wave propagation analyses are fluid-structure interaction, geophysics, acoustics and electromagnetism.

The so-called *radiation condition* is the key to a sound analysis of dynamic soil-structure interaction problems. This condition requires the unboundness of the whole domain under consideration to avoid wave reflections at artificial boundaries that are not present in reality but exist due to model constraints. This chapter is opened with a brief statement of that condition.

Generally, the methods for analysing dynamic soil-structure interaction problems can be classified into two main groups: the substructure method and the direct method [Wolf, 1988; Antes and Spyrakos, 1997; Tsynkov, 1998]. Depending on this classification, a rigorous or an approximate modelling of the unbounded domain is demanded. In the second section of this chapter, the two methods for examining wave radiation problems and their different approaches are introduced. Thereupon, the two mentioned types of modelling, the *rigorous modelling* and the *approximate modelling*, are described in the subsequent sections and brief outlines of their well-established realisations are given.

3.1 Radiation condition

The central topic in dynamic soil-structure interaction is the question how to treat the dynamic behaviour at infinity of the unbounded soil. Thereto, the unbounded soil has to fulfil the condition that no energy may radiate from infinity into the structure-soil system. In other words, the reflection of waves at infinity back into the domain under consideration has to be avoided.

The description of a unique solution of the response of the unbounded medium in mathematical terms requires, next to the governing equations of elastodynamics and the initial and boundary condition stated in Chap. 2, the definition of an additional boundary condition. Since, a condition of vanishing displacements is insufficient [Wolf, 1985], a boundary condition has to be defined which allows to transfer energy from the bounded to the unbounded domain irreversibly and omit reflections at the interface of those two domains. This condition is termed radiation condition.

The detailed proof of the derivation of the radiation condition was done for the first time by [Sommerfeld, 1949]. Hence, the term *Sommerfeld's radiation condition* is also common. Here, only the conclusions are briefly stated. For an extended discussion refer to, e.g., [Wolf and Song, 1996].

In frequency-domain, the radiation condition is formulated at infinity. Since this work deals with dynamic problems in time-domain, this case is not closer addressed. The radiation condition in time-domain is formulated at a boundary at a finite distance from the domain under consideration. This boundary has to be chosen such that no displacements exist outside the boundary. The domain of influence, i.e., the excited internal domain, at a specific time is defined as the part of the unbounded medium which is surrounded by the wave-front of the fastest wave type, i.e., the *P*-wave. With each increase of time the

domain of influence grows. That means, that the medium adjacent to the former wave-front is excited. Since this process requires energy which is deprived from the previous domain of influence, a damping effect can be realised which is called *radiation damping*.

At the interface of the bounded and unbounded domain, the initial response due to a load can be determined. Assuming an unbounded domain that is initially at rest and applying a load per unit area p during the first infinitesimal time, leads to a description for the initial response perpendicular to the interface of bounded and unbounded domain

$$p = \rho c_P \dot{u} \, . \tag{3.1}$$

It can be recognised that the initial response p is modelled by a dashpot with a coefficient consisting of density ρ and P-wave velocity c_P. This coefficient ρc_P is called *impedance*. Analogously, the initial response in tangential direction is formulated by means of the S-wave velocity c_S as

$$p = \rho c_S \dot{u} \, . \tag{3.2}$$

For the implementation of the introduced radiation conditions in numerical models, generally two methods can be distinguished which are explained in the following.

3.2 Substructure and direct method

The approaches for the numerical modelling of dynamic soil-structure interaction problems can be classified in substructure methods and direct methods. In any case, the bounded medium of finite dimensions can be modelled by a domain procedure with a finite number of degrees of freedom. Usually, and also in this work, the finite element method is incorporated. This part of the analysis is well-established and allows a detailed modelling of the so-called *near-field*.

The unbounded medium, in contrast, has infinite dimensions and, therefore, cannot be modelled with a finite number of degrees of freedom without a special treatment. The first step of that treatment is to choose an *interaction horizon*. This horizon has to embrace the structure, but the distance to the structure can be chosen arbitrarily and has no physical significance. Due to this arbitrariness, two extreme positions of the interaction horizon are possible. Firstly, the horizon is identical to the interface of bounded and unbounded domain. This case leads to the *substructure method* and is sketched in Fig. 3.1(a). To achieve sufficient accuracy, it is necessary to enforce *rigorous boundary conditions* to prevent wave reflections at the interaction horizon.

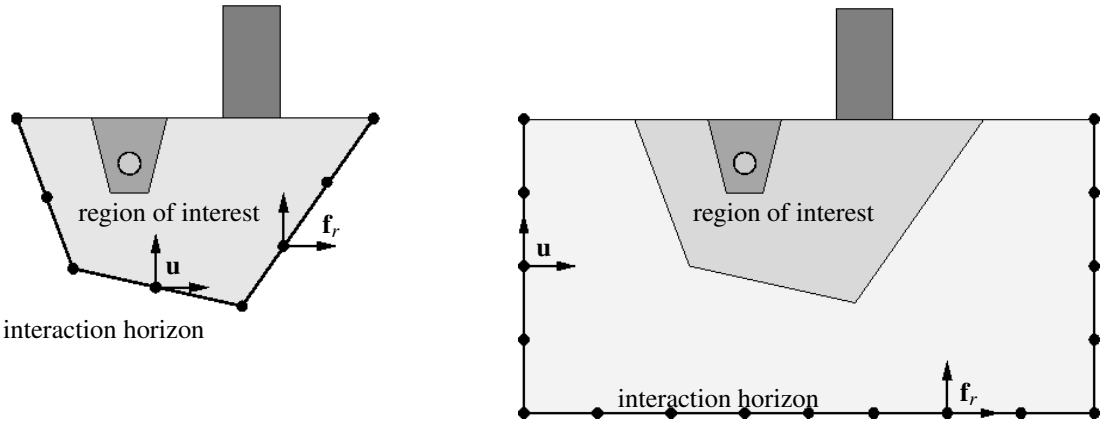

(a) Substructure method: interaction horizon is identical to interface of bounded and unbounded domain.

(b) Direct method: interaction horizon is an artificial boundary at a certain distance to region of interest.

Figure 3.1: Considered domains and interaction horizon for substructure and direct method.

Secondly, the interaction horizon is placed at a certain distance to the bounded domain. So, the part of the unbounded domain inside the horizon can also be modelled with a finite domain procedure. This is called the *direct method*. Ideally, when the medium at the interaction horizon is nearly at rest, i.e., if the waves that are reflected into the domain under consideration are neglectable, no boundary condition needs to be applied. Since such domains have huge extensions, the effort for meshing and computation is often not justifiable, e.g., in seismic problems. Therefore, smaller domains have to be chosen and *approximate boundary conditions* and, thus, simpler ones than for the substructure method can be applied.

Both types of boundary conditions, the rigorous and the approximate, are formulated in the degrees of freedom of the nodes on the interaction horizon. Hence, the conditions are equal to the relationship between the interaction force $\mathbf{f}_r$ and the displacement $\mathbf{u}$ displayed in Fig. 3.1. Depending on the kinds of boundary conditions, the methods for modelling the response of the unbounded domain can be grouped into the more advanced rigorous modelling and into the more simplified approximate modelling.

3.3 Rigorous modelling with global procedures

As explained before, the rigorous modelling of the unbounded domain is performed when the dynamic soil-structure interaction problem is analysed with the substructure method. In this method, the entire domain is subdivided into a near-field which is the region of interest where the examined structure is present, and into a far-field being the unbounded domain (see Fig. 3.1(a)).

As already discussed, the boundary condition defined at the nodes of interaction horizon is equal to the interaction force $\mathbf{f}_r$ - displacement $\mathbf{u}$ relationship. For time-domain analyses, this stiffness relationship in its rigorous form is *global in time and space*. This means that the interaction force $f_r(x_i,t)$ of a specific degree x_i of freedom at a specific time t depends on the displacements corresponding to all degrees of freedom at all previous times. This dependency follows from the fact that an unit impulsive force applied in a specific degree of freedom will lead to responses in all degrees of freedom (spatial globality) also at all later times (temporal globality).

The interaction force-displacement relationship is used in the substructure method in its rigorous form providing the same accuracy as for the discretised bounded medium. The total dynamic system of the bounded and unbounded domain can be described by assembling the interaction force-displacement relationship of the unbounded medium with the equations of motion of the bounded medium.

In the following, the established rigorous procedures used in substructure analyses are addressed, namely the *boundary element method*, the *thin layer method*, the *exact non-reflecting boundary conditions*, and the *scaled boundary finite element method*. As the latter is an essential part of this thesis and the developed methodology, a whole chapter (Chap. 6) is dedicated to its idea, derivation and evolutions. Hence, the scaled boundary finite element method is addressed in this section only in brief to show its fields of application. In contrast, the boundary element method is attended in the present chapter somewhat more extended, because this method, though it is not an integral part of the introduced methodology of this thesis, will be used in Sec. 9.2 as a first application to show the potentials of the later introduced domain reduction method (Sec. 7.2).

3.3.1 Boundary element method

The boundary element method (BEM) is a numerical approximation method to solve differential equations. Such methods are well-established in engineering sciences where they are used for complex problems which cannot be solved analytically.

Using the interaction force-displacement relationship in its rigorous form, the radiation condition has to be satisfied which enforces that no energy is radiated from infinity. The radiation condition can be incorporated in certain analytical solutions. Those solutions can be used as so-called *fundamental solutions* to formulate the boundary integral equation, which discretised form is the BEM. Detailed derivations and application examples of the BEM can be found, e.g., in [Beer, 2001; Antes, 2002; Wrobel

and Aliabadi, 2002; Gaul *et al.*, 2003]. Therefore, only some basic properties are discussed and the derivation is outlined.

Idea: One possibility to solve partial differential equations is the *method of weighted residuals*. Via this method, a differential equation is transferred from its strong form to an integral and therewith to a weak expression where the integrand is multiplied with a *weighting function*. The idea of this method is that the differential equation is not exactly fulfilled in its defined domain. Thus, an error is accepted which is requested to vanish when integrating over the domain. This request is accomplished by the multiplication of the error, the *residual*, with a weighting function such that this product vanishes under the integral. Whereas in the general application of the method of weighted residuals this weighting function is chosen arbitrary, it is the fundamental solution in the BEM. Through this procedure, the derivatives from the partial differential equations can be shifted to the weighting functions, i.e., to the fundamental solutions, incorporating integration by parts. The aim is to keep only the searched function in its undifferentiated form as sole unknown.

Comparison to FEM: Both the BEM and the most known and widely-used numerical approximation method, the later discussed finite element method (FEM) (Chap. 5), have in common that they are discretisation procedures. Those procedures yield an algebraic system of equations from spatial and temporal discretisations of the analysed problem. The advantage of the BEM over the FEM is that problems are described solely through quantities on the boundary. Therefore, only the boundary and not the whole analysed domain, like in the FEM, has to be discretised. Hence, the spatial dimension of the problem is, compared to domain procedures, reduced by one. Nevertheless, utilising the BEM, the solution of a problem can be obtained for any location inside the domain once the boundary values are determined. The BEM is well suited to model an unbounded domain, as the fundamental solution satisfies the boundary conditions at infinity exactly.

Disadvantageous to the FEM is the appearance of a fully populated and usually non-symmetric system of equations in the BEM. Exceptions, where symmetry could be implemented in BE methods are given, e.g., [Bonnet *et al.*, 1998] or [Lehmann and Antes, 2001]. Its solution enforces a strong increase of the computational effort compared to the FEM which provides symmetric sparse coefficient matrices. Furthermore, for the utilisation of the BEM, the knowledge of a fundamental solution of the differential equations is necessary. Even though there exist many remarkable high-order BE-methods, the treatment of inhomogeneous and non-linear problems with the BEM still becomes difficult with increasing complexity of the analysed problem. The adaptability is limited not least due to the fact that a fundamental solution is not always available.

To avoid the respective drawbacks of the two numerical methods, substructure coupling procedures where suggested by [Antes, 1989; Coifman *et al.*, 1993; Antes *et al.*, 1995; von Estorff and Firuziaan, 2000; Nishimura, 2002] where each method is applied profitably, i.e., the FEM for the detailed modelling of the near-field, and the BEM for simulating the response of the unbounded domain.

3.3.1.1 Fundamental solution

In the BEM, the fundamental solution of the treated differential equation is employed as weighting function. In mathematical terms, a fundamental solution is the solution of the homogeneous differential equation in every point $\mathbf{x}$ except the source point $\boldsymbol{\xi}$ where it exhibits a singularity. In other words, fundamental solutions are analytical free space solutions of the governing differential equations under the action of a point source. Physically interpreted, fundamental solutions describe the response of an infinite continuum due to an impulsive unit force. The radiation condition is satisfied implicitly as part of the fundamental solution.

The mentioned impulsive unit excitation $\mathbf{b}$ which generates the response of the continuum described by

the fundamental solution, can be characterised in mathematical form as

$$b_i^*(\mathbf{x},\boldsymbol{\xi},t,\tau) = \delta(t-\tau)\delta(\mathbf{x}-\boldsymbol{\xi})\delta_{ij}\,. \tag{3.3}$$

The fundamental solution quantifies the response of the continuum at a field-point $\mathbf{x}$ of time t in consequence of a Dirac impulse δ which is pointing in the direction of the unit-vector, displayed by Kronecker's symbol δ_{ij}, and is applied at the source point $\boldsymbol{\xi}$ of time τ. The continuum reacts on this excitation $\mathbf{b}^*(\mathbf{x},\boldsymbol{\xi},t,\tau)$ with the displacement field $\mathbf{u}^*(\mathbf{x},\boldsymbol{\xi},t,\tau)$. Because an impulsive excitation in one direction causes displacements in all spatial directions, $\mathbf{u}^*$ has the form of a tensor.

For an elastic, infinite medium, the fundamental solution $\mathbf{u}^*$ can be derived via adopting the load $\mathbf{b}^*$ from Eq. (3.3) into Navier's equation (2.10):

$$\rho\ddot{u}_{ij}^*(\mathbf{x},\boldsymbol{\xi},t,\tau) - \mu u_{ij,kk}^*(\mathbf{x},\boldsymbol{\xi},t,\tau) - (\mu+\lambda)u_{kj,ik}^*(\mathbf{x},\boldsymbol{\xi},t,\tau) = \delta(t-\tau)\delta(\mathbf{x}-\boldsymbol{\xi})\delta_{ij}\,. \tag{3.4}$$

Employing Cauchy's theorem (2.2), Hooke's law (2.8) and the strain-displacement relationship (2.9) in Eq. (3.4) yields the fundamental solution of the stress vector $\mathbf{t}^*$ for the elastodynamic full-space. This fundamental solution is derived in, e.g., [Stokes, 1849; Bonnet, 1995; Gaul *et al.*, 2003; Kausel, 2006].

Generally, fundamental solutions in time-dependent problems exhibit, in addition to the characteristics stated above, three attributes: *translation*, *reciprocity* and *causality* [Gaul *et al.*, 2003]. Translation means, that solely the difference in space and time, respectively, between source point and field point is crucial. Reciprocity enables the permutability of source and field point and of load and observation time. Causality assures that a point is not excited before the *P*-wave arrival.

3.3.1.2 Derivation of boundary integral equation

As stated above, the determination of displacements from the Navier's equation (2.11) can be achieved by the method of weighted residuals. This method yields a boundary integral equation which describes the dynamic response of the analysed domain. Several methods exist to obtain this boundary integral equation. Here, the *reciprocal work theorem* [Wheeler and Sternberg, 1968] is utilised which actually is a generalisation of *Betti's theorem* [Betti, 1872] for elastodynamics.

Reciprocal work theorem: Consider two elastodynamic states $\left[u_i^I, t_i^I, b_i^I\right]$ and $\left[u_i^{II}, t_i^{II}, b_i^{II}\right]$ which are uniquely determined in the domain Ω, with the initial conditions $\left[u_i^I(\mathbf{x},0), \dot{u}_i^I(\mathbf{x},0)\right] = \left[u_{i0}^I(\mathbf{x}), v_{i0}^I(\mathbf{x})\right]$ and $\left[u_i^{II}(\mathbf{x},0), \dot{u}_i^{II}(\mathbf{x},0)\right] = \left[u_{i0}^{II}(\mathbf{x}), v_{i0}^{II}(\mathbf{x})\right]$, respectively. The reciprocal work theorem states that the work of the forces b_i^I on the displacements u_i^{II} are equal to the work of the forces b_i^{II} on the displacements u_i^I. With this, the *reciprocity identity of elastodynamics* can be derived for times $t > 0$, as shown in [Bonnet, 1995; Gaul *et al.*, 2003]:

$$\begin{aligned}
&\int_\Gamma t_i^I * u_i^{II} d\Gamma_x + \int_\Omega \left(b_i^I * u_i^{II} + \rho\left\{ v_{i0}^I \cdot u_i^{II} + u_{i0}^I \cdot \dot{u}_i^{II} \right\} \right) d\Omega_x \\
&= \int_\Gamma t_i^{II} * u_i^I d\Gamma_x + \int_\Omega \left(b_i^{II} * u_i^I + \rho\left\{ v_{i0}^{II} \cdot u_i^I + u_{i0}^{II} \cdot \dot{u}_i^I \right\} \right) d\Omega_x\,.
\end{aligned} \tag{3.5}$$

By means of the reciprocity identity Eq. (3.5), from one known elastodynamic state, a boundary integral equation for a second unknown state can be derived.

Boundary integral equation: Assuming that the fundamental solutions u_{ij}^* and t_{ij}^* are known. When the body force is now chosen as in Eq. (3.3), the known state is $[u_i^*, t_i^*, b_i^*]$. Because of the causality, the initial conditions vanish implicitly:

$$u_{ij}^*(\mathbf{x},0) = u_{ij0}^* = 0 \quad \text{and} \tag{3.6}$$

$$\dot{u}_{ij}^*(\mathbf{x},0) = v_{ij0}^* = 0\,. \tag{3.7}$$

For the characteristic values of the unknown state for which the boundary integral equation is searched, the indices are omitted in the following: $[u_i, t_i, b_i]$.

Applying the before described assumptions and using the Dirac distribution (A.8) as filter, the domain-integral $b_i^I * u_i^{II} = b_i^* * u_i$ from the reciprocal work theorem given in Eq. (3.5) results in

$$\int_\Omega b_i^* * u_i d\Omega = \int_\Omega \int_0^{t^+} \delta(t-\tau)\delta(\mathbf{x}-\boldsymbol{\xi})\delta_{ij}\, u_i(\mathbf{x},\tau)\, d\tau d\Omega = u_j(\boldsymbol{\xi},t)\ , \tag{3.8}$$

which actually is the weighted residual statement with b_i^* being the weighting function. As mentioned before, a directed impulse-excitation results in displacements in all directions in space. However, the appearance of Kronecker's symbol δ_{ij} in Eq. (3.8) causes vanishing displacements $u_i = 0$ for $i \neq j$. Due to the non-defindness of the filter property of δ_{ij} on the boundary, Eq. (3.8) is only valid for points of the inner domain Ω, but not on the boundary Γ. The integration over time τ in Eq. (3.8) is performed up to the time $t^+ = t + \varepsilon$ with $\varepsilon \to 0$ to avoid a singularity a its end. So, the reciprocity identity for displacements in the inner domain can be derived by adopting Eqs. (3.6) to (3.8) to Eq. (3.5):

$$\int_\Gamma \Big(t_i * u_{ij}^* - t_{ij}^* * u_i \Big) d\Gamma + \int_\Omega \Big(b_i * u_{ij}^* + \rho \left\{ v_{i0} \cdot u_{ij}^* + u_{i0} \cdot \dot{u}_{ij}^* \right\} \Big) d\Omega = u_j(\boldsymbol{\xi},t)\ . \tag{3.9}$$

The determination of the displacements $u_j(\boldsymbol{\xi},t)$ with Eq. (3.9) requires the complete knowledge of the boundary values of stresses and displacements. Indeed, only one boundary condition from Eq. (2.15) or Eq. (2.16) is defined per point .

To potentiate the calculation of the missing boundary values, the source point $\boldsymbol{\xi}$ is shifted to the boundary Γ. If the source point $\boldsymbol{\xi}$ coincides on the boundary with the field point $\mathbf{x}$, the fundamental solution becomes singular. Whereas the Dirichlet fundamental solution u_{ij}^* is *weakly singular*, the Neumann fundamental solution t_{ij}^* is *strongly singular*. In three-dimensional problems, weakly singular means a singularity like $\frac{1}{r}$, and strongly singular means a singularity like $\frac{1}{r^2}$. Another difficulty arises from the fact that the Dirac distribution is not defined on the boundary.

To overcome these difficulties, the singular point $\mathbf{x} = \boldsymbol{\xi}$ is skipped during the integration process and the boundary is augmented by a small extension in the vicinity of this point. Even though the shape of this extension is arbitrary, the use of a spherical extension, as shown in Fig. 3.2, is advantageous.

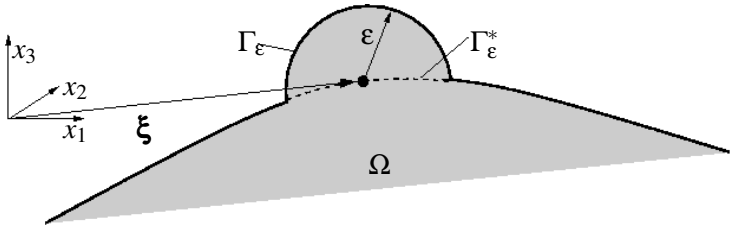

Figure 3.2: Cross section of the three dimensional domain Ω with spherical extension around source point $\boldsymbol{\xi}$.

By taking the limit $\varepsilon \to 0$, i.e., by contracting the boundary extension Γ_ε to the singular point $\boldsymbol{\xi}$, the modified boundary approaches the original boundary $\Gamma = \lim_{\varepsilon\to 0}(\Gamma - \Gamma_\varepsilon^* + \Gamma_\varepsilon)$ and $\boldsymbol{\xi}$ becomes a boundary point again. Eq. (3.9) can then be rewritten as

$$\underbrace{\lim_{\varepsilon\to 0} \int_{\Gamma-\Gamma_\varepsilon^*} \Big(t_i * u_{ij}^* - t_{ij}^* * u_i \Big) d\Gamma}_{\text{boundary integral } BI_1} + \underbrace{\lim_{\varepsilon\to 0} \int_{\Gamma_\varepsilon} \Big(t_i * u_{ij}^* - t_{ij}^* * u_i \Big) d\Gamma}_{\text{boundary integral } BI_2}$$
$$+ \int_\Omega \Big(b_i * u_{ij}^* + \rho \left\{ v_{i0} \cdot u_{ij}^* + u_{i0} \cdot \dot{u}_{ij}^* \right\} \Big) d\Omega = u_j(\boldsymbol{\xi},t)\ . \tag{3.10}$$

Concerning the first integral BI_1, the weakly singular parts, containing u^*_{ij}, exist as improper integrals, i.e., they have in spite of the singularity a finite limit value. The strongly singular parts, containing t^*_{ij}, can be determined by means of *Cauchy's principal value*. For both singular parts, numerical procedures can be found. The second integral BI_2 in Eq. (3.10) yields the so-called *integral free term*. Together with the right part of the equation $u_j(\boldsymbol{\xi},t)$, the boundary matrix c_{ij} is gained. The derivation of c_{ij} is explained, e.g., in [Hartmann, 1981; Mantic, 1993].

With those treatments, the reciprocity identity from Eq. (3.9) reads

$$c_{ij}(\boldsymbol{\xi})u_j(\boldsymbol{\xi},t) = \int_\Gamma t_i(\mathbf{x},\tau) * u^*_{ij}(\mathbf{x},\boldsymbol{\xi},t,\tau)d\Gamma - \oint_\Gamma t^*_{ij}(\mathbf{x},\boldsymbol{\xi},t,\tau) * u_i(\mathbf{x},\tau)d\Gamma$$
$$+ \int_\Omega \Big(b_i(\mathbf{x},\tau) * u^*_{ij}(\mathbf{x},\boldsymbol{\xi},t,\tau) + \rho \left\{ v_{i0}(\mathbf{x}) \cdot u^*_{ij}(\mathbf{x},t) + u_{i0}(\mathbf{x}) \cdot \dot{u}^*_{ij}(\mathbf{x},t) \right\} \Big) d\Omega \,, \tag{3.11}$$

where the C on the second integral denotes Cauchy's principal value. Considering problems without body forces b_i and with vanishing initial conditions v_{i0} and u_{i0}, Eq. (3.11) is reduced to

$$c_{ij}(\boldsymbol{\xi})u_j(\boldsymbol{\xi},t) = \int_\Gamma t_i(\mathbf{x},\tau) * u^*_{ij}(\mathbf{x},\boldsymbol{\xi},t,\tau)d\Gamma - \oint_\Gamma t^*_{ij}(\mathbf{x},\boldsymbol{\xi},t,\tau) * u_i(\mathbf{x},\tau)d\Gamma \,. \tag{3.12}$$

Eq. (3.12) is called *boundary integral equation*. For an arbitrary domain, the integral equation cannot be solved analytically. Therefore, a discretisation is necessary for a solution procedure, leading to a numerical treatment, e.g., the boundary element method. Subsequently, basing on Eq. (3.12), the boundary element formulation is depicted briefly.

3.3.1.3 Boundary element formulation

The boundary element method implies the following successive procedure. Initially, time and space of the domain are discretised. Accordingly, the boundary surface Γ, the time and the boundary conditions are discretised by shape functions (see, e.g., [Beer, 2001; Gaul *et al.*, 2003; Bonnet, 1995; Paris and Canas, 1997]). Whereas the integration in space is performed numerically, the integration in time is analytically.

Introducing the spatial shape functions $N^f_e(\boldsymbol{\eta})$ in Eq. (3.12) and assembling the entire system with E elements and F nodes yields the discretised form of the boundary integral equation

$$c_{ij}(\boldsymbol{\xi})\tilde{u}_i(\boldsymbol{\xi},t) \;\; = \sum_{e=1}^{E}\sum_{f=1}^{F} \left[\int_{\Gamma_e} u^*_{ij}(\mathbf{x},\boldsymbol{\xi},t) N^f_e(\boldsymbol{\eta})\, d\Gamma_e * t^{ef}_i(t) - \oint_{\Gamma_e} t^*_{ij}(\mathbf{x},\boldsymbol{\xi},t) N^f_e(\boldsymbol{\eta})\, d\Gamma_e * u^{ef}_i(t) \right] . \tag{3.13}$$

If body forces should be considered, the first part of the third integral in Eq. (3.11) has to be evaluated. Here, no test functions are necessary because the integrand is a priori known and needs only to be integrated numerically over the domain. In some special cases, e.g., for the gravity force, the domain integral can be shifted on the boundary [Antes and Tröndle, 1992].

The numerical evaluation of the boundary integrals on every discrete point to any discrete time would lead to a non-justifiable computational effort. As stated in Sec. 3.3.1.1, fundamental solutions own the property of translation, i.e., the independence on t but dependence on the difference $(t-\tau)$, which leads to significant simplifications of the evaluation [Schanz, 2001].

After the integration on the boundary, a linear equation system is established. From this equation system, the boundary values are determined by means of a point collocation, i.e., the boundary integral equation is accomplished point wise. Thereon, the originated algebraic equation system has to be solved for the current time-step.

Time-stepping procedure: In the time-discretisation procedure, interpolation functions for the time-variable are introduced and, as stated above, the time-integration is performed analytically in each time-step. This method was first introduced by [Mansur, 1983]. Alternatively, a different time-stepping procedure based on the convolution quadrature can be utilised [Schanz, 2001].

The time-stepping procedure proposed by [Mansur, 1983] and later extended to non-zero initial conditions by [Antes, 1985] approximates the spatial behaviour with polynomial shape functions. Hereon, the time t is discretised in N equal time-steps Δt and also approximated by polynomials, which are generally linear for displacement and constant for traction. A different approach is proposed by [Karabalis and Rizos, 1993] where spline functions are used to approximate the time-history.

Using linear polynomials for the displacements and constant ones for the tractions and inserting those functions in the integral equation (3.12) yields

$$c_{ij}(\boldsymbol{\xi})\tilde{u}_i(\boldsymbol{\xi},t) = \sum_{e=1}^{E}\sum_{f=1}^{F}\sum_{m=1}^{N}\left[\int_{\Gamma_e} N_e^f(\boldsymbol{\eta}) \int_{t_{m-1}}^{t_m} u_{ij}(\mathbf{x},\boldsymbol{\xi},t-\tau)\,d\tau\; d\Gamma_e \right. \\ \left. - \oint_{\Gamma_e} N_e^f(\boldsymbol{\eta}) \int_{t_{m-1}}^{t_m} t_{ij}(\mathbf{x},\boldsymbol{\xi},t-\tau)\left(u_{if}^{em-1}\frac{t_m-\tau}{\Delta t} + u_{if}^{em}\frac{\tau-t_{m-1}}{\Delta t}\right) d\tau\, d\Gamma_e\right] . \tag{3.14}$$

For time-dependent fundamental solutions consist of Dirac distributions and Heaviside functions, the time-integration within each time-step is performed analytically. Gaussian quadrature formulas are used for the spatial integration, except when $\mathbf{x}$ coincides $\boldsymbol{\xi}$. In this singular case, the same regularisation methods as described above are applied. Point collocation and the properties of the fundamental solutions, causality and translation, yield a time-stepping procedure

$$\mathbf{C}^1\mathbf{d}^n = \mathbf{D}^1\bar{\mathbf{d}}^n + \sum_{k=2}^{\bar{n}}\left(\mathbf{U}^k\mathbf{t}^{n-k+1} - \mathbf{T}^k\mathbf{u}^{n-k+1}\right) \quad n = 1,2,\ldots,N \tag{3.15}$$

with the matrix of the time-integrated fundamental solutions of the tractions $\mathbf{T}^k$ and displacements $\mathbf{U}^k$. In the matrices $\mathbf{C}^1$ and $\mathbf{D}^1$ are the time-integrated fundamental solutions of the first time-step. They are assembled concerning the unknown boundary data $\mathbf{d}$ and the known boundary data $\bar{\mathbf{d}}$, respectively. The upper limit of the sum $\bar{n}$ is determined by the fact that for three-dimensional analyses, the fundamental solutions for the full-space are zero after the passing of the S-wave, i.e., $\bar{n} = \min(n, \frac{r_{max}}{c_S\Delta t} + 2)$. For more details about this direct approach in time-domain see, e.g., [Dominguez, 1993] or [Mansur and Brebbia, 1983].

3.3.2 Thin layer method

The thin layer method, also named consistent boundary or hyperelement method, was first developed by [Lysmer and Waas, 1972] for dynamic analyses of unbounded domains subject to anti-plane loads and was later extended by, e.g., [Waas, 1972; Hartmann and Waas, 1986; Kausel, 1999; Park and Kausel, 2004]. This semi-analytical method derives the displacement wave-field in horizontal direction analytically to satisfy the radiation condition. In vertical direction, an expansion is used consistent to the FEM modelling. Because the thin layer method is based on the FEM, it does not require a fundamental solution, as the BEM does. The method is exact in horizontal direction and converges to the exact solution in the finite element sense in vertical direction.

The thin layer method is well suited to model horizontal layers with varying properties. The boundary conditions on the free surface and on the layer interfaces are rigorous satisfied implicitly. Also, the implementation in a FEM analysis is easy. However, the consistency between the two methods has to be considered. In other words, wave radiation in vertical unbound direction will only be roughly considered because local boundary conditions at the bottom are necessary in the thin layer method.

The method is originally formulated in frequency-wavenumber domain, but was extended into time-domain by [Kausel, 1994]. Latter formulation starts with the expression of the governing equations in frequency-wavenumber domain. Subsequently, a linear real-valued eigenvalue problem in the frequency-variable is solved. Afterwards, an analytical transformation of the displacement functions over frequencies is performed and, finally, the displacement functions are numerically transformed over wavenumbers. With this strategy, the later addressed Green's functions (Sec. 4.2.1) which imply the radiation condition for impulsive sources can be directly determined in the time-domain.

3.3.3 Exact non-reflecting boundary conditions

The exact non-reflecting boundary conditions are another global procedure for the dynamic analysis of unbounded domains [Keller and Givoli, 1989; Tsynkov, 1998]. Those boundary conditions are constructed from analytical solutions for unbounded domains of simple geometries and material properties. They involve integral transforms along the boundary and are essentially based on the separation of variables. Various exact non-reflecting boundary conditions for different wave equations were reviewed by [Givoli, 1992]. An example for an exact non-reflecting boundary condition is the so-called Dirichlet to Neumann map. Generally, their application is limited by the availability and complexity of the analytical solution.

3.3.4 Scaled boundary finite element method

As mentioned above, the SBFEM developed by [Wolf and Song, 1996; Wolf, 2003] will be discussed extensively in a Chap. 6. Therefore, in this sections just the fields of application of the SBFEM are mentioned. The method was used for the simulation of unbounded domains in statics [Deeks and Wolf, 2002] and dynamics [Wolf, 2002; Zhang *et al.*, 1999b; Crouch and Bennet, 2000; Lehmann, 2005b; Lehmann and Borsutzky, 2006; Lehmann *et al.*, 2007; Lane *et al.*, 2007]. Unbounded layered media were studied by [Genes and Kocak, 2005] with a coupled FE-BE-SBFEM. [Doherty and Deeks, 2003a,b; Bazyar and Song, 2006b,a] employed the SBFEM for the analysis of non-homogeneous material in the unbounded domain, whereas [Lindemann and Becker, 2002; Song, 2004] applied it to fracture mechanics. Finally, the SBFEM was applied to acoustic problems [Lehmann, 2005c,a].

3.4 Approximate modelling with local procedures

In contrast to the substructure method, the direct method does not claim for the use of rigorous boundary conditions but employs, due to less influences to the overall system, approximative boundary conditions. From the rigorous form of the interaction force-displacement relationship of the unbounded domain, a simpler, approximate form can be derived.

This simplified stiffness relationship is *local in time and space* for time-domain considerations. The information used to obtain the behaviour of a node on the interaction horizon is only taken from this specific node or the nodes of the finite element mesh of its instantaneous surrounding (spatial locality). Also, the considered time is restricted, at most, to a limited past time (temporal locality). It is obvious that the thus achieved reduction of the computational effort is accompanied by the increase of inaccuracy. On the other hand, if the interaction horizon is chosen at sufficiently large distance, results of sufficient accuracy can be obtained Of course, this is only possible for the price of higher computational effort.

In the last four decades, various local procedures have been proposed. Even though, many possibilities exist to construct approximative solutions for the response of the unbounded domain, [Wolf and Song, 1996] state that most of the developed procedures are mainly based on the theory of wave propagation, enforcing outgoing plane waves.

3.4.1 Transmitting boundaries

Since [Lysmer and Kuhlmeyer, 1969] developed the first transmitting boundaries for elastodynamics, many types of boundary conditions were expanded. The idea behind most of them is to use the mathematical representation of plane wave propagation to eliminate the impinging waves under a specific angle of incident.

Whereas the *classical viscous boundary condition* from [Lysmer and Kuhlmeyer, 1969] absorbs only plane waves perpendicular to the artificial boundary, this condition was advanced over the years. For example, [White *et al.*, 1977; Akiyoshi, 1978; Smith, 1974; Underwood and Geers, 1981] developed forms of boundary conditions [Givoli, 2004] calls Sommerfeld-like transmitting boundary conditions, because the absorption of the incident waves is solely modelled by dashpots (compare Eqs. (3.1) and (3.2)). Even though they are applicable to scalar and vector wave equations, they generate low accuracy in the results.

In contrast to those relatively simple conditions, *higher-order transmitting boundary conditions*, also named *non-consistent boundary conditions*, have been proposed. They are computational efficient, local formulations with the potential to lead to accurate results with increasing orders of approximation. The original evolutions by, e.g., [Lindman, 1975; Engquist and Majda, 1977; Higdon, 1986; Liao and Wong, 1984] are formulated by means of high-order-derivatives. Due to incompatibility to the FEM and instability problems, new approaches of higher-order transmitting boundary conditions were suggested by, e.g., [Wolf and Song, 1995; Grote and Keller, 1995; Ruge *et al.*, 2001; Krenk, 2002; Guddati and Lim, 2006]. In this new developments, the higher-order-derivatives are eliminated by auxiliary variables which are constructed a system of ordinary differential equations which, in turn, yields from methods of separating variables or analytical solutions. Although, higher-order transmitting boundary conditions give well-balanced results between accuracy, efficiency, and ability to be implemented into FE-schemes, they have the disadvantage to be restricted to relatively simple geometries, because the mentioned separation of variables is not applicable for complex geometries.

3.4.2 Infinite elements

Infinite elements [Bettess, 1992; Astley, 2000] have been developed on the basis of the finite element method for the absorption of waves at the near-field boundaries. They gain effectiveness from its origin, since their equation systems are compatible to those of the FEM and thus easy to handle in coupling procedures.

Infinite elements are characterised by two kinds of shape functions. The first is displacement function which decays to infinity, whereas the second is a function of geometry which grows in the infinite direction. Thus, the amplitudes of the outgoing waves decrease with increasing distance to the near-field. Mostly, infinite elements are formulated in frequency-domain, e.g., by [Bettess, 1992; Zhang *et al.*, 1999a; Zhao and Liu, 2003]. Since, the shape functions of those elements are formulated for specific frequencies of waves, their performance in absorbing transient waves in time-domain is often poor. To overcome this problem, frequency-independent infinite elements are developed, e.g., by [Mahran, 2004].

3.4.3 Layer methods

The local procedures of layer methods can be generally classified in three categories. The first category are the *absorbing layers* where a layer of finite thickness and material properties which reduce the wave reflection replaces the unbounded domain. The consideration of artificial material damping to this layer leads to the *sponge layers* [Israeli and Orszag, 1981]. Finally, the *perfectly matched layers* [Berenger, 1996; Basu and Chopra, 2004] introduce to the governing equations for unbounded domains an artificial attenuation of waves which travel in a specific direction to infinity. Since the wave propagation in the not considered directions is not attenuated, the transmission to infinity is mainly restricted to plane waves.

4 Fundamentals of seismology

Since the subject of this work is the seismic analysis of buried lifelines, it is necessary to introduce the fundamentals of seismology. At first, the seismic process, i.e., the circumstances that lead to the occurrence of an earthquake, and the classification of seismic events are addressed. Accordingly, methods are discussed which are used to describe the seismic process in quantitative terms. Thereby, the topic of seismic wave propagation is as well addressed as the description of the source mechanism. The chapter closes by the review of observation and modelling of ground motion.

4.1 Seismic process

Studying engineering structures under seismic excitation requires to understand the major components of what is exciting those structures, i.e., the earthquake. Even though, an earthquake is a highly complex process which is by far not completely understood by now, the science of seismology (Greek *seismos* for earthquake and *logos* for science) made great strides in the last century in understanding the behaviour of the earth. This chapter is intended to give an overview of the seismic process and of the parameters used to describe an earthquake. For more detailed explanations refer to, e.g., [Kramer, 1996; Shearer, 1999; Aki and Richards, 2002].

4.1.1 Internal structure of earth

The earth is roughly a spherical with a diameter of approximately 12700km. The first achievements in seismology were to understand the inner structure of the earth by analysing recorded wave arrivals of large earthquakes all around the globe. From different wave arrivals, seismologists could conclude on different wave travel times due to diffraction, different densities, and aggregate states (compare Secs. 2.2 and 2.3) in the inner of the earth and, there with, on its structure.

The earth is divided into a *core*, a surrounding *mantle*, and an outlying *crust* (Fig. 4.1). The crust is solid and with a thickness of 25km to 40km, it is the thinnest layer of the earth. Underlying, the about 2850km thick mantle is situated which can be divided into an upper and lower mantle. Whereas the lower mantle is liquid, the upper mantle consists of a viscous, semimolten material. It acts like a solid to sudden applied stresses, but flows like a fluid in response to long-term stresses. This indicates that earthquakes can occur in the upper mantle (and, of course, in the crust) but never in the liquid lower mantle. The inner section of the earth is the core which again is split into an outer and an inner core. The outer core is approximately 2260km thick and consists primarily of molten iron, whereas the inner core is a very dense solid (specific gravity up to 15 g/cm^3).

The temperature in the earth increases with depth. For the crust as outermost layer is subject to oceans and atmosphere, it is the coolest layer. Underneath, i.e., in the upper mantle, the temperature rises to values of 700 to 1300°C. In the lower mantle, the temperature ranges from 1800 to 2800°C, and rises up to 3200°C in the outer core. The temperature in the inner core is estimated to be about 4500°C, even though works, e.g., [Kubala and Rao, 1996], indicate a much higher temperature there.

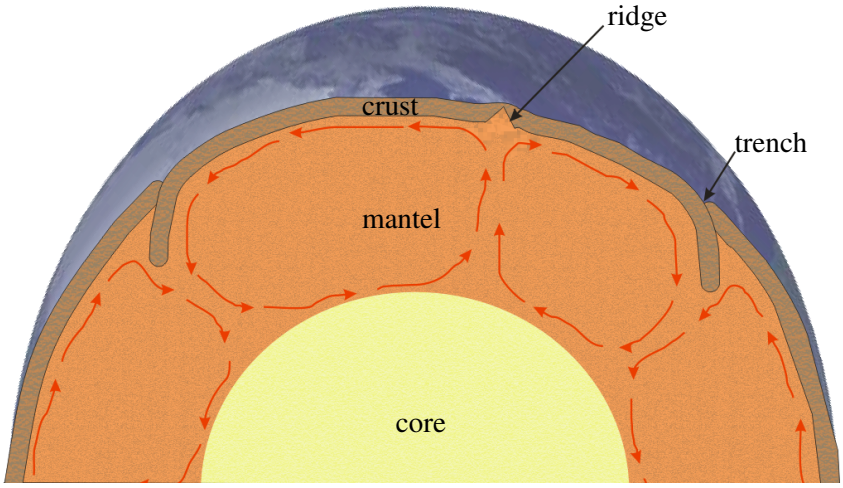

Figure 4.1: Structure of the earth consisting of core, mantle and crust. The convection due to temperature differences in the earth mantle leads to divergent motion of the plates, in which the crust is divided. Where the plates move apart from each other, ridges occur. Trenches appear where the motion is toward each other.

4.1.2 Plate tectonics and plate boundaries

The beginning of the exploration of the ocean floor some fifty years ago, helped to develop the relatively new theory of *plate tectonics*. Its basic hypothesis is that the earth's crust consists of several large blocks which are called plates and that those plates move relatively to each other. The earth's crust is divided into six continental-sized and about 14 sub-continental-sized plates. The plates and their boundaries are shown in Fig. 4.2. Nowadays, the hypothesis of plate tectonics could be verified by modern technology, like the global positioning system.

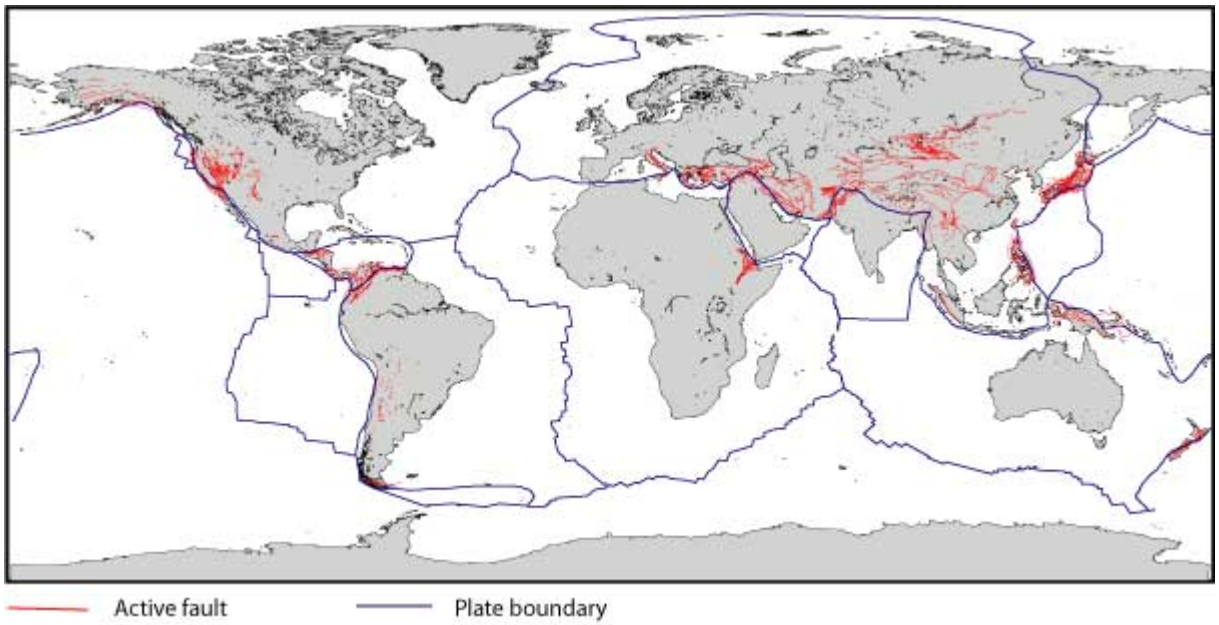

Figure 4.2: The tectonic plates of the earth's crust (from [COMET, 2007]. The plate boundaries are marked as blue lines, whereas active seismic faults are marked as red dots. Most of the faults are positioned in the vicinity of the plate boundaries.

The theory of plate tectonics is a kinematic one, i.e., it states that the plates are moving, but it does not deal with the question why they are moving. The most accepted theory for the reason of plate movement gives as cause the convection in the mantle of the earth. Due to the temperature differences in the

earth mantle (see Sec. 4.1.1), density gradients, and hence, pressure gradients occur. Those pressure gradients initiate a motion of the liquid or semimolten material, respectively, like shown in Fig. 4.1. The semimolten material of the upper mantle sticks to the, in plates divided, earth's crust and initiates its motion.

Following the theory of plate tectonics, the plates, no matter why, move with respect to each other. This relative movement causes deformations which are restricted to the plate boundaries. If those deformations are slowly and continuously, they are called *aseismic* deformations. If the deformations occur spasmodical, i.e., in form of earthquakes, they are called *seismic*. Basically, three distinct types of plate boundaries have been identified. At *spreading ridge boundaries*, the plates move apart from each other (Fig. 4.1), molten rock from the underlying mantle rises to the surface and, hence, the amount of material of the plates increases at the ridge. To balance this increase, plate material is consumpted at the *sub-ducting zone boundaries* where the plates move toward each other, one plate subducts beneath, whereas the second overrides the other and a trench in the earth's crust occurs (Fig. 4.1). *Transform boundaries* are present where the plates move past each other without creating new crust or consuming old crust. The different characteristics of those plate boundaries influence the nature of the earthquakes that occur along them, as will be discussed in the subsequent section.

4.1.3 Faults

In general, the seismic process, i.e., the origin of earthquakes, can be described as follows. The roughness of the plate boundaries causes the plates to get stuck to each other and ascending stresses occur at their boundaries. When the stresses exceed the resistance of the crust material at the plate boundaries, it comes to a rupture of the rock with a sudden stress relief. From this rupture area, called *fault*, body waves propagate through the inner of the earth. At inhomogeneities, like, e.g., the earth surface or material layer interfaces, surface waves arise.

Thus, the initiation process of an earthquake is not limited to a certain point in the inner of the earth crust, but takes places on an extended area, the fault. In seismology, it is common and reasonable, also because of insufficient information, to describe this area as a rectangular plane.

In order to describe the fault mechanism, some geometric parameters are introduced subsequently. The fault plane has the length L and the width W. The position of this fault area is determined, next to the depth, by two angles as displayed in Fig. 4.3(a). The first angle is the *strike* $\hat{\phi}$ which describes the azimuth, i.e., the angle to the North direction, of the fault's horizontal edge. The second angle is the *dip* $\hat{\delta}$ giving the slope of the fault area.

The nucleation point on the fault, i.e., the point from where the rupture starts, is called *hypocentre* or *focus*. The projection of the hypocentre to the surface of the earth is called *epicentre* and the distance between hypocentre and epicentre is the *hypocentral depth* $\hat{h}$. The rupture on the fault leads to two adjacent fault surfaces where the relative displacement, i.e., the difference of the displacements on the two surfaces, is called *slip* $[\mathbf{u}]$. The direction of the rupture propagation is described by the *rake* angle $\hat{\lambda}$ as depicted in Fig. 4.3(a).

Even though, the fault rupture process is quite complex, the movement on the fault is usually reduced to components in the direction of strike $\hat{\phi}$ and dip $\hat{\delta}$. Whereas this movement proceeds generally in both directions, usually one direction is predominant. So, analogously to the three basic types of plate boundaries, three different types of fault movement can be distinguished. The fault movement that primarily occurs in dip direction is referred to as *dip-slip*. Depending on the relative movement on the fault, the dip-slip mechanism can either occur as *normal-slip* as shown in Fig. 4.3(b)(i) or as *reverse-slip* depicted in Fig. 4.3(b)(ii). Finally, fault movement parallel to the strike is called *strike-slip* (Fig. 4.3(b)(iii)).

Seismic moment: The angles strike, dip and rake, as well as the slip vector define the most basic seismic model of the fault mechanism. It can be shown that the seismic energy radiated from such a fault

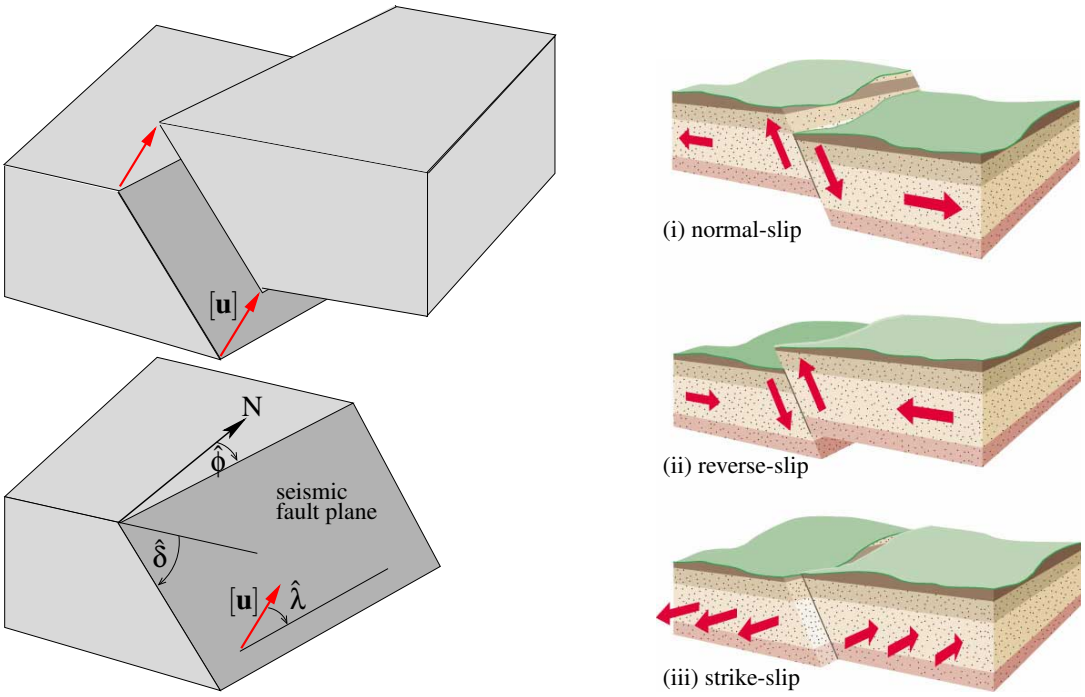

(a) Sketch of a fault with the definition of the angles of strike $\hat{\phi}$, dip $\hat{\delta}$ and rake $\hat{\lambda}$. The fault slip $[\mathbf{u}]$ is marked.

(b) The three fault mechanisms (from [Pickett *et al.*, 2000]).

Figure 4.3: Terms of the rupture process and the three fault mechanisms.

can be modelled as double-couple sources [Shearer, 1999]. Those double-couple sources incorporate the scalar *seismic moment* M_0 which is defined as product of the shear modulus μ in the faulting region, the rupture area S and the average amount of the slip $[\bar{u}]$

$$M_0 = \mu S [\bar{u}] \, . \tag{4.1}$$

This seismic moment is named a moment because of its unit. However, it is rather a measure of the work performed by the earthquake and, thus, correlates well with the energy released during a seismic event.

4.1.4 Size of earthquakes

To analyse earthquakes and their effects, it is necessary to have an idea of the size of the seismic event. Since this size is not a physically determined parameter, different methods were developed to characterise the earthquake.

Earthquake intensity: The oldest measure for earthquakes is the *earthquake intensity* which is a qualitative description of the seismic effects at a particular location, as evidenced by human reactions and observed damages. The most famous of those earthquake intensity measures is the *Modified Mercalli Intensity Scale* which bases on the works of [Mercalli, 1883] and was modified by [Richter, 1958] to suite the conditions in California. This intensity scale classifies an earthquake from level I (not felt) to level XII (total observed damage).

Earthquake magnitude: Earthquake intensity scales are more or less subjective characterisations of earthquakes. With the development of modern seismic instrumentation, more objective, quantitative measures of ground motion became available. In the last 70 years, this development gave rise to the

classification of seismic events by so-called *earthquake magnitudes*. The majority of those magnitudes uses measured data to quantify the size of an earthquake. The most common earthquake magnitudes are

- the *Richter local magnitude* M_L [Richter, 1935]:

$$M_L = \log A - \log A_0 \tag{4.2}$$

  which relates the maximum amplitude A recorded at a epicentral distance of 100km on a particular seismometer (Wood-Anderson) to the maximum amplitude A_0 of a reference seismic event.

- the *surface wave magnitude* M_s [Gutenberg and Richter, 1936]:

$$M_s = \log A + 1.66 \log \Delta + 2.0 \tag{4.3}$$

  where A is the maximum ground displacement and Δ the angle of the epicentral distance of the seismometer in degrees. The angle Δ=360° corresponds to the circumference of the earth.

- the *body wave magnitude* m_b [Gutenberg, 1945]:

$$m_b = \log A - \log T + 0.01\Delta + 5.9 \tag{4.4}$$

  where A is the P-wave amplitude and T the period of the P-wave.

- the *moment magnitude* M_w [Hanks and Kanamori, 1979]:

$$M_w = \frac{2}{3} \log(M_0) - 10.73 \tag{4.5}$$

  which directly relates the magnitude to the seismic moment M_0, i.e., to a physical property of the source.

4.2 Quantitative seismology

In this section, mathematical representations for the displacements that typically occur in seismology are discussed (see, e.g., [Aki and Richards, 2002] or [Shearer, 1999]). The representations are formulas for the displacement at a general point in space and time in terms of the quantities that originate the motion. These quantities are either body forces and applied tractions or displacements over a surface of the earth which is usually interpreted as elastic medium.

For an earthquake that occurs on a fault, the seismic source is complicated to handle because, firstly, it extends over a finite fault plane or even volume, secondly, it lasts a finite interval of time, and thirdly, it might involve motions at the source with varying directions and magnitudes. To consider all these effects, so-called *representation theorems* were introduced to seismology. [Aki and Richards, 2002] describe those theorems as bookkeeping devices, which synthesise displacements derived from the simplest sources, i.e., the unidirectional unit impulse, to a displacement field generated by a realistic source.

4.2.1 Green's function

As stated in Sec. 3.3.1.1, the elastic response in an elastic full-space to such a unidirectional unit impulse is called fundamental solution. In seismic analyses, rather half-spaces with certain homogeneous boundary conditions at their surfaces are considered than full-spaces. When those homogeneous boundary conditions are additionally incorporated in the fundamental solution, it is called *Green's function*. In the following, a brief description of the characteristics of Green's functions is given. For a more detailed discussion refer to, e.g., [Roach, 1995; Duffy, 2001; Kausel, 2006].

Definition: The definition of the term Green's function is not used consistently in literature. Often, the term Green's function is employed in the same sense as fundamental solution, e.g., in [Kausel, 2006]. In the present work, Green's functions are understood as special fundamental solutions, as is explained below, which are only identical to fundamental solutions in very particular cases.

Following [Antes, 2005], a boundary value problem is described by a differential equation, e.g., in elastodynamics Navier's equation of motion (Eq. (2.10)), and the conditions prescribed on the boundary from Eqs. (2.15) and (2.16). When $L(D)$ is a linear differential operator, the differential equation can be expressed as

$$L(D)u_i(\mathbf{x},t) = b_i(\mathbf{x},t)\ . \tag{4.6}$$

In this equation, the solution $u_i(\mathbf{x},t)$ in the interior of the analysed domain as well as the non-prescribed boundary reactions, i.e., the displacements $u_i(\mathbf{x},t)$ on Γ_t and the tractions $t_i(u_i(\mathbf{x},t))$ on Γ_u, are unknown. In general, those boundary conditions are not zero along the respective boundary.

A Green's function [Green, 1828] is defined as a special fundamental solution $\mathbf{G}^*(\mathbf{x},\boldsymbol{\xi},t,\tau)$ of such a boundary value problem

$$L(D)G^*_{ij}(\mathbf{x},\boldsymbol{\xi},t,\tau) = \delta(t-\tau)\delta(\mathbf{x}-\boldsymbol{\xi})\delta_{ij} \tag{4.7}$$

which implicitly satisfies the homogeneous conditions for those boundary states which are prescribed in the actual problem. When such a Green's function of a boundary value problem is available, the solution of the problem can be formulated in an integral form which contains no unknown terms. The meaning of this definition is shown in the following for a Green's function in elastodynamics.

Green's function in elastodynamics: As stated in Sec. 3.3.1.2, the interior displacements $u_j(\boldsymbol{\xi},t)$ in an elastic domain Ω are given by Eq. (3.9). Separating the boundary integrals depending on the prescribed boundary conditions $\bar{u}_i$ and $\bar{t}_i$ into the parts Γ_u and Γ_t and assuming zero initial states, gives

$$u_j(\boldsymbol{\xi},t) = \int_{\Gamma_u} \left(t_i * u^*_{ij} - t^*_{ij} * \bar{u}_i\right) d\Gamma_u + \int_{\Gamma_t} \left(\bar{t}_i * u^*_{ij} - t^*_{ij} * u_i\right) d\Gamma_t + \int_{\Omega} b_i * u^*_{ij} d\Omega\ , \tag{4.8}$$

where u^*_{ij} and t^*_{ij} denote the fundamental solutions. If now a Green's function G^*_{ij}, i.e., a special fundamental solution $u^*_{ij} = G^*_{ij}$, is found that satisfies the homogeneous boundary conditions

$$u^*_{ij} = G^*_{ij}(\mathbf{x},\boldsymbol{\xi},t,\tau) = 0 \text{ on } \Gamma_u \text{ and} \tag{4.9}$$

$$t^*_{ij} = t^*_{ij}(G^*_{ij}(\mathbf{x},\boldsymbol{\xi},t,\tau)) = 0 \text{ on } \Gamma_t\ , \tag{4.10}$$

Eq. (4.8) simplifies to

$$u_j(\boldsymbol{\xi},t) = -\int_{\Gamma_u} t^*_{ij}(G^*_{ij}) * \bar{u}_i d\Gamma_u + \int_{\Gamma_t} \bar{t}_i * G^*_{ij} d\Gamma_t + \int_{\Omega} b_i * G^*_{ij} d\Omega\ . \tag{4.11}$$

The displacements $u_j(\boldsymbol{\xi},t)$ in the whole domain Ω can be directly determined by evaluating Eq. (4.11), since the fundamental solutions G^*_{ij} and $t^*_{ij}(G^*_{ij})$ as well as the prescribed body forces b_i and the prescribed boundary values $\bar{u}_i$ and $\bar{t}_i$ are known. Thus, Eq. (4.11) does not contain any unknowns and no further treatment to this equation is needed, as it is, e.g., necessary in the BEM (see Sec. 3.3.1). The particular cases mentioned above, where the terms fundamental solution and Green's functions can be used without distinction, can now be realised as the case where the analysed problem does not involve any boundaries on which homogeneous boundary states can occur, like in the full-space.

Since Green's functions are special fundamental solutions, they exhibit the properties which are referred to in Sec. 3.3.1.1 and which are characteristic for fundamental solutions: translation, reciprocity and

causality. In mathematical terms, the translation, i.e., the sole dependence on the time-interval and not on the absolute time-points, is formulated as

$$G^*_{ij}(\mathbf{x},\boldsymbol{\xi},t,\tau) = G^*_{ij}(\mathbf{x},\boldsymbol{\xi},t-\tau,0) = G^*_{ij}(\mathbf{x},\boldsymbol{\xi},-\tau,-t) \tag{4.12}$$

and the reciprocity, i.e., the permutability of load point $\mathbf{x}$ and observation point $\boldsymbol{\xi}$ and of load time t and observation time τ, as

$$G^*_{ij}(\mathbf{x},\boldsymbol{\xi},t,\tau) = G^*_{ji}(\boldsymbol{\xi},\mathbf{x},-\tau,-t)\ . \tag{4.13}$$

In many cases, it is difficult to construct Green's functions. However, for particular problems, analytical Green's functions were derived, e.g., for the three-dimensional elastodynamic half-space [Triantafyllidis, 1984, 1991]. Semi-analytical or so-called numerical Green's functions considering the response of layered half-spaces in frequency-domain are developed by, e.g., [Waas, 1972; Apsel and Luco, 1983; Luco and Apsel, 1983; Kausel and Peek, 1982] and in time-domain by [Kausel, 1994].

Once a Green's function is established, it can be used, e.g., in quantitative seismology to describe the displacement wave propagation initiated by an earthquake by means of representation theorems.

4.2.2 Representation theorems

Representation theorems are used in seismology to describe the motion that occurs in an earthquake. They combine the Green's functions G^*_{ij} to a seismic ground motion that is caused by a complex fault as is depicted in Fig. 4.4 in an integral form.

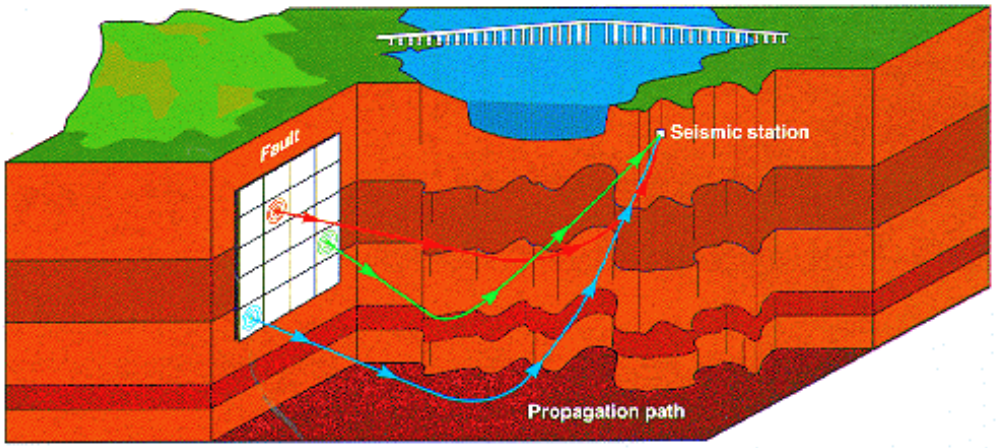

Figure 4.4: Synthesis procedure of a representation theorem (from [Hutchings, 2007]). The Green's functions G^*_{ij} are calculated for every discrete point on the seismic fault. Then, the Green's functions G^*_{ij} are scaled by the rupture intensity derived from the seismic fault process and summed up in an integral form.

When an appropriate Green's function $G^*_{ij}(\mathbf{x},\boldsymbol{\xi},t,\tau)$ is used, such a representation theorem can be derived from Eq. (4.8) which describes the displacements u_j at point $\boldsymbol{\xi}$ and time t. Incorporating the translation and reciprocity of Green's functions from Eqs. (4.12) and (4.13), respectively, and omitting the distinction between the boundary parts ($\Gamma = \Gamma_u + \Gamma_t$), leads to a description for the displacement u_i at point $\mathbf{x}$ and time t:

$$\begin{aligned} u_i(\mathbf{x},t) = &\int_\Gamma \left(t_j(\boldsymbol{\xi},\tau) * G^*_{ij}(\mathbf{x},\boldsymbol{\xi},t-\tau,0) - t^*_{ij}(G^*_{ij}(\mathbf{x},\boldsymbol{\xi},t-\tau,0)) * u_j(\boldsymbol{\xi},\tau) \right) d\Gamma \\ &+ \int_\Omega b_j(\boldsymbol{\xi},\tau) * G^*_{ij}(\mathbf{x},\boldsymbol{\xi},t-\tau,0) d\Omega\ . \end{aligned} \tag{4.14}$$

In this representation theorem, the displacements $u_i(\mathbf{x},t)$ originate from the forces throughout the body Ω and contributions from the tractions $\bar{t}_i$ and displacements $\bar{u}_i$ applied at the surfaces Γ_t and Γ_u, respectively. So far, the essential property of the Green's function G^*_{ij}, namely the satisfaction of homogeneous boundary conditions on the surface Γ, was not included in Eq. (4.14). To consider this essential property, two extreme cases are possible and shall be examined.

For the first case, the Green's function $G^{*\text{rigid}}_{ij}$ is determined with a rigid boundary $\Gamma = \Gamma_u$, so that the homogeneous displacement boundary condition applies on the entire boundary

$$G^{*\text{rigid}}_{ij}(\mathbf{x},\boldsymbol{\xi},t-\tau,0) = 0 \text{ on } \Gamma\,. \tag{4.15}$$

Recalling Cauchy's theorem of Eq. (2.2), Hooke's law of Eq. (2.6) and denoting that the strain on the surface is $\varepsilon_{pq} = u_{p,q}$, enables the formulation of the tractions by means of the displacements

$$t_j = \sigma_{jk} n_k = C_{jkpq}\varepsilon_{pq} n_k = C_{jkpq} u_{p,q} n_k\,. \tag{4.16}$$

so that the Green's function in terms of tractions $t^*_{ij}(G^*_{ij})$ holds

$$t^*_{ij}(G^*_{ij}(\mathbf{x},\boldsymbol{\xi},t-\tau,0)) = C_{jkpq}\, n_k\, G^*_{ip,q}(\mathbf{x},\boldsymbol{\xi},t-\tau,0)\,. \tag{4.17}$$

With Eqs. (4.15) and (4.17), an alternative form of the representation theorem can be derived from Eq. (4.14):

$$u_i(\mathbf{x},t) = -\int_\Gamma \left(C_{jkpq}\, n_k\, G^{*\text{rigid}}_{ip,q}(\mathbf{x},\boldsymbol{\xi},t-\tau,0) * \bar{u}_j(\boldsymbol{\xi},\tau)\right) d\Gamma + \int_\Omega b_j(\boldsymbol{\xi},\tau) * G^{*\text{rigid}}_{ij}(\mathbf{x},\boldsymbol{\xi},t-\tau,0) d\Omega\,. \tag{4.18}$$

For the second extreme case, the Green's function $G^{*\text{free}}_{ij}$ is constructed regarding a traction free boundary $\Gamma = \Gamma_t$. Then, the homogeneous traction boundary condition applies

$$t^*_{ij}(G^{*\text{free}}_{ij}(\mathbf{x},\boldsymbol{\xi},t-\tau,0)) = 0 \text{ on } \Gamma \tag{4.19}$$

and Eq. (4.14) is simplified to the expression

$$u_i(\mathbf{x},t) = \int_\Gamma \bar{t}_j(\boldsymbol{\xi},\tau) * G^{*\text{free}}_{ij}(\mathbf{x},\boldsymbol{\xi},t-\tau,0) d\Gamma + \int_\Omega b_j(\boldsymbol{\xi},\tau) * G^{*\text{free}}_{ij}(\mathbf{x},\boldsymbol{\xi},t-\tau,0) d\Omega\,. \tag{4.20}$$

Both representation theorems Eqs. (4.18) and (4.20) explicitly require that the prescribed tractions or displacements, respectively, are applied on the external boundary Γ. When motion due to a buried seismic source should be analysed, it is more convenient to obtain the possibility to apply tractions or displacements inside the domain, e.g., on the seismic fault. The procedure of applying those conditions in the inner of the domain is discussed in the following.

4.2.2.1 Discontinuities on an internal surface

The seismic motions recorded at the earth's surface are a result both of propagation effects and of source effects. To consider both factors, a representation theorem needs to contain, besides the Green's functions which describe the wave propagation effects, a term that specifies the behaviour of the source as well. The treatment of this latter term is addressed here.

A seismic source can be expressed as body force or as discontinuity of displacements or tractions, respectively. When the source mechanism is formulated as body force b_j, it can be regarded directly in the representations from Sec. 4.2.2 in the volume integrals. Also, if the initial seismic excitation is modelled as discontinuities on an internal surface, the representation theorems can be employed, but some modifications have to be applied. Anyhow, an equivalent expression for the representation of the source as body forces can be revealed.

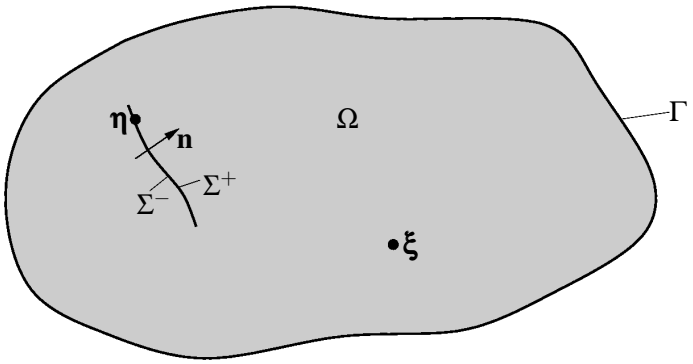

Figure 4.5: Finite elastic domain Ω, which could represent a part of the earth crust, with external surface Γ and internal surface Σ. The internal surface represents the buried seismic fault and contains two opposing surfaces Σ^+ and Σ^-. Points within Ω are denoted as $\boldsymbol{\xi}$, whereas points on the surfaces Σ^+ and Σ^- are referred to as $\boldsymbol{\eta}$. The normal vector $\mathbf{n}$ points from Σ^- to Σ^+ on the internal surface.

In order to demonstrate how displacement discontinuities on a buried fault can be implemented in the representation theorems, two adjacent internal surfaces Σ^+ and Σ^- are added inside the domain Ω as depicted in Fig. 4.5.

The internal surfaces Σ^+ and Σ^- represent the opposite faces of the fault where the discontinuities (indicated by squared brackets $[.]$) of displacements and tractions, respectively, are denoted by

$$[u_j(\boldsymbol{\xi},t)] = u_j^{\Sigma^+}(\boldsymbol{\xi},t) - u_j^{\Sigma^-}(\boldsymbol{\xi},t) \quad \text{and} \tag{4.21}$$

$$[t_j(\boldsymbol{\xi},t)] = t_j^{\Sigma^+}(\boldsymbol{\xi},t) - t_j^{\Sigma^-}(\boldsymbol{\xi},t)\,. \tag{4.22}$$

When the boundary is divided into the external part Γ and the internal part $\Sigma = \Sigma^+ + \Sigma^-$, the displacements u_i at the domain point $\mathbf{x}$ and time t can be computed analogously to Eq. (4.14) with

$$\begin{aligned} u_i(\mathbf{x},t) = &\int_\Sigma \left([t_j(\boldsymbol{\xi},\tau) * G_{ij}^*(\mathbf{x},\boldsymbol{\xi},t-\tau,0)] - [t_{ij}^*(G_{ij}^*(\mathbf{x},\boldsymbol{\xi},t-\tau,0)) * u_j(\boldsymbol{\xi},\tau)] \right) d\Sigma \\ &+ \int_\Gamma \left(t_j(\boldsymbol{\xi},\tau) * G_{ij}^*(\mathbf{x},\boldsymbol{\xi},t-\tau,0) - t_{ij}^*(G_{ij}^*(\mathbf{x},\boldsymbol{\xi},t-\tau,0)) * u_j(\boldsymbol{\xi},\tau) \right) d\Gamma \\ &+ \int_\Omega b_j(\boldsymbol{\xi},\tau) * G_{ij}^*(\mathbf{x},\boldsymbol{\xi},t-\tau,0) d\Omega\,, \end{aligned} \tag{4.23}$$

where the square brackets are used for the differences between the values on Σ^+ and Σ^-. Assume that a Green's function is incorporated that satisfies homogeneous boundary conditions on Γ, but not on Σ^+ and Σ^-. Additionally assume that the addressed problem satisfies the same homogeneous boundary conditions as the Green's function, i.e., $\bar{u}_j = 0$ where $G_{ij}^* = 0$ and $\bar{t}_j = 0$ where $t_{ij}^*(G_{ij}^*) = 0$. In doing so, the second integral in Eq. (4.23) (over the boundary Γ) becomes zero. Supposing that the entire seismic excitation is expressed exclusively by discontinuities on the fault and not by body forces acting inside the domain Ω, causes the third integral in Eq. (4.23) (over the domain Ω) to vanish as well.

So far, nothing has been stated for the boundary conditions on Σ. If a spontaneous rupture is hypothesised on the fault, it can be assumed that the crack occurs at all points on Σ at the same time. Whereas the displacement differences are $[u_j] = u_j^{\Sigma^+} - u_j^{\Sigma^-} \neq 0$, the tractions due to the sudden stress relief of the spontaneous rupture can be assumed to be continuous over the fault, so that for their difference yields

$$[t_j] = t_j^{\Sigma^+} - t_j^{\Sigma^-} = 0 \text{ on } \Sigma\,. \tag{4.24}$$

This implies that even the first integrand $[t_j * G_{ij}^*]$ of the remaining integral in Eq. (4.23) over the boundary Σ becomes zero.

As the Green's function G^*_{ij} can be constructed as it is appropriate, the simplest and most common way is to define G^*_{ij} and its derivatives to be continuous across Σ. In other words, the internal surface is not considered in the Green's function G^*_{ij}, but just in the displacement field u_j. Thus, G^*_{ij} satisfies the equation of motion in the entire domain Ω (even on Σ) which is just bounded by Γ where the homogeneous boundary conditions are satisfied. Under this assumption, the fundamental solution G^*_{ij} fulfils the requirements for being a Green's function. Nevertheless, following the strict definition of Green's functions, the boundaries are required to be the same for u_j and G^*_{ij}. So, it could be complained that though the homogeneous boundary conditions of G^*_{ij} are satisfied, the boundaries are not the same for u_j and G^*_{ij}. This problem can be overcome by defining the source mechanism as body forces, as will be shown in the subsequent section.

Anyhow, using the discontinuity formulation, the displacements $u_i(\mathbf{x},t)$ can be derived from the modified Eq. (4.23), when taking also Eq. (4.17) into account, by

$$\begin{aligned} u_i(\mathbf{x},t) &= -\int_\Sigma \left[t^*_{ij}(G^*_{ij}(\mathbf{x},\boldsymbol{\xi},t-\tau,0)) * u_j(\boldsymbol{\xi},\tau)\right] d\Sigma \\ \Leftrightarrow u_i(\mathbf{x},t) &= -\int_\Sigma C_{jkpq}\, n_k\, G^*_{ip,q}(\mathbf{x},\boldsymbol{\xi},t-\tau,0) * [u_j(\boldsymbol{\xi},\tau)]\, d\Sigma\,. \end{aligned} \tag{4.25}$$

From this representation theorem, it can be seen that only the displacement discontinuity $[u_j(\boldsymbol{\xi},\tau)]$ on the fault Σ needs to be known to determine the displacement $u_i(\mathbf{x},t)$ at any point in the entire domain Ω. Of course, this is only possible if an adequate Green's function G^*_{np} can be constructed that fulfils the discussed boundary conditions.

Note in Eq. (4.25) that both factors specifying the seismic motion, the wave propagation and the source mechanism, appear independently in Eq. (4.25). Therefore, both factors can be determined separately at first before they enter the representation theorem Eq. (4.25). Thus, all complexity of the source mechanism, like non-uniform motions on the fault, can be exclusively considered in the determination of the slip function $[u_j(\boldsymbol{\xi},\tau)]$.

4.2.2.2 Body force equivalents

The earthquake model from Eq. (4.25) does not directly involve any body forces. Still, it is possible to express the same seismic motion due to body forces instead of discontinuities on the internal surface Σ. Hence, G^*_{ij} and u_j are consistent, since they consider the same boundaries which is not the case described in Sec. 4.2.2.1. Strictly speaking, the fundamental solution G^*_{ij} in Eq. (4.25) cannot be named Green's function, because it satisfies homogeneous boundary conditions on Γ but lacks this satisfaction on Σ, since it does not exhibit Σ as a boundary. When the discontinuities on Σ can be expressed as body forces, it is also for u_j not necessary to introduce an internal surface Σ. Then, the domain Ω is only bounded by Γ where the homogeneous boundary conditions are satisfied by G^*_{ij} and, thus, G^*_{ij} fulfils all requirements for being a Green's function.

To transform the discontinuity formulation to a body force representation of the seismic source, the delta-function-derivative $\partial\delta(\boldsymbol{\eta}-\boldsymbol{\xi})/\partial\eta_q$ is used to localise the points of Σ within Ω (see Fig. 4.5). This function has the property

$$\frac{\partial}{\partial\xi_q} G^*_{ip}(\mathbf{x},\boldsymbol{\xi},t-\tau,0) = \int_\Omega \frac{\partial\delta(\boldsymbol{\eta}-\boldsymbol{\xi})}{\partial\eta_q} G^*_{ip}(\mathbf{x},\boldsymbol{\eta},t-\tau,0)\, d\Omega\,. \tag{4.26}$$

That way, the displacement u_i at point $\mathbf{x}$ and time t can be restated from Eq. (4.25) as

$$u_i(\mathbf{x},t) = \int_\Omega \Big(-\int_\Sigma [u_j(\boldsymbol{\xi},\tau)]\, C_{jkpq} n_k \frac{\partial \delta(\boldsymbol{\eta}-\boldsymbol{\xi})}{\partial \eta_q} d\Sigma \Big) * G^*_{ip}(\mathbf{x},\boldsymbol{\eta},t-\tau,0) d\Omega \tag{4.27}$$

$$= \int_\Omega b_p^{[u]}(\boldsymbol{\xi},\tau) * G^*_{ip}(\mathbf{x},\boldsymbol{\eta},t-\tau,0) d\Omega \,, \tag{4.28}$$

with the body force equivalent $b_p^{[u]}$ of a displacement discontinuity $[u_j]$ on Σ:

$$b_p^{[u]}(\boldsymbol{\xi},\tau) = -\int_\Sigma [u_j(\boldsymbol{\xi},\tau)]\, C_{jkpq} n_k \frac{\partial \delta(\boldsymbol{\eta}-\boldsymbol{\xi})}{\partial \eta_q} d\Sigma \,. \tag{4.29}$$

Hence, with Eqs. (4.25) and (4.28), two equivalent representations of a seismic displacement field $u_i(\mathbf{x},t)$ are presented which are initiated by an excitation on a buried fault, modelled as displacement discontinuity and body force, respectively.

4.2.3 Source representation

In the representation theorems Eqs. (4.25) and (4.28), basically a convolution is performed with the two factors: the wave propagation, expressed by the Green's function G^*_{np}, and the source mechanism. As shown above, latter is expressed in the representation theorems, implicitly or explicitly, by the displacement discontinuity $[u_p]$ on the fault. The options to describe this rupture process on the fault in order to scale the Green's functions, are briefly addressed in this section.

The physical process that occurs in the source region is highly complicated. Its understanding requires to study stress-dependent material properties, like the nucleation and spreading of the material failure on the fault, or the rapidly relieving stresses that had slowly risen due to long term tectonic processes. This is a dynamic problem which is very difficult to formulate and to solve. In addition there exist lacks of information of the source region. Therefore, simpler kinematic models are common in seismic analyses (see, e.g., [Aki, 1967]). Nevertheless, for the derivation of correct seismic motions at a point of interest, it is essential to consider all important influences on the earthquake rupture process during the formulation of the source term.

Kinematic modelling: Even though there exist more sophisticated kinematic approaches, the simplest kinematic model commonly used in quantitative seismology leads to sufficient results. In this model the source mechanism is only mapped by five parameters [Aki and Richards, 2002]. Those five parameters are the length L and width W of the fault, the rupture velocity the final offset D and the rise time t_r which denotes the time-span that is needed for a particular point on the fault to reach its final position after the rupture. The five-parameter model is widely used in quantitative seismology and was originally studied by [Haskell, 1964]. For a more detailed description of the source mechanism, additional parameters like nucleation of motion or spreading of rupture can be incorporated. The parameters on which the kinematic models are based can be determined by empirical scaling laws suggested by, e.g., [Wells and Coppersmith, 1994].

When Haskell's five-parameter source model is used for simulating seismic ground motion, some characteristics in the corresponding frequency-spectrum simulated for the far-field of the source can be observed (see Fig. 4.6). The spectrum is flat near $f = 0$ where the amplitude value of the frequency f is proportional to the product of the final offset D and the rupture area $S = WL$. Thus, it is proportional to the seismic moment defined in Eq. (4.1). For frequencies higher than a certain *cutoff frequency* f_c, a decay of the amplitude spectrum can be observed. The frequencies decay as f^{-2} or f^{-3}, depending on the fault effects considered. This decay in the frequency-spectrum can also be observed in recorded seismograms. Such a frequency-decay of a seismogram is depicted in Fig. 4.6 where the frequency-amplitude of the record of the later referred earthquake is shown that stroke the city of Forlì, Italy, in the year 2003.

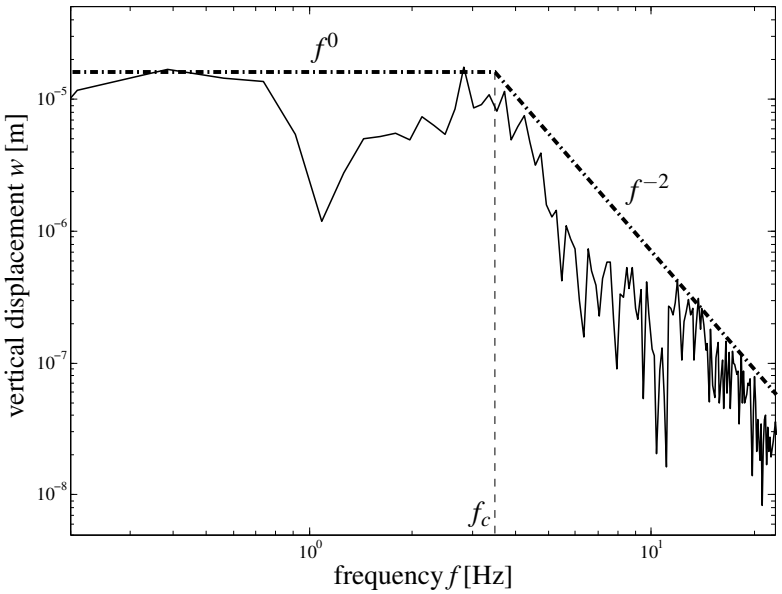

Figure 4.6: Frequency-spectrum of the vertical surface displacement recorded during the $M_w = 4.25$ earthquake in Forlì, Italy. Whereas at low frequencies, the amplitudes are distributed flatly, for frequencies higher than the cutoff frequency f_c, a decay as f^{-2} can be realised.

Concept of self-similarity: The decaying behaviour of the amplitude spectrum of the motion on the earth surface, which is mostly assumed as f^{-2} decay, can be connected with the motion on the fault surface by self-similarity relations. In order to explain the conclusions from those relations, it is necessary to introduce the concept of *self-similarity* as done, e.g., in [Aki and Richards, 2002]. A wave propagation phenomenon which has no inherent scale in space nor in time is called self-similar. This phenomenon appears the same at all scales of space and time. From the self-similarity results a simplicity in the space time-dependence that can be used to allow an exact solution of the displacement and stresses for all points in space and time.

The initial seismic fault movement is assumed to be self-similar to the motion recorded in the far-field of the fault. So, considering the motion on the fault, a similar behaviour as the f^{-2} decay of the surface ground motion is expected to arise there. Based on this assumption, many approaches to describe the rupture process on the fault were developed, e.g., by [Andrews, 1981; Frankel, 1991; Herrero and Bernard, 1994]. The details of the respective models should not be discussed here. In this work, the seismic source process is represented by the kinematic k^{-2}-model by [Herrero and Bernard, 1994] which is addressed in Sec. 7.4.2.

4.3 Ground motion

The motion of the ground is of central interest in earthquake engineering. The behaviour and, thus, the failure of the analysed structure, might it be the soil or an engineering structure on top or embedded in it, strongly depends on the particular ground motion initiated by an earthquake. Hence, it is of high importance to describe the motion on the surface properly. For this purpose, meaningful *ground motion parameters* were developed which are addressed subsequently. The question how to derive seismic ground motion as excitation for computational models in order to achieve quantitative statements concerning the earthquake behaviour and resistance of structures is discussed afterwards.

4.3.1 Ground motion parameters

The ground motion at a particular point initiated by an earthquake is determined completely by three components of translation and three components of rotation in the time-interval of interest. If those components are recorded, it is still complicated to evaluate the records in order to describe the properties of the ground motion. For engineering purposes, it is often reasonable to characterise the ground motion at one site with only a few but meaningful, quantitative parameters. Those *ground motion parameters* embrace characteristics of amplitude, duration and frequency-content of the motion. The several proposed ground motion parameters contain values of one or more of those characteristics. In practice, it is usually necessary to use multiple parameters to describe a particular ground motion adequately.

Amplitude parameters: The most common ground motion parameters are measures of the amplitudes of the time history of a particular ground motion. Since time-histories are usually available for displacements and their time-derivatives, the maximum amplitudes of those three components give a quantitative information about the motion. Those ground motion parameters are the *peak ground acceleration* (PGA), the *peak ground velocity* (PGV) and the *peak ground displacement* (PGD). PGV is the parameter that is commonly used when analysing the seismic failure of buried pipelines [O'Rourke and Liu, 1999; O'Rourke, 1995].

Duration: The earthquake damage is strongly influenced by the duration of the seismic ground motion, since long lasting ground motions imply many load or stress reversals. Large numbers of reversals can lead in certain types of structures to the degradation of stiffness and strength or in the case of loose, saturated sands to the build-up of pore-water pressure (liquefaction). The duration of the seismic ground motion is related to the energy dissipated by the motion, e.g., the acceleration. For engineering purposes only the strong motion part of an accelerogram is of interest. Several approaches for evaluating the duration of the strong motion have been proposed. The most common definitions are the strong motion duration by [Trifunac and Brady, 1975] D_s which accords to the time-interval between 5% and 95% of total energy, whereas [Bolt, 1969] states the *bracket duration* to last from the first to the last exceedance of a threshold acceleration. This threshold is usually chosen as 5% of earth's gravity g, i.e., $0.05g$.

Intensities: Physically, intensity is defined as energy per time per area. So, the *total intensity* I_0 of a ground motion up to a certain time t_d can be expressed as the integral over the squared acceleration time-history $\ddot{u}_i(t)$

$$I_{0i} = \int_0^{t_d} \ddot{u}_i(t)^2 dt \ . \tag{4.30}$$

When the total intensity should be expressed for a particular ground motion it is necessary to use one of the strong ground motion duration definitions, as discussed above. An intensity expression that is independent of the definition of the strong ground motion duration, is the *Arias intensity* I_A [Arias, 1970]

$$I_{Ai} = \frac{\pi}{2g} \int_0^{\infty} \ddot{u}_i(t)^2 dt \ , \tag{4.31}$$

where the squared accelerations are integrated over the entire duration of motion. Because of its independence from the duration definition, Arias intensity is most popular in seismic engineering.

Frequency-content parameters: The motion produced by earthquakes imply a broad band of frequencies. Since the distribution of those frequencies strongly influences the behaviour of structures examined in engineering analyses, several frequency-content parameters of the ground motion were suggested. For

that purpose, the time-history of the ground motion is transferred to the frequency-domain, whereupon spectral parameters, like predominant period, bandwidth, central frequency or shape factor, are obtained. For details on those parameters see, e.g., [Kramer, 1996].

When the time-dependent ground motion, expressed as function $f(t)$, is Fourier transformed

$$F(\omega) = \int_{-\infty}^{\infty} f(t) e^{-i\omega t} dt \,, \tag{4.32}$$

the *Fourier spectrum* $F(\omega)$ contains the amplitude $A(\omega) = |F(\omega)|$ and the phase angle $\phi(\omega) = \angle F(\omega)$. Those spectra provide a complete description of the ground motion, since the time-sequence $f(t)$ can be totally recovered by the inverse Fourier transform

$$f(t) = \frac{1}{2\pi} \int_{-\infty}^{\infty} A(\omega) e^{i(\omega t + \phi(\omega))} d\omega \,. \tag{4.33}$$

The shape of the Fourier amplitude spectrum indicates the domination of particular frequencies, i.e., a narrow shape implies dominant frequencies, whereas a broad spectrum corresponds to a motion that contains a variety of frequencies. Fourier amplitude spectra transformed from seismic records show the largest amplitudes between a *corner frequency* f_0 on the low side and a cutoff frequency f_c on the high side. Whereas the corner frequency f_0 is proportional to the seismic moment M_0 [Brune, 1971], the characterisation of the cutoff frequency f_c is not well understood. Some authors relate it to source effects [Papageorgiou and Aki, 1983], others to near-field effects [Hanks, 1982].

Next to the Fourier spectra, mainly two other kinds of spectra are incorporated in earthquake engineering: the *power spectra* and the *response spectra*. A power spectrum expresses the total intensity I_0 given in Eq. (4.30) of an earthquake in the frequency-domain. The power spectrum is useful in characterising an earthquake as a random process. A response spectrum describes the maximum response of a single-degree-of-freedom system to a particular input motion as a function of the natural frequency and the damping ratio of the system. Whereas elastic response spectra assume a linear structural force-displacement behaviour, inelastic response spectra are used to account non-linear effects of the single-degree-of-freedom system, e.g., by means of a ductility factor. Generally, response spectra reflect the ground motion characteristics indirectly, since they only describe the response of the single-degree-of-freedom system and moreover only its maximum values.

4.3.2 Ground response analysis

In earthquake engineering, one of the most important tasks is to determine the motion of the ground initiated by an earthquake. Even though, the effects of earthquakes spread over domains of several tenth to hundreds of kilometres, civil engineers are mainly interested in the motion and wave propagation effects in the vicinity of the examined structure.

To address those effects properly, some useful terms are introduced in the following. Seismic waves are travelling from their initial fault through the rocky inner of the earth (see Fig. 4.7(a)). Only a very thin layer at the surface is soil. The rock directly under the soil is called *bedrock* (see Fig. 4.7(b)). When the seismic waves arrive at the bedrock-soil-interface, their amplitudes and propagation directions change significantly. The examination of the motion in the soil surrounding the structures of interest, i.e., the near-field, is subsumed under the concept of *ground response analysis*. The central topic in ground response analyses is the determination of the motion that excites the near-field soil. Obviously, this excitation plays a key-role in engineering problems, since all motion and, therewith, all strains and stresses in the examined structure depend on the initial excitation of the near-field. The ground motion at the surface which is only caused by wave propagation through the soil without any structures inside or on top, is termed *free-field motion* (see Fig. 4.7(b)). Usually in ground response analyses, the free-field

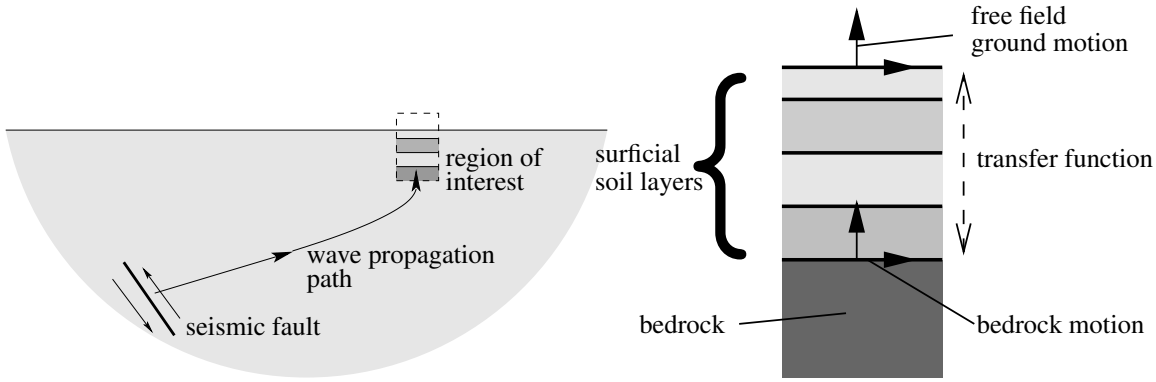

(a) Sketch of the earth crust depicted as half-space with the seismic wave propagation path. The waves are initiated at the seismic fault and travel through the inner of the earth to the region of interest. Due to changing wave velocities, the wave propagation direction in deeper regions has a dominant horizontal component and becomes nearly vertical when the waves reach the surface.

(b) Region of interest or near-field containing the surficial soil layers down to the bedrock. The transfer function is sketched which relates the free-field ground motion at the surface to the bedrock motion.

Figure 4.7: Seismic wave propagation path and motions in the surficial soil layers.

motion of the ground is considered. This is done mainly to achieve an undisturbed response of the soil in order to give statements about the changing behaviour of the waves during the passage of the soil.

In seismic analyses, the propagation path in the near-field is the following. Firstly, the seismic waves enter the near-field domain at the near-field/far-field interface, whereupon the waves propagate through the near-field domain and excite it. Subsequently, the waves reach the surface of the ground where they are partly reflected and refracted and pass again the near-field. The motion of an earthquake is usually recorded on the surface of the ground. So, the place where the ground motion is known, i.e., the surface, is not the same place from where the near-field is excited. Hence, the central question in ground response analyses is how to determine the initial motion at the near-field/far-field interface, i.e., the incidencing waves that excite the near-field.

Deconvolution: For a realistic modelling of the wave propagation inside the near-field, it is desirable to determine the initial motion from the recorded surface motion. When the problem is treated that way, an inverse problem needs to be solved in which the causing, i.e., the initial excitation on the interface, is determined from the reaction, i.e., the motion on the surface. This procedure is called *deconvolution*. When a material is considered to behave linear or equivalent-linear, the dynamic responses at two points are uniquely related to each other. So, the soil material necessarily needs to be assumed to behave linear to perform the deconvolution operation successfully. In contrast, the soil motion at one point is not uniquely related to the motion at an other point in a non-linear analysis and, hence, the deconvolution operation does not provide a unique solution in this case.

If the seismic excitation of the near-field is assumed to be a plane *SH*-wave incident vertically at the bottom of the near-field (the bedrock motion in Fig. 4.7(b)), the deconvolution problem is reduced to one dimension. For this special case, the inverse problem can be solved straightforward by means of a so-called *transfer function* as sketched in Fig. 4.7(b). This transfer function describes the response on the stress-free surface due to a unit-impulse load at the bedrock in frequency-domain. Hence, it is nothing else than a Green's function (Sec. 4.2.1). The procedure of such a one-dimensional ground response analysis is described in [Kramer, 1996]. The transfer function is constructed in frequency-domain from geometry and material parameters. Thus, the time-history of the surface motion is also transformed to frequency-domain, so that the Fourier transform of the surface motion can be multiplied by the transfer function. This yields the frequency-content of the bedrock motion from which the bedrock motion in

time-domain can be revealed by means of an inverse Fourier transform.

The deconvolution procedure was studied extensively by [Kane *et al.*, 2002]. Even though the deconvolution yields good results in cases similar to the one discussed above, the procedure is more or less restricted to one-dimensional problems or at least to problems with a few degrees of freedom. Otherwise, the solution of the inverse problem becomes too complicated.

Near-field excitation: Often in earthquake engineering, the one-dimensional deconvolution is performed for problems which are not one-dimensional as well, e.g., to study the behaviour of the soil layers under earthquake conditions [Venkatesan *et al.*, 2006] or to compute the ground motion as seismic excitation at the bottom of a building [Fahmi and Malkawi, 1998]. In some studies, without any further treatment the recorded surface motion is just applied as excitation at the bedrock. Those simplifications are justifiable for some applications, e.g., when the considered near-field has no large extensions in terms of earthquake considerations. Anyway, in some cases these simplifications are not defensible, e.g., when the near-field extends over large dimensions or when wave propagation in more than the vertical direction is considered. This is clearly the case when analysing buried lifelines under seismic wave propagation effects. For those cases, other approaches have to be found to obtain the seismic excitation of the near-field. This topic is discussed in Chap. 7 and an advanced approach for determining a reliable, i.e., realistic seismic excitation for the near-field is introduced.

Part II

Methodology

5 Finite element method

The finite element method (FEM) is the most popular numerical method for simulating engineering problems. Detailed descriptions of this well-established method are widely available (see, e.g., [Zienkiewicz *et al.*, 2005] or [Bathe, 1996]). Hence, this chapter gives just a brief introduction to the FEM.

Generally, the FEM can be seen as an application of the Rayleigh-Ritz method and is mostly based on a displacement approximation [Axelsson, 1996]. Utilising the FEM, the analysed domain is spatially discretised into non-overlapping elements interconnected at nodes on the element edges (see Fig. 5.1). In each of those elements, e.g., the displacements are interpolated by shape functions in the form of polynomials. Standard numerical integration of these regular functions leads to a simple approximation for the behaviour of each finite element consisting of symmetric coefficient matrices. Those local representations are then patched together enforcing compatibility and equilibrium leading to the global model. A major strength of the FEM is the ease with which complex geometries, materials and boundary conditions can be regarded. For an unbounded domain, the FEM cannot satisfy the boundary conditions at infinity exactly. Due to the finite size of the elements, the spatial discretisation is terminated on an artificial boundary where the truncated domain outside the boundary up to infinity can only be represented approximately.

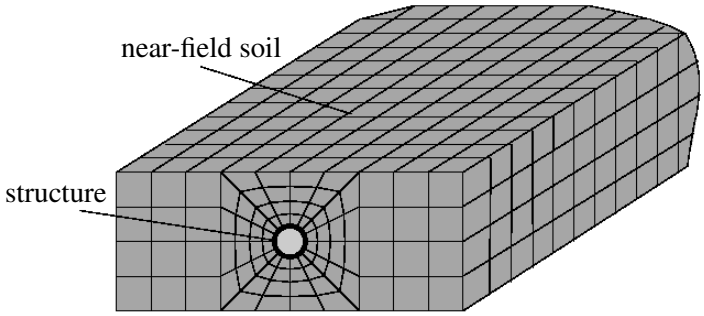

Figure 5.1: Three-dimensional FEM discretisation of a soil-structure interaction problem.

On the basis of the governing equations of three-dimensional elastodynamics, the main steps of the FEM will be explained in the following.

5.1 Governing equations in symbolic notation

As it is necessary for the derivation of the FEM, the governing equations of elastodynamics congruently to Sec. 2.1 will be reproduced in symbolic notation.

Dynamic equilibrium: Introducing the gradient operator $\mathbf{D}$

$$\mathbf{D} = \begin{bmatrix} \frac{\partial}{\partial x_1} & 0 & 0 & 0 & \frac{\partial}{\partial x_3} & \frac{\partial}{\partial x_2} \\ 0 & \frac{\partial}{\partial x_2} & 0 & \frac{\partial}{\partial x_3} & 0 & \frac{\partial}{\partial x_1} \\ 0 & 0 & \frac{\partial}{\partial x_3} & \frac{\partial}{\partial x_2} & \frac{\partial}{\partial x_1} & 0 \end{bmatrix}^T , \tag{5.1}$$

the dynamic equilibrium in time-domain from Eq. (2.4) reads

$$\mathbf{D}^T\boldsymbol{\sigma}(t) + \mathbf{b}(t) - \rho\ddot{\mathbf{u}}(t) = \mathbf{0}\,. \tag{5.2}$$

Constitutive equation: Considering isotropic, linear elastic material leads to Hooke's law of Eq. (2.8) which reads in symbolic notation

$$\boldsymbol{\sigma} = \mathbf{E}\boldsymbol{\varepsilon}\,. \tag{5.3}$$

Strain-displacement relationship: The relationship between strains $\boldsymbol{\varepsilon}$ and displacement $\mathbf{u}$ for linear theory from Eq. (2.9) is formulated with the differential operator $\mathbf{D}$ as

$$\boldsymbol{\varepsilon} = \mathbf{D}\mathbf{u}\,. \tag{5.4}$$

5.2 Weak form of governing equations (Virtual work formulation)

After setting up the governing equations, the intention is to derive a displacement field $\mathbf{u}$ which satisfies the dynamic equilibrium Eq. (5.2) in the domain Ω and fulfils the conditions Eqs. (2.15) and (2.16) on the boundary and Eqs. (2.17) and (2.18) at the initiation. This can be achieved by requiring the variational or weak form of the equilibrium equation (5.2) to be zero.

The virtual work theorem is such a weak form where a virtual displacement δu is an arbitrary function. This arbitrary function is multiplied with the strong form of the equation, i.e., Eq. (5.2), and integrated over the domain Ω. The resulting variation of the scalar quantity $\delta\Pi_{eq}$ is set to zero:

$$\delta\Pi_{eq} = \int_\Omega \delta\mathbf{u}\left[\mathbf{D}^T\boldsymbol{\sigma} + \mathbf{b} - \rho\ddot{\mathbf{u}}\right] d\Omega = 0. \tag{5.5}$$

This equation can be rearranged by applying integration by parts and noting the symmetry of the stress tensor. When enforcing the displacement boundary conditions point wise and impose a constraint that $\delta\mathbf{u}$ vanishes on Γ_u, the virtual work equation reads

$$\delta\Pi_{eq} = \underbrace{\int_\Omega \delta(\mathbf{D}\mathbf{u})^T\boldsymbol{\sigma}\, d\Omega}_{\text{internal work}} - \underbrace{\int_\Omega \delta\mathbf{u}^T\rho\ddot{\mathbf{u}}\, d\Omega}_{\text{work of internal loads}} - \underbrace{\int_\Omega \delta\mathbf{u}^T\mathbf{b}\, d\Omega}_{\text{external work of body loads}} - \underbrace{\int_\Gamma \delta\mathbf{u}^T\mathbf{t}\, d\Gamma}_{\text{external work of tractions}} = 0\,. \tag{5.6}$$

The dynamic equilibrium is satisfied in a weak sense, if this equation is satisfied for a subset of virtual displacement fields. This weak form provides the basis from which a finite element formulation of equilibrium may be deduced.

5.3 Approximative solution

As stated above, the FEM is an approximation procedure, i.e., not the exact but only an approximative solution $\tilde{\boldsymbol{u}}$ for the displacements $\boldsymbol{u}$ is quested. Therefore, the considered domain Ω is divided into subdomains Ω_e, called elements:

$$\Omega \approx \hat{\Omega} = \sum_e \Omega_e\,. \tag{5.7}$$

Each element Ω_e is associated with a a set of n nodes $\mathbf{z}^b$ ($1 \le b \le n$, in local numbering). At each of those nodes $\mathbf{z}^b$, interpolation functions $N_b(\boldsymbol{\xi})$, also called shape functions, are defined in local coordinates $\boldsymbol{\xi}$.

Displacement approximation: The finite element approximation for displacements $\hat{\mathbf{u}}$ is then given by

$$\mathbf{u}(\mathbf{x},t) \approx \hat{\mathbf{u}}(\mathbf{x},t) = \sum_{b=1}^{n} N_b(\boldsymbol{\xi})\tilde{\mathbf{u}}_b(t) = \mathbf{N}\tilde{\mathbf{u}}(t) \tag{5.8}$$

where $\tilde{\mathbf{u}}_b(t)$ are the time-dependent nodal displacements. Generally, the local coordinates $\boldsymbol{\xi} = (\xi_1, \xi_2, \xi_3)$ of every element differ from the global Cartesian coordinates $\mathbf{x} = (x_1, x_2, x_3)$, in which the re-assembling of the elements is performed. These coordinate systems are related by the mapping

$$\mathbf{x}(\boldsymbol{\xi}) = \sum_{i=1}^{n} N^i(\boldsymbol{\xi})\mathbf{x}^i\,, \quad \boldsymbol{\xi} \in \Delta_e \tag{5.9}$$

where Δ_e is the isoparametric parent element. The two coordinate systems and the mapping is sketched in Fig. 5.2.

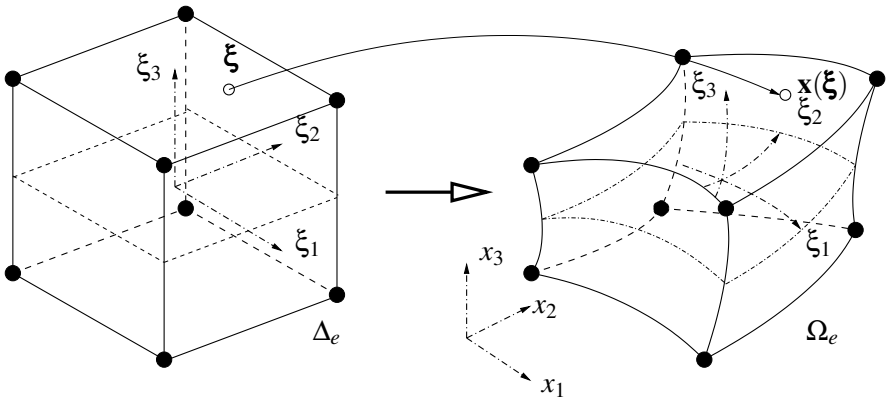

Figure 5.2: Mapping of a three-dimensional parent element Δ_e to an eight-node finite element Ω_e.

Strain-displacement equations: Using Eq. (5.4), the strains associated with the approximative displacement field $\tilde{\mathbf{u}}$ are given by:

$$\boldsymbol{\varepsilon}(\mathbf{x},t) = \mathbf{D}\mathbf{u}(\mathbf{x},t) \approx \sum_{b=1}^{n} (\mathbf{D}N_b)\tilde{\mathbf{u}}_b(t) = \mathbf{D}\mathbf{N}\tilde{\mathbf{u}}(t)\,. \tag{5.10}$$

Concordantly to the previous Eqs. (5.8) and (5.10), the virtual displacements $\delta\mathbf{u}$ as well as the virtual strains can be approximated via

$$\delta\mathbf{u}(\mathbf{x},t) \approx \sum_{b=1}^{n} N_b(\boldsymbol{\xi})\delta\tilde{\mathbf{u}}_b(t) = \mathbf{N}\delta\tilde{\mathbf{u}}(t) \quad \text{and} \tag{5.11}$$

$$\delta\boldsymbol{\varepsilon}(\mathbf{x},t) = \mathbf{D}\delta\mathbf{u}(\mathbf{x},t) \approx \sum_{b=1}^{n} (\mathbf{D}N_b)\delta\tilde{\mathbf{u}}_b(t) = \mathbf{D}\mathbf{N}\delta\tilde{\mathbf{u}}(t)\,. \tag{5.12}$$

Weak form: Since, generally, the shape functions $\mathbf{N}$ do not satisfy the governing differential equation, the stresses will not satisfy the internal equilibrium at any point as well. Therefore, the virtual work statement Eq. (5.6) is used to require equilibrium at least in a weak sense. An approximate solution consisting of a linear combination of n shape functions can be made to satisfy the virtual work equation for a virtual displacement space spanned by n independent virtual displacement fields. The Galerkin approach applies the same shape functions used to construct $\tilde{\mathbf{u}}$ to provide the n independent virtual displacement fields. In this case, the virtual work equation must be satisfied for any linear combination of the shape functions.

Substituting the approximative terms from Eqs. (5.11) and (5.12) into the weak form of equilibrium, given in Eq. (5.6), yields for a single element

$$\delta\Pi_{eq}^{(e)} = \delta\tilde{\mathbf{u}}^T \left[\int_\Omega \mathbf{N}^T \rho \mathbf{N} \ddot{\tilde{\mathbf{u}}}\, d\Omega + \int_\Omega (\mathbf{DN})^T \boldsymbol{\sigma}\, d\Omega - \int_\Omega \mathbf{N}^T \mathbf{f}\, d\Omega - \int_\Gamma \mathbf{N}^T \mathbf{t}\, d\Gamma \right] = 0\,. \tag{5.13}$$

The element arrays from Eq. (5.13),

$$\mathbf{M}^{(e)} = \int_\Omega \mathbf{N}^T \rho \mathbf{N} \ddot{\tilde{\mathbf{u}}}\, d\Omega\,, \tag{5.14}$$

$$\mathbf{P}^{(e)}(\boldsymbol{\sigma}) = \int_\Omega (\mathbf{DN})^T \boldsymbol{\sigma}\, d\Omega\,, \tag{5.15}$$

$$\mathbf{f}^{(e)} = \int_\Omega \mathbf{N}^T \mathbf{f}\, d\Omega + \int_\Gamma \mathbf{N}^T \mathbf{t}\, d\Gamma\,, \tag{5.16}$$

are named mass matrix $\mathbf{M}^{(e)}$, stress divergence $\mathbf{P}^{(e)}$ and vector of equivalent nodal forces $\mathbf{f}^{(e)}$. Performing the sum over all elements, i.e., summing up the discrete arrays

$$\mathbf{M} = \sum_e \mathbf{M}^{(e)}\,, \quad \mathbf{P} = \sum_e \mathbf{P}^{(e)} \text{ and } \quad \mathbf{f} = \sum_e \mathbf{f}^{(e)}$$

and having in mind that the virtual displacements $\delta\tilde{\mathbf{u}}$ are arbitrary, a set of ordinary differential equations can be obtained from Eq. (5.13)

$$\mathbf{M}\ddot{\tilde{\mathbf{u}}} + \mathbf{P}(\boldsymbol{\sigma}) = \mathbf{f} \tag{5.17}$$

which actually describes a semi-discrete problem for the complete domain.

Irreducible displacement method: In the case of linear elasticity, the constitutive equations are given by Eq. (5.3), so that the stress divergence $\mathbf{P}^{(e)}$ from Eq. (5.15) becomes, under consideration of Eq. (5.4),

$$\mathbf{P}^{(e)}(\boldsymbol{\sigma}) = \left(\int_{\Omega_e} (\mathbf{DN})^T \mathbf{E} (\mathbf{DN}) d\Omega \right) \tilde{\mathbf{u}} = \mathbf{K}^{(e)} \tilde{\mathbf{u}}\,, \tag{5.18}$$

where $\mathbf{K}^{(e)}$ is the linear stiffness matrix. When assembling the local element arrays, like done above, and considering the, so far, neglected damping terms, the finite element equation of motion Eq. (5.17) becomes

$$\mathbf{M}\ddot{\tilde{\mathbf{u}}} + \mathbf{C}\dot{\tilde{\mathbf{u}}} + \mathbf{K}\tilde{\mathbf{u}} = \mathbf{f}\,. \tag{5.19}$$

In practice, it is difficult, if not impossible, to determine the element damping parameters for general finite element assemblages, in particular because the damping properties are frequency-dependent. For this reason, the damping matrix $\mathbf{C}$ is generally not assembled from element damping matrices, but is constructed using the global mass and stiffness matrices of the complete element assemblage:

$$\mathbf{C} = c_m \mathbf{M} + c_k \mathbf{K}\,. \tag{5.20}$$

Experimental results should verify the amount of damping. In the present work, the terms of damping are omitted.

For convenience and more clarity, the approximative displacement fields as well as their time-derivatives are denoted as $\mathbf{u}$ instead of $\tilde{\mathbf{u}}$ in the following. To solve Eq. (5.17) and Eq. (5.19) numerically, two main types of solution procedures exist, the direct integration type and the mode superposition, respectively. In the next subsection, a brief description of direct integration methods is given.

5.4 Time-integration

In this section, numerical step-by-step procedures are explained which integrate Eq. (5.19) directly. Direct numerical time-integration is based on two ideas. Firstly, instead of trying to satisfy Eq. (5.19) at any time t, equilibrium is only requested at discrete time-stations. Therefore, all solution techniques employed in static analysis may also be used in direct time-integration. Secondly, a variation of displacements, velocities and accelerations within each time-interval Δt is assumed. The way of assuming this variation determines the accuracy, stability, and computational cost of the solution procedure.

At time $t_0 = 0$, it is assumed that the displacement $\mathbf{u}_0$, the velocity $\dot{\mathbf{u}}_0$, and the acceleration $\ddot{\mathbf{u}}_0$ are known a priori. The solution of Eq. (5.19) is searched for the considered time span t_n which is subdivided into n equal time-intervals $\Delta t = \frac{t_n}{n}$.

5.4.1 Newmark algorithm

The most common time-integration method for linear problems in structure dynamics is the family of Newmark procedures. For the current time $t_{n+1} = t_n + \Delta t$ where $\mathbf{u}_{n+1}$, $\dot{\mathbf{u}}_{n+1}$ and $\ddot{\mathbf{u}}_{n+1}$ denote the approximations of $\mathbf{u}$, $\dot{\mathbf{u}}$ and $\ddot{\mathbf{u}}$ and $\mathbf{f}_{n+1} = \mathbf{f}(t_{n+1})$, the equation of motion reads

$$\mathbf{M}\ddot{\mathbf{u}}_{n+1} + \mathbf{C}\dot{\mathbf{u}}_{n+1} + \mathbf{K}\mathbf{u}_{n+1} = \mathbf{f}_{n+1} \; . \tag{5.21}$$

When the displacements $\mathbf{u}_n$, velocities $\dot{\mathbf{u}}_n$, and accelerations $\ddot{\mathbf{u}}_n$ of the previous time-step n are known, the predictor variables $\hat{\mathbf{u}}_{n+1}$ and $\hat{\dot{\mathbf{u}}}_{n+1}$ for the current time are defined as

$$\hat{\mathbf{u}}_{n+1} = \mathbf{u}_n + \Delta t \dot{\mathbf{u}}_n + \Delta t^2 \left(\frac{1}{2} - \beta \right) \ddot{\mathbf{u}}_n \quad \text{and} \tag{5.22}$$

$$\hat{\dot{\mathbf{u}}}_{n+1} = \dot{\mathbf{u}}_n + (1-\gamma)\Delta t \ddot{\mathbf{u}}_n \; , \tag{5.23}$$

with the algorithm parameters β and γ. With the predictors $\mathbf{u}_{n+1}$ and $\dot{\mathbf{u}}_{n+1}$ of the current time-step can be approximated by

$$\mathbf{u}_{n+1} = \hat{\mathbf{u}}_{n+1} + \beta \Delta t^2 \ddot{\mathbf{u}}_{n+1} \quad \text{and} \tag{5.24}$$

$$\dot{\mathbf{u}}_{n+1} = \hat{\dot{\mathbf{u}}}_{n+1} + \gamma \Delta t \ddot{\mathbf{u}}_{n+1} \; , \tag{5.25}$$

The parameters β and γ are responsible for the stability and accuracy of the method. For $\gamma = \frac{1}{2}$, the Newmark method is of second order accuracy. For $\beta = \frac{1}{4}$ and $\gamma = \frac{1}{2}$, this method becomes the trapezoid rule or average acceleration method which is implicit and unconditionally stable. Those properties do not dependent on the chosen time-step [Hughes, 1983]. Additionally, the conservation of total energy is fulfilled for linear systems.

5.4.2 Hilber-Hughes-Taylor-α method

When choosing $\gamma \neq \frac{1}{2}$ in the Newmark algorithm, an algorithmic damping of high frequencies can be achieved which also reduces the accuracy. For this reason, the Hilber-Hughes-Taylor-α (HHT-α) method [Hilber *et al.*, 1977] was developed for linear problems as a variant of the Newmark method. The HHT-α integration scheme is used in the coupled FE-SBFE scheme which will be introduced in Sec. 6.5.

The HHT-α algorithm adds a third parameter α into the Newmark method in order to regard the decrease of accuracy resulting from introducing numerical damping. Setting $\alpha = 0$ reduces the problem to a standard Newmark method. Choosing $\alpha \in [-\frac{1}{3}, 0]$, $\beta = \frac{(1-\alpha)^2}{4}$ and $\gamma = \frac{1-2\alpha}{2}$ results in an unconditionally stable, second-order accurate algorithm [Hughes, 1987] with included algorithmic damping of high frequencies.With those three parameters, the temporal discretised equation of motion in the HHT-α method is written

$$\mathbf{M}\ddot{\mathbf{u}}_{n+1} + (1+\alpha)\mathbf{C}\dot{\mathbf{u}}_{n+1} - \alpha\mathbf{C}\dot{\mathbf{u}}_n + (1+\alpha)\mathbf{K}\mathbf{u}_{n+1} - \alpha\mathbf{K}\mathbf{u}_n = \mathbf{f}_{n+1+\alpha} \; . \tag{5.26}$$

with $\mathbf{f}_{n+1+\alpha} = \mathbf{f}(t_{n+1} + \alpha\Delta t)$. The standard Newmark finite difference formulas Eqs. (5.24) and (5.25) are used as approximations for $\mathbf{u}_{n+1}$ and $\dot{\mathbf{u}}_{n+1}$. An implicit update equation can be achieved with $\mathbf{u}_{n+1}$ as the only unknown by rearranging Eq. (5.24) and substituting the result along with Eq. (5.25) into the equation of motion Eq. (5.26). If the left hand coefficient matrix is denoted as $\hat{\mathbf{L}}$ and the right hand contributions excluding the force vector as $\hat{\mathbf{R}}$, then the update equation is

$$\hat{\mathbf{L}}\mathbf{u}_{n+1} = \hat{\mathbf{R}}_{n+1} + \mathbf{f}_{n+1+\alpha} \tag{5.27}$$

with

$$\hat{\mathbf{L}} = \mathbf{M} + \gamma\Delta t\mathbf{C} + (1+\alpha)\beta\Delta t^2\mathbf{K} \quad \text{and} \tag{5.28}$$

$$\hat{\mathbf{R}}_{n+1} = [\mathbf{M} + \gamma\Delta t\mathbf{C}]\,\hat{\mathbf{u}}_{n+1} - (1+\alpha)\beta\Delta t^2\mathbf{C}\hat{\dot{\mathbf{u}}}_{n+1} + \alpha\beta\,\Delta t^2\,[\mathbf{C}\dot{\mathbf{u}}_n + \mathbf{K}\mathbf{u}_n]\ . \tag{5.29}$$

6 Scaled boundary finite element method

In this chapter, the main idea and the derivation of the scaled boundary finite element method (SBFEM) for elastodynamic analyses in time-domain is presented. As discussed in Chap. 3, the SBFEM belongs to the so-called rigorous methods for modelling the wave radiation to infinity. Precedent works on the basic idea of the discussed method were published by [Silvester *et al.*, 1977; Thatcher, 1978; Dasgupta, 1982], whereupon the SBFEM was originally developed under the name *consistent infinitesimal finite element cell method* [Wolf and Song, 1996] for the numerical simulation of wave propagation in unbounded media. Formulations for problems of incompressible elastic media, diffusion, the vector wave equation or the scalar wave equation were addressed [Song and Wolf, 1995, 1996a,b, 1997]. Nowadays, this method is named SBFEM [Wolf, 2003]. The main field of its application is the analysis of wave propagation problems in an elastic half-space which is present when soil-structure interaction problems are addressed.

Idea and steps of procedure: The basic idea of the SBFEM is the transformation of the governing partial differential equations describing a problem to a coordinate system consisting of the radial direction and the local circumferential directions which are parallel to the boundary. The number of the circumferential coordinates is one or two for problems of two or three dimensions, respectively. In this circumferential direction, the boundary is discretised by surface finite elements, reducing the governing partial differential equations to ordinary differential equations in the radial coordinate. Applying the finite element approximation in circumferential direction, the coefficients of the ordinary differential equations can be determined, whereupon latter can be solved analytically in radial direction. With this procedure, the SBFEM can be termed a semi-analytical method since the solution of a problem is obtained approximatively in the circumferential directions and analytically in the radial one. For an unbounded domain, the radial coordinate points to infinity, where the radiation condition can be incorporated exactly in the analytical solution.

Comparison to FEM and BEM: Advantages and disadvantages of the two most appealing numerical methods, the FEM and the BEM, were discussed in Chap. 5 and Sec. 3.3.1. The SBFEM combines the most attractive features of both methods. Advantages kept from the FEM are that no fundamental solution is required, that singular integrals are avoided and that the coefficient matrices are symmetric. Beneficial properties assigned from the BEM are that the spatial dimension is reduced by one, that the boundary conditions at infinity are satisfied exactly and that no other approximation than the one of the elements on the boundary is introduced. In addition, the SBFEM provides own advantageous properties as no spatial discretisation of certain free and fixed boundaries and interfaces is required. An other advantage of the SBFEM is that the influence of the infinite far-field can be stored in form of the acceleration unit-impulse response matrix which describes the response of the unbounded domain in time-domain. Therefore, the SBFE computation can be performed before starting the simulation of the entire problem. For unchanged far-field properties, the SBFE computation can be executed only once, enabling multiple over-all simulations where different near-field conditions may be considered.

Application in soil-structure interaction: The SBFEM was mainly developed to simulate the response of infinite domains with fulfilled radiation condition. In soil-structure analyses, the entire domain is divided into a near-field and a far-field, as depicted in Fig. 6.1. To avoid artificial wave reflections

at the near-field/far-field interface Γ which exist just in the model and is not present in reality, Γ is discretised by scaled boundary finite elements (SBFEs) in order to introduced them as absorbing boundary conditions. Therefore, it is just necessary to place SBFEs on Γ and not at the free surface Γ^0 of the infinite domain as shown in Fig. 6.1.

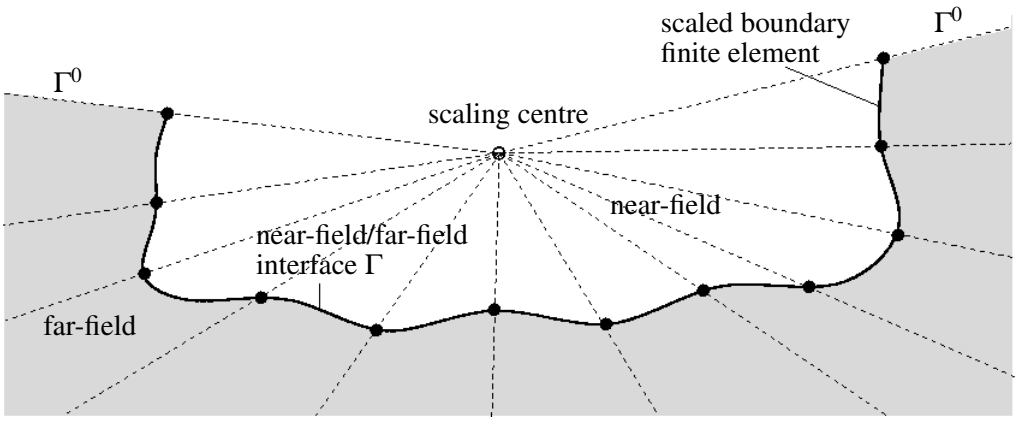

Figure 6.1: Two-dimensional SBFE discretisation of an unbounded media.

When the SBFEM is incorporated to analyse soil-structure interaction, a hybrid FE-SBFE method is utilised. In this hybrid scheme, the FEM is employed to model the near-field in detail and the SBFEM is applied to enable the wave radiation to infinity in the unbounded domain. Fig. 6.2 shows the discretisation of the hybrid method applied to a soil-structure interaction problem. The structure, e.g., a buried pipeline, and the local, i.e. the near-field soil are discretised by FEs. Within this part of the domain, complex geometries and non-linear effects can be considered. The near-field/far-field interface is discretised by SBFEs for which the spatial dimensions are reduced by one compared to the FEs mapping the near-field soil. When a direct coupling of the FEM and the SBFEM is performed, like it is done in the present work and which is addressed in Sec. 6.5, the nodes of both element types on the interface have to be congruent.

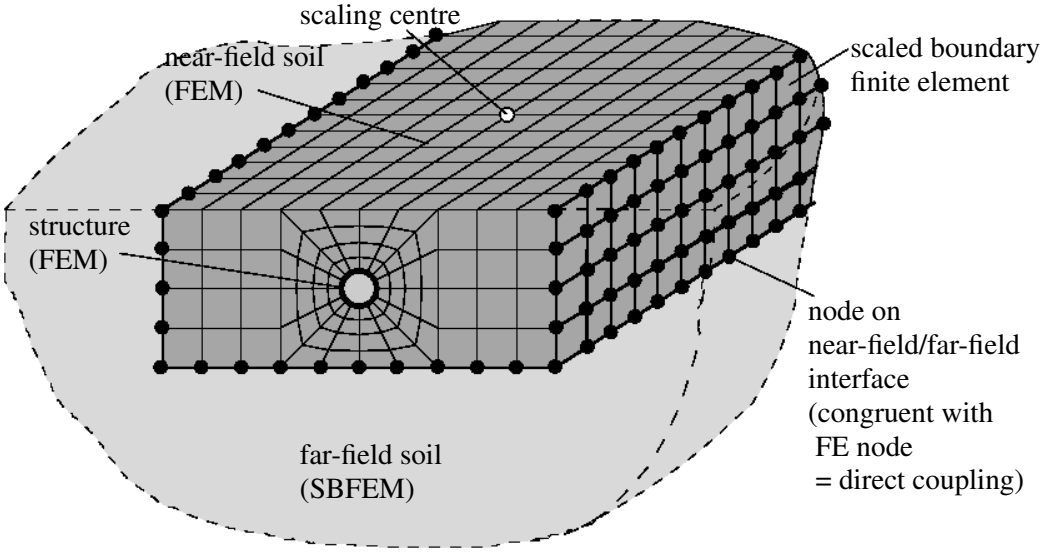

Figure 6.2: Three-dimensional FEM and SBFEM discretisation of a soil-structure interaction problem analysed by a hybrid, direct coupled FE-SBFEM.

6.1 Scaled boundary transformation

The geometry of a three-dimensional problem analysed by the SBFEM is described by two-dimensional finite elements with the local coordinates η, ζ on the boundary and the radial coordinate ξ. This scaled boundary coordinate system $[\xi, \eta, \zeta]$ is related to the Cartesian coordinate system $\mathbf{x}_i = [x_1, x_2, x_3] = [x, y, z]$ by the so-called *scaled boundary transformation* which describes similarity. The radial coordinate ξ measures the distance from the scaling centre O depicted in Fig. 6.3. So, ξ is a scaling factor for which applies $\xi = 0$ at the scaling centre, $\xi = 1$ at the interface of near-field and far-field and $\xi = \infty$ at infinity.

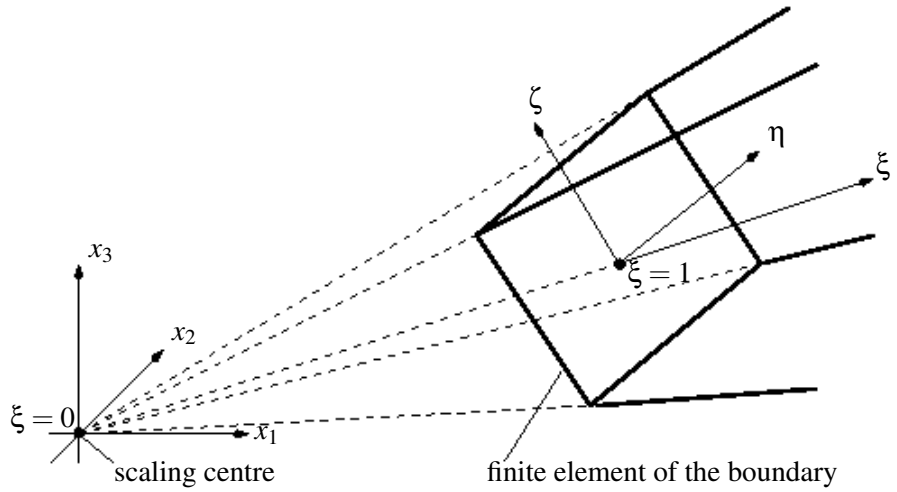

Figure 6.3: Scaled boundary transformation for three-dimensional problems: finite element and coordinate systems.

This scaled boundary coordinate system permits a numerical treatment in the circumferential directions basing on a weighted residual technique as discussed in the theory of finite elements (Chap. 5). Thus, the partial differential equations which describe the problem will be transformed into ordinary differential equations in the radial coordinate ξ. The transformation permits the determination of their coefficients by the finite element approximation in the circumferential directions. For an unbounded medium, the radial coordinate ξ points from the boundary to infinity (see Fig. 6.3) where the boundary condition at infinity, i.e., the radiation condition, can be incorporated in an analytical solution. To apply the SBFEM to a problem, it is at first necessary to formulate the governing equations in scaled boundary coordinates.

Governing equations in scaled boundary coordinates: Even though the SBFEM is also used for time-domain simulations, its formulation starts in frequency-domain. After deriving the formulation for displacement and dynamic stiffness, this formulation will be transferred to time-domain.

The dynamic equilibrium from Eq. (2.4) or Eq. (5.2), respectively, reads in frequency-domain

$$\mathbf{D}^T \hat{\boldsymbol{\sigma}} + \hat{\mathbf{f}} + \omega^2 \rho \hat{\mathbf{u}} = \mathbf{0} \,, \tag{6.1}$$

where ω is the frequency, $\hat{\boldsymbol{\sigma}}$, $\hat{\mathbf{f}}$ and $\hat{\mathbf{u}}$ are the spatial dependent amplitudes of stresses, body forces, and displacements, respectively and ρ denotes the material density. For abbreviation, the hat $(\hat{\cdot})$ is omitted for amplitudes in the following.

The geometry of a finite element on the boundary is represented by interpolating its nodal coordinates $\mathbf{x}_i$ with the mapping functions $\mathbf{N} = \mathbf{N}(\eta, \zeta)$ using the local coordinates η and ζ:

$$x_i(\eta, \zeta) = \mathbf{N}(\eta, \zeta)\mathbf{x}_i \,. \tag{6.2}$$

An arbitrary point in the modelled domain can now be described by scaling its corresponding point on the boundary with the radial coordinate ξ:

$$\mathbf{x}(\xi, \eta, \zeta) = \xi \mathbf{x}(\eta, \zeta) \,. \tag{6.3}$$

The description of the governing equations of elastodynamics in those transformed coordinates affects only the spatial coordinates. The components of the displacements, strains and stresses are still defined in the original Cartesian coordinate system x_i. This is analogous to the mapping of parent elements to curvilinear elements in the FEM (see Fig. 5.2). Thus, only the differential operator $\mathbf{D}$ needs to be modified in the governing equations of elastodynamics Eqs. (6.1), (5.4) and (5.2) in the scaled boundary coordinate system.

Performing the scaled boundary transformation to all spatial coordinates and its derivatives, as done in, e.g., [Wolf, 2003; Lehmann, 2007] yields for the differential operator $\mathbf{D}$ from Eq. (5.1)

$$\mathbf{D} = \mathbf{A}_1 \frac{\partial}{\partial \xi} + \frac{1}{\xi} \left[\mathbf{A}_2 \frac{\partial}{\partial \eta} + \mathbf{A}_3 \frac{\partial}{\partial \zeta} \right] , \tag{6.4}$$

with:

$$\mathbf{A_1} = \frac{1}{|\mathbf{J}|} \begin{bmatrix} n_1^\xi & 0 & 0 \\ 0 & n_2^\xi & 0 \\ 0 & 0 & n_3^\xi \\ 0 & n_3^\xi & n_2^\xi \\ n_3^\xi & 0 & n_1^\xi \\ n_2^\xi & n_1^\xi & 0 \end{bmatrix} , \; \mathbf{A_2} = \frac{1}{|\mathbf{J}|} \begin{bmatrix} n_1^\eta & 0 & 0 \\ 0 & n_2^\eta & 0 \\ 0 & 0 & n_3^\eta \\ 0 & n_3^\eta & n_2^\eta \\ n_3^\eta & 0 & n_1^\eta \\ n_2^\eta & n_1^\eta & 0 \end{bmatrix} \text{ and } \mathbf{A_3} = \frac{1}{|\mathbf{J}|} \begin{bmatrix} n_1^\zeta & 0 & 0 \\ 0 & n_2^\zeta & 0 \\ 0 & 0 & n_3^\zeta \\ 0 & n_3^\zeta & n_2^\zeta \\ n_3^\zeta & 0 & n_1^\zeta \\ n_2^\zeta & n_1^\zeta & 0 \end{bmatrix} . \tag{6.5}$$

Here, $|\mathbf{J}|$ is the determinant of the Jacobian matrix $\mathbf{J}(\xi, \eta, \zeta)$ containing the derivatives of x_i in the transformed $[\xi, \eta, \zeta]$-coordinate system and $\mathbf{n}^\xi$, $\mathbf{n}^\eta$ and $\mathbf{n}^\zeta$ are the outward normal vectors to the surfaces (η, ζ), (ξ, ζ) and (ξ, η), respectively.

6.2 Scaled boundary finite element equation in frequency-domain

In order to achieve an expression for the nodal force-displacement relationship, i.e., the dynamic stiffness in scaled boundary coordinates in time-domain, it is firstly necessary to determine this relationship in frequency-domain. In a first step the scaled boundary finite element equation is expressed in dependency of displacement terms (Sec. 6.2.1). Then, this expression is adjusted to a relationship in terms of dynamic stiffness (Sec. 6.2.2). By obtaining this expression, it is possible to transform this relationship to time-domain (Sec. 6.3).

6.2.1 Scaled boundary finite element equation in displacements

A virtual-work formulation is applied to the governing equations in scaled boundary coordinates. This formulation is developed along similar lines as in the classical finite element method (see Chap. 5). Starting with the differential equations of motion which are formulated, as far as the geometry is concerned, in the scaled boundary coordinates. Following the derivation of [Wolf, 2003], body loads are present, but for the sake of simplicity, no non-zero prescribed surface tractions on the boundary Γ_t^0 (see Fig. 6.1) are applied.

The displacement amplitudes of the finite element on the boundary ($\xi = 1$) are interpolated by utilising the shape functions $\mathbf{N}(\eta, \zeta)$, which are the same mapping function as in Eq. (6.2). The same shape functions apply to the displacement vectors $\mathbf{u}(\xi)$ for all surfaces Γ_ξ with the same ξ:

$$\mathbf{u}(\xi, \eta, \zeta) = \mathbf{N}(\eta, \zeta)\mathbf{u}(\xi) . \tag{6.6}$$

From the mapping function Eq. (6.6), strains $\boldsymbol{\varepsilon}$ and stresses $\boldsymbol{\sigma}$ can be derived in dependency of the scaled

boundary coordinates as

$$\boldsymbol{\varepsilon}(\xi,\eta,\zeta) = \mathbf{B}_1\mathbf{u}(\xi)_{,\xi} + \frac{1}{\xi}\mathbf{B}_2\mathbf{u}(\xi) \text{ and} \tag{6.7}$$

$$\boldsymbol{\sigma}(\xi,\eta,\zeta) = \mathbf{E}\left(\mathbf{B}_1\mathbf{u}(\xi)_{,\xi} + \frac{1}{\xi}\mathbf{B}_2\mathbf{u}(\xi)\right) , \tag{6.8}$$

with the matrices

$$\mathbf{B}_1 = \mathbf{A}_1\mathbf{N}(\eta,\zeta) \text{ and} \tag{6.9}$$

$$\mathbf{B}_2 = \mathbf{A}_2\mathbf{N}(\eta,\zeta)_{,\eta} + \mathbf{A}_3\mathbf{N}(\eta,\zeta)_{,\zeta} , \tag{6.10}$$

using $\mathbf{A}_1$, $\mathbf{A}_2$ and $\mathbf{A}_3$ from (6.5). In analogy to Eqs. (6.6) and (6.7), the amplitudes of the virtual displacements $\delta\mathbf{u}$ and the virtual strains $\delta\boldsymbol{\varepsilon}$ can be expressed as

$$\delta\mathbf{u}(\xi,\eta,\zeta) = \mathbf{N}(\eta,\zeta)\delta\mathbf{u}(\xi) , \tag{6.11}$$

$$\delta\boldsymbol{\varepsilon}(\xi,\eta,\zeta) = \mathbf{B}_1\delta\mathbf{u}(\xi)_{\xi} + \frac{1}{\xi}\mathbf{B}_2\delta\mathbf{u}(\xi) . \tag{6.12}$$

The virtual work statement in frequency-domain reads in scaled boundary coordinates (compare Eq. (5.6) for FEM in time-domain)

$$\begin{aligned}\delta\Pi_{eq} = &\underbrace{\int_\Omega \delta\boldsymbol{\varepsilon}^T(\xi,\eta,\zeta)\boldsymbol{\sigma}(\xi,\eta,\zeta)\,d\Omega}_{\text{internal work}} - \underbrace{\int_\Omega \delta\mathbf{u}^T(\xi,\eta,\zeta)\rho\omega^2\mathbf{u}(\xi,\eta,\zeta)\,d\Omega}_{\text{work of internal loads}} \\ &- \underbrace{\int_\Omega \delta\mathbf{u}^T(\xi,\eta,\zeta)\mathbf{f}(\xi,\eta,\zeta)\,d\Omega}_{\text{external work of body loads}} - \underbrace{\int_\Gamma \delta\mathbf{u}^T(\xi=1,\eta,\zeta)\mathbf{t}(\eta,\zeta)\,d\Gamma}_{\text{external work of body tractions}} = 0 .\end{aligned} \tag{6.13}$$

The detailed derivation of the four integrals is extensively demonstrated in [Wolf, 2003]. Here, only the outcome is stated. After utilising Eqs. (6.6), (6.7), (6.8), (6.11) and (6.12), performing integration by parts and introducing the abbreviations

$$\mathbf{C}_1 = \int_\Gamma \mathbf{B}_1^T\mathbf{E}\mathbf{B}_1|\mathbf{J}|\,d\Gamma , \tag{6.14}$$

$$\mathbf{C}_2 = \int_\Gamma \mathbf{B}_2^T\mathbf{E}\mathbf{B}_1|\mathbf{J}|\,d\Gamma \text{ and} \tag{6.15}$$

$$\mathbf{C}_3 = \int_\Gamma \mathbf{B}_2^T\mathbf{E}\mathbf{B}_2|\mathbf{J}|\,d\Gamma , \tag{6.16}$$

the virtual work formulation (6.13) leads to

$$\begin{aligned}&\delta\mathbf{u}^T(\xi=1)\left(\mathbf{C}_1\mathbf{u}_{,\xi}(\xi=1) + \mathbf{C}_2^T\mathbf{u}(\xi=1) - \mathbf{f}_r\right) \\ &- \int_0^1 \delta\mathbf{u}^T\left[\mathbf{C}_1\xi^2\mathbf{u}_{,\xi\xi} + \left(2\mathbf{C}_1 - \mathbf{C}_2 + \mathbf{C}_2^T\right)\xi\mathbf{u}_{,\xi} + \left(\mathbf{C}_2^2 - \mathbf{C}_3\right)\mathbf{u} + \omega^2\mathbf{M}\xi^2\mathbf{u} + \xi^2\mathbf{f}_b\right] d\xi = 0 .\end{aligned} \tag{6.17}$$

Here, $\mathbf{f}_r$ are the amplitudes of the equivalent nodal forces due to the boundary tractions and $\mathbf{f}_b$ corresponds to the amplitudes of the nodal forces resulting from body loads. The coefficient matrix $\mathbf{M}$ assembles the finite element masses, like in Eq. (5.14).

The satisfaction of Eq. (6.17) for all $\delta\mathbf{u}$ with $0 \le \xi \le 1$ requires two conditions to be fulfilled. Firstly, the nodal force-displacement relationship formulated at the boundary has to be

$$\mathbf{f}_r = \mathbf{C}_1\mathbf{u}_{,\xi}(\xi=1) + \mathbf{C}_2^T\mathbf{u}(\xi=1) , \tag{6.18}$$

and, secondly, the factor under the integral in Eq. (6.17) has to be zero:

$$\mathbf{C}_1\xi^2\mathbf{u}_{,\xi\xi}(\xi)+\left(2\mathbf{C}_1-\mathbf{C}_2+\mathbf{C}_2^T\right)\xi\mathbf{u}_{,\xi}(\xi)+\left(\mathbf{C}_2^2-\mathbf{C}_3\right)\mathbf{u}(\xi)+\omega^2\mathbf{M}\xi^2\mathbf{u}(\xi)+\xi^2\mathbf{f}_b(\xi)=\mathbf{0}\,. \tag{6.19}$$

Eq. (6.19) represents the scaled boundary finite element equation in displacements, formulated in the frequency-domain for elastodynamics in three dimensions. This equation is the weak form of the differential equation of motion in the scaled boundary coordinate system. Eq. (6.19) describes a system of linear, second order, ordinary differential equations for the amplitudes $\mathbf{u}(\xi)$ with the dimensionless radial coordinate ξ as the independent variable. The formulation is valid for bounded ($0\leq\xi\leq 1$) and unbounded ($1\leq\xi\leq\infty$) domains.

6.2.2 Scaled boundary finite element equation in dynamic stiffness

The next step in deriving the fundamental equations for the SBFEM, is the formulation of the nodal force-displacement relationship, i.e., the dynamic stiffness $\mathbf{S}^\infty$ for an unbounded medium. Whereas Eq. (6.19) enables the determination of the displacement at any point in the analysed domain in dependency of the radial coordinate ξ, the dynamic stiffness $\mathbf{S}^\infty$ describes the relationship between a nodal interaction force $\mathbf{f}_r$ and the corresponding displacement vector $\mathbf{u}$. This relationship can be expressed, after [Wolf and Song, 1996], in frequency-domain as

$$\mathbf{f}_r(\omega)=\mathbf{S}^\infty(\omega)\mathbf{u}(\omega)\,. \tag{6.20}$$

In order to achieve the scaled boundary finite element equation in frequency domain, the derivation of the dynamic stiffness matrix $\mathbf{S}^\infty$ starts with the formulation of the virtual work for any surface Γ_ξ with constant ξ

$$\mathbf{w}(\xi)^T\mathbf{f}_q(\xi)=\int_{\Gamma_\xi}\mathbf{w}^T\mathbf{t}_\xi\,d\Gamma_\xi\,. \tag{6.21}$$

Here, $\mathbf{w}=\mathbf{w}(\xi,\eta,\zeta)=\mathbf{w}(\xi)\mathbf{N}(\eta,\zeta)$ is the weighting function, $\mathbf{f}_q(\xi)$ are the amplitudes of the internal forces and $\mathbf{t}_\xi$ means the resultants of surface tractions on the surface Γ_ξ with constant ξ. By means of Eq. (6.3), the infinitesimal surface $d\Gamma_\xi$ can be calculated as

$$d\Gamma_\xi=\xi^2|\mathbf{n}_\xi|\,d\eta d\zeta\,. \tag{6.22}$$

Substituting Eq. (6.22) in Eq. (6.21) for an arbitrary $\mathbf{w}(\xi)$ yields

$$\mathbf{f}_q(\xi)=\int_{\Gamma_\xi}\mathbf{N}^T\mathbf{t}_\xi\xi^2|\mathbf{n}_\xi|\,d\eta d\zeta\,. \tag{6.23}$$

The surface traction $\mathbf{t}_\xi$ in radial direction ξ expressed in scaled boundary coordinates, with A_1 from (6.5), reads

$$\mathbf{t}_\xi=\frac{|\mathbf{J}|}{\mathbf{n}^\xi}\mathbf{A}_1^T\boldsymbol{\sigma}\,. \tag{6.24}$$

Using the expression for the stresses in scaled boundary coordinates from Eq. (6.8) in Eq. (6.24) and regarding Eq. (6.9), Eq. (6.23) can be rewritten as

$$\mathbf{f}_q(\xi)=\int_{\Gamma_\xi}\mathbf{B}_1^T\mathbf{E}\left(\mathbf{B}_1\mathbf{u}_{,\xi}+\frac{1}{\xi}\mathbf{B}_2\mathbf{u}\right)\xi^2|\mathbf{J}|\,d\eta d\zeta\,. \tag{6.25}$$

With the coefficient matrices $\mathbf{C}_1$ and $\mathbf{C}_2$ from Eqs. (6.14) and (6.15), respectively, Eq. (6.25) becomes

$$\mathbf{f}_q(\xi)=\mathbf{C}_1\xi^2\mathbf{u}_{,\xi}+\mathbf{C}_2^T\xi\mathbf{u}\,. \tag{6.26}$$

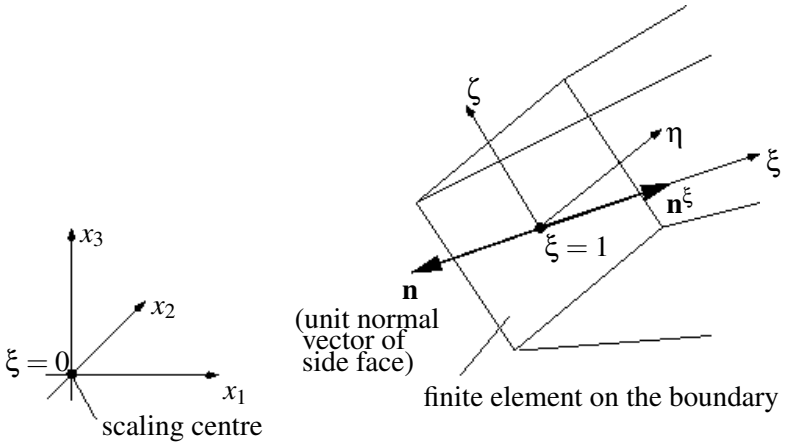

Figure 6.4: Unit normal vector of a scaled boundary finite element for the unbounded case.

For an unbounded medium, the surface normal vector $\mathbf{n}^{\xi}$ points to the opposite direction of the unit normal vector of the side-face (see Fig. 6.4). Thus, the nodal forces at the boundary are

$$\mathbf{f}_r(\xi) = -\mathbf{f}_q(\xi) \,. \tag{6.27}$$

In frequency-considerations, the displacement amplitudes $\mathbf{u}$ are related to the amplitudes of the nodal force $\mathbf{f}_r(\xi)$ by

$$\mathbf{f}_r(\xi) = \mathbf{S}\mathbf{u}(\xi) - \mathbf{f}_{bs}(\xi) \,, \tag{6.28}$$

where $\mathbf{S} = \mathbf{S}(\omega,\xi)$ denotes the dynamic stiffness on a surface with constant ξ and $\mathbf{f}_{bs}(\xi)$ represents the amplitudes of the nodal loads due to body loads and surface tractions. The substitution of Eqs. (6.26) and (6.28) in Eq. (6.27) yields the equation

$$-\mathbf{S}\mathbf{u} + \mathbf{f}_{bs} = \mathbf{C}_1\xi^2\mathbf{u}_{,\xi} + \mathbf{C}_2^T\xi\mathbf{u} \,. \tag{6.29}$$

Differentiating (6.29) with respect to ξ and adding the resulting equation to the SBFE equation in displacements, Eq. (6.19) leads to

$$-\mathbf{S}_{,\xi}\mathbf{u} + (-\mathbf{S} - \xi\mathbf{C}_2)\mathbf{u}_{,\xi} + \mathbf{f}_{bs,\xi} - \mathbf{C}_3\mathbf{u} + \omega^2\mathbf{M}\xi^2\mathbf{u} + \xi^2\mathbf{f}_b(\xi) = \mathbf{0} \,. \tag{6.30}$$

Reorganising Eq. (6.29) with respect to $\mathbf{u}_{,\xi}$ and substituting this expression in Eq. (6.30) multiplied by ξ, results in

$$\begin{aligned} &\left[(-\mathbf{S} - \xi\mathbf{C}_2)(\xi\mathbf{C}_1)^{-1}(-\mathbf{S} - \xi\mathbf{C}_2^T) - \xi\mathbf{S}_{,\xi} - \xi\mathbf{C}_3 + \omega^2\xi^3\mathbf{M}\right]\mathbf{u} \\ &+ \xi\mathbf{f}_{bs,\xi} + (-\mathbf{S} - \xi\mathbf{C}_2)(\xi\mathbf{C}_1)^{-1}\mathbf{f}_{bs} + \xi\mathbf{f} = \mathbf{0} \,. \end{aligned} \tag{6.31}$$

For an arbitrary $\mathbf{u}$, the coefficient matrix in square brackets $[\ldots]$ of Eq. (6.31) must vanish, so that

$$(-\mathbf{S} - \xi\mathbf{C}_2)(\xi\mathbf{C}_1)^{-1}(-\mathbf{S} - \xi\mathbf{C}_2^T) - \xi\mathbf{S}_{,\xi} - \xi\mathbf{C}_3 + \omega^2\xi^3\mathbf{M} = \mathbf{0} \,. \tag{6.32}$$

Introducing the dimensionless dynamic stiffness matrix $\bar{\mathbf{S}}(\omega,\xi)$

$$\mathbf{S}(\omega,\xi) = Gr_0\xi\bar{\mathbf{S}}(\omega,\xi) \tag{6.33}$$

as well as the dimensionless coefficient matrices $\bar{\mathbf{C}}_1$, $\bar{\mathbf{C}}_2$, $\bar{\mathbf{C}}_3$ and $\bar{\mathbf{M}}$

$$\mathbf{C}_1 = Gr_0\bar{\mathbf{C}}_1 \,, \tag{6.34}$$
$$\mathbf{C}_2 = Gr_0\bar{\mathbf{C}}_2 \,, \tag{6.35}$$
$$\mathbf{C}_3 = Gr_0\bar{\mathbf{C}}_3 \text{ and} \tag{6.36}$$
$$\mathbf{M} = \rho r_0^3\bar{\mathbf{M}} \tag{6.37}$$

into Eq. (6.32) yields the expression

$$-\bar{\mathbf{S}}-\bar{\mathbf{C}}_2\mathbf{C}_1^{-1}(-\bar{\mathbf{S}}-\bar{\mathbf{C}}_2^T)-\mathbf{C}_3^T-\bar{\mathbf{S}}-\xi\bar{\mathbf{S}}_{,\xi}+\left(\frac{\omega r_o}{c_S}\xi\right)^2\bar{\mathbf{M}}=\mathbf{0}\,, \tag{6.38}$$

where c_S is the shear-wave velocity from Eq. (2.28). The coefficient of the last term in Eq. (6.38) is defined as dimensionless frequency $a(\omega,\xi)$ for any ξ:

$$a(\omega,\xi)=\frac{\omega r_o}{c_s}\xi\,. \tag{6.39}$$

Thus, the fore-last addend in Eq. (6.38) $\xi\bar{\mathbf{S}}_{,\xi}$ can be expressed as

$$\xi\bar{\mathbf{S}}_{,\xi}=a\bar{\mathbf{S}}_{,a}\,. \tag{6.40}$$

The substitution of Eqs. (6.39) and (6.40) in Eq. (6.38), leaves a as the only independent variable in this equation. Thus, the dimensionless dynamic-stiffness matrix is a function of the variable a only

$$\bar{\mathbf{S}}(\omega,\xi)=\bar{\mathbf{S}}(a)\,. \tag{6.41}$$

The term with the derivative $a\bar{\mathbf{S}}(a)_{,a}$ can be interpreted either for varying ξ with fixed ω or for varying ω with fixed ξ:

$$a\bar{\mathbf{S}}_{,a}=\xi\bar{\mathbf{S}}_{,\xi}=\omega\bar{\mathbf{S}}(a)_{,\omega}\,. \tag{6.42}$$

Using Eq. (6.41) and Eq. (6.42) in Eq. (6.33), differentiated with respect to ξ, yields

$$\xi\mathbf{S}_{,\xi}=\mathbf{S}+\omega\mathbf{S}_{,\omega}\,. \tag{6.43}$$

That way, the spatial derivative with respect to ξ can be replaced by the frequency-derivative with respect to ω. Substituting Eq. (6.43) into Eq. (6.32) results in

$$(-\mathbf{S}-\xi\mathbf{C}_2)(\xi\mathbf{C}_1)^{-1}(-\mathbf{S}-\xi\mathbf{C}_2^T)-\xi\mathbf{C}_3-\mathbf{S}-\omega\mathbf{S}_{,\omega}+\omega^2\xi^3\mathbf{M}=\mathbf{0}\,. \tag{6.44}$$

For the boundary ($\xi=1$), the dynamic-stiffness matrix for an unbounded medium $S^\infty(\omega)$ is expressed as:

$$(\mathbf{S}^\infty(\omega)+\mathbf{C}_2)\mathbf{C}_1^{-1}(\mathbf{S}^\infty(\omega)+\mathbf{C}_2^T)-\mathbf{S}^\infty(\omega)-\omega\mathbf{S}^\infty(\omega)_{,\omega}-\mathbf{C}_3+\omega^2\mathbf{M}=\mathbf{0}\,. \tag{6.45}$$

Eq. (6.45) represents the SBFE equation in dynamic-stiffness, formulated in the frequency-domain for elastodynamics in three dimensions. It is a non-linear first-order ordinary differential equation, with the frequency ω as the independent variable. Thus, the force-displacement relationship is expressed in dependency of the frequency ω and not as in Eq. (6.19) in dependency of the radial coordinate ξ. Through this formulation, a description on the boundary becomes available which enables the modelling of wave radiation to infinity. Since, $\mathbf{S}^\infty$ relates a nodal interaction force to the resulting displacements in the analysed domain, it is also called *displacement unit-impulse response matrix*.

6.3 Scaled boundary finite element equation in time-domain

In time-domain, the interaction force-acceleration relationship is formulated as

$$\mathbf{f}_r(t)=\int_0^t\mathbf{M}^\infty(t-\tau)\ddot{\mathbf{u}}(\tau)\,d\tau\,, \tag{6.46}$$

where $\mathbf{M}^{\infty}(t)$ is the acceleration unit-impulse response matrix. With $\ddot{\mathbf{u}}(\omega) = (i\omega)^2\mathbf{u}(\omega)$, Eq. (6.46) reads in frequency-domain

$$\mathbf{f}_r(\omega) = \mathbf{M}^{\infty}(\omega)(i\omega)^2\mathbf{u}(\omega)\,. \tag{6.47}$$

Here, $\mathbf{M}^{\infty}(\omega)$ is the acceleration unit-impulse response matrix in frequency-domain. $\mathbf{M}^{\infty}(t)$ and $\mathbf{M}^{\infty}(\omega)$ are directly related by the Fourier transform. With Eq. (6.20), a relationship between the acceleration and the displacement unit-impulse response matrix can be stated as

$$\mathbf{M}^{\infty}(\omega) = \frac{\mathbf{S}^{\infty}(\omega)}{(i\omega)^2}\,. \tag{6.48}$$

With this relationship, the SBFE equation in dynamic stiffness Eq. (6.45) can be expressed by means of $\mathbf{M}^{\infty}(\omega)$ instead of $\mathbf{S}^{\infty}(\omega)$. Hereon, an inverse Fourier transform is applied to the modified SBFE equation, which yields the SBFE equation in time-domain

$$\underbrace{\int_0^t \tilde{\mathbf{M}}^{\infty}(t-\tau)\tilde{\mathbf{M}}^{\infty}(\tau)\,d\tau}_{\text{integral } J_1} + \tilde{\mathbf{C}}_2 \underbrace{\int_0^t\int_0^{\tau} \tilde{\mathbf{M}}^{\infty}(\tau')\,d\tau' d\tau}_{\text{integral } J_2}$$
$$+ \underbrace{\int_0^t\int_0^{\tau} \tilde{\mathbf{M}}^{\infty}(\tau')\,d\tau' d\tau}_{\text{integral } J_2}\,\tilde{\mathbf{C}}_2^T + t\underbrace{\int_0^t \tilde{\mathbf{M}}^{\infty}(\tau)\,d\tau}_{\text{integral } J_3} - \frac{t^3}{6}\tilde{\mathbf{C}}_3 H(t) - t\tilde{\mathbf{M}}H(t) = \mathbf{0}\,. \tag{6.49}$$

Here, $H(t)$ is the Heaviside step function and the coefficient matrices are

$$\tilde{\mathbf{C}}_1 = \mathbf{U}^T\mathbf{U}\,, \tag{6.50}$$
$$\tilde{\mathbf{C}}_2 = \mathbf{U}^{-1\,T}\mathbf{C}_2\mathbf{U}^{-1} - 2\mathbf{I}\,, \tag{6.51}$$
$$\tilde{\mathbf{C}}_3 = \mathbf{U}^{-1\,T}\left(\mathbf{C}_3 - \mathbf{C}_2\mathbf{C}_1^{-1}\tilde{\mathbf{C}}_2^T\right)\mathbf{U}^{-1} \text{ and} \tag{6.52}$$
$$\tilde{\mathbf{M}} = \mathbf{U}^{-1\,T}\mathbf{M}\mathbf{U}^{-1}\,, \tag{6.53}$$

incorporating Eqs. (6.34) to (6.37). $\mathbf{U}$ results from a Cholesky decomposition of $\tilde{\mathbf{C}}_1$. An approximation for $\tilde{\mathbf{M}}^{\infty}(t)$ can be gained from the discretised Eq. (6.49) with respect to time. The desired acceleration unit-impulse response matrix $\mathbf{M}^{\infty}(t)$ can then be derived from

$$\mathbf{M}^{\infty}(t) = \mathbf{U}^T\tilde{\mathbf{M}}^{\infty}(t)\mathbf{U}\,. \tag{6.54}$$

6.4 Time-discretisation

Discretising Eq. (6.49) in t_i time-steps, yields an equation for the acceleration unit-impulse response matrix $\tilde{\mathbf{M}}^{\infty}(t)$ at each time-station i. The response matrix $\tilde{\mathbf{M}}^{\infty}(t)$ is assumed to be piecewise constant over each time-step $\Delta t = t_{i+1} - t_i$. This assumption will also be made for the acceleration $\ddot{\mathbf{u}}$ in the constant acceleration Newmark method, when determining the interaction force $\mathbf{f}_r$ using Eq. (6.46). The discretisation of Eq. (6.49) in time requires the discretisation of its three integral parts J_1, J_2 and J_3 which are in discrete form

$$J_1(t_i) = \Delta t\sum_{j=1}^{i}\tilde{\mathbf{M}}_{i-j+1}^{\infty}\tilde{\mathbf{M}}_j^{\infty}\,, \tag{6.55}$$

$$J_2(t_i) = \int_0^{i\Delta t}\int_0^{\tau}\tilde{\mathbf{M}}^{\infty}(\tau')\,d\tau' d\tau = J_2(t_{i-1}) + \Delta t J_3(t_{i-1}) + \frac{\Delta t^2}{2}\tilde{\mathbf{M}}_i^{\infty} \text{ and} \tag{6.56}$$

$$J_3(t_i) = \int_0^{i\Delta t}\tilde{\mathbf{M}}^{\infty}(\tau)\,d\tau = J_1(t_{i-1}) + \Delta t\tilde{\mathbf{M}}_i^{\infty}\,. \tag{6.57}$$

6.4.1 First time-step

For the first time-step t_0 for which applies $t \in [0;\Delta t]$, the convolution integral of Eq. (6.49) leads to a quadratic equation in the unknown matrix $\tilde{\mathbf{M}}^{\infty}$. Therefore, a special treatment is necessary for the first time-step. The integrals J_1, J_2 and J_3 for this first time-step in their discrete form are

$$J_1(t_0) = \Delta t \tilde{\mathbf{M}}_0^{\infty} \,, \tag{6.58}$$

$$J_2(t_0) = \frac{\Delta t^2}{2} \tilde{\mathbf{M}}_0^{\infty} \quad \text{and} \tag{6.59}$$

$$J_3(t_0) = \Delta t \tilde{\mathbf{M}}_0^{\infty} \tilde{\mathbf{M}}_0^{\infty} = \Delta t (\tilde{\mathbf{M}}_0^{\infty})^2 \,. \tag{6.60}$$

Inserting those expressions in Eq. (6.49), dividing this equation by Δt and rearranging the results in the algebraic *Riccati equation* in $\tilde{\mathbf{M}}_0^{\infty}$

$$(\tilde{\mathbf{M}}_0^{\infty})^2 + \frac{\Delta t}{2} \left(\tilde{\mathbf{C}}_2 + \mathbf{I}\right) \tilde{\mathbf{M}}_0^{\infty} + \tilde{\mathbf{M}}_0^{\infty} \frac{\Delta t}{2} \left(\tilde{\mathbf{C}}_2 + \mathbf{I}\right) - \frac{\Delta t^2}{6} \tilde{\mathbf{C}}_3 - \tilde{\mathbf{M}} = \mathbf{0} \,. \tag{6.61}$$

This equation can be solved by applying the *Schur factorisation* which is widely applied in solving eigenvalue problems. In doing so, Eq. (6.61) is solved by introducing the matrix

$$\mathbf{Z} = \begin{bmatrix} -\frac{\Delta t}{2}\left(\tilde{\mathbf{C}}_2^T + \mathbf{I}\right) & -\mathbf{I} \\ -\frac{\Delta t^2}{6}\tilde{\mathbf{C}}_2 - \mathbf{M} & \frac{\Delta t}{2}\left(\tilde{\mathbf{C}}_2 + \mathbf{I}\right) \end{bmatrix} . \tag{6.62}$$

A real orthogonal transformation $\mathbf{V}$ is applied to $\mathbf{Z}$ which yields the real Schur form with the matrix $\mathbf{S}$ in the quasi-upper triangular form

$$\mathbf{V}^T \mathbf{Z} \mathbf{V} = \mathbf{S} = \begin{bmatrix} \mathbf{S}_{11} & \mathbf{S}_{12} \\ 0 & \mathbf{S}_{22} \end{bmatrix} . \tag{6.63}$$

$\mathbf{S}$ is arranged such that the real parts of the eigenvalues of $\mathbf{S}_{11}$ are negative and those of $\mathbf{S}_{22}$ are positive. $\mathbf{V}$ is partitioned conformably as

$$\mathbf{V} = \begin{bmatrix} \mathbf{V}_{11} & \mathbf{V}_{12} \\ \mathbf{V}_{21} & \mathbf{V}_{22} \end{bmatrix} . \tag{6.64}$$

So, the solution of the Ricatti equation (6.61) is formulated as

$$\tilde{\mathbf{M}}_0^{\infty} = \mathbf{V}_{21} \mathbf{V}_{11}^{-1} \,. \tag{6.65}$$

Herewith, the acceleration unit-impulse response matrix at the first time-station $\mathbf{M}_0^{\infty}$ can be derived from the discrete form of Eq. (6.54).

6.4.2 *i*-th time-step

For time-steps t_i with $i \geq 1$, the convolution integral term in Eq. (6.49) is linear in the unknown $\tilde{\mathbf{M}}_i^{\infty}$. The transformed acceleration unit-impulse matrix $\tilde{\mathbf{M}}_i^{\infty}$ can be gained from the discrete form of Eq (6.49). Substituting, the integrals J_1, J_2 and J_3 by their discrete forms from Eqs. (6.55) to (6.57) into Eq (6.49) and rearranging this equation, leads to

$$\begin{aligned} &-\frac{J_1(t_{i-1})}{\Delta t} - \tilde{\mathbf{C}}_2 \left[\frac{J_2(t_{i-1})}{\Delta t} + J_3(t_{i-1})\right] - \left[\frac{J_2(t_{i-1})}{\Delta t} + J_3(t_{i-1})\right] \tilde{\mathbf{C}}_2^T + \frac{t^3}{6\Delta t}\tilde{\mathbf{C}}_3 + \frac{t}{\Delta t}\left[\tilde{\mathbf{M}} - J_3(t_{i-1})\right] \\ &= \left[\tilde{\mathbf{M}}_0^{\infty} + \frac{\Delta t}{2}\tilde{\mathbf{C}}_2\right] \tilde{\mathbf{M}}_i^{\infty} + \tilde{\mathbf{M}}_i^{\infty} \left[\tilde{\mathbf{M}}_0^{\infty} + \frac{\Delta t}{2}\tilde{\mathbf{C}}_2^T\right] + t\tilde{\mathbf{M}}_i^{\infty} \,. \end{aligned} \tag{6.66}$$

Eq. (6.66) is the *Lyapunov equation* in the form $\mathbf{C} = \mathbf{A}\mathbf{X} + \mathbf{X}\mathbf{A}^T + t\mathbf{X}$ with the unknown $\mathbf{X} = \tilde{\mathbf{M}}_i^{\infty}$. The solution procedure for the remaining equation

$$\mathbf{C} = \mathbf{A}\mathbf{X} + \mathbf{X}\mathbf{A}^T \tag{6.67}$$

is described in [Bartels and Stewart, 1972] and briefly addressed below. Accordingly to the solution procedure for the first time-step, a Schur factorisation is applied to $\mathbf{A}$: $\mathbf{V}^T\mathbf{A}\mathbf{V} = \mathbf{S}$. Here, $\mathbf{V}$ is the orthogonal transformation matrix which results in the quasi-upper triangular matrix $\mathbf{S}$. Eq. (6.67) is pre-multiplied by $\mathbf{V}^T$ and post-multiplied by $\mathbf{V}$ yielding

$$\mathbf{Y}^T\mathbf{C}\mathbf{V} = \mathbf{S}\mathbf{Y} + \mathbf{Y}\mathbf{S}^T + t\mathbf{Y} \tag{6.68}$$

with $\mathbf{Y} = \mathbf{V}^T\mathbf{X}\mathbf{V}$. The orthogonal matrix $\mathbf{V}$ satisfies $\mathbf{V}\mathbf{V}^T = \mathbf{V}^T\mathbf{V} = \mathbf{I}$, with $\mathbf{I}$ being the unit-matrix. Herewith, Eq. (6.68) is rewritten as

$$\mathbf{V}^T\mathbf{C}\mathbf{V} = \left[\mathbf{S} + \frac{1}{2}t\mathbf{I}\right]\mathbf{Y} + \mathbf{Y}\left[\mathbf{S} + \frac{1}{2}t\mathbf{I}\right] . \tag{6.69}$$

The matrix $\mathbf{S} + \frac{1}{2}t\mathbf{I}$ represents the real Schur form. This allows Eq. (6.69) to be solved for each time-station t_i successively, leading to $\mathbf{Y}$. With $\mathbf{Y}$, the matrix $\mathbf{X}$ can be computed by $\mathbf{X} = \mathbf{V}\mathbf{Y}\mathbf{V}^T$. Matrix $\mathbf{A}$ from Eq. (6.67) is independent of the time-stations. Thus, the Schur factorisation has to be performed only once. The computational effort does not increase by including the term $t\mathbf{X}$.

With this treatment, the acceleration unit-impulse response matrix $\mathbf{M}_i^\infty$ can finally be calculated for each time-step by the discrete form of Eq. (6.54). Generally, $\mathbf{M}_i^\infty$ is fully populated, but symmetric.

6.5 Numerical implementation: near-field/far-field coupling

In this section, an overview of the numerical implementation of the SBFEM for elastodynamic problems in time-domain is given. The treatment of the SBFEM as rigorous method in the substructure method for soil-structure interaction analyses is addressed. As discussed in Chap. 3 the entire domain is divided into a near-field which contains the structure of interest, and a far-field which allows the wave radiation to infinity. In this work, the modelling of the near-field is performed by the FEM, whereas the behaviour of the far-field is simulated by SBFEs. The coupling procedure of those two numerical methods is discussed in the following.

For a numerical treatment in the time-domain, a time-discretisation of the convolution integral from Eq. (6.46) is required. This time-discretisation is addressed above in Sec. 6.4. Assuming a piecewise constant approximation of the acceleration unit-impulse response matrix $\mathbf{M}^\infty$

$$\mathbf{M}^\infty(t) = \begin{cases} \mathbf{M}_0^\infty & t \in [0;\Delta t] \\ \mathbf{M}_1^\infty & t \in [\Delta t; 2\Delta t] \\ \vdots & \\ \mathbf{M}_{n-1}^\infty & t \in [(n-1)\Delta t; n\Delta t] \end{cases} , \tag{6.70}$$

leads to the discrete form of Eq. (6.46)

$$\mathbf{f}_r(t_n) = \sum_{j=1}^{n} \mathbf{M}_{n-j}^\infty \int_{(j-1)\Delta t}^{j\Delta t} \ddot{\mathbf{u}}(\tau)\, d\tau = \sum_{j=1}^{n} \mathbf{M}_{n-j}^\infty (\dot{\mathbf{u}}_j - \dot{\mathbf{u}}_{j-1}) . \tag{6.71}$$

When the γ-parameter of the HHT-α implicit time-integration scheme from Sec. 5.4.2 is introduced and the unknown acceleration vector $\ddot{\mathbf{u}}_i$ for time-step n is separated, the interaction force $\mathbf{f}_r(t_n)$ can be computed with

$$\mathbf{f}_r(t_n) = \gamma\Delta t\mathbf{M}_0^\infty\ddot{\mathbf{u}}_n + \sum_{j=1}^{n-1} \mathbf{M}_{n-j}^\infty (\dot{\mathbf{u}}_j - \dot{\mathbf{u}}_{j-1}) \tag{6.72}$$

$$= \gamma\Delta t\mathbf{M}_0^\infty\ddot{\mathbf{u}}_n + \tilde{\mathbf{f}}_r(t_n) . \tag{6.73}$$

For the simulation of many time-steps, i.e., for large n, the direct solution of Eq. (6.72) is requires much time- and computational effort. Nevertheless, an approximation in time which is presented in the next section Sec. 6.6 leads to a fast recursive algorithm.

The equation of motion for elastodynamics in time-domain from the standard FEM Eq. (5.19) can be split into a near-field and far-field part. In doing so, the force-acceleration relationship from Eq. (6.72) can be easily implemented to the equation of motion

$$\begin{bmatrix} \mathbf{K}_{ss} & \mathbf{K}_{sb} \\ \mathbf{K}_{bs} & \mathbf{K}_{bb} \end{bmatrix} \begin{bmatrix} \mathbf{u}_s(t) \\ \mathbf{u}_b(t) \end{bmatrix} + \begin{bmatrix} \mathbf{C}_{ss} & \mathbf{C}_{sb} \\ \mathbf{C}_{bs} & \mathbf{C}_{bb} \end{bmatrix} \begin{bmatrix} \dot{\mathbf{u}}_s(t) \\ \dot{\mathbf{u}}_b(t) \end{bmatrix} + \begin{bmatrix} \mathbf{M}_{ss} & \mathbf{M}_{sb} \\ \mathbf{M}_{bs} & \mathbf{M}_{bb} + \gamma \Delta t \mathbf{M}_0^{\infty} \end{bmatrix} \begin{bmatrix} \ddot{\mathbf{u}}_s(t) \\ \ddot{\mathbf{u}}_b(t) \end{bmatrix} = \begin{bmatrix} \mathbf{f}_s(t) \\ \mathbf{f}_b(t) - \tilde{\mathbf{f}}_r(t) \end{bmatrix} . \tag{6.74}$$

The subscript s stands for structure and denotes the near-field parts which describe, despite of the name, not only structure components but can also include a portion of the soil in soil-structure interaction problems. This region is modelled with FEs. The subscript b denotes the boundary where the interaction forces $\mathbf{f}_r(t)$ from the convolution integral of Eq. (6.46) are applied and which is congruent with the SBFE discretisation.

6.6 Improvement of efficiency

The SBFEM is a rigorous method to model wave propagation to infinity. As already discussed, these methods are global in time and space. From a computational point of view those characteristics are drawback because they lead to storage consuming calculations with high computational time-effort.

The globality in time results in the convolution integral Eq (6.46). Taking the n-th time-step, $n-1$ matrix-vector multiplications with the fully populated unit-impulse acceleration influence matrices have to be performed. Therefore, the computational effort grows quadratic depending on the simulation time. To reduce this computation effort to a linear time-dependency, a recursive algorithm is introduced by [Lehmann *et al.*, 2004]. This algorithm is addressed in the following.

Furthermore, the globality in space causes fully populated unit-impulse acceleration influence matrices for each time-step. These matrices lead to immense storage consummation for problems with a large number of degrees of freedom, i.e., for large near-field/far-field interfaces. Additionally, a different influence matrix has to be assembled for each time-station which yields unacceptable storage requirements for long simulation times. Here, a storage reduction method is presented, which leads to a banded structure of the influence matrices, like the stiffness matrices in finite elements.

The combined use of the recursive algorithm and the storage reduction method improves the efficiency of the SBFEM significantly. Applications of these techniques for increasing the efficiency of the SBFEM are performed in Chap. 7.1.

6.6.1 Reduction of non-locality in time

As stated above, the calculation of the interaction force vector on the near-field/far-field interface $\mathbf{f}_r(t)$ for long simulation periods is computing time-consuming Thus, a recursive algorithm is elaborated which leads to a reduction of computational effort [Lehmann *et al.*, 2004].

Considering the time-dependent behaviour of the entries of the acceleration unit-impulse matrix $\mathbf{M}^{\infty}$, as it is exemplary shown in Fig. 6.5, a linear growth from a certain time-step t_m can be realised.

This linear behaviour enables the development of a recursive algorithm. Initially, the acceleration unit-impulse matrix is decomposed, from time-step t_m on, as

$$\mathbf{M}^{\infty}(t_i) = \mathbf{T}^{\infty} t_i + \mathbf{C}^{\infty} \tag{6.75}$$

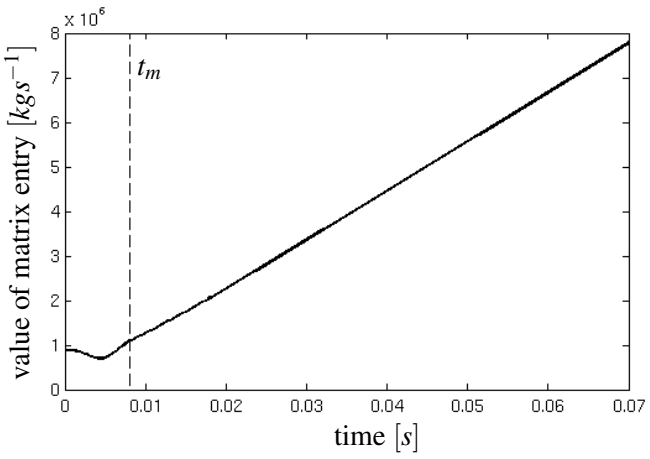

Figure 6.5: Growth of a certain entry of the unit-impulse influence matrix $\mathbf{M}^{\infty}$ in dependency on the simulation time.

where $\mathbf{T}^{\infty}$ is the matrix containing the gradients $(\frac{\Delta \mathbf{M}^{\infty}}{\Delta t})$ and $\mathbf{C}^{\infty}$ a constant matrix. The computation of $\mathbf{T}^{\infty}$ is reduced for equidistant time-steps $t_i = i\Delta t$ to

$$\mathbf{T}^{\infty} = \left(\mathbf{M}^{\infty}_{m+1} - \mathbf{M}^{\infty}_{m}\right) \quad \text{with} \quad \mathbf{M}^{\infty}_{m} = \mathbf{M}^{\infty}(t_m)\,. \tag{6.76}$$

For matrix entries of $\mathbf{M}^{\infty}$ behaving linear in time, the interaction force vector $\tilde{\mathbf{f}}_r(t_n)$ from Eq. (6.72) can be split into a non-linear term (for time-steps $t_i, 0 \leq i \leq m$) and a linear term (time-steps $t_i,\ i > m$)

$$\begin{aligned}\tilde{\mathbf{f}}_r(t_n) &= \tilde{\mathbf{f}}_r(t_n)^{lin} + \tilde{\mathbf{f}}_r(t_n)^{nonlin} \\ &= \sum_{j=1}^{n+1-m} \mathbf{M}^{\infty}_{n-j+1}(\dot{\mathbf{u}}_j - \dot{\mathbf{u}}_{j-1}) + \sum_{j=n+2-m}^{n-1} \mathbf{M}^{\infty}_{n-j+1}(\dot{\mathbf{u}}_j - \dot{\mathbf{u}}_{j-1})\,.\end{aligned} \tag{6.77}$$

With Eq. (6.75), the linear part of Eq. (6.77) can be rewritten as

$$\begin{aligned}\tilde{\mathbf{f}}_r(t_n)^{lin} &= \sum_{j=1}^{n+1-m} \left[\mathbf{T}^{\infty}\,(n-j+1) + \mathbf{C}^{\infty}\right](\dot{\mathbf{u}}_j - \dot{\mathbf{u}}_{j-1}) \\ &= \left[\mathbf{T}^{\infty}\,m + \mathbf{C}^{\infty}\right](\dot{\mathbf{u}}_{n+1-m} - \dot{\mathbf{u}}_{n-m}) + \sum_{j=1}^{n-m}\left[\mathbf{T}^{\infty}\,(n-j+1) + \mathbf{C}^{\infty}\right](\dot{\mathbf{u}}_j - \dot{\mathbf{u}}_{j-1}) \\ &= \mathbf{M}^{\infty}_{m}\,(\dot{\mathbf{u}}_{n+1-m} - \dot{\mathbf{u}}_{n-m}) + \sum_{j=1}^{n-m}\left[\mathbf{T}^{\infty}\,(n-j+1) + \mathbf{C}^{\infty}\right](\dot{\mathbf{u}}_j - \dot{\mathbf{u}}_{j-1})\,.\end{aligned} \tag{6.78}$$

The preceding force $\tilde{\mathbf{f}}_r(t_{n-1})^{lin}$, which is essential for a recursive algorithm, can be computed by

$$\tilde{\mathbf{f}}_r(t_{n-1})^{lin} = \sum_{j=1}^{n-m}\left[\mathbf{T}^{\infty}\,(n-j) + \mathbf{C}^{\infty}\right](\dot{\mathbf{u}}_j - \dot{\mathbf{u}}_{j-1}). \tag{6.79}$$

With this equation, the linear increment of the interaction force in time-step n $\tilde{\mathbf{f}}_r(t_n)^{lin} - \tilde{\mathbf{f}}_r(t_{n-1})^{lin}$ can be rewritten, and the recursive formulation reads finally

$$\tilde{\mathbf{f}}_r(t_n)^{lin} = \tilde{\mathbf{f}}_r(t_{n-1})^{lin} + \mathbf{M}^{\infty}_{m}\,(\dot{\mathbf{u}}_{n+1-m} - \dot{\mathbf{u}}_{n-m}) + \mathbf{T}^{\infty}\,(\dot{\mathbf{u}}_{n-m} - \dot{\mathbf{u}}_0)\,. \tag{6.80}$$

Computational tests performed by [Lehmann, 2005b] show a reduction of the computational effort of 81% for an example with $n = 5000$ simulated time-steps and $m = 500$ time-steps evaluated. In the following applications, a tolerance threshold ε_t is used when comparing the matrix entries of subsequent time-steps in order to check if a linear behaviour can be observed or not.

6.6.2 Reduction of non-locality in space

In addition to the recursive algorithm, the efficiency of the SBFEM can be improved by reducing the non-locality in space [Lehmann, 2005b]. As in rigorous modelling each node of the near-field/far-field interface influences every other node on that interface, the influence matrices $\mathbf{M}^{\infty}(t)$ is fully populated. Whereas this influence behaviour is evident for small, compact interfaces, the influence of nodes situated at spatially large distances from each other, e.g., on large or long interfaces, is neglectable without a significant error.

To neglect the influence of distant nodes, a zero-element threshold ε_z is introduced, When a matrix entry falls under this threshold, it is set to zero:

$$\text{if } m_{ij} \leq \varepsilon_z \rightarrow m_{ij} := 0 \,, \tag{6.81}$$

where m_{ij} is a matrix entry of ith row and jth column of a influence matrix $\mathbf{M}_n^{\infty}$. Fig. 9.2 depicts an example for the varying populations of influence matrices of the near-field/far-field interface different zero-element thresholds ε_z. The matrix entries $m_{ij} \neq 0$ are marked as black dots.

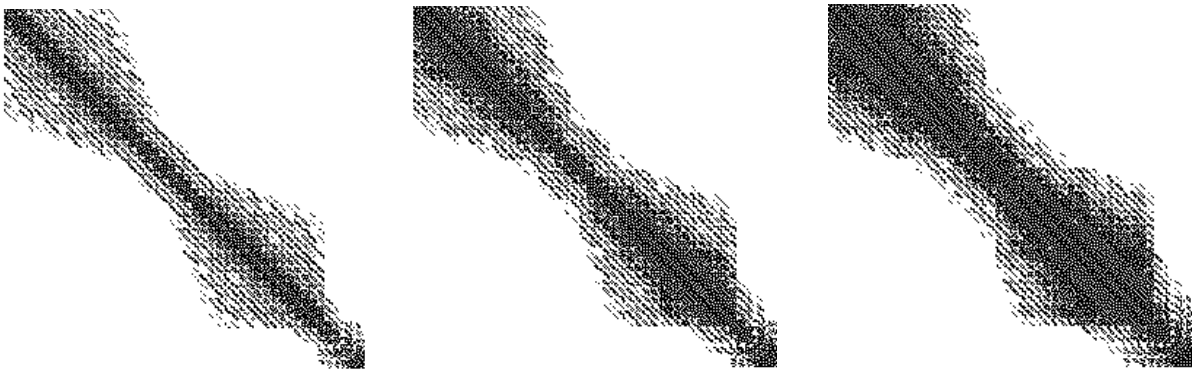

(a) Zero-element threshold $\varepsilon_z = 10^{-4}$. (b) Zero-element threshold $\varepsilon_z = 10^{-5}$. (c) Zero-element threshold $\varepsilon_z = 10^{-6}$.

Figure 6.6: Population of the influence matrix $\mathbf{M}^{\infty}(t_n)$ of the same problem for varying zero-element thresholds ε_z at the same time-station t_n (from [Lehmann and Borsutzky, 2007]).

To achieve a banded structure $\mathbf{M}^{\infty}$, like in Fig. 9.2, the entries of the influence matrices have to be reordered, e.g., with the Cuthill/McKee algorithm [Cuthill and McKee, 1969]. After rearranging and introducing a zero-element threshold, the matrix population is significantly reduced and shows a banded structure. Thus, effective storage and calculation techniques, like sparse matrix vector multiplication algorithms, are applicable. Consequently, introducing this zero-element threshold reduces the storage and computational time-consumption significantly, without significant loss of accuracy.

6.7 Substructuring

So far, SBFEM modelling of the unbound medium as one single domain was addressed. However, there exist some problems where it is reasonable to split the domain modelled by the SBFEM into a certain number of subdomains, also called substructures (see Fig. 6.7).

At first glance, the use of substructures is legitimated for complex shaped boundaries of bounded SBFEM domains (see Fig. 6.8(a)). This follows from the condition that the scaled boundary transformation requires a scaling centre from which the whole boundary of the analysed domain needs to be visible. When this boundary has a complex shape and it is not completely visible from one scaling centre, substructuring with more than one scaling centre is necessary. This case is discussed, e.g., in [Wolf, 2003].

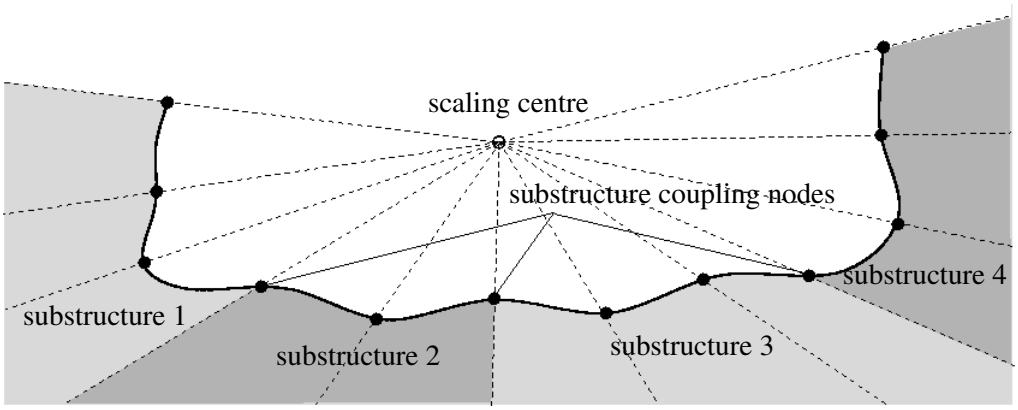

Figure 6.7: Two-dimensional SBFE substructure domains of an unbounded media.

For unbounded domains, substructuring with different scaling centres leads to overlapping domains in the far-field as shown in Fig. 6.8(b). Those overlapping domains could be interpreted physically as stiff wedges in the unbounded domain. The presence of the wedges results in incorrect wave radiation when a homogeneous half-space is intended to be modelled. Thus, substructuring can not always be incorporated for analysing the response of unbounded domains.

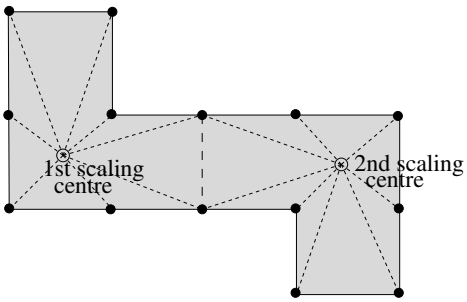

(a) Modelling of a bounded domain with two SBFEM substructures. The coupling can be performed without problems.

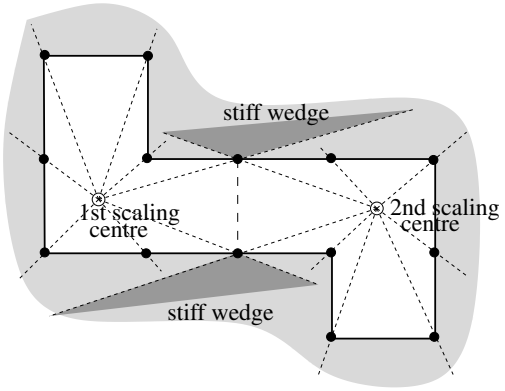

(b) Modelling of an unbounded domain with two SBFEM substructures. The coupling of the two SBFEM domains leads to overlapping which can be physically interpreted as stiff wedges.

Figure 6.8: Substructuring of complex shaped domains. Only a part of the entire boundary is visible from one scaling centre.

In addition to the case where substructuring is strictly necessary (but cannot always be achieved), a second legitimation for the use of substructures can be conceived. This case is the increase in computational efficiency which can be achieved by substructuring for certain applications. Therefore, SBFEM substructuring is included in the methodology developed in this work and its procedure is explained briefly.

Substructuring the far-field domain implies to analyse at first each substructure separately. For each substructure S, a separate influence matrix $\mathbf{M}_S^\infty$ is established. Afterwards, those substructure influence matrices are assembled to the global influence matrix $\mathbf{M}^\infty$ describing the unit-impulse response of the entire domain. The separate analysis of each substructure leads to a decoupling of most nodes of the different subdomains. The subdomains are only connected via the degrees of freedom that belong to nodes at their substructure-interfaces. These substructure nodes are marked in Fig. 6.7. The decoupling, i.e., the lacking of influence leads to a global influence matrix $\mathbf{M}^\infty$ which is structured in quadrants as

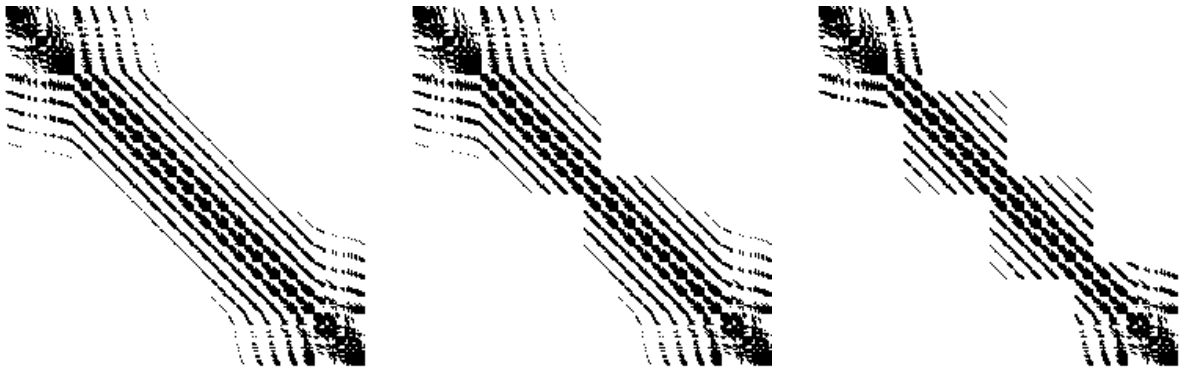

(a) Influence matrix $\mathbf{M}^{\infty}(t_n)$ one substructure

(b) Influence matrix $\mathbf{M}^{\infty}(t_n)$ two substructures

(c) Influence matrix $\mathbf{M}^{\infty}(t_n)$ four substructures

Figure 6.9: Population of the influence matrix $\mathbf{M}^{\infty}(t_n)$ for varying number of substructures at the same time-station t_n and the same zero element threshold $\varepsilon_z = 10^{-4}$.

depicted in for two substructures in Fig. 6.9(b) and for four substructures in Fig. 6.9(c).

For compact domains where many nodes have high influences on each other, substructuring could lead to non-satisfactory results. This is caused by the entries apart from the diagonal which are compared to the diagonal entries not low valued. Thus, the influence of those values on the entire solution is not neglectable.

In contrast, for long slender domains where many nodes are distant from each other and where the influence of the degrees of freedom of those distant nodes is neglectable, substructuring represents an efficient method which still yields satisfactory results. This is approved in Sec. 9.1 where the influences of substructuring on the global response are studied in.

7 Modelling of seismic excitation

In this chapter, an advanced treatment of the seismic excitation of the near-field is introduced. This treatment includes the derivation and application of a realistic synthetic earthquake wave field. The seismic wave field is synthesised in a computational efficient large scale simulation which involves the seismic source as well as the region of interest, i.e., the near-field. Once the wave field is computed, the seismic motion is converted into equivalent forces which are used to excite the near-field.

Initially in this chapter, the necessity for an advanced procedure of deriving and applying the seismic motion for wave propagation analyses in expanded near-fields is discussed, whereupon, the particular methods of the advanced procedure are introduced. The special method for applying the seismic excitation to the near-field is addressed at first. This method, named domain reduction method (DRM) [Bielak *et al.*, 2003], is the basis of the methodology introduced in this chapter. Accordingly, the computation of the seismic wave field is treated. Hereby, firstly, the description of the wave propagation from the seismic fault to the near-field is addressed. This description is accomplished by means of numerical Green's functions derived from the discrete wavenumber finite element method (DWFEM) [Olson *et al.*, 1984]. Secondly, the reproduction of the seismic source mechanism, assumed as extended finite fault, is illustrated. At last, a summarising schematic explanation of the general steps of the advanced procedure is given.

7.1 Necessity for an advanced procedure

In many applications in earthquake engineering, it is assumed that the initial motion at the truncation boundaries of the modelled region of interest is known a priori. But in the multitude of the analysed problems this is not the case, and therefore, it is necessary to develop methods to determine the initial seismic motion that excites the examined region. The topic of ground response analyses was addressed in Sec. 4.3.2. In that section, the usual practices for applying the seismic excitation to the near-field were discussed. Further, it was indicated that those practices are not adequate for the tasks addressed in this work. Therefore, the necessity for an advanced procedure of applying the seismic excitation to the near-field will be explained in more detail.

The seismic waves arise at the seismic fault in the earth crust and propagate through the body of the earth. The propagation path of the fastest waves travelling to the surface of the earth is not straight but curved in the sense that the direction vector has a dominant horizontal component in deeper regions and a dominant vertical component in the adjacency of the surface (see Fig. 7.1(a) and 7.1(c)). This curved shape of the path is caused by increasing wave velocities with depth in the earth crust. When a domain at the surface of the earth is considered, the seismic waves incident to this domain from several directions. Whereas the fastest body waves might incident almost vertically, the slower waves, i.e., the surface waves and the body waves with a different propagation path, incident in both vertical and horizontal directions.

The ground motion approaches, in which the seismic excitation is applied at the bottom of the near-field, are based on the assumption that just the fastest body waves and in most cases only one component of the *S*-wave, namely the *SH*-wave, is important for analysing the behaviour of soil and structure. Then, the seismic excitation is modelled as a plane wave with a vertical angle of incidence to the region of interest. For certain problems this assumption is reasonable, at least for small epicentral distances where

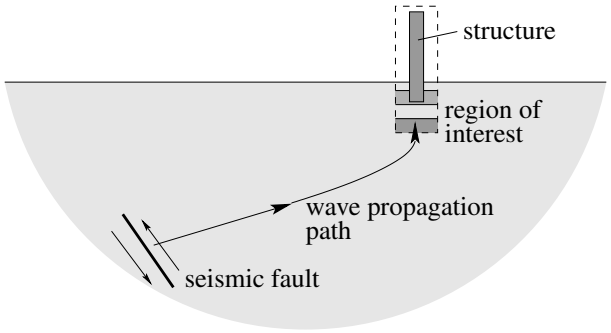

(a) Curved wave propagation path from the seismic fault to the region of interest containing the structure. The waves incident nearly vertical to the region of interest.

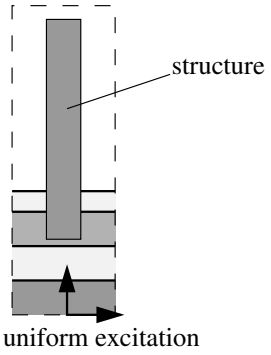

(b) Relatively small region of interest containing a structure. Since the seismic motion inside the near-field does not differ much, it is justifiable to apply an uniform earthquake motion at the boundaries of the near-field.

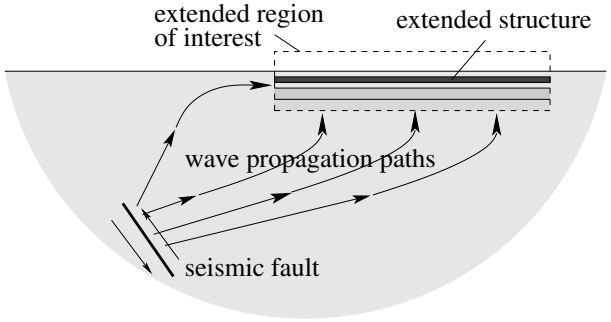

(c) Multiple curved wave propagation paths from the seismic fault to the extended region of interest containing the extended structure. The different waves incident at different angles at different points to the region of interest.

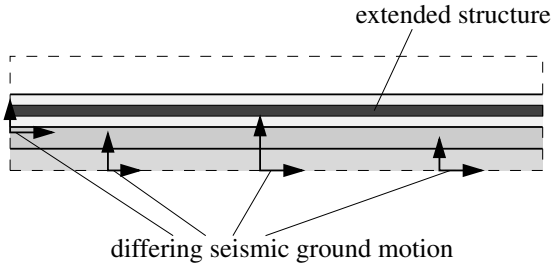

(d) Extended region of interest containing an extended structure. Due to the large extension, the seismic motion at the boundaries is non-uniform.

Figure 7.1: Seismic wave propagation paths and different seismic excitations at the boundaries of compact and spatial extended near-fields.

the *S*-wave generates the controlling, i.e., destructive motion. At larger epicentral distances where the Rayleigh-wave induces the largest ground motion, the assumption of a solely vertically incidencing wave is not justifiable any more. Hence, in some studies which analyse problems at larger epicentral distances, only Rayleigh-waves are considered as excitation. If the wave propagation in the near-field of all wave types should be analysed, the above mentioned approaches are insufficient since only one kind of wave is considered as excitation.

Not only the epicentral distance decides whether an approach for the seismic excitation is meaningful or warrantable, but also the definition of the analysed problem is decisive. If a structure in or on a soil domain with relatively small dimensions, as depicted in Fig. 7.1(b), is examined, it can be appropriate to apply one single plane wave type at the bottom or at the side boundaries of the near-field, since the seismic motion does not differ much in the small domain. An example for problems where this treatment is reasonable, is when just the dynamic effects due to the varying distribution of stiffness in the structure should be analysed, or when local effects in the soil, like the pore pressure progression, are studied. In those cases, the excitation at the bottom of the near-field can be derived by a one-dimensional deconvolution operation as explained in Sec. 4.3.2.

For problems where the spatial dimensions as well as the analysed phenomena are not locally restricted, other treatments of the application of the seismic excitation to the near-field have to be found. In those problems, significantly different seismic waves strike the extended near-field at different places as it is

sketched in Fig. 7.1(c). Obviously, those waves lead to a non-uniform distribution of the excitation of the near-field as shown in Fig. 7.1(d). Those non-uniform motions cause strains and stresses in the analysed structure and soil that are not neglectable. Thus, in cases where expanded structures like, e.g., lifelines in a broader sense (pipelines, bridges, streets, etc.) or large soil basins are analysed, the exciting motion of the near-field cannot be found by performing a one-dimensional deconvolution of the recorded ground motion.

Addressing those more complicated problems of extended dimensions, a simplified approach, often used in practice, is to apply the measured seismic record itself as initial motion at the bedrock-soil-interface at the bottom of the near-field. This simplified assumption is, e.g., made in [Bielak and Christiano, 1984; Naggar, 2003; Woodward-Clyde Consultants, 1988; Yang *et al.*, 2003; Zhang *et al.*, 2003]. In those investigations, the examined structures are characterised by being all situated on the top of the soil and not surrounded by it. To a certain degree, this justifies the noted simplified approach. An important characteristic of buried pipelines is not only their large extension in longitudinal direction, but also their position embedded in the soil. Because of both of those factors, the wave propagation inside the model is of high importance and, therefore, an exact as possible assumption of the initial motion is decisive. Therefore, it is necessary to find a more precise way to deal with the seismic excitation of the near-field model than it is done in the mentioned works.

One possibility is to perform a large scale simulation which includes the source and the near-field, like done in [Romanel and Kundu, 1993; Halldórsson, 1999; Kim *et al.*, 2003]. When the problem is solved only by one large scale model, i.e., in one step of simulation, the solution becomes computational very expensive. This is due to the fact that the mapping of the near-field, and if considered also of the seismic source, requires a high resolution of the model which needs to be transferred, at least partly, also to the wave propagation path in the earth crust. To overcome those problems and to obtain at the same time a reliable, i.e., realistic seismic excitation for the extended near-field, an advanced approach is introduced in the subsequent section.

7.2 Domain reduction method

The DRM is a numerical two-step method for modelling earthquake induced ground movements in three-dimensional problems. The method was developed and verified by Bielak and his co-workers [Bielak *et al.*, 2003; Yoshimura *et al.*, 2003] to overcome the problem of multiple physical scales which are present when considering the earthquake source, the wave propagation path and the region of interest at the surface. The historical development of the DRM leads back to [Bielak and Christiano, 1984; Cremonini *et al.*, 1988]. Similar two-step procedures have been presented by [Clough and Penzien, 1975; Kausel *et al.*, 1978; Aydinoglu, 1980]. Whereas all these methods were concerned with two-dimensional applications, more recent publications, e.g., [Oprsal and Zahradník, 2002] deal also with the extension of those procedures to three-dimensional problems.

The DRM divides the entire problem, consisting of the seismic source and of the structure under consideration, into two simpler ones. The first is an auxiliary problem where a domain of large scale is simulated which contains the seismic source as well as the region of interest, i.e., the neighbourhood of the structure to be analysed. This domain contains a rough reproduction of the composition of the earth's crust, i.e., the wave propagation path, but neither the structure of interest itself nor a detailed mapping of the near-field is modelled (Fig. 7.2(a) and 7.5(a)). Since all localised features are removed in this first step of simulation, it is referred to as background problem. The propagation of the complete seismic wave field is simulated from the hypocentre to the region of interest. For the first step of the DRM, any appropriate method can be utilised. The aim is to compute motions that can be transferred to a seismic excitation for the second step.

In this second step, the domain is reduced to the neighbourhood of the structure of interest (Figs. 7.2(b) and 7.5(b)) and loaded with forces equivalent to the initial seismic excitation from the first step. These forces induce the seismic waves into the considered domain which contains now the structure of interest

that can be analysed in detail. The reduction of the analysed domain in this second step is enabled since the equivalent seismic forces act only within one single layer of elements adjacent to the interface between the region of interest and the exterior domain. Through this method the wave propagation from the large scale simulation can be transferred to a model which describes only the near-field of the structure, i.e., the buried lifeline. For the second step, the FEM has to be used which is coupled with the SBFEM in the present work. The aim is to analyse the response of the structure and the region of interest.

7.2.1 Formulation

The DRM applies to problems of a semi-infinite region under earthquake conditions a shown in Fig. 7.5(a) that might contain special localised features and a seismically active fault. The geometry is arbitrary, the material behaviour linear elastic, and the seismic excitation is prescribed as a kinematic source along a predetermined fault. Generally, the earthquake fault on which the seismic excitation is caused, is far away from the structure which is the actual object of interest of of analysis. The impetus for the development of the DRM was the wish to define a better solvable problem in which the seismic excitation is brought closer to the region of interest. In doing so, the requirement needs to be fulfilled that the so obtained ground motion inside the region of interest is identical to the motion inside this region caused by the original seismic source. This requirement is satisfied through the DRM by determining appropriate expressions for the equivalent seismic excitation at the boundaries of the region of interest.

For the formulation of the DRM, the use of the FEM is premised. Hence, it needs to be firstly assumed that the large scale domain is truncated, since the FEM is unable to map infinite domains. Secondly, the truncation boundary has to be chosen far enough from the fault and the region of interest so that no reflected wave disturb the response. Both conditions are removed later.

Free-field: Initially, the free-field motion in the large scale domain as depicted in Fig. 7.2(a) is considered. The large domain contains the seismic source represented by the body force vector $\mathbf{f}_{seis}$ as well as the region of interest without any local features, like the structure. The possibility of expressing the rupture process on the seismic fault as displacement discontinuity or equally as body forces was discussed in Sec. 4.2.2. In general, the free-field problem is easier to solve than considering additional localised features, since those features increase the complexity of the overall solution.

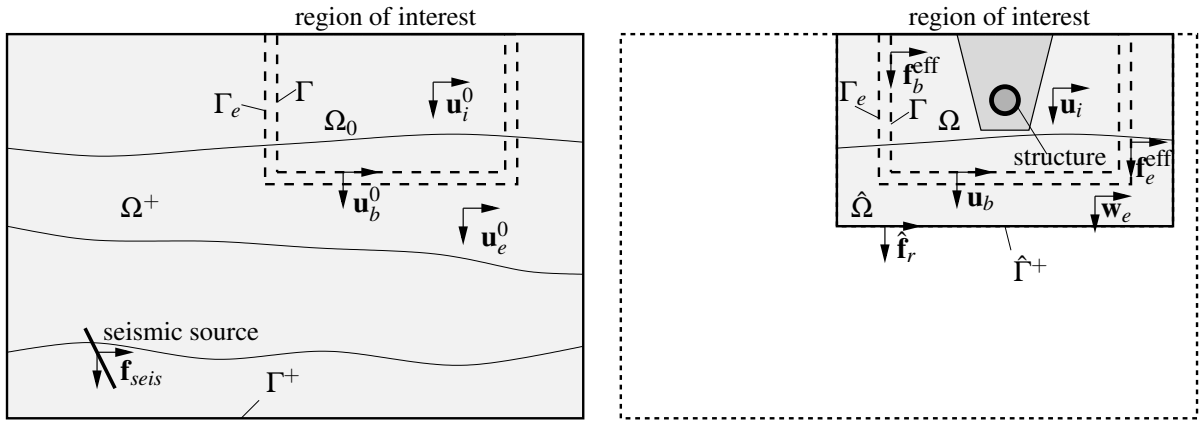

(a) Step I: Large scale domain containing the seismic source as well as the region of interest Ω_0, but without localised features (structure). The free-field motion $\mathbf{u}^0$ is determined on the two adjacent interfaces Γ and Γ_e at the boundary of Ω_0.

(b) Step II: Reduced domain containing the structure but not the seismic source. The free-field motion $\mathbf{u}^0$ from the first step is transformed to forces $\mathbf{f}^{\text{eff}}$. Those forces act on the interfaces Γ and Γ_e and are equivalent to the original seismic excitation $\mathbf{f}_{seis}$.

Figure 7.2: Schematic sketch of the two steps of the domain reduction method.

In order to find expressions of forces close to the region of interest which are equivalent to the seismic source term $\mathbf{f}_{seis}$, the large domain is subdivided into the region of interest Ω_0 and the outer domain Ω^+ which is bounded by Γ^+. The two domains Ω_0 and Ω^+ are connected at the interface Γ where the equivalent forces should act. Let index i denote the terms in the inner sub-domain Ω_0, index e the terms in the outer sub-domain Ω^+ and index b the terms on the interface Γ. Then, the equation of motion known from the FEM Eq. (5.19) can be split into the respective parts, so that it can be written with omitted damping terms as

$$\begin{bmatrix} \mathbf{M}_{ii}^{\Omega_0} & \mathbf{M}_{ib}^{\Omega_0} & \mathbf{0} \\ \mathbf{M}_{bi}^{\Omega_0} & \mathbf{M}_{bb}^{\Omega_0}+\mathbf{M}_{bb}^{\Omega^+} & \mathbf{M}_{be}^{\Omega^+} \\ \mathbf{0} & \mathbf{M}_{eb}^{\Omega^+} & \mathbf{M}_{ee}^{\Omega^+} \end{bmatrix} \begin{bmatrix} \ddot{\mathbf{u}}_i^0 \\ \ddot{\mathbf{u}}_b^0 \\ \ddot{\mathbf{u}}_e^0 \end{bmatrix} + \begin{bmatrix} \mathbf{K}_{ii}^{\Omega_0} & \mathbf{K}_{ib}^{\Omega_0} & \mathbf{0} \\ \mathbf{K}_{bi}^{\Omega_0} & \mathbf{K}_{bb}^{\Omega_0}+\mathbf{K}_{bb}^{\Omega^+} & \mathbf{K}_{be}^{\Omega^+} \\ \mathbf{0} & \mathbf{K}_{eb}^{\Omega^+} & \mathbf{K}_{ee}^{\Omega^+} \end{bmatrix} \begin{bmatrix} \mathbf{u}_i^0 \\ \mathbf{u}_b^0 \\ \mathbf{u}_e^0 \end{bmatrix} = \begin{bmatrix} \mathbf{0} \\ \mathbf{0} \\ \mathbf{f}_{seis} \end{bmatrix} . \quad (7.1)$$

Since the sub-domain Ω_0 does not contain the structure to be analysed, the fields of motion $\mathbf{u}_i^0$,$\mathbf{u}_b^0$ and $\mathbf{u}_e^0$ with superscript 0 are the free-field motions. From the last row of Eq. (7.1), an expression for the seismic excitation $\mathbf{f}_{seis}$ on the fault can be derived in terms of the free-field motions $\mathbf{u}^0$

$$\mathbf{f}_{seis} = \mathbf{M}_{eb}^{\Omega^+}\ddot{\mathbf{u}}_b^0 + \mathbf{M}_{ee}^{\Omega^+}\ddot{\mathbf{u}}_e^0 + \mathbf{K}_{eb}^{\Omega^+}\mathbf{u}_b^0 + \mathbf{K}_{ee}^{\Omega^+}\mathbf{u}_e^0 . \quad (7.2)$$

Domain containing structure: When introducing the structure and other localised features into the region of interest which is now named Ω, the displacements $\mathbf{u}$ can analogously to Eq. (7.1) be determined from the equation of motion

$$\begin{bmatrix} \mathbf{M}_{ii}^{\Omega} & \mathbf{M}_{ib}^{\Omega} & \mathbf{0} \\ \mathbf{M}_{bi}^{\Omega} & \mathbf{M}_{bb}^{\Omega}+\mathbf{M}_{bb}^{\Omega^+} & \mathbf{M}_{be}^{\Omega^+} \\ \mathbf{0} & \mathbf{M}_{eb}^{\Omega^+} & \mathbf{M}_{ee}^{\Omega^+} \end{bmatrix} \begin{bmatrix} \ddot{\mathbf{u}}_i \\ \ddot{\mathbf{u}}_b \\ \ddot{\mathbf{u}}_e \end{bmatrix} + \begin{bmatrix} \mathbf{K}_{ii}^{\Omega} & \mathbf{K}_{ib}^{\Omega} & \mathbf{0} \\ \mathbf{K}_{bi}^{\Omega} & \mathbf{K}_{bb}^{\Omega}+\mathbf{K}_{bb}^{\Omega^+} & \mathbf{K}_{be}^{\Omega^+} \\ \mathbf{0} & \mathbf{K}_{eb}^{\Omega^+} & \mathbf{K}_{ee}^{\Omega^+} \end{bmatrix} \begin{bmatrix} \mathbf{u}_i \\ \mathbf{u}_b \\ \mathbf{u}_e \end{bmatrix} = \begin{bmatrix} \mathbf{0} \\ \mathbf{0} \\ \mathbf{f}_{seis} \end{bmatrix} . \quad (7.3)$$

When substituting Eq. (7.2) in Eq. (7.3), the ground motion of the entire domain $\mathbf{u}_i$, $\mathbf{u}_b$ and $\mathbf{u}_e$ can be determined when the free-field motion $\mathbf{u}_b^0$ and $\mathbf{u}_e^0$ is known. This formulation by itself offers no advantage over an approach that solves the entire problem in one step since Eq. (7.2) includes the terms $\mathbf{M}_{ee}^{\Omega^+}\ddot{\mathbf{u}}_e^0$ and $\mathbf{K}_{ee}^{\Omega^+}\mathbf{u}_e^0$. This requires that the displacement and acceleration free-field in the entire domain Ω^+ needs to be stored for evaluating an equivalent expression for the seismic force term $\mathbf{f}_{seis}$. This entails an undue computational effort.

An increase of the computational efficiency can be achieved by a transformation of variables. In this transformation the total wave field $\mathbf{u}_e$ of the outer domain Ω^+ is described as the sum of the free-field motion $\mathbf{u}_e^0$ of the background problem and the residual motion $\mathbf{w}_e$ due to the localised features as

$$\mathbf{u}_e = \mathbf{u}_e^0 + \mathbf{w}_e \text{ and} \quad (7.4)$$

$$\ddot{\mathbf{u}}_e = \ddot{\mathbf{u}}_e^0 + \ddot{\mathbf{w}}_e . \quad (7.5)$$

When substituting those equations in Eq. (7.3) and reordering the result so that all terms which contain the free-field motion are written on the right side, yields

$$\begin{bmatrix} \mathbf{M}_{ii}^{\Omega} & \mathbf{M}_{ib}^{\Omega} & \mathbf{0} \\ \mathbf{M}_{bi}^{\Omega} & \mathbf{M}_{bb}^{\Omega}+\mathbf{M}_{bb}^{\Omega^+} & \mathbf{M}_{be}^{\Omega^+} \\ \mathbf{0} & \mathbf{M}_{eb}^{\Omega^+} & \mathbf{M}_{ee}^{\Omega^+} \end{bmatrix} \begin{bmatrix} \ddot{\mathbf{u}}_i \\ \ddot{\mathbf{u}}_b \\ \ddot{\mathbf{w}}_e \end{bmatrix} + \begin{bmatrix} \mathbf{K}_{ii}^{\Omega} & \mathbf{K}_{ib}^{\Omega} & \mathbf{0} \\ \mathbf{K}_{bi}^{\Omega} & \mathbf{K}_{bb}^{\Omega}+\mathbf{K}_{bb}^{\Omega^+} & \mathbf{K}_{be}^{\Omega^+} \\ \mathbf{0} & \mathbf{K}_{eb}^{\Omega^+} & \mathbf{K}_{ee}^{\Omega^+} \end{bmatrix} \begin{bmatrix} \mathbf{u}_i \\ \mathbf{u}_b \\ \mathbf{w}_e \end{bmatrix}$$
$$= \begin{bmatrix} \mathbf{0} \\ \mathbf{0} \\ \mathbf{f}_{seis} \end{bmatrix} + \begin{bmatrix} \mathbf{0} \\ -\mathbf{M}_{be}^{\Omega^+}\ddot{\mathbf{u}}_e^0 - \mathbf{K}_{be}^{\Omega^+}\mathbf{u}_e^0 \\ -\mathbf{M}_{ee}^{\Omega^+}\ddot{\mathbf{u}}_e^0 - \mathbf{K}_{ee}^{\Omega^+}\mathbf{u}_e^0 \end{bmatrix} . \quad (7.6)$$

Finally, after substituting the seismic source term expressed by the free-field motion in Eq. (7.2), the desired equation can be obtained

$$\begin{bmatrix} \mathbf{M}_{ii}^{\Omega} & \mathbf{M}_{ib}^{\Omega} & \mathbf{0} \\ \mathbf{M}_{bi}^{\Omega} & \mathbf{M}_{bb}^{\Omega}+\mathbf{M}_{bb}^{\Omega^+} & \mathbf{M}_{be}^{\Omega^+} \\ \mathbf{0} & \mathbf{M}_{eb}^{\Omega^+} & \mathbf{M}_{ee}^{\Omega^+} \end{bmatrix} \begin{bmatrix} \ddot{\mathbf{u}}_i \\ \ddot{\mathbf{u}}_b \\ \ddot{\mathbf{w}}_e \end{bmatrix} + \begin{bmatrix} \mathbf{K}_{ii}^{\Omega} & \mathbf{K}_{ib}^{\Omega} & \mathbf{0} \\ \mathbf{K}_{bi}^{\Omega} & \mathbf{K}_{bb}^{\Omega}+\mathbf{K}_{bb}^{\Omega^+} & \mathbf{K}_{be}^{\Omega^+} \\ \mathbf{0} & \mathbf{K}_{eb}^{\Omega^+} & \mathbf{K}_{ee}^{\Omega^+} \end{bmatrix} \begin{bmatrix} \mathbf{u}_i \\ \mathbf{u}_b \\ \mathbf{w}_e \end{bmatrix} = \begin{bmatrix} \mathbf{f}_i^{\text{eff}} \\ \mathbf{f}_b^{\text{eff}} \\ \mathbf{f}_e^{\text{eff}} \end{bmatrix} \quad (7.7)$$

in which the equivalent seismic forces $\mathbf{f}^{\text{eff}}$ are acting just in the vicinity of the region of interest

$$\mathbf{f}^{\text{eff}} = \begin{bmatrix} \mathbf{f}_i^{\text{eff}} \\ \mathbf{f}_b^{\text{eff}} \\ \mathbf{f}_e^{\text{eff}} \end{bmatrix} = \begin{bmatrix} \mathbf{0} \\ -\mathbf{M}_{be}^{\Omega^+}\ddot{\mathbf{u}}_e^0 - \mathbf{K}_{be}^{\Omega^+}\mathbf{u}_e^0 \\ \mathbf{M}_{eb}^{\Omega^+}\ddot{\mathbf{u}}_e^0 + \mathbf{K}_{eb}^{\Omega^+}\mathbf{u}_e^0 \end{bmatrix} . \tag{7.8}$$

From Eq. (7.8), it can be realised that the equivalent seismic forces $\mathbf{f}^{\text{eff}}$ have the key property that they involve only the sub-matrices $\mathbf{M}_{be}$, $\mathbf{K}_{be}$, $\mathbf{M}_{eb}$ and $\mathbf{K}_{eb}$ which vanish everywhere except in a single finite element layer in Ω^+ which is adjacent to Γ. This small layer is bounded by Γ and Γ_e, as depicted in Fig. 7.2, where the equivalent forces exclusively act. This means that the only wave fields that need to be obtained from the background simulation, are the free-field motions $\mathbf{u}_b^0$ on Γ and $\mathbf{u}_e^0$ on Γ_e. Thus the forces $\mathbf{f}^{\text{eff}}$ that are equivalent to the original seismic excitation at the fault can be derived. The advantage over the formulation in Eq. (7.3) is that not the whole free-field motion in the outer domain Ω^+ needs to be stored to obtain an expression for the equivalent forces, but just the wave fields on the interfaces Γ and Γ_e.

Hence, the outer domain can be drastically reduced for the second step, as depicted in Fig. 7.2(b), where the region of interest contains all localised features and the seismic excitation is applied in form of the equivalent forces $\mathbf{f}^{\text{eff}}$. Due to this reduction in the second sub-problem, the method is named domain reduction method. Anyway, it has to be noted that the reduction of the domain which is named $\hat{\Omega}^+$ still requires the use of absorbing boundary conditions on its truncation boundary $\hat{\Gamma}^+$ (see Fig. 7.2(b)). This is due, since even though in $\hat{\Omega}^+$ not the total wave field $\mathbf{u}_e$ appears, the residual wave field $\mathbf{w}_e$ does. This residual wave field is caused by the localised features in the region of interest. So, it only vanishes when those features are removed and thus a free-field analysis is performed for which no subdivision in two problems needs to be performed.

7.2.2 Two-step procedure

On basis of the transformations and the results of the previous section, a two-step procedure for analysing the earthquake response of a region containing a structure of interest and other localised features can be established.

Step I: In the first step, as shown in Fig (7.2(a)), a background problem is analysed which embraces the domains Ω_0 and Ω^+ including the earthquake source. The interface Γ between the two domains Ω_0 and Ω^+ defines the boundary of what will be the region of interest in the second step. Then, the free-field motions $\mathbf{u}_e^0$ and $\mathbf{u}_b^0$ are computed on the adjacent surfaces Γ and Γ_e and stored for the respective nodes. For this step, any appropriate method can be used by which the wave propagation between the seismic source and the region of interest can be simulated. The usage of the FEM is computational expensive in this case and requires the implementation of absorbing boundaries. More efficient alternatives are, amongst others, the BEM (see [Borsutzky and Lehmann, 2005]), the thin layer method or, as employed in the present work, Green's functions.

Step II: In the second step, depicted in Fig. (7.2(b)), the region of interest Ω is now modelled with the structure as well as all localised features. At the same time, the outer domain Ω^+ is reduced to a domain $\hat{\Omega}^+$ which does not need to include the seismic fault. This reduction is possible since the effective forces $\mathbf{f}^{\text{eff}}$ of the seismic excitation from Eq. (7.8) are solely acting on the bounding layers Γ and Γ_e adjacent to the region of interest. This equivalent forces are computed from the free-field motion $\mathbf{u}_e^0$ and $\mathbf{u}_b^0$ with Eq. (7.8). Hereupon, the total fields of motion $\mathbf{u}_i$, $\mathbf{u}_b$ and the residual field $\mathbf{w}_e$ can be derived from Eq. (7.7). Those fields of motion describe the behaviour of the region of interest, i.e., of the detailed modelled soil and of the structure connected to it.

7.2.3 Implementation in hybrid FE-SBFEM

If the inner domains Ω and Ω_0 from both steps of the DRM correspond to each other, obviously, the residual motion $\mathbf{w}_e$ in the outer domain $\hat{\Omega}^+$ vanishes. When inserting local features into the region of interest Ω_0 which are not present in the free-field Ω, it is necessary to implement transmitting boundary conditions on the boundary $\hat{\Gamma}^+$ (see Fig. 7.2(b)) to prevent unwanted reflections of waves back into the domain Ω. A suitable method for modelling the wave radiation into the infinite half-space is the SBFEM, that is used in this work. Subsequently, the implementation of the DRM into the hybrid FE-SBFEM scheme from Eq. (6.74) will be addressed in brief.

As explained in Sec. 6.5, the interaction forces $\hat{\mathbf{f}}_r$ are applied at the interface between the near-field, i.e., the region of interest, modelled by the FEM and the far-field, i.e., the infinite half-space modelled by the SBFEM. The interaction forces $\hat{\mathbf{f}}_r$ represent the response behaviour of the half-space at this interface which is in the DRM named $\hat{\Gamma}^+$ (see Fig. 7.2(b)). Introducing a fourth index r for the terms on this interface Γ^+, the combination of the two equations of motion, i.e., Eq. (7.7) of the DRM and Eq. (6.74) of the FE-SBFEM, yields

$$\begin{bmatrix} \mathbf{M}_{ii}^{\Omega} & \mathbf{M}_{ib}^{\Omega} & \mathbf{0} & \mathbf{0} \\ \mathbf{M}_{bi}^{\Omega} & \mathbf{M}_{bb}^{\Omega}+\mathbf{M}_{bb}^{\hat{\Omega}^+} & \mathbf{M}_{be}^{\hat{\Omega}^+} & \mathbf{0} \\ \mathbf{0} & \mathbf{M}_{eb}^{\hat{\Omega}^+} & \mathbf{M}_{ee}^{\hat{\Omega}^+} & \mathbf{M}_{re}^{\hat{\Omega}^+} \\ \mathbf{0} & \mathbf{0} & \mathbf{M}_{er}^{\hat{\Omega}^+} & \mathbf{M}_{rr}^{\hat{\Omega}^+}+\gamma\Delta t\mathbf{M}_0^{\infty} \end{bmatrix} \begin{bmatrix} \ddot{\mathbf{u}}_i \\ \ddot{\mathbf{u}}_b \\ \ddot{\mathbf{w}}_e \\ \ddot{\mathbf{w}}_r \end{bmatrix} + \begin{bmatrix} \mathbf{K}_{ii}^{\Omega} & \mathbf{K}_{ib}^{\Omega} & \mathbf{0} & \mathbf{0} \\ \mathbf{K}_{bi}^{\Omega} & \mathbf{K}_{bb}^{\Omega}+\mathbf{K}_{bb}^{\hat{\Omega}^+} & \mathbf{K}_{be}^{\hat{\Omega}^+} & \mathbf{0} \\ \mathbf{0} & \mathbf{K}_{eb}^{\hat{\Omega}^+} & \mathbf{K}_{ee}^{\hat{\Omega}^+} & \mathbf{K}_{re}^{\hat{\Omega}^+} \\ \mathbf{0} & \mathbf{0} & \mathbf{K}_{er}^{\hat{\Omega}^+} & \mathbf{K}_{rr}^{\hat{\Omega}^+} \end{bmatrix} \begin{bmatrix} \mathbf{u}_i \\ \mathbf{u}_b \\ \mathbf{w}_e \\ \mathbf{w}_r \end{bmatrix} = \begin{bmatrix} \mathbf{f}_i^{\text{eff}} \\ \mathbf{f}_b^{\text{eff}} \\ \mathbf{f}_e^{\text{eff}} \\ \mathbf{f}_r^{\text{eff}}-\hat{\mathbf{f}}_r \end{bmatrix} = \begin{bmatrix} \mathbf{0} \\ \mathbf{f}_b^{\text{eff}} \\ \mathbf{f}_e^{\text{eff}} \\ -\hat{\mathbf{f}}_r \end{bmatrix}. \tag{7.9}$$

The force vector on the very right side of this equation has zero entries for the nodes inside the region of interest Ω, i.e., $\mathbf{f}_i^{\text{eff}} = \mathbf{0}$. Presuming that the interfaces Γ_e and $\hat{\Gamma}^+$ do not coincidence at any node, also the equivalent seismic forces $\mathbf{f}_r^{\text{eff}}$ on $\hat{\Gamma}^+$ are zero. In the present work, Eq. (7.9) is the central equation to analyse the dynamic response to seismic wave propagation inside the region of interest, containing the buried lifeline and its surrounding soil.

7.3 Discrete wavenumber finite element method

Various methods were developed for large scale simulations of seismic ground motions which are specified, e.g., in [Kramer, 1996; Anderson, 2003]. In the present work, the realisation of the large scale simulation is performed by numerical techniques which are mostly described in [Spudich and Archuleta, 1987]. Those techniques enable the calculation of synthetic ground motion seismograms for hypothetical fault ruptures occurring on faults of finite spatial extent.

The quantitative description of seismic ground motions by means of representation theorems was discussed in Sec. 4.2.2. Here, the representation theorem for the consideration of discontinuities on the seismic fault Eq. (4.25) is used. A key property of those mathematical representations is the appearance of the seismic source term and the wave propagation term as separate factors. Therefore, it is possible to determine both factors apart from each other, at first, and adopt them in the representation theorem Eq. (4.25) afterwards. In this section, the determination of the seismic wave propagation term is addressed. Therefore, the discrete wavenumber finite element method (DWFEM) is incorporated to calculate Green's functions for laterally heterogeneous half-spaces which consist of piecewise linear functions. Since this Green's function is computed by means of numerical methods, it is referred to as numerical Green's function.

Method: The DWFEM was developed by [Olson *et al.*, 1984] to calculate Green's functions for wave propagation in a three-dimensional vertically heterogeneous, non-attenuating half-space. For the hori-

zontal dependence, the method uses a discrete wavenumber decomposition of the wave motion. Therefore, a Fourier-Bessel series is utilised which is exact when summed to infinity. For the vertical and time-dependent components of the waves, a system of partial differential equations is solved numerically by a combined FE /finite difference method (FDM) which accommodates arbitrary vertical heterogeneities. The response of an arbitrary horizontal layered half-space due to tractions on its surface can be determined this way. Incorporating the reciprocity of Green's functions, the determination of the response of the half-space with a traction-free surface due to a excitation in the inner is potentiated.

The limits of the method should be mentioned briefly. The DWFEM is not able to model attenuation effects, i.e., the applications for simulating realistic ground motions are limited to source receiver distances to approximately 20-30km. Furthermore, the method assumes a horizontal flat layered earth, i.e., local effects on the seismic wave path or sloping layers cannot be modelled. Nevertheless, having this restrictions in mind this method yields good results for synthetic ground motions.

In the following, the main steps of the derivation of the DWFEM are discussed. Firstly, the elastic response of a vertical stratified medium is addressed, whereupon secondly, the numerical solution procedure in dependence of depth and time is considered.

7.3.1 Elastic wave propagation in a vertically stratified half-space

Starting the derivation of the DWFEM, requires to recall the equation of motion in vertically heterogeneous media given in Eq. (2.14). In the present section, the partial solution of this equation is addressed. At first, the separable solutions of the equation of motion for linear isotropic material are presented using a cylindrical coordinate system in which the elastic parameters vary with changing depth coordinate. Whereas the horizontal dependency of the solution is thus known and involves a radial wavenumber and a azimuthal frequency, the vertical and time-variables remain as unknowns in a system of partial differential equations. After the set-up of the separable solutions, they are superposed in order to use a discrete wavenumber expansion for vertically and horizontally oriented delta-function vectors. The response to those impulsive forces takes the form of a Fourier-Bessel series.

7.3.1.1 Separable solutions of the elastic equation of motion

In order to obtain a solution of the equation of motion in a homogeneous layer, it is comfortable to transform the system of partial differential equations into a system of ordinary ones. This can be achieved by the separation of the equation of motion. The separability is often used to obtain the elastic response of vertically layered media (see, e.g., [Pan, 2003]).

When the medium is vertically inhomogeneous, the equation of motion Eq (2.14) remains, at least in Cartesian, cylindrical or spherical coordinates, separable. For cylindrical coordinates (z, r, ϕ), the separability is potentiated in the horizontal coordinates r and ϕ, the time-dependence may be Fourier transformed, but the vertical dependence of the solution is not known explicitly. Therefore, after [Takeuchi and Saito, 1972], a set of six coupled first-order differential equations depending solely on z needs to be solved. Four of those equations represent *P/SV*-wave propagation and are decoupled from the remaining two equations representing *SH*-wave motion. According to this approach, the surface vector harmonics $\mathbf{R}_k^m$, $\mathbf{S}_k^m$ and $\mathbf{T}_k^m$ are defined as

$$\mathbf{R}_k^m(r,\phi) = Y_k^m(r,\phi)\mathbf{e}_z \,, \tag{7.10}$$

$$\mathbf{S}_k^m(r,\phi) = \frac{1}{k}Y_{k,r}^m(r,\phi)\mathbf{e}_r + \frac{1}{kr}Y_{k,\phi}^m(r,\phi)\mathbf{e}_\phi \,, \tag{7.11}$$

$$\mathbf{T}_k^m(r,\phi) = \frac{1}{kr}Y_{k,\phi}^m(r,\phi)\mathbf{e}_r \,, + \frac{1}{k}Y_{k,r}^m(r,\phi)\mathbf{e}_\phi \,. \tag{7.12}$$

Here, $m = 0, \pm 1, \pm 2, \ldots$ is the integer angular frequency, k the horizontal wavenumber and $\mathbf{e}_z, \mathbf{e}_r, \mathbf{e}_\phi$ are the unit vectors in cylindrical coordinates. Further, the Bessel function of the second kind Y_k^m is defined

as

$$Y_k^m(r,\phi) = J_m(kr)e^{(im\phi)} \tag{7.13}$$

where the Bessel function of the first kind $J_m(kr)$ of order m is used. With the surface vector harmonics $\mathbf{R}_k^m$, $\mathbf{S}_k^m$ and $\mathbf{T}_k^m$, the separation in cylindrical coordinates for a body force vector $\mathbf{b}$ and a displacement vector $\mathbf{u}$ is represented by

$$\mathbf{b}(r,\phi,z,t) = \sum_{m=-\infty}^{\infty} \int_{k=0}^{\infty} \left(B_{zk}^m(z,t)\mathbf{R}_k^m(r,\phi) + B_{rk}^m(z,t)\mathbf{S}_k^m(r,\phi) + B_{\phi k}^m(z,t)\mathbf{T}_k^m(r,\phi) \right) dk \quad \text{and} \tag{7.14}$$

$$\mathbf{u}(r,\phi,z,t) = \sum_{m=-\infty}^{\infty} \int_{k=0}^{\infty} \left(U_{zk}^m(z,t)\mathbf{R}_k^m(r,\phi) + U_{rk}^m(z,t)\mathbf{S}_k^m(r,\phi) + U_{\phi k}^m(z,t)\mathbf{T}_k^m(r,\phi) \right) dk \, . \tag{7.15}$$

The dependency of $\mathbf{b}$ and $\mathbf{u}$ on the horizontal coordinate r and ϕ is solely regarded by the surface vector harmonics which are identical in both cases. The dependency on z and t is considered in terms of the complex scalar coefficients $B_{zk}^m, B_{rk}^m, B_{\phi k}^m$ and $U_{zk}^m, U_{rk}^m, U_{\phi k}^m$. The additional subscripts z, r or ϕ of those coefficients remind that they are the concerning components in the far field, what can be realised from Eqs. (7.10) to (7.12) when considering for the surface vector harmonics the limit $r \to \infty$.

The substitution of Eqs. (7.14) and (7.15) in the equation of motion Eq. (2.14) yields for fixed angular frequencies m and horizontal wavenumbers k

$$\left\{ (\lambda+2\mu)U_{zk,z}^m - k\lambda U_{rk}^m \right\}_{,z} - k\mu U_{rk,z}^m - k^2\mu U_{zk}^m + B_{zk}^m = \rho \ddot{U}_{zk}^m \, , \tag{7.16}$$

$$\left\{ \mu(U_{rk}^m + kU_{zk}^m) \right\}_{,z} + k\lambda U_{zk,z}^m - k^2(\lambda+2\mu)U_{rk}^m + B_{rk}^m = \rho \ddot{U}_{rk}^m \, , \tag{7.17}$$

$$\left\{ \mu U_{\phi k}^m \right\}_{,z} - k^2\mu U_{\phi k}^m + B_{\phi k}^m = \rho \ddot{U}_{\phi k}^m \, . \tag{7.18}$$

Those three separated equations depend only on z and t and correspond to the $\mathbf{R}_k^m$, $\mathbf{S}_k^m$ and $\mathbf{T}_k^m$ components of the equation of motion, respectively. Through Eqs. (7.14) and (7.15), all r and ϕ dependence is satisfied exactly. The terms in curly brackets on the left of Eqs. (7.16) to (7.18), are the $\mathbf{R}_k^m$, $\mathbf{S}_k^m$ and $\mathbf{T}_k^m$ components representing the tractions on surfaces with outward normal $\mathbf{e}_z$. This could be, e.g., the surface of a half-space bounded by the plane $z = 0$.

If the Eqs. (7.16) to (7.18) are solved under the conditions that, firstly, at the free half-space boundary either displacements or tractions are prescribed, and, secondly, the initial displacements and velocities are defined at every depth z, the displacement field $\mathbf{u}$ from Eq. (7.15) due to the body force density $\mathbf{b}$ from Eq. (7.14) can be determined. In Eq. (7.18), only the displacements $U_{\phi k}^m$ occur, whereas in Eqs. (7.16) and (7.17) the two remaining coefficients U_{zk}^m and U_{rk}^m are solely present. Since $U_{\phi k}^m$ represents the *SH* motion consisting entirely of shear motion, and U_{zk}^m and U_{rk}^m represent the $P-SV$ motion coupling both shear and compressional energy, it is expressed by the set of equations, Eqs. (7.16) to (7.18), that both wave types propagate independently in the vertically stratified medium.

7.3.1.2 Discrete wavenumber expansion for the impulse response

The solution of the equation of motion Eq. (2.14) due to an impulsive point force directed along a coordinate axis describes the impulse response of the elastic medium. As discussed in Sec. 3.3.1.1, those displacement fields are called fundamental solutions. When, additionally, the homogeneous boundary conditions, e.g., the vanishing tractions at the free half-space surface, are satisfied within the fundamental solutions leads to Green's functions (Sec. 4.2.1). Due to the linearity of Eq. (2.14), the wave radiation from a distributed source (like the seismic fault mechanism is assumed in this work) can be expressed as a spatial and temporal convolution of the Green's functions by means of representation theorems

(Sec. 4.2.2). Hence, in the present section the impulse response of an elastic vertically heterogeneous half-space due to an impulsive point force will be addressed at first.

When representations of $\mathbf{b}$ and $\mathbf{u}$ from Eqs. (7.14) and (7.15), respectively, are expressed as a discrete sum of the surface vectors from Eqs. (7.10) to (7.12) over a discrete set of wavenumbers k_n and angular frequencies m,

$$\mathbf{b}(r,\phi,z,t) = \sum_{m=-\infty}^{\infty} \sum_{n=0}^{\infty} B^m_{zk_n}(z,t)\mathbf{R}^m_{k_n}(r,\phi) + B^m_{rk_n}(z,t)\mathbf{S}^m_{k_n}(r,\phi) + B^m_{\phi k_n}(z,t)\mathbf{T}^m_{k_n}(r,\phi) \quad \text{and} \tag{7.19}$$

$$\mathbf{u}(r,\phi,z,t) = \sum_{m=-\infty}^{\infty} \sum_{n=0}^{\infty} U^m_{zk_n}(z,t)\mathbf{R}^m_{k_n}(r,\phi) + U^m_{rk_n}(z,t)\mathbf{S}^m_{k_n}(r,\phi) + U^m_{\phi k_n}(z,t)\mathbf{T}^m_{k_n}(r,\phi)\,, \tag{7.20}$$

the complex coefficients $B^m_{zk}, B^m_{rk}, B^m_{\phi k}$ and $U^m_{zk}, U^m_{rk}, U^m_{\phi k}$ can be determined by finite Fourier and Bessel transforms. The completeness of this discrete wavenumber sum and the sampling of the wavenumber k_n is demonstrated in detail in [Olson *et al.*, 1984] for the interval $0 \le r \le R_{\max}$.

The expressions of the coefficients can be evaluated for delta-function vectors along the horizontal and vertical coordinate axes depicted in Fig. 7.3 which represent the impulsive forces in those directions. By

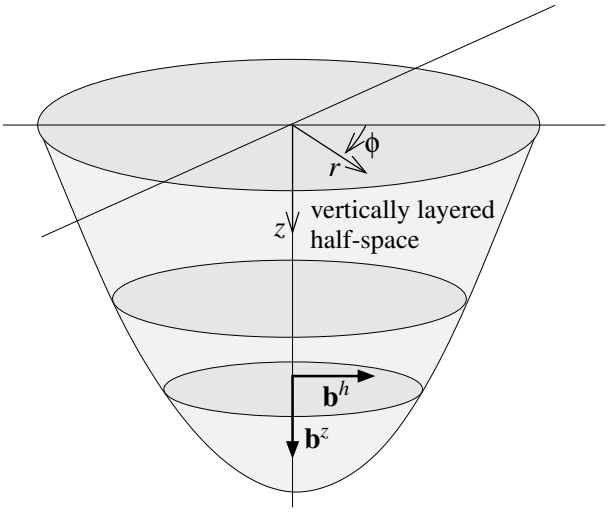

Figure 7.3: Vertically layered half-space with cylindrical coordinate system. The unit impulsive forces $\mathbf{b}^h$ and $\mathbf{b}^z$ act in the horizontal and vertical direction, respectively, at a source point in the inner of the half-space.

the application of the Fourier and Bessel transforms, the horizontal impulsive force $\mathbf{b}^h$ for $\phi = 0$ and the vertical impulsive force $\mathbf{b}^z$ can be written by means of the auxiliary variables

$$W^h_n = \frac{1}{\pi(R_{\max}J_0(k_nR_{\max}))^2} \quad \text{and} \quad W^z_n = \frac{1}{\pi(R_{\max}J_1(k_nR_{\max}))^2}\,, \tag{7.21}$$

as the discrete wavenumber expansions for the interval $0 \le r \le R_{\max}$

$$\begin{aligned}\mathbf{b}^h &= \lim_{r_0\to\infty}\left(\frac{1}{r_0}\delta(r-r_0)\delta(\phi)\delta(z-z_0)\delta(t)\mathbf{e}_r\right)\\ &= \sum_{m=\pm1}\sum_{n=0}^{\infty}\frac{m}{2}W^h_n\delta(z-z_0)\delta(t)\mathbf{S}^m_{k_n}(r,\phi) + \frac{-i}{2}W^h_n\delta(z-z_0)\delta(t)\mathbf{T}^m_{k_n}(r,\phi) \quad \text{and}\end{aligned} \tag{7.22}$$

$$\begin{aligned}\mathbf{b}^z &= \lim_{r_0\to\infty}\left(\frac{1}{r_0}\delta(r-r_0)\delta(\phi)\delta(z-z_0)\delta(t)\mathbf{e}_z\right)\\ &= \sum_{n=0}^{\infty}W^z_n\delta(z-z_0)\delta(t)\mathbf{R}^0_{k_n}(r,\phi)\,.\end{aligned} \tag{7.23}$$

Due to the symmetry about the z-axis, the wavenumber expansion of $\mathbf{b}^z$ involves only the $m = 0$ term which has no ϕ dependence, whereas in the wavenumber expansion of $\mathbf{b}^h$ only $m = \pm 1$ terms are considered. Finally, the use of the surface vectors $\mathbf{R}^m_{k_n}, \mathbf{S}^m_{k_n}, \mathbf{T}^m_{k_n}$ in a series expansion for the delta-functions enables the separated equations of motion Eqs. (7.16) to (7.18) to be solved for each term of the discrete wavenumber expansion Eqs. (7.22) to (7.23). Thus, the complex scalar coefficients $B^m_{zk_n}, B^m_{rk_n}, B^m_{\phi k_n}$ can be computed, so that it is possible to obtain the Green's function of a vertically stratified half-space.

The displacement Green's functions for the discrete wavenumber k_n due to the loads $\mathbf{b}^h$ and $\mathbf{b}^z$ can be determined when applying $B^{+1}_{rk_n} = B^{+1}_{\phi k_n} = \delta(z-z_0)\delta(t)$ in Eqs. (7.17) and (7.18) and $B^0_{zk_n} = \delta(z-z_0)\delta(t)$ in Eq. (7.16), respectively. Hence, the solution for the total motion due to the horizontal load $\mathbf{b}^h$ is given by

$$\mathbf{u}^h_z = \sum_{n=0}^{\infty} W^h_n U^1_{zk_n}(z,t,z_0) J_1(k_n r)\cos(\phi)\ , \tag{7.24}$$

$$\mathbf{u}^h_r = \sum_{n=0}^{\infty} W^h_n \left[U^1_{rk_n}(z,t,z_0)\left(\frac{1}{k_n r}J_1(k_n r) - J_2(k_n r)\right) + U^1_{\phi k_n}(z,t,z_0)\frac{1}{k_n r}J_1(k_n r)\right]\cos(\phi)\ , \tag{7.25}$$

$$\mathbf{u}^h_\phi = -\sum_{n=0}^{\infty} W^h_n \left[U^1_{\phi k_n}(z,t,z_0)\left(\frac{1}{k_n r}J_1(k_n r) - J_2(k_n r)\right) + U^1_{rk_n}(z,t,z_0)\frac{1}{k_n r}J_1(k_n r)\right]\sin(\phi)\ , \tag{7.26}$$

and the motion due to the vertical load $\mathbf{b}^z$ by

$$\mathbf{u}^z_z = \sum_{n=0}^{\infty} W^z_n U^0_{zk_n}(z,t,z_0) J_0(k_n r)\ , \tag{7.27}$$

$$\mathbf{u}^z_r = -\sum_{n=0}^{\infty} W^z_n U^0_{rk_n}(z,t,z_0) J_1(k_n r) \quad \text{and} \tag{7.28}$$

$$\mathbf{u}^z_\phi = 0\ . \tag{7.29}$$

Here, $\mathbf{u}^h_z, \mathbf{u}^h_r, \mathbf{u}^h_\phi$ are the components of the displacement field in the cylindrical coordinates (z, r, ϕ), respectively, due to the impulsive force $\mathbf{b}^h$, and, analogously, $\mathbf{u}^z_z, \mathbf{u}^z_r, \mathbf{u}^z_\phi$ due to $\mathbf{b}^z$. The Bessel functions define the delta-functions only over the interval $0 \le r \le R_{\max}$. Therefore, the vectors $\mathbf{b}^h$ and $\mathbf{b}^z$ do not vanish for $r > R_{\max}$. Physically interpreted, this means that at time $t = 0$ the domain outside of the radius $R_{\max}$ is excited. Hence, the Green's functions Eqs. (7.24) to (7.29) are just valid for times t less than the P-wave travel time $t_{\max} = R_{\max}/c_P$. In the numerical implementation, where $R_{\max}$ cannot be chosen infinitely large, this implies unwanted wave arrivals for long simulation times. Also, the infinite sums are truncated in practice at some large value $k_{\max}$, which causes high-frequency contributions in the elastic response. Hence, both maximum values $R_{\max}$ and $k_{\max}$ have to be chosen sufficiently large to prevent disturbances in the elastic response.

7.3.2 Finite element / finite difference approximation

In Sec. 7.3.1, the elastic radiation of waves due to a point source is only solved partially depending on r and ϕ. This solution is expressed as a Fourier-Bessel series. However, the coefficients in those series are determined by solving a coupled system of partial differential equations in dependency of z and t. To solve this system of equations numerically, the FEM (see Chap. 5) and the FDM are employed. As stated in other chapters, numerical solutions are approximative, i.e., the continuously varying components of displacements and body forces are defined in terms of their nodal values at discrete element grid-points z_j and time-points t_i. Herein, the displacement field at one time t_i depends on the previous displacements and the prescribed nodal force terms.

Maximum resolving frequency: The FEM is applied to approximate the z dependence of the differential equation system. Its procedure is discussed in Chap. 5 and, therefore, not addressed here. Just one

remark should be given concerning the maximum frequency to which the elastic response of the layered half-space can be resolved into. To map the propagation of a wave of wavelength λ in the medium, the distance of the FE-nodes Δz should be chosen as

$$\lambda_{\min} = 6\Delta z \, . \tag{7.30}$$

This means, that at least the displacements at six nodes are needed to describe the motion of one sinus wave properly. Hence, the maximum resolving frequency $f_{\max}$ is reciprocally proportional to the minimum resolving wavelength $\lambda_{\min}$. The factor of the reciprocal of $\lambda_{\min}$ is the slowest wave velocity, i.e., the *S*-wave velocity c_S in full-space. So, the maximum frequency $f_{\max}$ that can be analysed, is given as

$$f_{\max} = \frac{1}{\Delta t} = \frac{c_S}{\lambda_{\min}} = \frac{c_S}{6\Delta z} \, . \tag{7.31}$$

Thus, the maximum resolving frequency $f_{\max}$ depends on the material parameter c_S and the chosen grid space Δz. Since a higher resolution of the frequency leads to a decreasing time-step width Δt and a decreasing grid space Δz, the computational effort increases squared. To limit the computational effort but obtain at the same time reliable results, the influence of the maximum resolving frequency $f_{\max}$ on the behaviour of buried lifelines is studied in Sec. 9.3.6.

Time-dependence: To solve the time-dependence of the separated equation system Eqs. (7.16) to (7.18), the FDM is incorporated. In the FDM (see, e.g., [Mitchell and Griffiths, 1980]) continuous derivatives are replaced directly by their difference approximations. Those approximations are derived from Taylor series expansions of the displacement components at the node points. Applying the FDM with the initial conditions Eqs. (2.17) to (2.18), the continuous differential equations (7.16) to (7.18) are represented in terms of the discrete matrices $\mathbf{G}$ and $\mathbf{H}$ as

$$\mathbf{G}\tilde{\mathbf{u}}(t_i) - \tilde{\mathbf{u}}(t_{i-1}) + \mathbf{H}\tilde{\mathbf{b}}(t_i) = \tilde{\mathbf{u}}(t_{i+1}) \, . \tag{7.32}$$

Here, the vectors $\tilde{\mathbf{u}}(t_i)$ and $\tilde{\mathbf{b}}(t_i)$ contain the (z, r, ϕ)-components of all N nodes discretising the domain in z direction

$$\tilde{\mathbf{u}}(t_i) = \left[U_z(z_1,t_i), U_r(z_1,t_i), U_\phi(z_1,t_i), ..., U_z(z_N,t_i), U_r(z_N,t_i), U_\phi(z_N,t_i)\right] \quad \text{and} \tag{7.33}$$

$$\tilde{\mathbf{b}}(t_i) = \left[B_z(z_1,t_i), B_r(z_1,t_i), B_\phi(z_1,t_i), ..., B_z(z_N,t_i), B_r(z_N,t_i), B_\phi(z_N,t_i)\right] \, . \tag{7.34}$$

For simplicity, the subscript k and the superscript m from the previous section have been omitted, since they are constants from the point of view of this section. The recursion formulated in Eq. (7.32) requires the displacement field at two consecutive time-steps to determine the displacements at the next time-step. Higher order difference schemes can be employed as well, if the initial boundary conditions are adjusted and the minimum number of consecutive time-steps is at least three involving two time-derivatives.

In Eq. (7.32), the boundary conditions in z-coordinate, e.g., the stress free surface of the half-space or the displacements continuity at layer interfaces, are incorporated in the coefficient matrix $\mathbf{G}$. That way, the homogeneous boundary conditions are satisfied and the displacement field $\mathbf{u}$ can be termed Green's function.

7.4 Representation of the seismic source

For the representation of the seismic source, a kinematic model is incorporated. As announced in Sec. 4.2.3, those models describe the dynamic process on the fault by means of parameters like length L and width W of the fault, rupture velocity v_R, final offset $[\mathbf{u}]$ and rise time t_r. Those parameters of the fault and the rupture can be empirical related to the size of an earthquake by scaling laws. This source scaling is addressed firstly, then the fault rupture model is addressed which describes a complex slip distribution by a kinematic self-similar approach which regards some randomness.

7.4.1 Seismic source scaling

This section covers the scaling of the source geometry and the characteristic terms of the rupture process by empirical relationships. According to [Hanks and Kanamori, 1979], the moment magnitude M_w of an earthquake is related to the seismic moment M_0 by Eq. (4.5). The area S of a seismic fault can be calculated from the moment magnitude M_w, using the empirical relationship stated by [Wells and Coppersmith, 1994]

$$\log(S) = a + b \cdot M_w \tag{7.35}$$

where $(a,b) = (-3.42, 0.90), (-2.87, 0.82), (-3.99, 0.98)$ for strike-, normal-, reverse-slip, respectively. Following [Priolo *et al.*, 2002] the length L and the width W of the fault can be approximately related to each other by

$$L \approx 2W \ . \tag{7.36}$$

Using the fault area S and the rupture velocity v_R, [Heaton, 1990] estimates the duration τ_R of the rupture process on the whole fault with

$$\tau_R = \frac{2}{3}\frac{\sqrt{S}}{v_R} \ . \tag{7.37}$$

[Kanamori and Anderson, 1975] estimate the average final slip $[\bar{u}]$ and stress drop $[\bar{\sigma}]$ on the fault by

$$[\bar{u}] = \frac{M_0}{\mu LW} \ , \tag{7.38}$$

$$[\bar{\sigma}] = \frac{2}{\pi}\mu\frac{[\bar{u}]}{W} \quad \text{for strike-slip mechanisms, and} \tag{7.39}$$

$$[\bar{\sigma}] = \frac{4(\lambda+\mu)}{\pi(\lambda+2\mu)}\mu\frac{[\bar{u}]}{W} \quad \text{for dip-slip mechanisms} \tag{7.40}$$

where Lame's constants μ and λ represent the rigidity of the fault region.

The simulation of wave radiation of the extended fault due to its rupture requires a discretisation of the fault. Dividing the fault into F_s subfaults, the seismic moment M_0 can be expressed as the sum of all elementary sources M_0^{ij} as

$$M_0 = \sum_{ij=1}^{F_s} M_0^{ij} \ . \tag{7.41}$$

Those elementary moments M_0^{ij} can be derived analogously to Eq. (4.1) from

$$M_0^{ij} = \mu^{ij} S^{ij} [\bar{u}]^{ij} \tag{7.42}$$

where $S^{ij} = (LW)/F_s$ is the area of each subfault, whereas $[\bar{u}]^{ij}$ is the spacial varying final slip at the subfault with indices ij. The fault discretisation, i.e., the size of the subfaults should be related to a constant uniform rupture velocity v_R on the fault by

$$S^{ij} = \left(\frac{v_R}{10 f_{\max,rup}}\right)^2 \ . \tag{7.43}$$

Here, $f_{\max,rup}$ is the maximal frequency of the rupture propagation. The slip velocity in which the slip gets to its final value $[\bar{u}]^{ij}$ can be expressed for the discrete fault by

$$[\dot{\bar{u}}]^{ij}(t) = [\bar{u}]^{ij} s^{ij} \tag{7.44}$$

where s^{ij} is the source-time-function. The source-time-function s^{ij} describes the velocity in which the the final slip $[\bar{u}]^{ij}$ at the fault point with indices ij occurs. In the scope of this work, it is assumed that the slip occurs instantaneous, i.e., the source-time-function is a Dirac delta-function: $s^{ij} = \delta_{ij}$.

7.4.2 Fault rupture model

For a complex distribution of the final slip $[\mathbf{u}]$ on the fault, each discrete fault point is assigned to a different slip value. Since the slip distribution on an earthquake fault cannot be visibly observed, several methods were proposed to achieve a probable distribution of the final slippage in order to synthesise realistic ground motion.

Whereas the low frequencies and wavenumbers of body-waves radiated from seismic sources can be related to the causing seismic moment M_0, the high frequencies and wavenumbers are usually characterised by a power law of the decay of its spectral amplitudes at frequencies greater than the cutoff frequency (see Sec. 4.2.3). The classical approach, introduced by [Aki, 1967], is the ω^{-2}-model which adopts a ω^{-2} decay at high frequencies. The apparent stochastic nature of the phase at high frequencies was utilised in a number of methods proposed for synthesising seismograms. Whereas some of those methods do not consider the details of the physical origin of the radiated waves, e.g., [Boore, 2003], other methods involve kinematic models of finite faults with some random rupture process coupled with empirical Green's functions, e.g., [Papageorgiou and Aki, 1983]. Those methods present some difficulties to match the spectral amplitude decay.

The works of [Andrews, 1981; Frankel, 1991; Herrero and Bernard, 1994] and others state that the spectra are related to a self-similar distribution of the final slip $[u]$ and the stress-drop $[\sigma]$ on the fault. Assuming a constant rupture velocity v_R, those distributions follow a negative power law of the radial wavenumber k.

k^{-2}-model: In this work, the deterministic-stochastic k^{-2}-model of [Herrero and Bernard, 1994] is used. This model describes the final slip distribution on the fault by the inverse 2D Fourier transform of the complex function

$$[u](k_x,k_z) = \frac{const.}{1+(k/k_c)^2}\, e^{i\Phi(k_x,k_z)} \,. \tag{7.45}$$

In Eq. (7.45), k_x and k_z are the radial wavenumbers in the two fault directions, $k = \sqrt{k_x^2+k_z^2}$, and k_c is a cutoff wave number, which corresponds to the minimum fault dimensions, i.e., $k_{cx} = 1/L$ and $k_{cz} = 1/W$. The phase angle $\Phi(k_x,k_z)$ is chosen randomly for wave numbers $k > k_c$. The constant in the numerator of Eq. (7.45) is evaluated that way that the whole slip distribution on the fault leads to a desired seismic moment M_0. The k^{-2}-model was used and validated by, e.g., [Klinc *et al.*, 2004; Gallovic and Brokesová, 2004; Emolo *et al.*, 2004; Zollo *et al.*, 1997].

To avoid sharp slip transitions at the edges of the fault and negative slip values, a technique developed by [Klin and Priolo, 2006] from the *Istituto Nazionale di Oceanografia e di Geofisica Sperimentale* is applied. In this technique, the slip distribution gained from the k^{-2}-model is added by its lowest negative value to ensure positive slip values $[u]$. Accordingly, the distribution is shifted on the fault to avoid the mentioned sharp slip transitions. An example of a final slip distribution on a seismic fault derived by the above described procedures is shown in Fig. 7.4.

Time-dependent behaviour: The k^{-2}-model describes the distribution of the final slip on the fault, but not the dynamic properties of the seismic rupture process. The dynamic effects are considered by the rupture velocity v_R, the propagation direction of the rupture on the fault and the rise time t_r. It is assumed that heterogeneities in the slip distribution produce a dominant effect on the far-field seismic radiation with respect to irregularities in the shape of the rupture front. [Zollo *et al.*, 1997] state this assumption to be reasonable when the rupture velocity v_R is smoothly, i.e., not highly discontinuous variable along the fault. Following this assumption the rupture velocity v_R is set to a constant value. v_R which usually varies between $0.6c_S$ and $0.85c_S$, is set to 80% of the local shear wave velocity c_S

$$v_R = 0.8c_S \,. \tag{7.46}$$

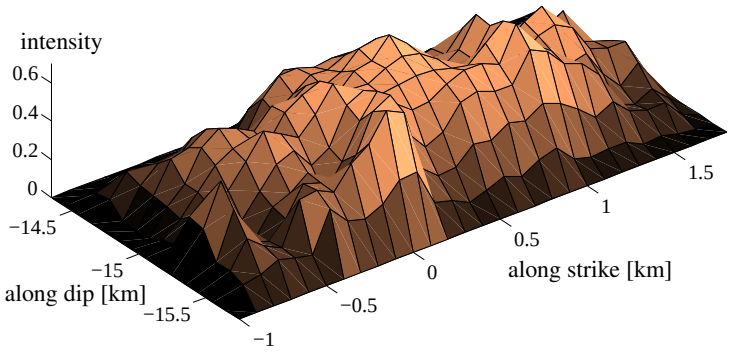

Figure 7.4: Final slip distribution on a seismic fault generated by the deterministic-stochastic k^{-2}-model. The distribution was treated by the technique of [Klin and Priolo, 2006].

The rupture is assumed to radiate in circles from a nucleation point on the fault. This rupture nucleation point, where the circular rupture fronts are initiated, is chosen randomly, with the restriction not to be at a point with a zero final slip. When the rupture front arrives at a fault point it is supposed that the final slip at this point is appears immediately, so that the rise time is zero. This instantaneous slip occurrence was established above by assigning the source-time-function to be a Dirac delta-function $s^{ij} = \delta_{ij}$.

7.5 Multi-method approach

Summarising, an overview of the advanced approach, introduced in this chapter, is given. This multi-method approach applies seismic excitation to an extended near-field by incorporating different methods on basis of the DRM. Those methods are the DWFEM, the k^{-2}-rupture-model, the FEM, and the SBFEM. The derivation and the details of those methods are addressed in previous chapters and sections. In this section it should be just repeated that the DRM is a two-step method, i.e., the analysis of the overall problem is subdivided into two parts.

The two steps are sketched in Fig. 7.5. In the first step (Fig. 7.5(a)), a large scale simulation is performed in order to determine the seismic motion at the boundaries of the near-field. The large scale model embraces the seismic source, modelled as finite fault, and the region of interest without the structure. Hence, the free-field ground motion is gained in this first step. The propagation path of the seismic waves is modelled as vertically stratified half-space. In this half-space, the wave propagation is simulated by means of numerical Green's functions which are constructed with the DWFEM (Sec. 7.3). The rupture process as well as the complex slip distribution on the finite seismic fault is described by the k^{-2}-model (Sec. 7.4).

In the second step of the multi-method approach which is sketched in Fig. 7.5(b), the near-field containing the extended structure, e.g., a buried lifeline, is considered. The dynamic behaviour of the structure and the surrounding soil is modelled by the FEM (Chap. 5). The free-field ground motion which was determined in the first simulation step at the near-field boundaries is transformed to forces. Those forces act at the boundaries of the near-field and induce the same seismic motion in the near-field as the seismic source would do. Hence, those forces are called equivalent forces to the initial excitation at the earthquake fault. Due to the structure that is introduced in the second simulation step, and due to the different approximations in the different numerical methods used in the multi-method approach, scattering waves arrive at the boundaries of the near-field. To absorb those waves, the SBFEM (Chap. 6) is also incorporated into the multi-method approach to model the far-field and permit the waves to travel to infinity without reflections.

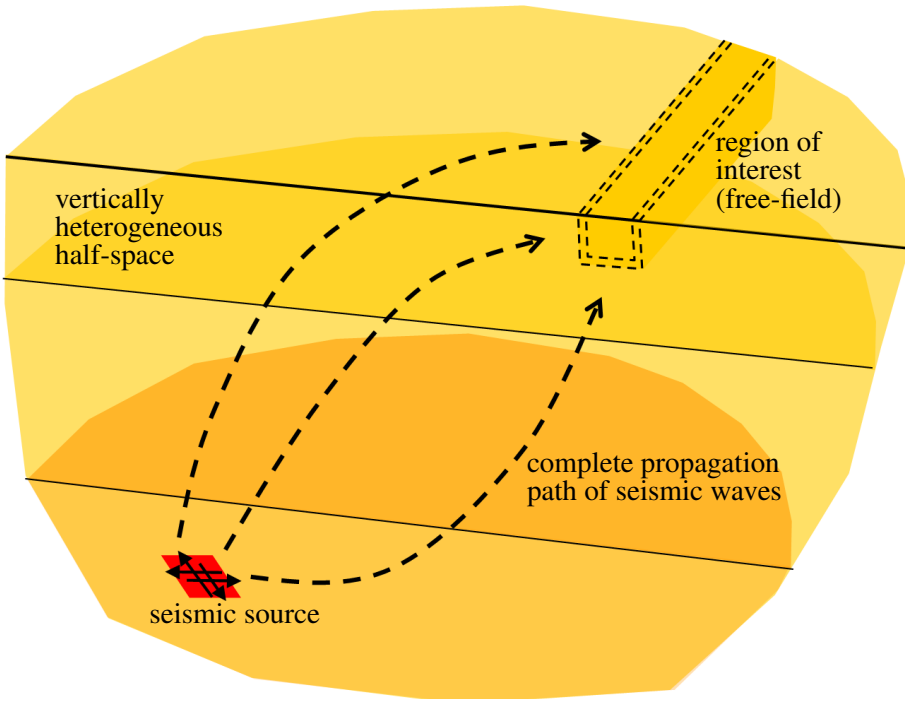

(a) Step I: Large scale analysis which includes the earthquake source, the seismic wave propagation path and the region of interest as free field. The methods used are the DWFEM (Sec. 7.3) and k^{-2}-model (Sec. 7.4).

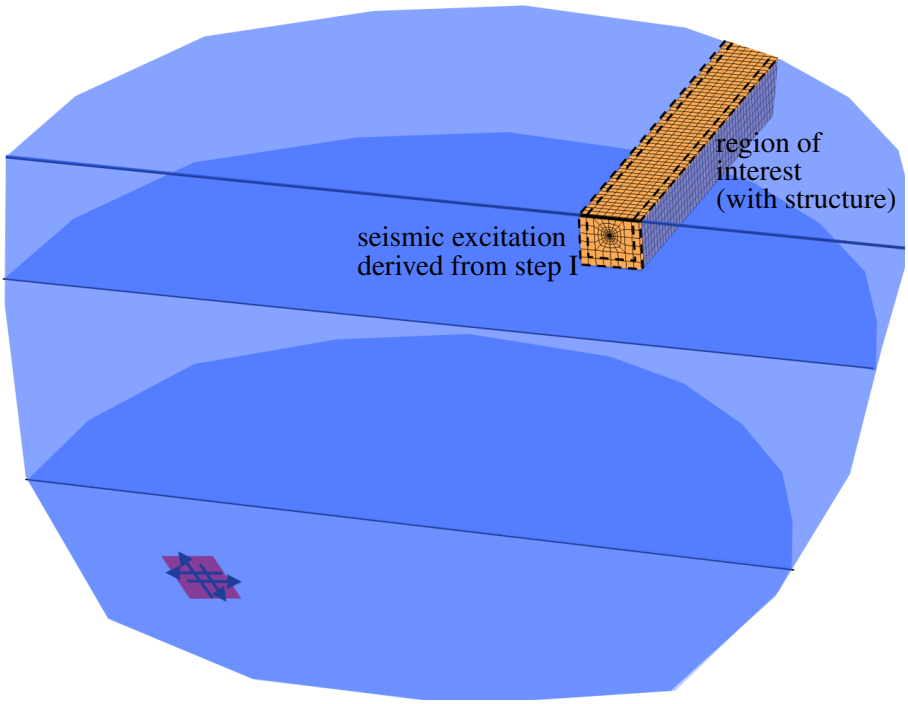

(b) Step II: Near-field analysis which includes the structure in the region of interest. The region is excited by forces, equivalent to the seismic source, derived from step 1. The methods used are the FEM (Chap. 5) and the SBFEM (Chap. 6).

Figure 7.5: The two steps of simulating seismic wave propagation in the region of interest, following the DRM (Sec. 7.2).

8 Probabilistic determination of failure

In order to examine the damage risk of buried lifelines exposed to seismic wave propagation effects, it is essential not only to determine the dynamic response of the structure-soil system but, moreover, to define quantitative terms of failure. Even though, at first, this failure might be derived in a deterministic way, it is obvious from the definition of risk in Eq. (1.1) that it is necessary to analyse it from a stochastic point of view in order to determine the failure probability P_f of the lifeline.

Since the resistance of structures relies on the strains and stresses induced by a certain loading, their determination is addressed at first. This is done in the context of the FEM, which is used to model the pipeline and its surrounding soil. Hereafter, the failure criteria of underground pipelines are treated which are incorporated in the present work. So, quantities for deterministic failures are achieved.

In this work, an efficient concept to determine the failure probability of seismic endangered structures of large extensions is introduced. Therefore, the deterministic failure quantities of buried lifelines are used in order to determine their failure probability. The concept employs a probabilistic method named point estimate method (PEM) which was first introduced by [Rosenblueth, 1975]. Thus, this method is discussed, whereupon the details of the probabilistic concept are addressed.

8.1 Computation of strains and stresses

To achieve a quantity for the failure of a seismic excited buried pipeline, it is necessary to compute the critical strains and stresses in the wall of the pipe. In this work, the FEM, described in Chap. 5, is used to determine the dynamic near-field response of the structure-soil system. As can be realised from the equation of motion Eq. (5.19), the displacements and its derivatives are the direct output from a FEM simulation. The strains and stresses are not computed explicitly. Nevertheless, they are used in the derivation of the FEM and, thus, can be calculated in a successive step after the actual computation.

The strains in finite element can be determined directly from the strain-displacement relationship from Eq. (5.10). In linear elasticity, the constitutive equation Eq. (5.3) relates the element strains to the element stresses by means of the elasticity matrix $\mathbf{E}$. So, the stress vector $\boldsymbol{\sigma}$ of an element can be computed by

$$\boldsymbol{\sigma}^{(e)} = \mathbf{EDN}\tilde{\mathbf{u}} \,. \tag{8.1}$$

The vector $\boldsymbol{\sigma}^{(e)}$ contains the stress components of the element coordinate system. For the determination of the failure, it is necessary to determine the principal and the comparison stresses. When the stress components are inserted in the stress tensor $\mathbf{S}$, the principal stresses $\boldsymbol{\sigma}^P$ are the solutions of the equation

$$\det(\mathbf{S} - \boldsymbol{\sigma}^P \cdot \mathbf{I}) = 0 \tag{8.2}$$

where $\mathbf{I}$ is the unit matrix. After obtaining the principal stresses $\boldsymbol{\sigma}_n^P = [\sigma_n^{\mathrm{I}}, \sigma_n^{\mathrm{II}}, \sigma_n^{\mathrm{III}}]^T$ at point n, a criterion for the failure of the material is needed.

Material failure: In this work, the *von Mises criterion* is incorporated. This criterion is based on the *Tresca criterion*

$$\sigma_n^{\mathrm{Tresca}} = \max\left(|\sigma_n^{\mathrm{I}} - \sigma_n^{\mathrm{II}}|; |\sigma_n^{\mathrm{II}} - \sigma_n^{\mathrm{III}}|; |\sigma_n^{\mathrm{III}} - \sigma_n^{\mathrm{I}}|\right) \tag{8.3}$$

but takes into account the assumption that hydrostatic stresses do not contribute to material failure. The *von Mises comparison stress* is defined as an effective stress under uniaxial loading, subtracting the hydrostatic stresses. Further, it is claimed that all effective stresses greater than the stress which causes material failure in uniaxial loading will result in plastic deformation. The von Mises stress is most applicable to ductile materials, like steel. So, the von Mises stress σ_n^{Mises} at point n can be computed with

$$\sigma_n^{\text{Mises}} = \sqrt{\frac{(\sigma_n^{\text{I}} - \sigma_n^{\text{II}})^2 + (\sigma_n^{\text{II}} - \sigma_n^{\text{III}})^2 + (\sigma_n^{\text{III}} - \sigma_n^{\text{I}})^2}{2}} \,. \tag{8.4}$$

The pipeline is mapped by two-dimensional shell-elements. Hence, only two principal stresses exist and, thus, the von Mises stress simplifies under plane stress considerations to

$$\sigma_n^{\text{Mises}} = \sqrt{\frac{\sigma_n^{\text{II}2} + \sigma_n^{\text{I}\,2} - \sigma_n^{\text{I}}\sigma_n^{\text{II}}}{2}} \,. \tag{8.5}$$

After the derivation of strains and stresses, their critical values for buried lifelines have to be defined.

8.2 Failure criteria

Generally, two types of pipelines exist: *continuous pipelines* and *segmented pipelines*. Depending on this classification, the pipelines exhibit a different dynamic response behaviour and, thus, different failure modes can be specified.

8.2.1 Continuous pipelines

Continuous pipelines were broadly examined and their failures were associated with four effects, as stated by, e.g., [European Committee for Standarization (CEN), 1998; Moser, 2001; O'Rourke, 1995; O'Rourke and Liu, 1999; Newmark and Hall, 1975; Ramberg and Osgood, 1943; Hall and Newmark, 1978]. These effects are local buckling, the exceedance of a allowable tensile stress, the exceedance of an allowable tensile strain, and the exceedance of an allowable maximum swing velocity. The four failure modes lead to the following criteria:

- **Local buckling:** Laboratory tests performed by [Hall and Newmark, 1978] indicate that compressional wrinkling in a pipe begins at a strain of one third to one fourth of the theoretical value

  $$\varepsilon_{p,\text{theo}} = 0.6\frac{t_p}{r_p} \tag{8.6}$$

  where t_p is the thickness of the pipe wall and r_p the pipe radius. Hence, the criterion for local buckling is defined as

  $$\varepsilon_p \leq 0.175\frac{t_p}{r_p} = 0.175\frac{2t_p}{d_p} \,, \tag{8.7}$$

  where ε_p is the existent pressure strain and d_p the pipe diameter.

- **Tensile stress:** Amongst others, [O'Rourke, 1995] requires the tensile stress not to exceed 85% of the yield stress:

  $$\sigma_t \leq 0.85 f_y \,, \tag{8.8}$$

  with σ_t being the existent tensile stress and f_y the yield stress. For the analyses of the stresses performed in Part III of this work, the von Mises criterion is incorporated

  $$\sigma^{\text{Mises}} \leq f_y \,. \tag{8.9}$$

- **Tensile strain:** The tensile strain is required not to ε_t exceed an allowed strain $\varepsilon_{t,\mathrm{lim}}$ as it is, e.g., defined in [Hall and Newmark, 1978].

$$\varepsilon_t \leq \varepsilon_{t,\mathrm{lim}} \,. \tag{8.10}$$

- **Swing velocity:** In [Deutsches Institut für Normung, 1999], the occurrence of a failure is also expected when a maximum swing velocity v is exceeded:

$$v \leq 0.10\mathrm{m/s} \,. \tag{8.11}$$

Whereas the first three criteria are independent of each other the fourth criterion is not autonomous. Therefore, only the first three criteria are incorporated in this work.

8.2.2 Segmented pipelines

Segmented pipelines fail due to different criteria as continuous pipelines. This is due to the fact that segmented pipelines imply weak points which are the joints. Hence, buckling as a reason for the failure of a segmented pipeline is nearly completely excluded, because a failure of the joint would occur before. The failure modes for segmented pipelines are the axial pull-out at the joints [Elhmadi and O'Rourke, 1989], the crushing of bell and spigot joints [Ayala *et al.*, 1990] and the circumferential failure and joint rotation [Elhmadi and O'Rourke, 1989]. Additionally, the limits of the stresses in the segments have not to be exceeded.

- **Relative axial joint displacements:** The relative axial displacements Δu_j^t at the joints are limited for axial-pull out to the half of the joint depth d_j:

$$\Delta u_j^t \leq 0.5 d_j \,. \tag{8.12}$$

  The maximum compression $\Delta u_{\mathrm{ult}}^p$ of the joints is limited to

$$\Delta u_j^p \leq \Delta u_{\mathrm{ult}}^p \,. \tag{8.13}$$

- **Relative axial joint rotation:** The relative rotation Θ_j at the joints is limited to a limit value

$$\Theta_j \leq 1.1\Theta_{\mathrm{lim}} \tag{8.14}$$

  where Θ_{lim} is the maximum allowable angular offset recommended by the manufacturer.

- **Tensile stress:** The tensile stress σ_t must not extend the yield stress f_y

$$\sigma_t \leq f_y \,. \tag{8.15}$$

- **Pressure stress:** The pressure stress σ_p has to be lower than a limit stress $\sigma_{p,\mathrm{lim}}$

$$\sigma_p \leq \sigma_{p,\mathrm{lim}} \,. \tag{8.16}$$

- **Swing velocity:** The maximum swing velocity is defined by [Deutsches Institut für Normung, 1999]:

$$v \leq 0.08\mathrm{m/s} \,. \tag{8.17}$$

Also for segmented pipeline, the swing velocity criterion is not incorporated in the analyses performed in Part III.

8.3 Probabilistic treatment

An important feature in risk analyses is the probabilistic concept, because risk is not depending on the deterministic failure of a structure, but on its failure probability (see Eq. (1.1)). Many probabilistic methods, like the widespread Monte Carlo method (see, e.g., [Warner and Kabaila, 1968]), request a large number of deterministic calculations with random input variables to receive a probability distribution of the output values from which the failure probability can be deduced. In this work, the deterministic multi-method approach described in Sec. 7.5 is used to simulate the dynamic behaviour of the pipeline under earthquake excitation. Since this hybrid model is three-dimensional and the simulation is performed in time-domain, the computation is indeed more exact, but also more expensive than simpler approaches. Due to the relatively long computational time needed for this exact computational procedure, a large number of calculation runs, as requested for the Monte Carlo simulation, is not reasonable. A probabilistic method that applies to the demands of the tasks of this project, is the point estimate method (PEM) [Rosenblueth, 1975]. The PEM enables the approximation of the probability distribution of the failure value by performing only a few deterministic simulation runs. Before the PEM is explained, a brief review on stochastic moments of probability distributions is given.

8.3.1 Moments of probability distributions

The basic value, to describe a random process in mathematical terms, is the random variable X which exhibits the probability distribution function $f_X(x)$. This function $f_X(x)$ can be represented by the random moments of the probability distribution. The first central moment μ_X of the probability distribution of the random function $f_X(x)$ depending on the random variable X is called the *mean* and is defined by

$$\mu_X = \int x\, f_X(x)\, dx\,. \tag{8.18}$$

Higher-order central moments of $f_X(x)$ of the order m are

$$\mu_{Xm} = \int (x-\mu_X)^m f_X(x)\, dx\,. \tag{8.19}$$

The moment of order $m = 2$ is called *variance* and its square root is the *standard deviation* σ_X. The moment of order $m = 3$ is the *skewness* ν_X of the distribution. Since there exist probability moments of infinitely high orders, the accuracy of the representation of the probability density function by those moments depends on the order up to which the moments are incorporated. Usually, good representational results can already be achieved by using the moments up to order $m = 3$. This representation of the central random moments is incorporated in the PEM.

8.3.2 Point estimate method

The PEM was originally developed by [Rosenblueth, 1975] and improved by several other researchers, e.g., [Hong, 1998; Schweiger *et al.*, 2001; Christian, 2004]. An extended discussion of the PEM and its numerous formulations can be found in [Baecher and Christian, 2003]. The procedure, that is common to all point estimate methods, is briefly described.

The PEM is a method for numerically approximating the low-order moments, like mean, standard deviation, skewness, of functions of random variables. Its derivation starts with the introduction of a second random variable Y which is a deterministic function of X:

$$Y = g(X)\,. \tag{8.20}$$

It is assumed that $g(X)$ is well-behaved and that the mth order moments of $f_X(x)$ exist. The PEM aims to answer the question how the low-order moments of $f_Y(y)$ can be approximated by using only

the low-order moments of $f_X(x)$ and the deterministic function $g(X)$. [Rosenblueth, 1975] approached this question by discretising the continuous random variable X such that the discrete probability mass function $p_X(x)$ has the same moments of order m as $f_X(x)$. Then, the discrete probability mass function $p_X(x)$ is transformed by means of Eq. (8.20), i.e., $p_Y(y) = g(p_X(x))$, so that the random moments of the continuous probability density function $f_Y(y)$ of the variable Y can be determined from $p_Y(y)$

$$\mu_{Ym} = \int (y-\mu_Y)^m f_Y(y)\, dy = \sum (y-\mu_Y)^m p_Y(y)\ . \tag{8.21}$$

In its original appearance by [Rosenblueth, 1975], only random moments of orders not higher than $m = 3$ are considered and the low-order moments are evaluated at two points. The evaluation of Y at those two defined points and the determination of the corresponding weights, yields the approximative expected value of Y raised to the power of m,

$$E(Y^m) \approx P_1 y_1^m + P_2 y_2^m\ , \tag{8.22}$$

which is related to the central moment μ_{Ym} of order m. The conversation between the expected value and the central moment is for the first three moments

$$\mu_Y = E(Y)\ \ ,\ \sigma_Y^2 = E(Y^2) - \mu_Y^2\ \ ,\ \nu_Y = \frac{E(Y^3)}{\sigma_Y^3}\ . \tag{8.23}$$

In Eq. (8.22) for two points $p = 1,2$, y_p is the value of Y evaluated at a point x_p, i.e., $y_p = g(x_p)$, and P_p is the weight at point p. Both, the determination of the evaluated points and the determination of the weights depend, in general, on the chosen form of the PEM.

This approach of approximating complicated functions by a series of simpler functions is the same as, e.g., performed in numerical quadrature procedures. Especially the Gaussian quadrature which is widely known and used, e.g., in the FEM, is concerned with choosing optimal values of coordinates, where integrands have to be evaluated, and their corresponding weights. In fact, [Christian and Baecher, 1999] shows that Rosenblueth's PEM is a special case of Gaussian quadrature and that it can be easily transferred to more general distributions of random variables than referred to in the original paper.

In the original formulation of the PEM, three cases are considered. The first case deals with a function Y of one variable X whose mean, variance and skewness are known. The second case considers the same function but X has now a symmetrical and approximate Gaussian probability distribution. The third case regards Y being a function of N variables $X_1, X_2, ..., X_N$ whose distributions are symmetric and which may be correlated. The first case is the basis for the probabilistic treatment performed in this work.

Random variables X with mean μ_X, standard deviation σ_X, and skewness v_X: In the first case, four conditions have to be satisfied to model the low-order moments of X accurately. Those conditions are

$$P_1 + P_2 = 1\ , \tag{8.24}$$

$$P_1 x_1 + P_2 x_2 = \mu_X\ , \tag{8.25}$$

$$P_1 (x_1 - \mu_X)^2 + P_2 (x_2 - \mu_X)^2 = \sigma_X^2 \quad \text{and} \tag{8.26}$$

$$P_1 (x_1 - \mu_X)^3 + P_2 (x_2 - \mu_X)^3 = \nu_X \sigma_X^3\ . \tag{8.27}$$

From those four conditions, the points x_1 and x_2 can be calculated from

$$x_1 = \mu_X + \sigma_X \left(\frac{\nu_X}{2} - \sqrt{N + \left(\frac{\nu_X}{2}\right)^2} \right) \quad \text{and} \tag{8.28}$$

$$x_2 = \mu_X + \sigma_X \left(\frac{\nu_X}{2} + \sqrt{N + \left(\frac{\nu_X}{2}\right)^2} \right)\ , \tag{8.29}$$

whereas the associated weights are

$$P_1 = \frac{1}{2}\left(1 + \frac{\nu_X}{2}\frac{1}{\sqrt{N + \left(\frac{\nu_X}{2}\right)^2}}\right) \quad \text{and} \tag{8.30}$$

$$P_2 = \frac{1}{2}\left(1 - \frac{\nu_X}{2}\frac{1}{\sqrt{N + \left(\frac{\nu_X}{2}\right)^2}}\right) . \tag{8.31}$$

In Rosenblueth's original notation, only one random variable X is considered ($N = 1$). [Hong, 1998] developed an extension of this case for multiple, uncorrelated and skewed variables. The formulas for determining the evaluation points and their corresponding weights Eqs. (8.28) to (8.31) remain the same as for one variable, only N is set to the number of random variables $X_1, X_2, ..., X_N$. In the PEM suggested by [Hong, 1998], for every computation run, all variables X_n (except the one under consideration which is evaluated at one of its evaluation points) are held at their mean. For example, the operation for the first random variable X_1 at the first evaluation point is performed by

$$y_{1,1} = g(x_{11}, \mu_{X_2}, \mu_{X_3}, ..., \mu_{X_N}) . \tag{8.32}$$

The result is then multiplied with the corresponding weight P_{11}. This is done for all $2N$ evaluation points, so that expected value of Y raised to the power of m (and hence the random moment μ_{Ym}) can be derived from

$$E(Y^m) \approx \sum_{n=1}^{N} P_{1n} y_{1n}^m + P_{2n} y_{2n}^m . \tag{8.33}$$

Even though the PEM is a stable, computational inexpensive and accurate probabilistic method it becomes unfunctional for a large number of random variables. Being aware of this fact, sensitivity analyses can be performed before the application of the PEM, like done in, e.g., [Schweiger *et al.*, 2001]. Those analyses can be executed, e.g., by means of a Taylor-Series-Finite-Difference analysis [Benjamin and Cornell, 1970]. Moreover, [Christian and Baecher, 2002] give an overview over the special PEMs developed for large number of random variables.

8.4 Probabilistic concept of failure determination

On the basis of the before described procedure, the probabilistic concept used in this work for determining the probabilistic failure of buried lifelines due to seismic wave propagation effects should be outlined.

As explained, the PEM used here, regards an output variable Y which depends on N randomly distributed input variables $X_1, X_2, ..., X_N$. Input and output are related through the deterministic function $g()$:

$$Y = g(X_1, X_2, ..., X_N) . \tag{8.34}$$

In the present work, the deterministic function $g()$ is the entire multi-method procedure described in Sec. 7.5. Hence, the input variables summarise, in general, all input that is needed to perform the multi-method procedure. Although it can be assumed that all of those input variables are somehow randomly distributed, it is reasonable to regard only a few of them with the strongest influence on the solution as random variables and the rest of them as deterministically set. Which of the input variables are assumed as random variables $X_1, X_2, ..., X_n$ depends on the particular application.

The output variable Y is, at least for continuous pipelines, either the stress or the strain in the wall of the pipeline (see Sec. 8.2.1). For segmented pipelines, also the relative motion at the pipe joints can be additionally treated as output variable (see Sec. 8.2.2). For those output variables Y, the low-order moments μ_{Ym} can be approximated by the PEM. The probability mass distribution of Y can be derived by means of those moments, so that the failure probability P_f is finally achieved.

Steps of probabilistic concept: The steps of the probabilistic procedure, which is imposed on the deterministic one, are the following. An example for the application of the probabilistic treatment is presented in Sec. 10.7.

1. Identify the N variables which are considered as randomly distributed $X_1, X_2, ..., X_N$.
2. Assign a probability density function $f_{X_n}(x_n)$ to every variable X_n.
3. Determine the low-order moments $\mu_{X_n}, \sigma_{X_n}, \nu_{X_n}$ of each random variable X_n from Eq. (8.18) or (8.19), respectively.
4. Calculate the evaluation points x_{1n} and x_{2n} of each variable X_n from Eqs. (8.28) and (8.29).
5. Calculate the corresponding weights P_{1n} and P_{2n} for each variable X_n from Eqs. (8.30) and (8.31).
6. Execute the entire multi-method procedure for each evaluation point, i.e., perform $2N$ deterministic computational runs. When the computation at the evaluation point x_{pn} of variable X_n is performed, all other $N-1$ variables are held to their mean. The result of each deterministic simulation is y_{pn}.
7. Approximate the low-order random moments μ_Y, σ_Y, ν_Y from Eq. (8.33) incorporating the results of the deterministic simulation y_{pn} and the corresponding weights P_{pn}.
8. From the random moments, the discrete probability mass function $p_Y(y)$ is achieved in order to determine the probability of failure P_f.

As completion of this part of the work, the position of the probabilistic concept in the entire developed methodology is recapitulative sketched in Fig. 8.1.

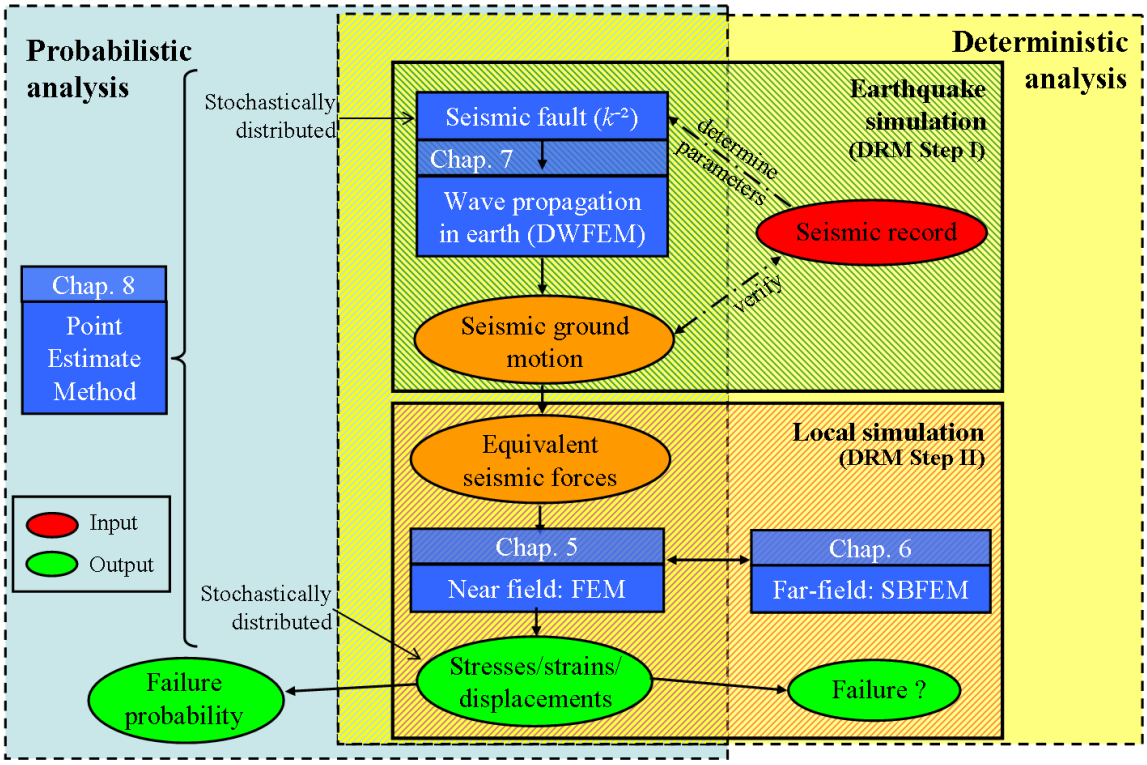

Figure 8.1: Schematic sketch of the methodology developed in this part of the work. The probabilistic analysis which is coloured in blue is based on the deterministic multi-method approach which is coloured in yellow.

Part III

Application

9 Studies of computational aspects

This and the subsequent chapter aim to present the applicability of the before introduced methodology of analysing the damage risk of buried lifelines under seismic wave propagation effects. The focus in this chapter is laid on the studies of computational aspects. Since the introduced methodology is a multi-method approach and each incorporated method exhibits its own characteristics, the studies of the computational aspects are separated after the methods.

The computer codes used for the studies in this and the subsequent chapter should be mentioned. For the generation of the seismic motion by means of a large scale simulation the code COMPSYN from [Spudich and Xu, 2003] is used. The BEM simulation was performed with a code developed at the *Institute of Applied Mechanics of the Technical University of Braunschweig* [Schanz, 2001]. The computation of the influence matrices was performed by the slightly modified program SIMILAR developed by [Wolf and Song, 1996]. The simulations incorporating the hybrid FE-SBFEM were executed by a code named kwikE which was developed under contributions of the author at the *Institute of Applied Mechanics* [Borsutzky and Lehmann, 2006b].

9.1 Wave radiation in the far-field via SBFEM

The SBFEM is a rigorous method to model the wave propagation in the far-field, e.g., in dynamic soil-structure analyses. Its derivation was extensively discussed in Chap. 6. In this work, the SBFEM is coupled with the FEM which is used to simulated the response of the near-field. In Sec. 6.7, it was announced that by dividing the entire far-field into substructures, which can be analysed separately at first and combined afterwards, a higher efficiency of the hybrid FE-SBFEM can be achieved. On the other hand, the SBFEM looses some of its rigorosity by substructuring the far-field. To show the potential of the substructure method still to give good results, i.e., to enable the wave radiation to infinity without reflections at the near-field/far-field interface, studies are performed in this section. Therefore, the dynamic response of a near-field/far-field soil domain excited by a transient force is simulated by the hybrid FE-SBFEM.

The near-field is mapped by a block-shaped FE model as shown in Fig. 9.1(a), where the soil is represented by eight node hexaedral brick FEs. On the boundaries at the side and at the bottom, two-dimensional SBFEs featuring the same boundary nodes as the FEs are coupled to those nodes. The SBFE mesh is depicted in Fig. 9.1(b). Both, near-field and far-field, have the soil material parameters $E_s = 272$ MN/m^2, $\nu_s = 0.45$ and $\rho_s = 1947$ kg/m^3.

Computation of $\mathbf{M}^\infty$: As explained before, when applying the SBFEM, unit impulse influence matrices $\mathbf{M}^\infty$, computed for every time-step, describe the response behaviour of the far-field. This computation can be performed before the actual simulation of the coupled FE-SBFE model in which Eq. (6.74) is solved. Thus, initially, the influence matrices $\mathbf{M}^\infty$ for different numbers of substructures should be analysed. Three different constellations are modelled: in the first, the far-field is mapped with only one SBFEM structure, in the second, two SBFEM substructures are incorporated, and in the third, four substructures are used. The constellation with four substructures and their interfaces between those substructures is shown in Fig. 9.1(b). For the second case when analysing two substructures, the entire SBFE

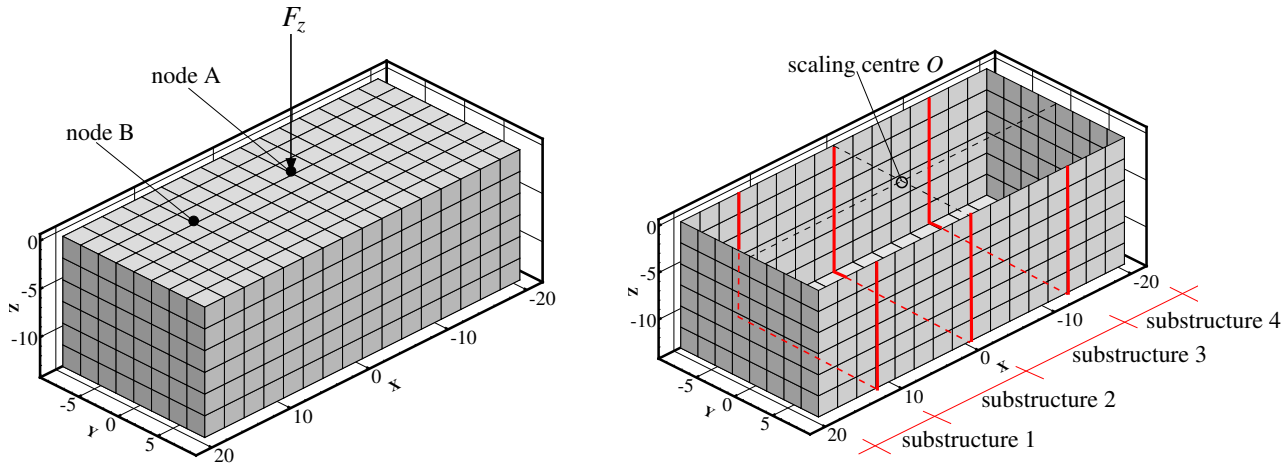

(a) FE mesh used to model the near-field soil. Nodes A and B are marked. The transient force applies at node A, whereas the induced motion is evaluated at both nodes.

(b) SBFE mesh used to model the far-field soil. The scaling centre O is depicted. Further, the interfaces between the four substructures are marked by red lines.

Figure 9.1: Meshes of FEM and SBFEM model which are combined in the hybrid FE-SBFE scheme to model near- and far-field.

domain is bisected, so that the interface between the two substructures is the middle one in Fig. 9.1(b). The computational parameters for the three constellations are listed in Tab. 9.1.

Table 9.1: Parameters for hybrid FE-SBFE computation.

FEM		SBFEM			time		
nodes	elements	N_S	nodes	elements	steps	$t_{\max}$ [s]	Δt [s]
1536	2079	1	441	416	20000	5.0	$2.5 \cdot 10^{-4}$
		2	231/231	208/208			
		4	126/126/126/126	108/100/100/108			

The discrete time-step Δt is a limiting factor for the transient calculations. Computational experience has shown that the SBFE simulations behave numerical stable when the time-step Δt is not exceeding the value given in Eq. (9.2). For comparison, Eq. (9.1) gives a maximum limit of the time-step in FE and FE-SBFE calculations, respectively (compare Eq. (7.31)).

$$\Delta t \leq \frac{l_e}{6 \cdot c_P} \qquad \text{(FEM)} \tag{9.1}$$

$$\Delta t \leq \frac{r_0}{30 \cdot c_P} \qquad \text{(SBFEM)} \tag{9.2}$$

From these equations it becomes clear that the two numerical methods require different optimal time-steps Δt depending on the P-wave velocity c_P. Whereas the FEM time-step is influenced by the smallest finite element length l_e, the SBFEM time-step depends on the distance r_0 between the scaling centre O and the closest SBFE node.

In Tab. 9.1, the time-steps correspond to the hybrid FE-SBFE computation, whereas the time-step width Δt is used also for the computation of the unit impulse influence matrix $\mathbf{M}^\infty$ of the SBFEM. For the computation of $\mathbf{M}^\infty$, the reduction of non-locality in time is used, as addressed in Sec. 6.6.1. Thereby, the linear development of the matrix entries in $\mathbf{M}^\infty$ is used to extrapolate the entries of later time-steps. So, the matrices $\mathbf{M}^\infty$ have just to be computed until this linear behaviour can be observed. With a tolerance

of ε_t=1.$\cdot 10^{-5}$, the matrix entries of one substructure exhibit this linear behaviour from time-step 200 on, whereas the substructures for $N_S = 2,4$ provide it from time-step 225 on.

The non-locality in space described in Sec. 6.6.2 is used here as well. In Fig. 9.2, the non-zero elements of the influence matrix $\mathbf{M}^{\infty}$ at time-station t_n=2.5$\cdot 10^{-3}$s are depicted. An entry is marked as black dot if its value is not zero. The matrices are shown for the three substructure constellations $N_S = 1,2,4$ (three columns) as well as for three different thresholds ε_z under which a value of an entry is set to zero (three rows). Those thresholds are $\varepsilon_z = 10^{-4}, 10^{-3}, 10^{-2}$ and are constant in a row of Fig. 9.2. In the left column of Fig. 9.2, the matrices for one SBFEM structure $N_S = 1$ is shown, exhibiting a strong diagonal banded structure. This is due to the renumbering of the nodes by the Cuthill/McKee algorithm which assigns values of neighbouring nodes also to neighbouring positions in the matrix. The banded structure exhibits that the response of nodes depends mostly on the response of nodes in their vicinity and not on nodes which lie apart. With an increasing threshold for the locality $\varepsilon_z = 10^{-4}$ to 10^{-2} (downward in the left column of Fig. 9.2), it can be realised that this banded structure is thinned out. This means that the entries, which are apart from the diagonal, have small values and, thus, do not have much influence on the solution of the hybrid FE-SBFE model.

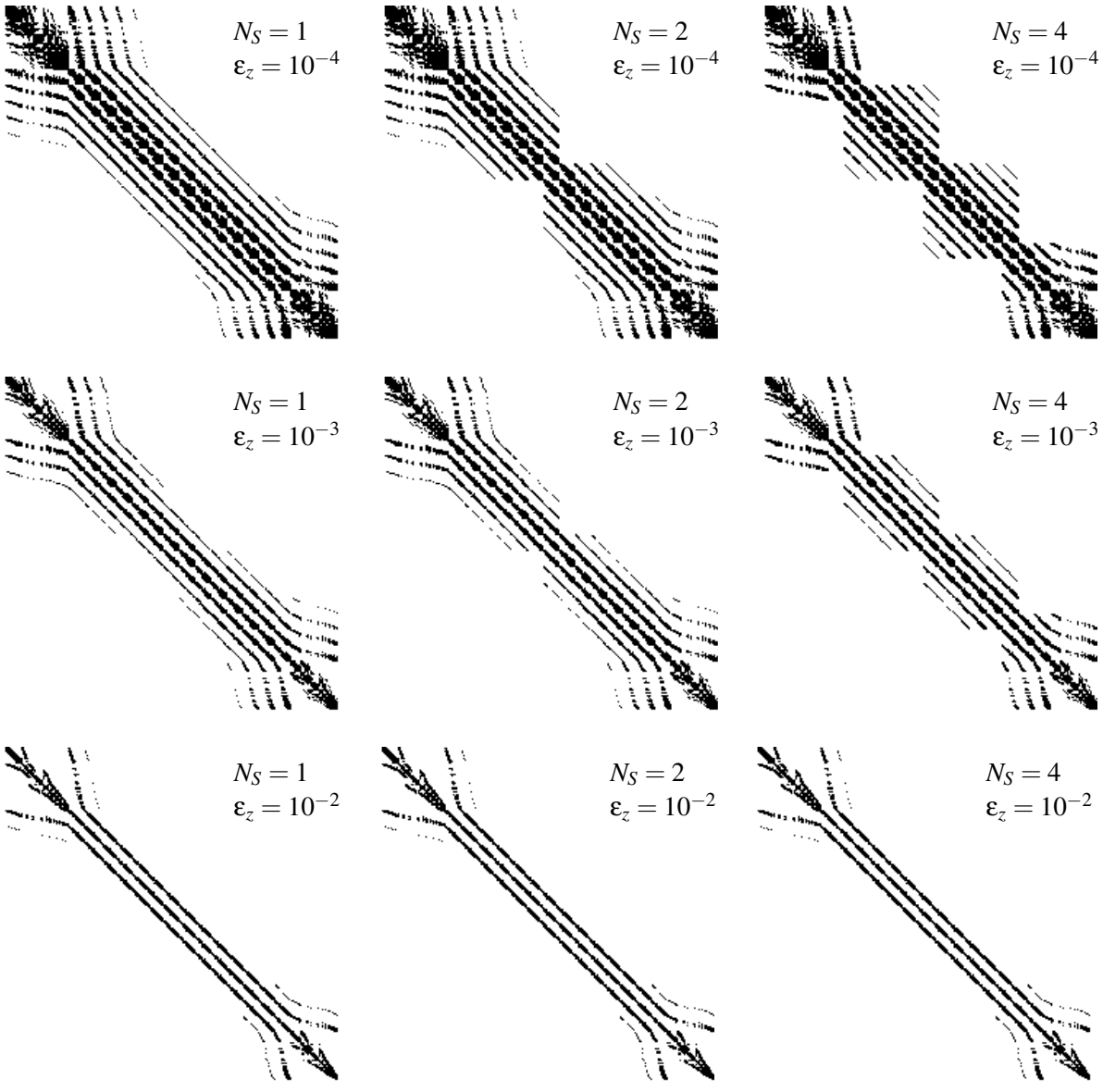

Figure 9.2: Population of the influence matrix $\mathbf{M}^{\infty}(t_n)$ for varying numbers of substructures N_S and zero-element thresholds ε_z at the same time-station t_n.

The columns in the middle and right of Fig. 9.2, show the influence matrices $\mathbf{M}^{\infty}$ composed of two and four substructures, respectively. Considering the first row with the zero-element threshold $\varepsilon_z = 10^{-4}$, the rectangular shape of the $N_S = 2$ and $N_S = 4$ submatrices can be clearly recognised. This implies that the substructure domains are not completely rigorous coupled since the influences of two nodes in two different substructure domains are not considered. But when the zero-element threshold ε_z is increased up to $\varepsilon_z = 10^{-2}$, no evidential difference of the entries of the influence matrices $\mathbf{M}^{\infty}$ can be observed for the three analysed substructure cases $N_S = 1, 2, 4$ (the last row in Fig. 9.2). Consequential, the matrix entries that are neglected by the substructuring, i.e., the differences of the matrices in the first row of Fig. 9.2, are only of low values ($< 10^{-2}$). Thus, those entries do not have much influence on the solution of the hybrid FE-SBFE model. Furthermore, it can be concluded that substructuring is especially useful for long near-field domains since the influence matrices $\mathbf{M}^{\infty}$ of those domains obviously exhibit a distinct banded structure.

Response of FE-SBFE simulation: To approve that the usage of substructuring still leads to good results, the wave radiation of the near-field/far-field domain due to a single transient force is modelled. As depicted in Fig. 9.1(a), this force F_z applies at node A and acts only in z-direction. The temporal progression of its vertical component is shown in Fig. 9.3(a). The hybrid simulation is performed with the parameters listed in Tab. 9.1. For the time-integration, the HHT-α algorithm is used with the three parameters ($\alpha;\beta;\gamma$)=(-0.3333;0.4444;0.8333).

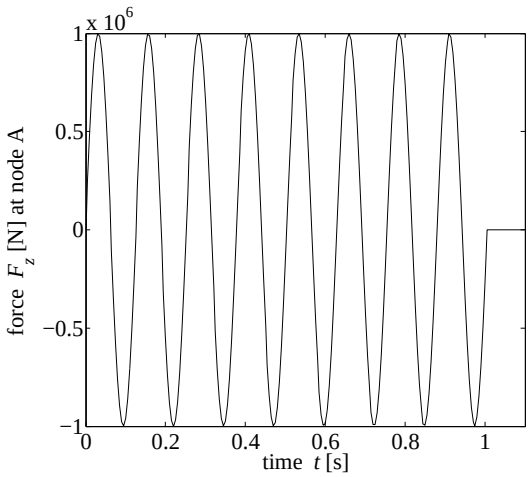

(a) Temporal progression of the vertical component of the sinusoidal force F_z applied at node A.

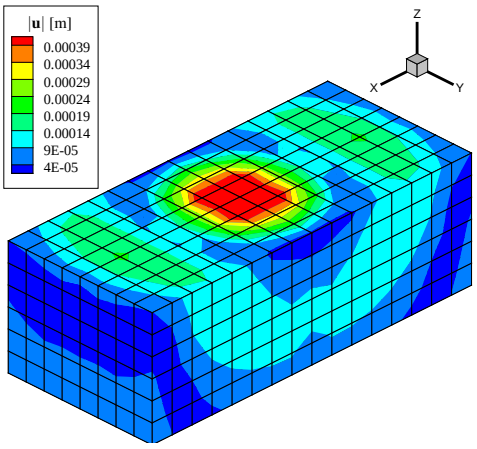

(b) Contour plot of the displacements of the FE mesh at time-step $t = 1.0$s where the SBFEM domain is modelled as one structure. The hemispherical propagation of the waves can be recognised ($|\mathbf{u}| = \sqrt{u^2 + v^2 + w^2}$).

Figure 9.3: Transient excitation of the analysed domain and contour plot of the resulting displacements.

At first, the SBFEM domain is modelled as one structure ($N_S = 1$). The contour plot of the resulting displacements of the FE model at time $t = 1.0$s is depicted in Fig. 9.3(b). The expected hemispherical shape of the displacement wave fronts can be recognised. Also, no reflection at the FE mesh boundaries can be observed. Having a closer look on the nodes A and B (see Fig. 9.1(a)), exhibits the vertical displacements shown in grey in Fig. 9.4. It can be realised that in the time-interval in which the sinusoidal force F_z acts, the displacements have also a sine shape but obviously with lower amplitudes at node B. After the transient loading time ($t > 1.0$s), the displacement amplitudes decline to zero at both nodes. This shows that the waves can leave the near-field and are not reflected at the near-field/far-field interface. Hence, the SBFEM enables the wave radiation to infinity and no waves are trapped in the near-field.

Fig. 9.4 also represents the results of the hybrid simulation when substructuring is used in the SBFEM ($N_S = 2, 4$). The resulting displacements of all three constellations agree very good. Also, at the critical

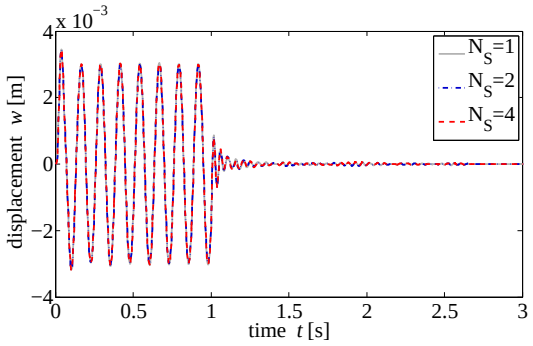

(a) Vertical displacement over time at node A.

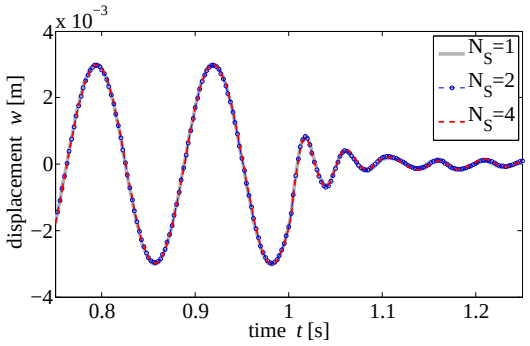

(b) Same as left in the time-interval $t = [0.75s; 1.25s]$.

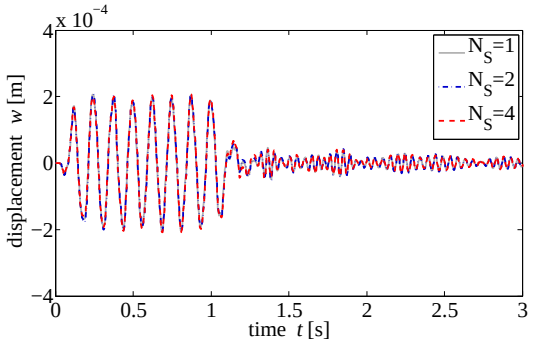

(c) Vertical displacement over time at node B.

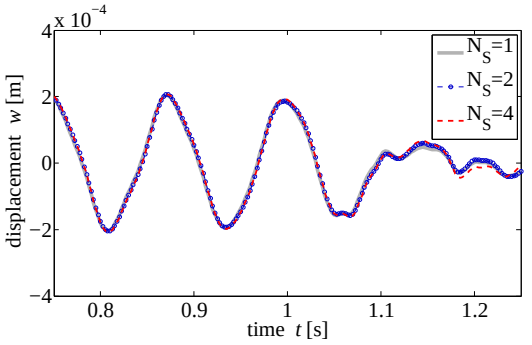

(d) Same as left in the time-interval $t = [0.75s; 1.25s]$.

Figure 9.4: Vertical displacements at the nodes A and B.

point in time, where the exciting force is removed from the model, a good accordance of the displacements of all three constellations $N_S = 1, 2, 4$ can be observed in Figs. 9.4(b) and 9.4(d).

Those according displacements indicate that substructuring the SBFEM model yields the same good results as modelling the far-field just as one SBFEM domain. To show that substructuring moreover enables a higher efficiency, in terms of disk-storage and CPU time for the computation of the influence matrices as well as for the entire hybrid simulation, those values are compared in Tab. 9.2.

Table 9.2: Comparison of disk space and CPU time for different substructures.

N_S	time-steps	disk space [MB]	CPU (SBFEM) [s]	CPU (FE-SBFEM) [s]
1	200	310 (100%)	58097 (100%)	19759 (100%)
2	225	2(156)=312 (100.7%)	6270 (10.8%)	13756 (69.6%)
4	225	2(69+65)=268 (86.5%)	1024 (677) (1.8%)	9985 (50.5%)

For the disk-storage of $N_S = 4$ domains, only 86.5% of the disk-storage of $N_S = 1$ domain is needed. The CPU time for the computation of $\mathbf{M}^{\infty}$ is drastically reduced to 1.8% and the time for the entire simulation is halved for the considered application. Thus, the reduction of computational time- and disk-storage as well as the ability of the substructure SBFEM to give the same results as the one structure SBFEM, proofs the efficiency of substructuring. Therefore, SBFEM substructuring is used in the further progress of this work.

9.2 Wave propagation in near-field via DRM

In Sec. 7.2, the DRM was introduced as a method which is able to simulate realistic seismic wave propagation in a near-field domain by an excitation that is equivalent to the original seismic source and that is acting at the near-field boundaries. The ability of the DRM to transform a motion from a large scale domain into the near-field, i.e., the potential of modelling seismic wave propagation in the near-field, is studied in the present section.

9.2.1 Step I: seismic excitation

In the first step of the DRM that usually contains the large scale simulation a relatively small domain is considered here which is still larger than the near-field. This domain is a linear-elastic soil half-space excited by an impulsive excitation on the surface. The excitation is intended to induce a Rayleigh wave in the surface-near soil. Rayleigh waves (see Sec. 2.3.1) transport up to 70% of the energy in seismic events. Therefore, and since their maximum amplitudes are located around the burial depth of an underground pipeline, the Rayleigh wave is believed to be the crucial wave type when analysing the failure of buried lifelines due to seismic wave propagation effects.

The dynamic response due to the impulsive excitation is modelled by the BEM (see Sec. 3.3.1) where it is only necessary to discretise the surface of the half-space. This discretisation with two-dimensional triangular elements is depicted in Fig. 9.5 where the force vectors $\mathbf{f}_{seis}$ are shown. They are considered as the original seismic excitation.

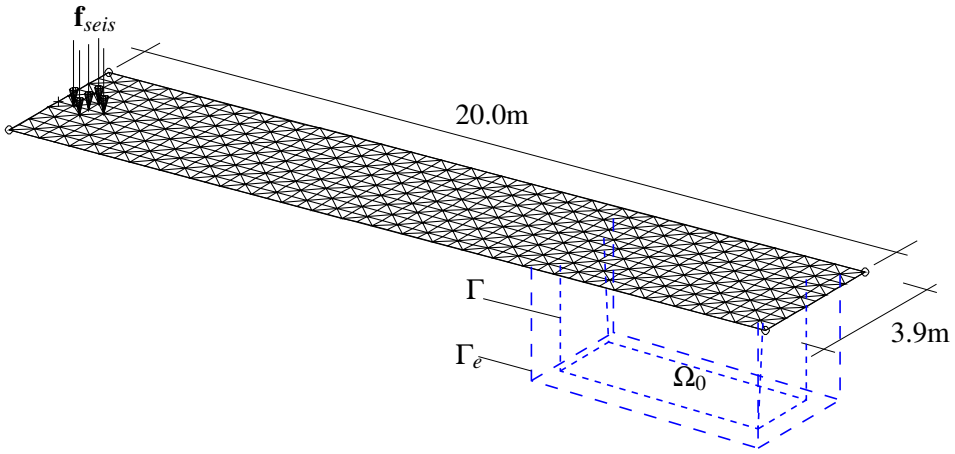

Figure 9.5: Surface of half-space discretised by two-dimensional BEs. The impulsive force which is considered here as original seismic excitation acts at the left of mesh. The interfaces Γ and Γ_e where the displacements are evaluated are marked by dashed lines.

The near-field domain Ω_0 with the two adjacent interfaces Γ and Γ_e is additionally sketched in Fig. 9.5. Ω_0 is chosen at a sufficiently large distance from $\mathbf{f}_{seis}$ so that a Rayleigh wave is generated inside of Ω_0 by this excitation. On the two interfaces Γ and Γ_e, the wave fields due to the impulsive excitation $\mathbf{f}_{seis}$ are computed and stored in order to transform them in the second step of the DRM to equivalent seismic forces. The motion at the BE nodes on the surface can be directly determined from the BEM, whereas the displacements at the points in the inner of the half-space have to be evaluated from a computation subsequent to the BEM simulation.

9.2.2 Step II: wave propagation in near-field

In the second step of the DRM, the dynamic response of the near-field is analysed with the hybrid FE-SBFEM. In this simulation, a diagonal lumped mass matrix $\mathbf{M}$ in Eq. (7.9) is considered. Therefore, the computation of the equivalent forces $\mathbf{f}^{\text{eff}}$ from Eq. (7.8) is simplified to

$$\mathbf{f}^{\text{eff}} = \begin{bmatrix} \mathbf{f}_i^{\text{eff}} \\ \mathbf{f}_b^{\text{eff}} \\ \mathbf{f}_e^{\text{eff}} \end{bmatrix} = \begin{bmatrix} \mathbf{0} \\ -\mathbf{K}_{be}^{\Omega^+}\mathbf{u}_e^0 \\ \mathbf{K}_{eb}^{\Omega^+}\mathbf{u}_e^0 \end{bmatrix} . \tag{9.3}$$

Thus, on the interfaces Γ and Γ_e only the displacements and not their temporal derivatives have to be evaluated and stored in the first step of the DRM. In the second step, two different cases are studied. In the first case, a near-field containing only soil is considered. In the second case, a buried pipeline is additionally embedded in the soil. The soil is described by three-dimensional eight-node hexaedral brick FEs, whereas the walls of the pipeline are mapped by two-dimensional four-node shell FEs of thickness $t_p = 0.01$m. For both reduced domains, two simulations are performed: one where the far-field wave radiation is considered by using the hybrid FE-SBFEM, and one where this wave radiation is hindered by performing a pure FE simulation which regards only the truncated near-field.

The computational parameters for the two reduced domain simulations are listed in Tab. 9.3. The HHT-α time-integration parameters are chosen as ($\alpha;\beta;\gamma$)=(0.;0.25;0.5) which reduces the time-integration to the Newmark scheme. The computation of SBFEM matrices are performed with the tolerances ε_z=$1\cdot10^{-4}$ and ε_t=$1\cdot10^{-5}$.

Table 9.3: Parameters for hybrid FE-SBFE computation.

	FEM			SBFEM			time	
pipeline	nodes	brick FEs	shell FEs	N_S	nodes	elements	$t_{\max}$ [s]	Δt [s]
without	1224	896	0	1	459	416	12.5	$2.5\cdot10^{-4}$
with	6208	1600	5088	1	489	464	12.5	$2.5\cdot10^{-4}$

The linear elastic material parameters for the soil are $E_s = 30$ MN/m^2, $\nu_s = 0.3333$ and $\rho_s = 1800$ kg/m^3 and for the pipe $E_p = 210$ GN/m^2, $\nu_p = 0.3$ and $\rho_p = 7850$ kg/m^3. Fig. 9.6(a) shows the bisected reduced near-field domain for the second case where the pipeline is included in the soil domain. The dashed lines mark corresponding to Fig. 9.5 the interfaces Γ and Γ_e where the forces $\mathbf{f}^{\text{eff}}$ equivalent to the original seismic excitation are applied.

Reduced soil domain without pipeline: At first, the free-field motion of the reduced domain Ω_0 is studied with the aim to verify the DRM. Since the large scale domain from step I and the reduced domain from step II are considering the same free-field conditions, i.e., they both do not exhibit any localised features as the pipeline, the ground motion is expected to be identical. The results of the simulation are shown in Figs. 9.6(b), 9.7(a) and 9.8(a). In Fig. 9.7(a) the displacements at node A which is depicted in Fig. 9.6(a) are plotted for the three Cartesian coordinate directions. The temporal progressions of the displacements derived from the large scale simulation with the BEM and from the reduced domain hybrid FE-SBFE simulation accord very well. Contra wise, the displacements derived from the pure FE simulation are strongly oscillating and differ much from the reference solution of the BEM. This oscillation results from the reflecting waves at the truncation boundaries of the reduced domain.

As explained at the end of Sec. 7.2.1, if the same methods were used for the simulations of step I and II, the relative free-field motion $\mathbf{w}_e$ in the outer domain $\hat{\Omega}_+$ would have vanished. When doing so, no waves would reach the boundaries of the reduced domain and, thus, no wave reflections would occur. Since the simulation methods used here are numerical and thus approximative, the simulated wave fields slightly differ. This is the reason why the relative free-field motion $\mathbf{w}_e$ in the outer domain $\hat{\Omega}_+$ does not vanish and wave reflections as shown in Fig. 9.7(a) occurs.

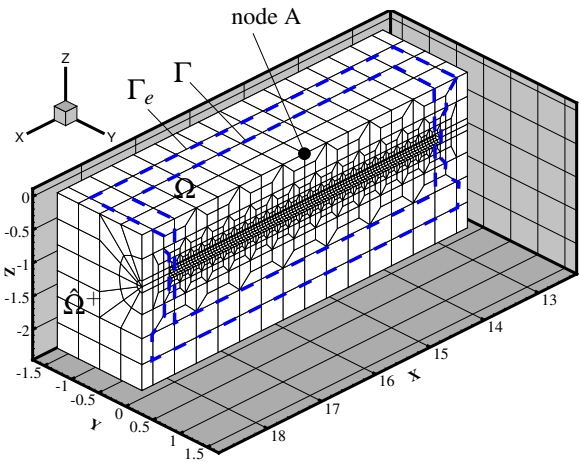

(a) FE mesh of the reduced near-field soil domain containing the buried lifeline. The inner domain Ω is bounded by the two adjacent interfaces Γ and Γ_e where the equivalent seismic forces are applied. In the outer domain $\hat{\Omega}^+$, just the motion different from the free-field motion appears.

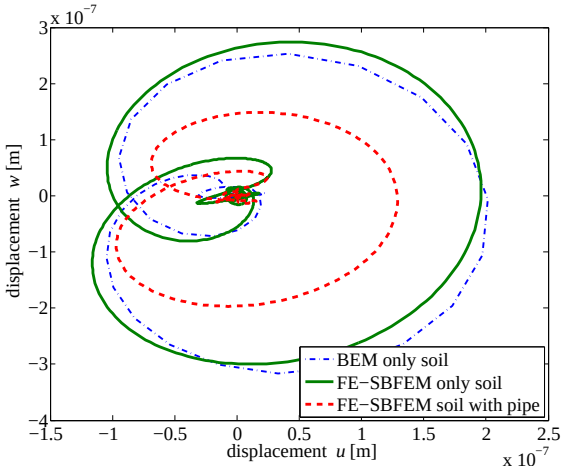

(b) Temporal progression of the displacements in the x,z-plane at node A. The motion exhibits the characteristic ellipsoidal shape induced by a Rayleigh wave.

Figure 9.6: FE mesh of the reduced near-field domain containing the pipeline and Rayleigh wave motion at node A.

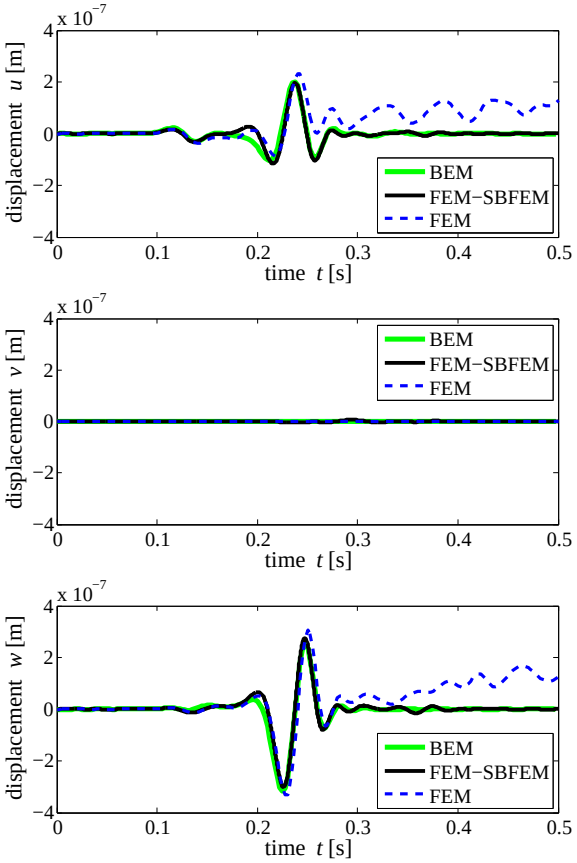

(a) Free-field displacements in x,y,z-direction at node A of the BEM simulation and of the near-field soil domain without the pipeline.

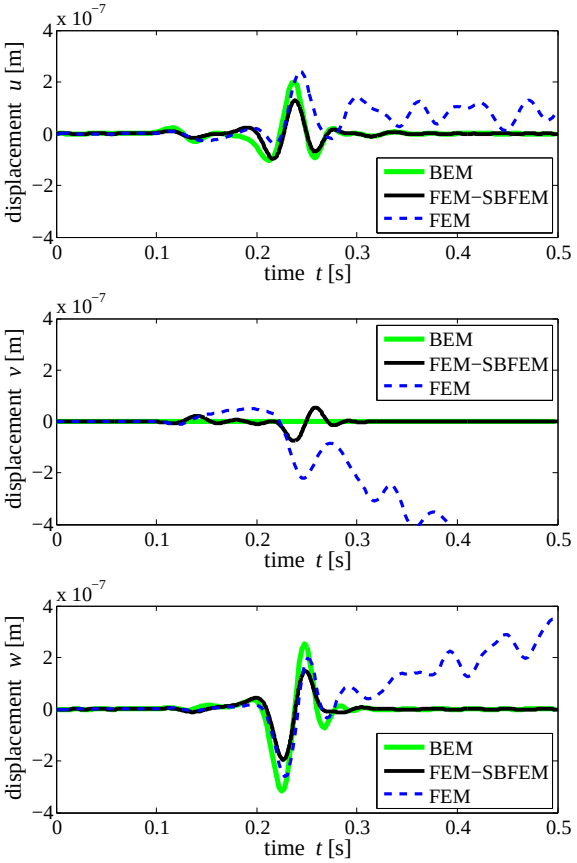

(b) Displacements in x,y,z-direction at node A of the BEM simulation and of the near-field soil domain containing the pipeline.

Figure 9.7: Displacements at node A simulated for reduced domains with and without buried pipeline.

The analyses performed in this section intend to model a Rayleigh wave. The characteristic motion of those waves which describes a retrograde ellipse is depicted in Fig. 9.6(b) where the resulting displacements in x-coordinate versus the one in z-coordinate at node A are depicted. Next to the successful modelling of the Rayleigh wave motion in the near-field, it can be realised that the ellipse resulting from the motion of the BEM simulation and the FE-SBFEM simulation are nearly identical. Since the area of those ellipse are proportional to the dissipated energy, Fig. 9.6(b) proofs also that the motion energy is transferred properly from the large scale to the near-field model.

Finally, the deformed near-field at particular time-stations, i.e., the wave propagation in the near-field can be observed in Fig. 9.8(a). It can be seen that the motion is induced at the nodes on the interface Γ and Γ_e (compare Fig. 9.6(a)). The domain outside of those interfaces is nearly at rest but not completely as discussed above. In the inner domain Ω_0, the expected typical Rayleigh wave propagation can be realised. The wave is entering the domain Ω_0 from the right ($t = 0.163s$), propagates through it ($t = 0.188$ to $0.263s$) and leaves the system at rest after the passage ($t = 0.288s$). Thus, the ability of the DRM to model seismic wave propagation in a near-field domain is demonstrated.

Reduced soil domain containing pipeline: After demonstrating that the DRM is able to model seismic free-field wave motion in a reduced near-field domain, a second case is studied where a local feature, namely a buried pipeline, is introduced to the near-field. Whereas the FE mesh is depicted in Fig. 9.6(a), the results of the two near-field simulations (hybrid FE-SBFEM and pure FEM), with reference to the large scale simulation, are plotted in Figs. 9.6(b), 9.7(b) and 9.8(b).

The displacements in the Cartesian directions resulting from the simulations of the large scale domain (BEM), of the reduced domain enabling wave radiation (FE-SBFEM) and of the reduced domain hindering wave radiation (FEM), are compared in Fig. 9.7(b). Using the results from the BEM simulation as reference, it can be recognised that the displacements derived from the FE-SBFEM simulation exhibit qualitatively the same shape but quantitatively with a lower magnitude. This indicates, as expected, that the soil-pipe system behaves stiffer than the pure soil system. For the y-direction, a deflection can be observed which might be due to the discretisation of the FEM. However, this disturbance fades rapidly. This shows that the waves are not trapped in the near-field, but can radiate to infinity. Considering the pure FEM simulation, an oscillating and differing progression of all three displacement components can be observed. As discussed above, this is due to the wave reflections at the near-field/far-field interface.

As for the free-field motion, the motion of a wave propagating in the x,z-plane at node A is depicted in Fig. 9.6(b). Also here, the characteristic elliptical shape of the Rayleigh wave motion can be recognised. But in this case, the ellipse is smaller as before. This implies that the system behaves stiffer as the pure soil system and, thus, less energy is dissipated by the soil. Nevertheless, still the wave characteristics are transformed from the large scale model to the reduced domain.

In Fig. 9.8(b), the wave propagation in the near-field is plotted. As for the free-field (see Fig. 9.8(a)), the same zones of pressure and tension which are typical for the Rayleigh wave motion can be observed. Also here, the displacements of the soil-pipeline system are lower than the ones of the soil domain.

Concluding, it can be stated that the DRM is able to transfer seismic waves with all their characteristics from a large scale simulation to a reduced domain model.

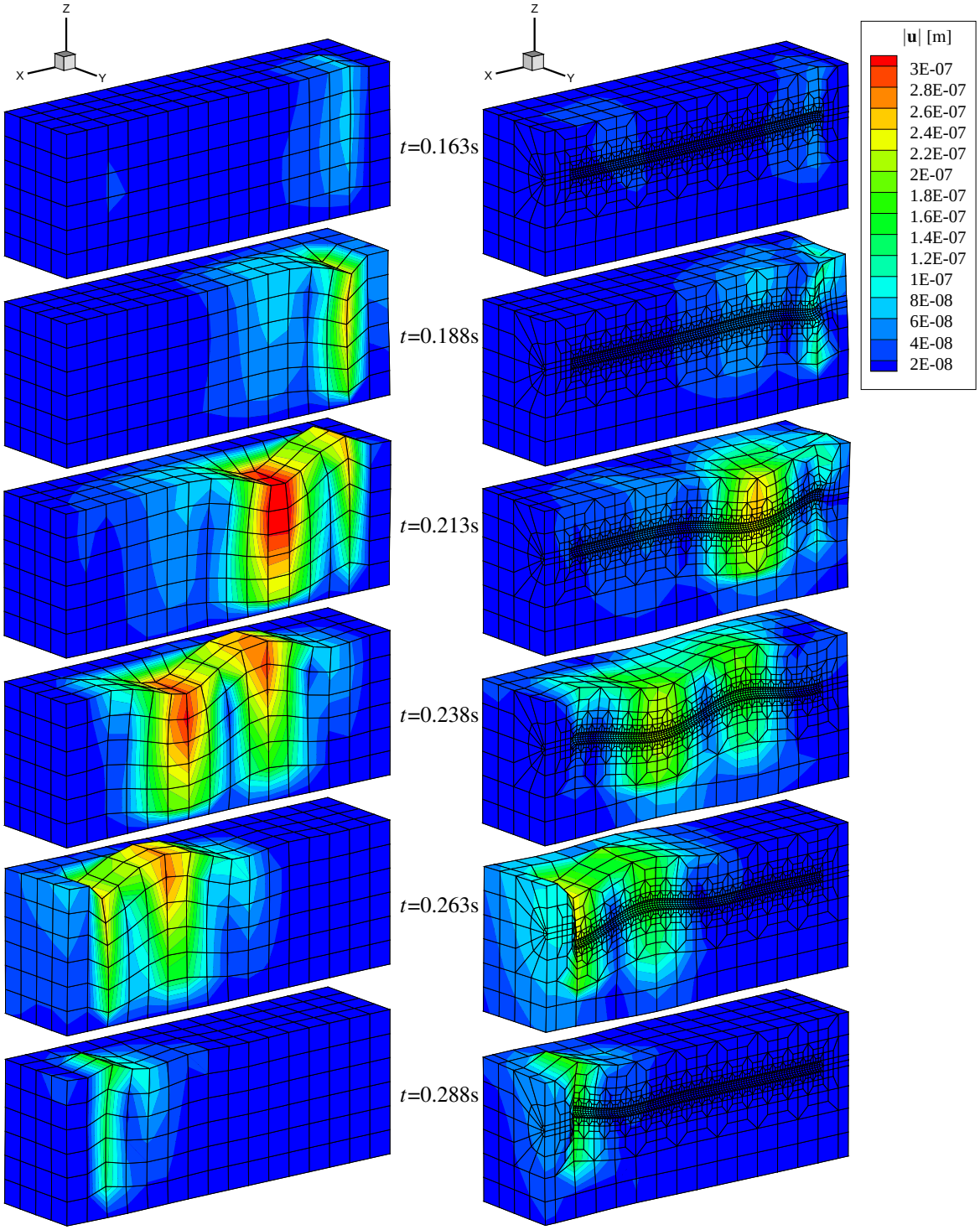

(a) Deformed soil without pipeline (b) Deformed soil containing pipeline

Figure 9.8: Wave propagation in the reduced domains which are excited by the forces equivalent to the original source. For representation reasons, the model is bisected along the x-axis and the displacements are magnified by the factor $2{\cdot}10^6$. The contours are plotted for $|\mathbf{u}| = \sqrt{u^2+v^2+w^2}$.

9.3 Simulation of a real earthquake via DWFEM and k^{-2}-model

In the previous section, the original seismic motion for the first step of the DRM was modelled by the BEM. Obviously, the case considered there does not represent the mechanisms and propagation effects of a real earthquake and was not intended to do it. The BEM study was thought to present the potentials of the DRM and not to model a realistic seismic excitation. Latter is the subject of the present section. It is aimed to simulate a real earthquake, in order to present the ability of the incorporated methods to model a realistic seismic motion and to generate a reliable excitation for the near-field model of the second step of the DRM.

9.3.1 Procedure

In the multi-method approach of this work, explained in Sec. 7.5, the large scale simulation to model the earthquake motion is performed by means of mainly two methods. Whereas the DWFEM (Sec. 7.3) calculates the Green's functions to model the wave propagation in the earth crust, the rupture process on the causing seismic fault is represented by the k^{-2}-model (Sec. 7.4). Those methods are applied in this section with the intention to generate realistic synthetic ground motions. The general procedure for the generation of the seismic ground motion contains four steps:

1. It is necessary to define the decisive parameters which describe the model of earth and seismic fault as depicted in Fig. 9.9. Those parameters are the profile of the earth crust which is termed in seismology the *velocity structure*, the fault location and its geometry and the receiver location where the ground motion shall be simulated. Moreover, for computational reasons the discretisation of the fault and the discretisation of the velocity structure have to be established.

2. The wave propagation from the fault to the receiver needs to be described. This is achieved by Green's functions G_{ij}^{*} which are computed with the DWFEM for every subfault, i.e., for every discrete point on the fault, like sketched in Figs. 4.4 and 9.9.

3. The rupture process on the causative fault for the analysed seismic event is quantified. So, the distribution of the final slip $[\bar{u}]^{ij}$ on the fault is provided by means of the k^{-2}-model and a rupture velocity v_R is specified.

4. The effects of the wave propagation in the earth crust and of the rupture on the seismic fault are conjuncted. The Green's functions G_{ij}^{*} and the slip values $[\bar{u}]^{ij}(t)$ at the respective points on the fault and at a defined time are evaluated by the representation theorem Eq. (4.25). Therewith, the seismic ground motion is synthesised for a rupture propagating with the velocity v_R along the fault.

9.3.2 Application

The procedure, explained above, is applied to simulate a real earthquake that stroke the city of Forlì in December 7th, 2003 with a medium magnitude of M_w=4.25. Forlì is the capital of the province Forlì-Cesena in the region Emilia-Romagna and is located at the eastern foothills of the Apennine Mountains in Italy.

This earthquake was chosen as application for several reasons. Firstly, the data of its seismic source parameters are available which provide the input for the large scale model. Secondly, this earthquake was recorded at a seismic station in Forlì. That way, the simulation results can be compared to those records in order to verify the numerical model and its input parameters. Thirdly, the soil profile was investigated at several sites in Forlì, so that also for the near-field soil domain reliable input parameters are provided. And finally, data of the network of underground lifelines are available for the city of Forlì. Those data from the network part in the vicinity of the seismic station are used for the numerical hybrid near-field model of the pipeline and its surrounding soil (see Chap. 10).

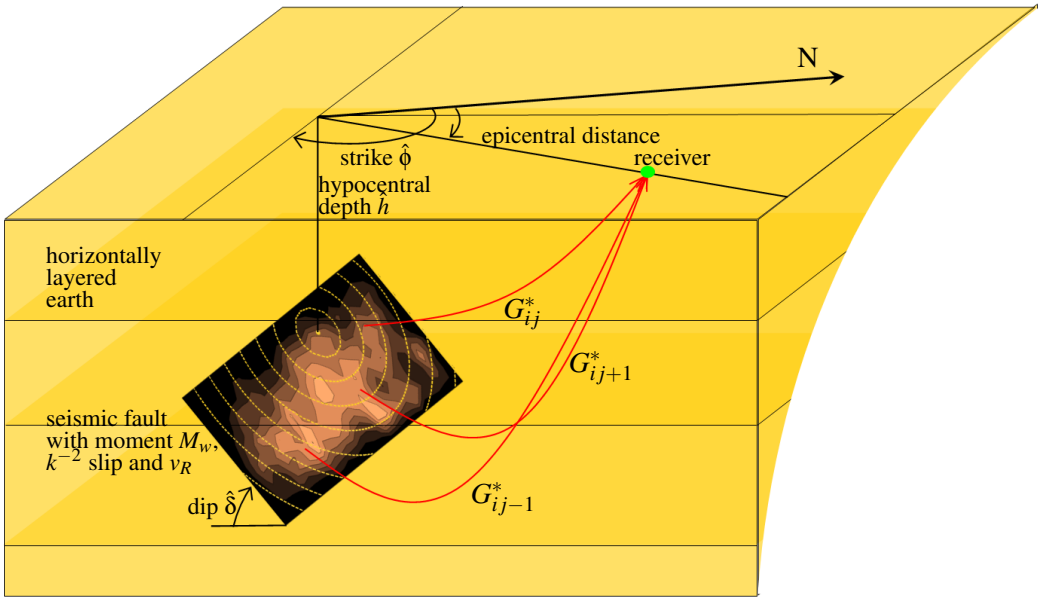

Figure 9.9: Sketch of the analysed seismic fault and the earth crust modelled as horizontally layered half-space. The Green's functions G^*_{ij} are calculated for fault-point/receiver point combination, scaled by the final fault slip and synthesised by an representation theorem.

9.3.3 Basic input parameters

This section provides the basic input parameters for the application. Those input parameters are sorted in this section by their location of occurrence. So, firstly, the source parameters are addressed, secondly the parameters of the wave propagation path and, thirdly, the parameters at the region of interest.

Source parameters: The basic parameters which specify the seismic source process are the moment magnitude M_w, the hypocentral depth $\hat{h}$, the angles of strike $\hat{\phi}$, dip $\hat{\delta}$ and rake $\hat{\lambda}$, as well as the rupture velocity v_R (see Fig. 9.9). All other parameters can be determined by the scaling laws described in Sec. 7.4.1. The basic source parameters can be obtained from observations and seismic inversions which were collected for many earthquakes, especially from those of recent date. The parameters are available from several data bases, like, e.g., EMMA [Vannucci and Gasperini, 2003], [PEER, 2003] or reports accounting particular earthquakes.

In this section, the above mentioned $M_w = 4.25$ earthquake from 2003 is analysed. This earthquake was recorded at a seismic station in Forlì [Osservatorio Sismico delle Strutture, 2003]. For this seismic event, the input data is provided by the EMMA data base [Vannucci and Gasperini, 2003]. Those data are used here as input and are listed in Tab. 9.4 where in brackets also the slightly differing parameters from the station report [Osservatorio Sismico delle Strutture, 2003] are given. In this work, the rupture velocity v_R is regarded as constant (compare Eq. (7.46)).

From these data, the remaining parameters describing the fault mechanism can be determined by empirical relationships. The scaling laws for those source parameters were described in Sec. 7.4.1 and yield the values listed in Tab. 9.5.

Profile of earth: In general, the data concerning the velocity structure of the earth's crust are gained mainly from seismic deconvolution. Thereby, the structure of the earth can be gathered from the run times and the shapes of seismic wave fields recorded at the surface of the earth. For the application undertaken within this work, the velocity structure of the earth crust down to a depth of 40km is taken from [Ponziani, 1994] and is mapped in Fig. 9.10(a).

Table 9.4: Source parameters for the analysed $M_w = 4.25$ earthquake supplied by the EMMA data base [Vannucci and Gasperini, 2003]. The corresponding differing parameters from the seismic station report in Forlì [Osservatorio Sismico delle Strutture, 2003] are given in brackets.

time (UTC)	M_w	latitude	longitude	hypocentral depth $\hat{h}$	strike $\hat{\phi}$	dip $\hat{\delta}$	rake $\hat{\lambda}$
07/12/2003, 10:20:33h	4.25 (4.0)	44.162N (44.04N)	012.18E (012.10E)	12.0 km	114°	55°	83°

Table 9.5: Calculated source parameters following the scaling laws from Sec. 7.4.1.

M_w	M_0 [Nm]	S [km^2]	L [km]	W [km]	v_R [km/s]	τ_R [s]	$[\bar{u}]$ [m]	$[\bar{\sigma}]$ [MN/m^2]
4.25	$2.95 \cdot 10^{15}$	4.121	2.87	1.44	2.8	0.48	0.234	4.36

Profile of soil: So far, the seismic source and the wave propagation path of the earth crust were addressed. The receiver location, i.e., the location were the seismic ground motion was measured and where it should be simulated needs to be taken into account. Since this region of interest is in the vicinity of the surface, the profile of the surficial soil layers of the earth must be specified more precisely than the velocity structure of the earth. The parameters of those surficial soil layers can usually be derived comparatively easy from measurements, e.g., down-hole tests at the site of interest.

The *Geotechnical Section of the Department of Civil Engineering of the University Florence* performed such down-hole tests in the vicinity of the seismic station considered here. Those investigations showed that the soil in the municipal of Forlì is approximately horizontally layered. The resulting P- and S-wave velocities c_P and c_S as well as the density ρ determined by the down-hole tests are depicted in Fig. 9.10(b).

Receiver location: To identify the epicentral distance as well as the relative angle of the receiver location to the fault plane, both depicted in Fig. 9.9, the location, where the seismic ground motion should be simulated, needs to be defined. Since the simulation results should be compared to the record of the seismic station, this location is chosen.

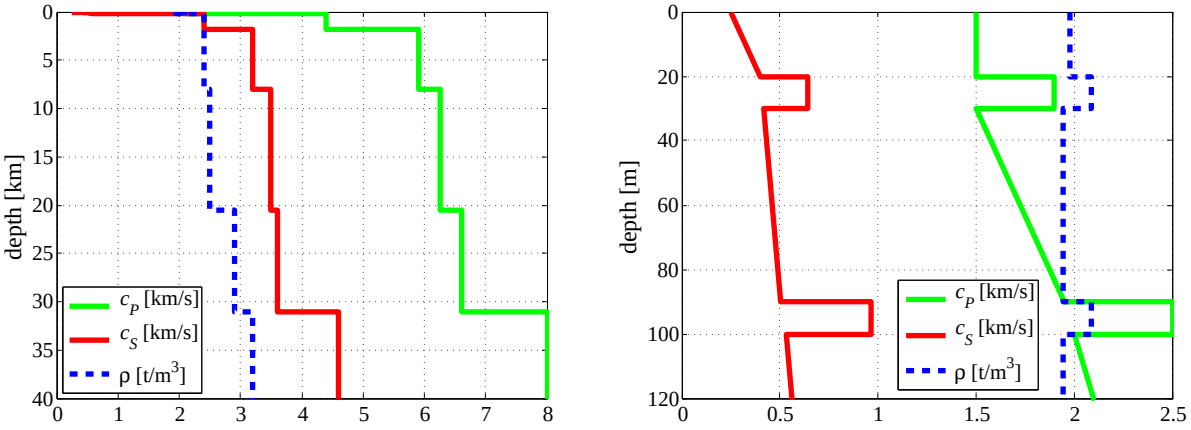

(a) Velocity structure (c_P, c_S, ρ) of the earth's crust in the region of Forlì after [Ponziani, 1994]. The profile reaches down to a depth of 40km.

(b) Profile of the soil in the vicinity of the seismic station derived from down-hole test performed by the *Geotechnical Section of the Department of Civil Engineering of the University Florence* down to a depth of 120m.

Figure 9.10: Profiles of c_P, c_S and ρ of the earth crust and the surficial soil used for the simulation.

The station, where the seismic motion was recorded, is located next to a school in the city centre of Forlì (see Fig. 9.11). The seismic response of this building was studied by [Facciorusso *et al.*, 2006]. The axes of the seismic free-field station, from which the reference motion for the simulation was recorded, are perpendicular to the building's outwalls. The position of the station is defined by the coordinates [44.22N, 012.05E]. Thus, it is located at an epicentral distance of 12.2km. The seismic motions, measured at this station in Forlì, are published in the report [Osservatorio Sismico delle Strutture, 2003].

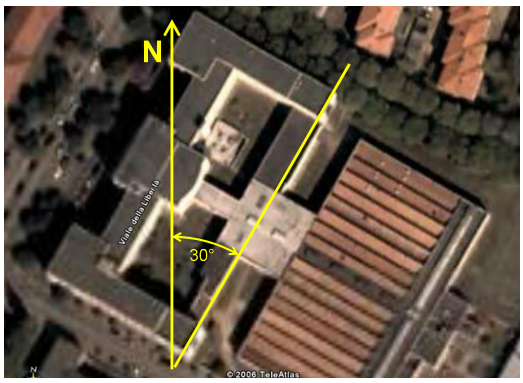

(a) Aerial view of the seismic station in Forlì [Google earth, 2006] with sketched azimuth.

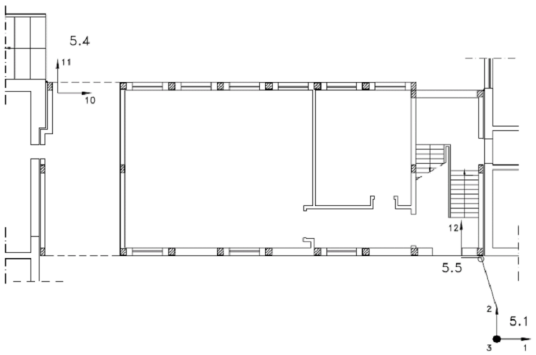

(b) Plan view of the ground floor of the seismic station in Forlì with the accelerometers [Osservatorio Sismico delle Strutture, 2003]. The free-field seismograph records the channels 1,2 and 3.

Figure 9.11: Location of the seismic station in Forlì.

Computational parameters: For the computation of the synthetic seismic ground motions, the program package COMPSYN [Spudich and Xu, 2003] is used. This package performs the computation of the Green's functions by means of the DWFEM and the synthesis according to the representation theorem from Eq. (4.25). The input parameters for the large scale earthquake simulation are listed in Tab. 9.6. The parameters $R_{\max}$ and $k_{\max}$ refer to the maximum radius and the maximum wavenumber, respectively, which were addressed in Sec. 7.3.1.2.

Table 9.6: Computational input parameters for the earthquake simulation.

Earth						Fault points	
$f_{\max}$ [Hz]	$R_{\max}$ [km]	$t_{\max}$ [s]	Δt [s]	$k_{\max}$ [1/m]	FE nodes	x	z
10 / 20	100.0	32.77	0.002	14000	686	29	15

The DWFEM enforces a maximum resolving frequency $f_{\max}$ (see Sec. 7.3.2) up to which the reliable results can be obtained by the computation of the seismic wave field. The computational effort for the numerical simulation increases squared with increasing $f_{\max}$. The simulation results are presented here for maximum resolving frequencies $f_{\max} = 10$Hz and $f_{\max} = 20$Hz.

9.3.4 Verification of the model

For the validation of the large scale model, the synthetic ground motion is compared to measurements of the real earthquake recorded at the seismic station in Forlì. As criteria for the quality of the simulation, the ground motion parameters, referred to in Sec. 4.3.1, are incorporated. Those parameters are the envelope of the acceleration, velocity, and displacement progression over time as well as their peak values PGA, PGV, PGD. Further, the Arias intensity I_A and the strong motion duration D_s after [Trifunac and Brady,

1975] are compared. In addition, the progressions of the frequency-spectra of acceleration, velocity and displacement are controlled, and the temporal developments of the Arias intensity are compared.

To have a single, clearly stated parameter for the quality of the simulation, a quality index for the ground motion Q_{GM} is introduced as

$$Q_{GMn} = \sum_{i=1}^{m} \left(\frac{\left| p_{in}^{\text{record}} \right|}{max \left| \mathbf{p}_i^{\text{record}} \right|} \left| p_{in}^{\text{record}} - p_{in}^{\text{simulation}} \right| \right) \tag{9.4}$$

where the ith ground motion parameter $\mathbf{p}_i$ for the three Cartesian directions of motion $n = 1,2,3$ is described by the vector $\mathbf{p}_i = [p_{i1}, p_{i2}, p_{i3}]$. The $m = 5$ parameters used for the determination of the ground motion index Q_{GM} are PGA, PGV, PGD, I_A and D_s. As can be seen from Eq. (9.4), the index gets smaller, the smaller the difference becomes between p_{in}^{record} and $p_{in}^{\text{simulation}}$. Thus, it can be stated: the smaller Q_{GMn} becomes, the higher gets the quality of the simulation. Anyhow, the quality index in Eq. (9.4) is not only the simple sum of the m errors of the ground motion parameters $\left| p_{in}^{\text{record}} - p_{in}^{\text{simulation}} \right|$, but weights the components depending on their importance, i.e., their quantity. That way, the quality index Q_{GM} allows to the fact that a strong component of motion is more attended than a weak one.

The final slip distribution and the nucleation point on the fault are, to a certain degree, random parameters. For the verification of the large scale model, 100 realisations are performed. This means that 100 different rupture processes for the fault are generated and judged by means of the quality index Q_{GM}.

9.3.5 Results of the simulation

The ground motion is simulated with the procedure described in Sec. 9.3.1 by using the input parameters supplied in Sec. 9.3.3. The large scale model is verified by means of the simulated and recorded ground motion parameters, as described in Sec. 9.3.4. As stated above, 100 different rupture mechanisms are studied for both resolving frequencies, $f_{\max}$ =10Hz and $f_{\max}$ =20Hz. The results incorporating both resolving frequencies are compared to the low-pass filtered records where the low-pass frequency f_{lp} is in both cases the respective resolving frequency. The comparison of the simulation results to the unfiltered records was done in [Borsutzky, 2006] and exhibited a good accordance. The quality index and the differences of the ground motion parameters are in the same range as the ones of the cases discussed here.

The slip distribution and the rupture propagation which yield the best results, according to the quality index Q_{GM}, are displayed in Fig. 9.12. The rupture nucleation point is marked as white dot in the middle of the circular rupture fronts, shown as dashed lines.

The best fitting simulation results, caused by this rupture mechanism, are depicted in Figs. 9.13 to 9.17 for the frequencies $f_{\max}$ =10Hz and f_{lp} =10Hz. The results of the frequency-pair $f_{\max}$ =20Hz and f_{lp} =20Hz are shown in Appendix B. The acceleration, velocity, and displacement progressions are shown in time-and frequency-domain. Additionally, the evolutions of the Arias intensity I_A in time are compared. The ground motion parameters used for the determination of the quality index Q_{GM} in Eq. (9.4) from Sec. 9.3.4 are listed and compared in Tab. 9.7.

The time-histories of the simulated and of the recorded ground motion, i.e., of the accelerations in Fig. 9.13, of the velocities in Fig. 9.14, and of the displacements in Fig. 9.15, accord very well in all of the three Cartesian directions. Also, the frequency-spectra, plotted in a double logarithmic scale in Fig. 9.16, show the same progression. The sudden amplitude decay of the simulation results marks the maximum resolving frequency $f_{\max}$= 10Hz. Fig. 9.17 shows that the development of the Arias intensity I_A is also well approximated. Tab. 9.7 exhibits that the ground motion parameters differ in average about 20% (error), whereas the mean of the quality index is $\bar{Q}_{GM}$=10.40.

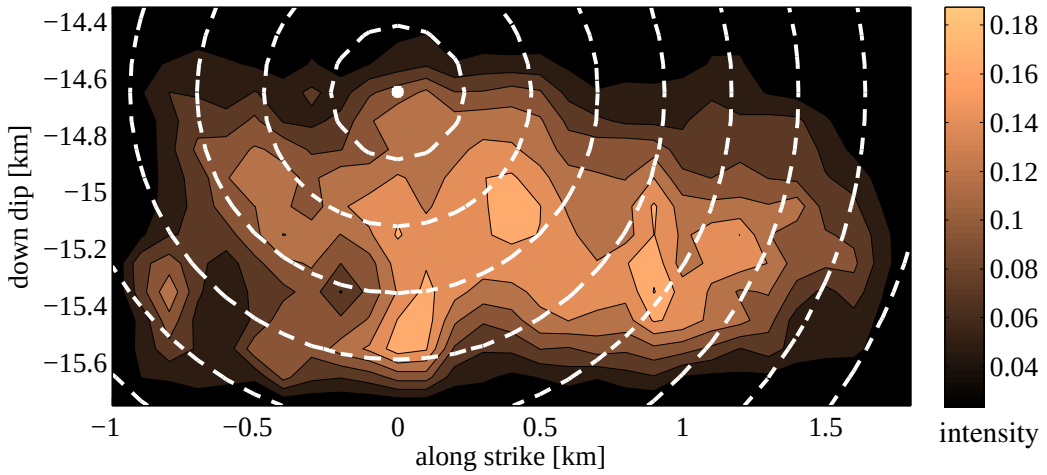

Figure 9.12: Best fitting final slip distribution on the fault (not to scale). The dashed lines denote the rupture propagation fronts.

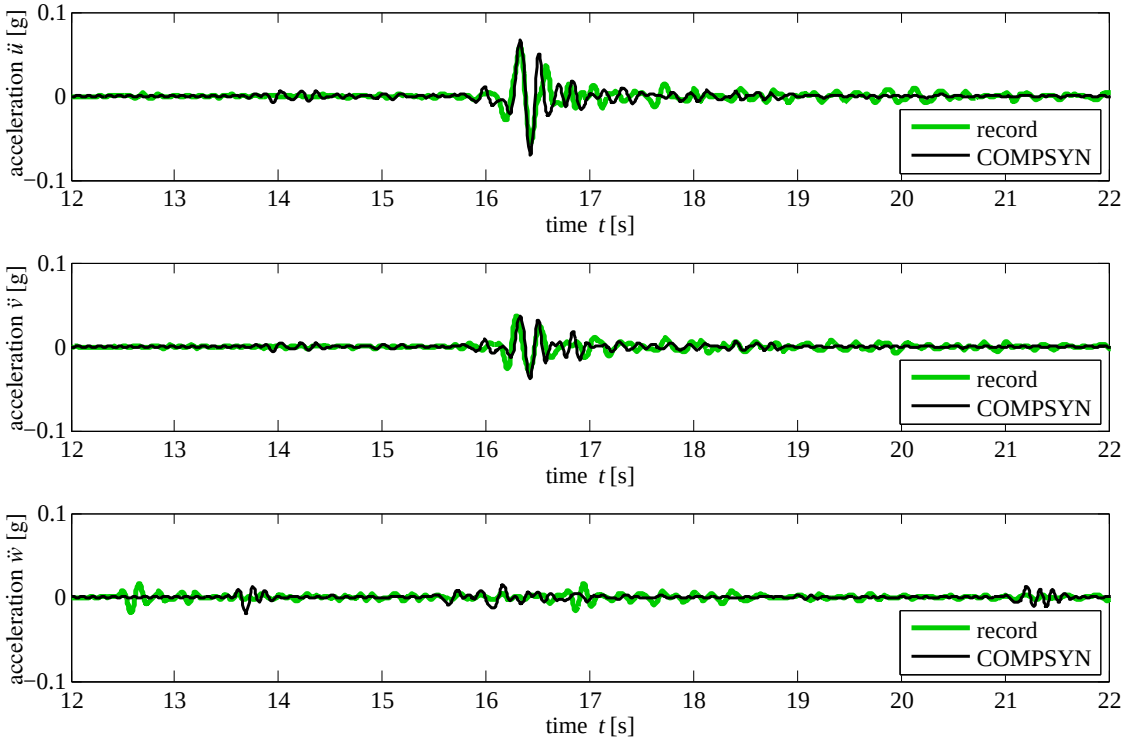

Figure 9.13: Recorded and simulated acceleration [g] at the receiver location for $f_{\max}$=10Hz and f_{lp}=10Hz.

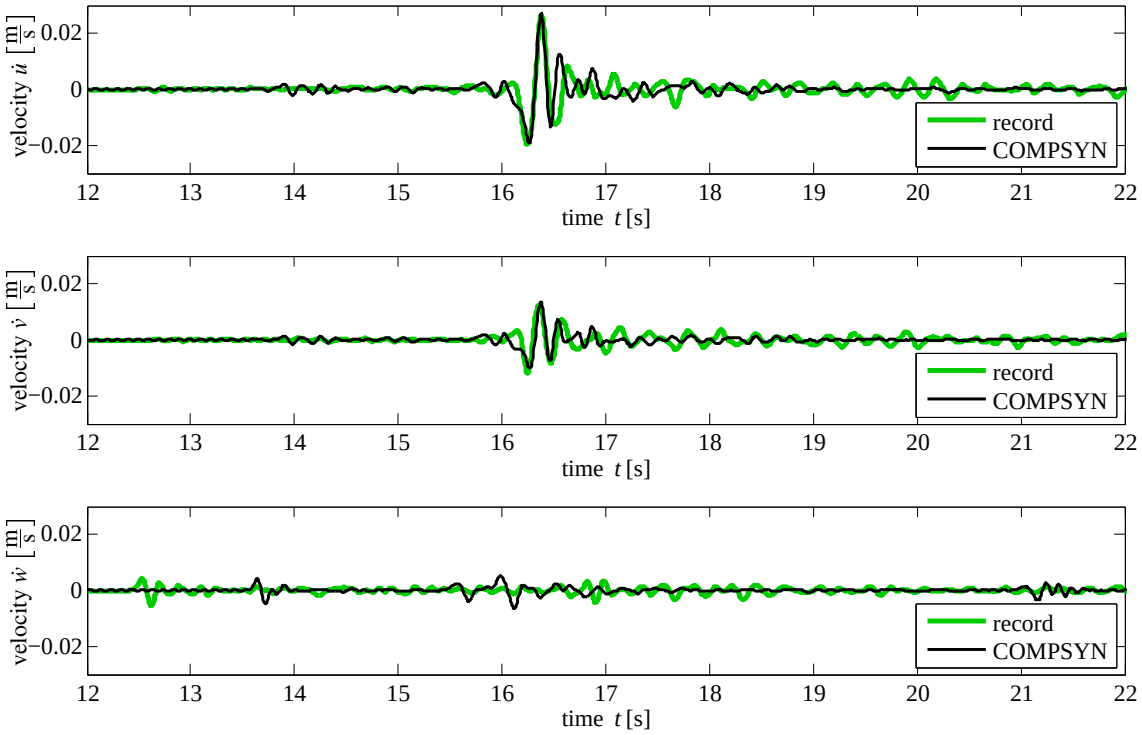

Figure 9.14: Recorded and simulated velocity $\left[\frac{\text{m}}{\text{s}}\right]$ at the receiver location for $f_{\max}$=10Hz and f_{lp}=10Hz.

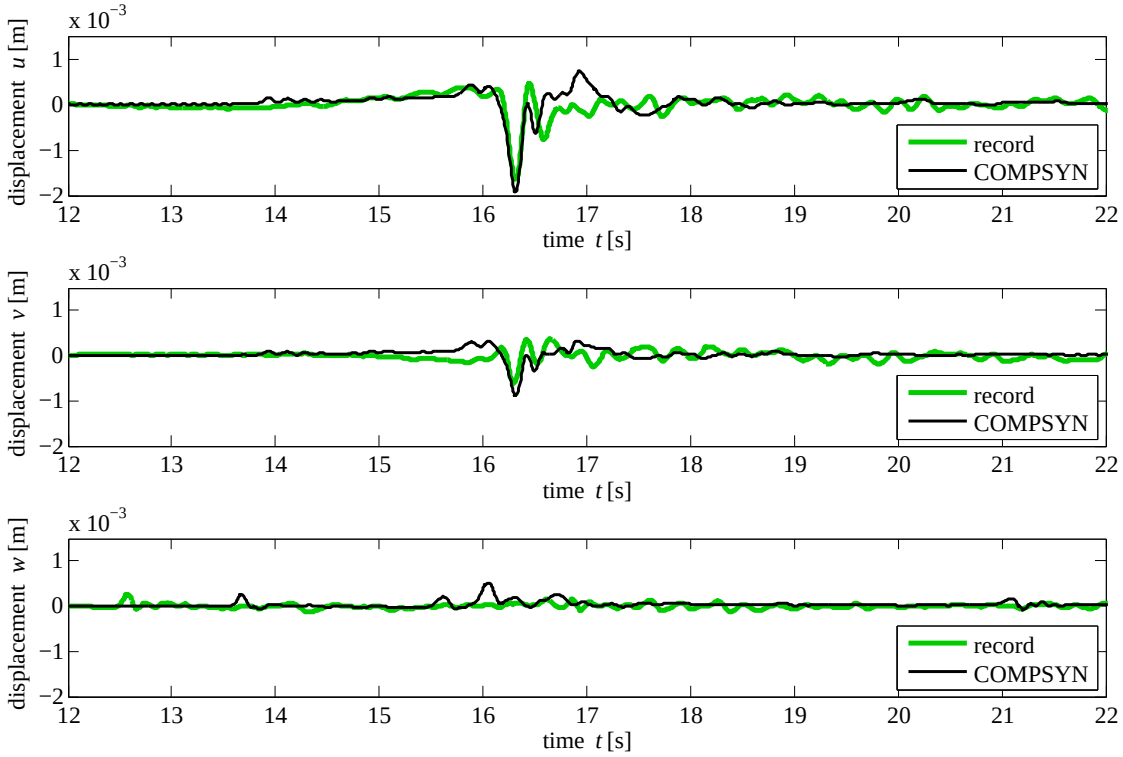

Figure 9.15: Recorded and simulated displacements [m] at the receiver location for $f_{\max}$=10Hz and f_{lp}=10Hz.

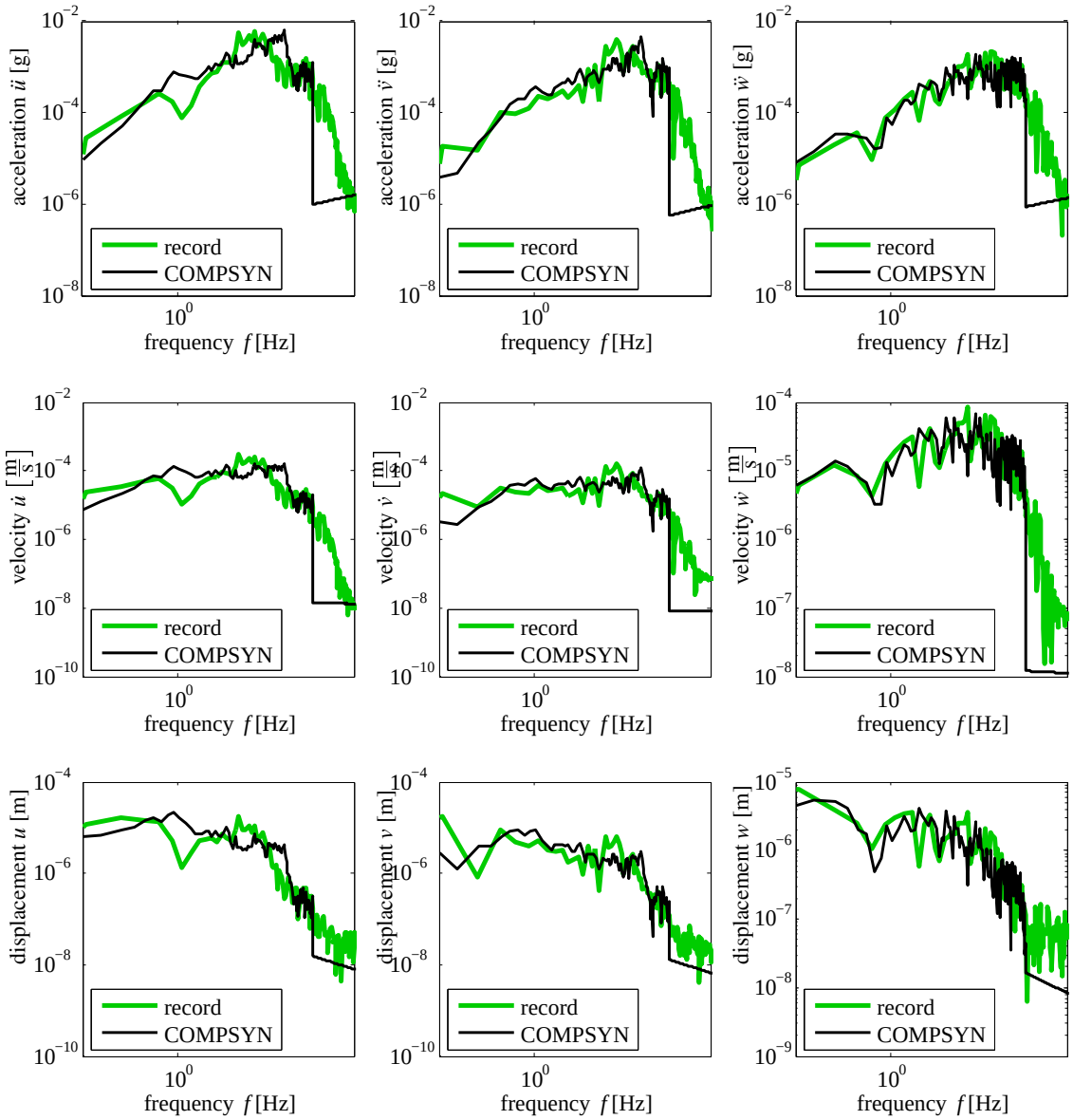

Figure 9.16: Recorded and simulated frequency-spectra at the receiver location for $f_{\max}$=10Hz and f_{lp}=10Hz. From top to bottom: frequency-spectra of acceleration, velocity, and displacement.

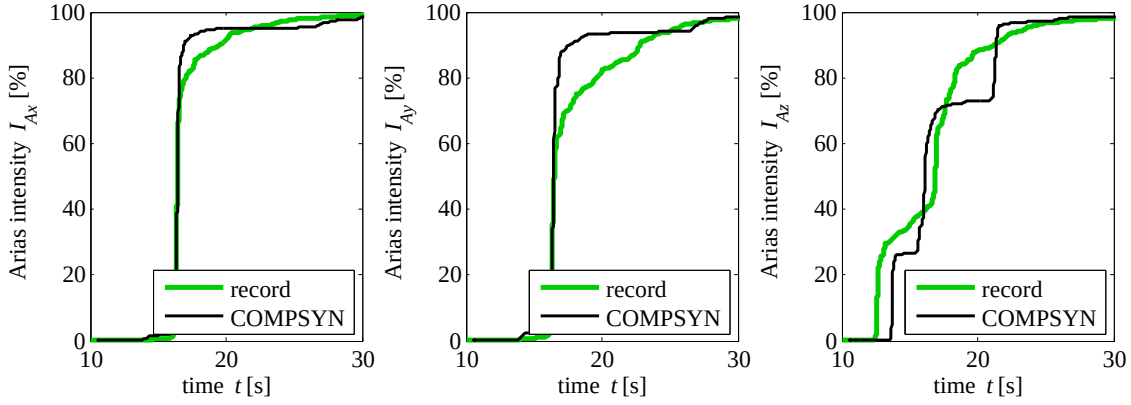

Figure 9.17: Recorded and simulated Arias intensity at the receiver location for $f_{\max}$=10Hz and f_{lp}=10Hz.

Table 9.7: Recorded and simulated ground motion parameters at the receiver location for $f_{\max}$=10Hz and f_{lp}=10Hz. The error denotes the difference between record and simulation.

		x	y	z
PGA [g]	record	$5.86{\cdot}10^{-2}$	$3.72{\cdot}10^{-2}$	$1.84{\cdot}10^{-2}$
	simulation	$7.06{\cdot}10^{-2}$	$3.83{\cdot}10^{-2}$	$1.93{\cdot}10^{-2}$
	error [%]	20.51	2.80	4.48
PGV $\left[\frac{\text{mm}}{\text{s}}\right]$	record	26.38	12.28	5.55
	simulation	26.98	13.32	6.25
	error [%]	2.30	8.48	12.45
PGD [mm]	record	1.66	0.62	0.26
	simulation	1.93	0.89	0.52
	error [%]	15.84	42.92	96.26
I_A $\left[\frac{\text{mm}}{\text{s}}\right]$	record	9.89	4.95	1.97
	simulation	11.70	4.06	1.59
	error [%]	18.26	-18.03	-19.25
D_s [s]	record	5.79	9.44	10.96
	simulation	5.26	10.73	7.85
	error [%]	-9.22	13.70	-28.43
error mean	[%]	13.22	17.19	32.17
Q_{GM}		12.35	8.52	10.32

Wave arrivals: In the recorded ground motions at the time between about t =12.5s and t =13.5s, ground motion oscillation can be observed, especially for the vertical component, which is not represented by the simulation results (see Figs. 9.13 to 9.15). To analyse this divergence, the wave arrival times are roughly estimated in the following. The epicentral and hypocentral distances are both approximately 12km. So, the distance $\tilde{d}$ of the shortest wave propagation path is estimated by $\tilde{d} = \sqrt{(12\text{km})^2 + (12\text{km})^2} \approx 17\text{km}$. Assuming that the velocities of the *P*-, *S*- and Rayleigh wave are constant for the entire wave propagation path and have values from about $c_P = 6\text{km/s}$, $c_S = 3.5\text{km/s}$, and $c_R = 3.25\text{km/s}$, the wave arrival times τ can be roughly estimated as

$$\tau_p \approx \frac{\tilde{d}}{c_P} = \frac{17\text{km}}{6\frac{\text{km}}{\text{s}}} = 2.83\text{s}\,, \quad \tau_s \approx \frac{\tilde{d}}{c_S} = \frac{17\text{km}}{3.5\frac{\text{km}}{\text{s}}} = 4.86\text{s}\,, \quad \tau_r \approx \frac{\tilde{d}}{c_R} = \frac{17\text{km}}{3.25\frac{\text{km}}{\text{s}}} = 5.22\text{s}\,. \tag{9.5}$$

To compare the synthetic ground motion with the record, the curves of the simulated motion were shifted in time to accord with the main characteristics of the record's motion. This time shift from about 10.57s is added to the arrival times τ. In Fig. 9.18, the acceleration curves from Fig. 9.13 are compared and the arrivals of the waves are marked by dashed lines.

It can be seen that the deviating motion occurs before the arrival of the first wave, i.e., the *P*-wave. From this fact the conclusion can be drawn that the early motion of the record (encircled by a dash-dot line in Fig. 9.18) is due to a previous smaller earthquake, that is not simulated here.

Conclusion: The results of the simulation show a good accordance with the recorded motions. This indicates that on the one hand, the utilised model seems to be appropriate for the analysed problem and, on the other hand, that the parameters for performing this simulations were chosen reasonably. The here introduced method can be employed to model seismic ground motion close to reality.

9.3.6 Strains and stresses for varying maximum resolving frequency $f_{\max}$

As discussed above, a key input parameter for the computation of the Green's functions by the DWFEM is the maximum resolving frequency $f_{\max}$. The ground motion simulations performed in this section

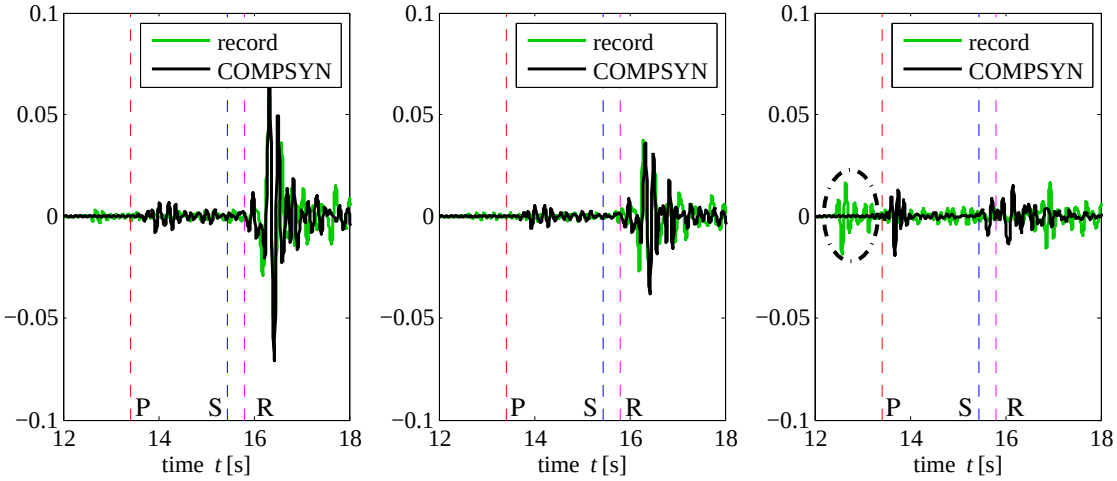

Figure 9.18: Recorded and simulated acceleration time-history (same as Fig. 9.13) with marked wave arrival times after Eq. (9.5) (P: *P*-wave, S: *S*-wave, R: Rayleigh wave).

were performed for two of those frequencies, namely $f_{\max}$=10Hz and $f_{\max}$=20Hz.

During the computation procedure, it was realised that the simulation for $f_{\max}$=20Hz is computationally very expensive. Although, the verification of the synthetic ground motion has to be computed for only one receiver point, the generation of the seismic input for the lifeline analysis enforces the computation at every FE node on the two adjacent interfaces Γ and Γ_e of the DRM. The entire computation with frequencies up to $f_{\max}$=20Hz is very expensive for this large amount of receiver points. Moreover, the simulation up to $f_{\max}$=20Hz might not be very reasonable because the velocity structure of the earth's crust can be mapped only very roughly. Thus, smaller local features on the seismic wave propagation path, which actually dominate the wave field at high frequencies, cannot be incorporated. However, the evaluation of the ground motion parameters and the envelopes of the time- and frequency-histories indicate no significant difference for $f_{\max}$=10Hz and $f_{\max}$=20Hz. Hence, is assumed to be justifiable that the simulations in the subsequent chapter for deriving the input excitation of the near-field of the lifeline are performed with the maximum resolving frequency $f_{\max}$=10Hz.

Regardless of this reasoning, it has to be assured that the final results of the simulation, i.e., the stresses and the strains in the pipe walls, do not change significantly for resolving frequencies above $f_{\max}$=10Hz. This will be demonstrated in the following by analysing the maximum strains and stresses of a buried continuous lifeline by means of the multi-method approach (see Sec. 7.5) on basis of the DRM.

Near-field model: Whereas in step I of the DRM, the large scale model for simulating the $M_w = 4.25$ earthquake is utilised, the hybrid FE-SBFEM is used in step II to determine the dynamic response of the soil-pipeline system in order to receive the strains and stresses in the pipe. The bisected FE model of the near-field containing soil and pipeline is depicted in Fig. 9.19(a), whereas the FE mesh of the pipeline is shown in Fig. 9.19(b).

The linear elastic material parameters for the soil (E_s, ν_s, ρ_s) and the pipeline (E_p, ν_p, ρ_p) are listed in Tab. 9.8. Additionally, the wall thickness t_p of the pipeline, the pipe diameter d_p and the burial depth h_b of the pipeline are given. The computational parameters which were discussed before are quoted in Tab. 9.9. The HHT-α time-integration parameters are chosen as $(\alpha;\beta;\gamma)$=(-0.3333;0.4444;0.8333) which

Table 9.8: Material and design parameters.

pipe	$E_p\left[\frac{\text{GN}}{\text{m}^2}\right]$	ν_p[-]	$\rho_p\left[\frac{\text{kg}}{\text{m}^3}\right]$	t_p[m]	d_p[m]	soil	$E_s\left[\frac{\text{MN}}{\text{m}^2}\right]$	ν_s[-]	$\rho_s\left[\frac{\text{kg}}{\text{m}^3}\right]$	h_b[m]
steel	210	0.3	7850	0.01	0.5		272	0.45	1947	2.0

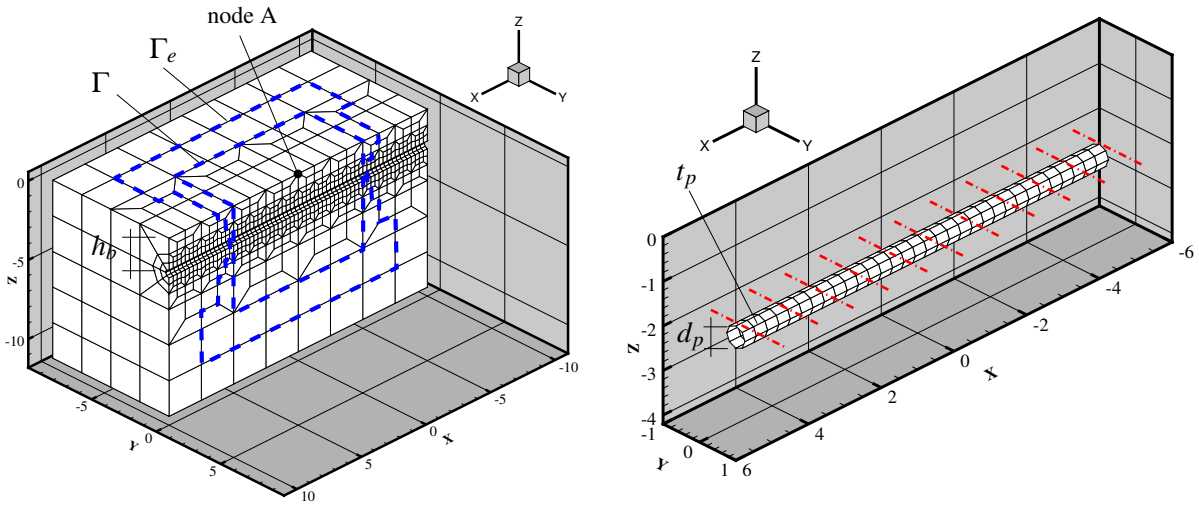

(a) FE mesh of the near-field domain featuring soil and pipeline. The interface Γ and Γ_e are marked as well as the burial depth h_b.

(b) FE mesh of the buried pipeline of thickness t_p and diameter d_p. The subdivision into the sections for which the strains and stresses are evaluated is marked with dash-dotted lines.

Figure 9.19: FE meshes of the near-field domain.

Table 9.9: Parameters for hybrid FE-SBFE computation.

FEM			SBFEM			time	
nodes	brick FEs	shell FEs	N_S	nodes	elements	$t_{\max}$ [s]	Δt [s]
2853	2096	256	2	$2 \cdot 153$	$2 \cdot 132$	11.25	$2.5 \cdot 10^{-4}$

is the lower limit of those parameters (see Sec. 5.4.2) The computation of SBFEM influence matrices are performed with the tolerances ε_z=$1 \cdot 10^{-4}$ and ε_t=$1 \cdot 10^{-5}$.

In Fig. 9.19(a) the interfaces Γ and Γ_e are marked. For all FE node locations on those interfaces, the ground motion has to be computed in DRM-step I, i.e., by the seismic large scale model described before. The interface Γ exhibits 119 nodes and the adjacent interface Γ_e 299 nodes. At all of those nodes, the ground motion is simulated in order to determine the forces which are equivalent to the original seismic rupture excitation. The analysed near-field domain is positioned as sketch in Fig. 9.20. So the propagation direction of the seismic waves is parallel to the longitudinal direction of the pipeline.

Motion depending on $f_{\max}$: The large scale simulation, i.e., the computation of the motion on the interfaces Γ and Γ_e, is performed for varying maximum resolving frequencies below and above $f_{\max}$=10Hz. Namely, four simulations are performed for $f_{\max}$=5Hz, 8Hz, 10Hz and 12Hz. This simulations are performed in order to analyse at what resolving frequency $f_{\max}$ the strains and stresses do not exhibit significant changes with increasing $f_{\max}$.

To observe the difference in the simulated motion due to the changing maximum resolving frequencies $f_{\max}$, the resulting surface ground motion of node A (see Fig. 9.19(a)) is plotted in Fig. 9.21. The time-histories of the motion with lower maximum frequencies $f_{\max}$ exhibit a more oscillating progression, whereas the simulated motions which contain also higher frequency-contributions develop more smoothly. Latter is due to the superposition of the lower and higher frequency-contents.

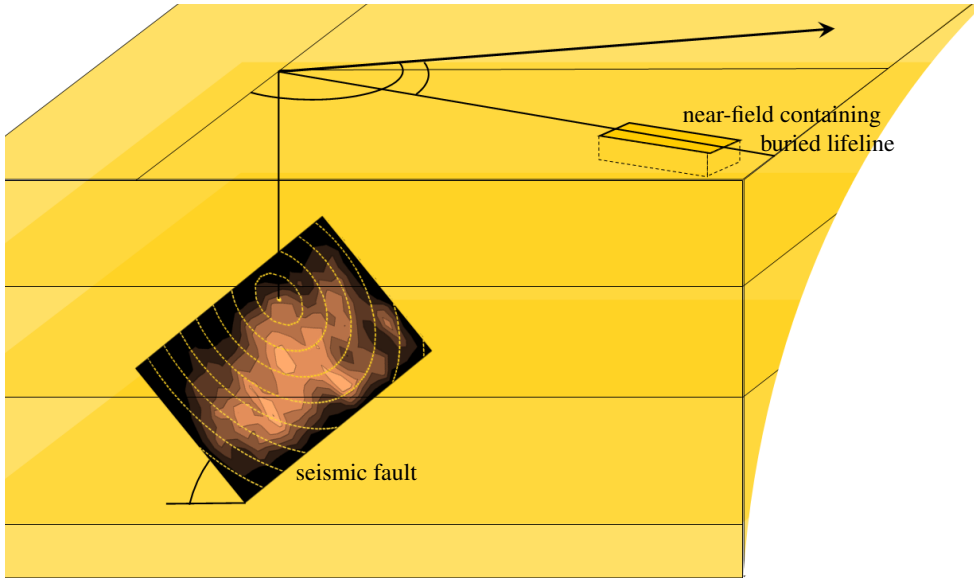

Figure 9.20: Sketch of the position of the near-field in the large scale model of the earth crust.

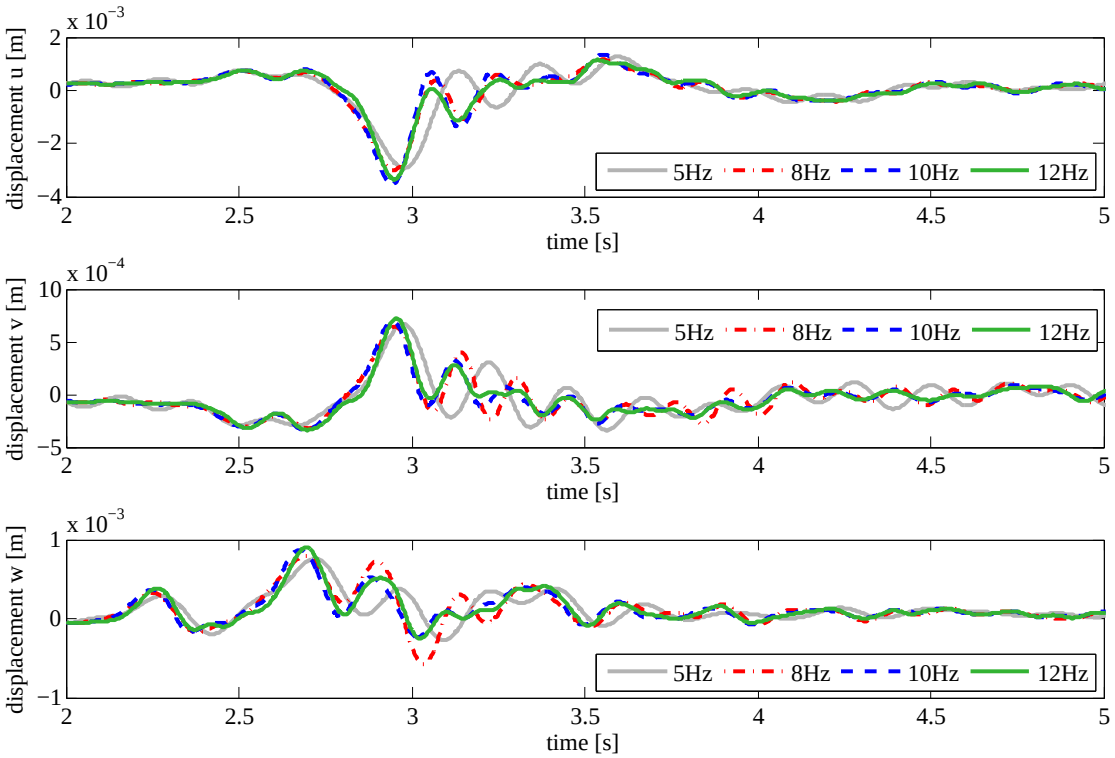

Figure 9.21: Temporal displacement progressions simulated at node A for varying maximum resolving frequencies $f_{\max}$=5Hz, 8Hz, 10Hz and 12Hz.

Evaluation of the maximum strains and stresses: In this section, the strains and stresses in the pipeline in the near-field domain shall be analysed. Therefore, the pressure strains ε_p and the von Mises stresses σ^{Mises} are determined and their maximum value is evaluated at every discrete FE node of the pipeline. To reduce the number of output values, the pipeline is subdivided into a certain number of sections. For each of those sections, the maximum value of the strains and of the stresses are assigned. Those maximum values per section are plotted along the longitudinal pipe axis as done in Fig. 9.22. Thereby, it does not matter at which node of the section the maximum values appear, e.g., whether the node is located on the top, on the side, or on the bottom of the pipelines's cross section.

Here, the 10m continuous pipeline is divided into 10 sections, each measuring the length of 1m. The resulting maximum values per pipe section for the varying maximum resolving frequencies are depicted in Fig. 9.22. Since waves, which contain higher frequencies, induce differing motions of points of

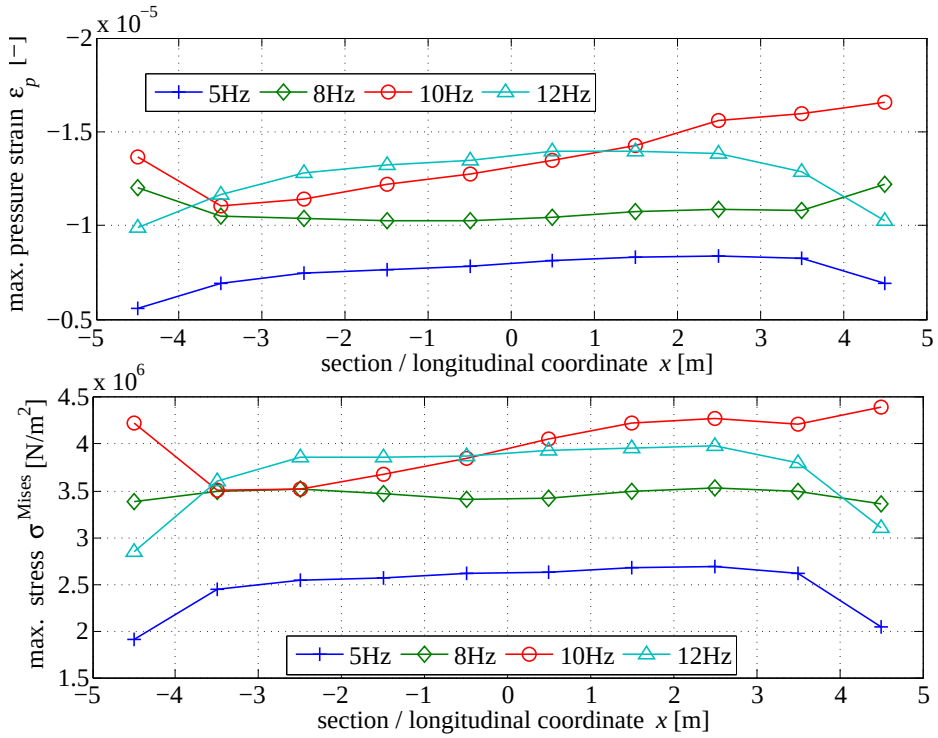

Figure 9.22: Maximum pressure strains ε_p and von Mises stresses σ^{Mises} in the pipeline sections marked in Fig. 9.19(b) for varying maximum resolving frequencies $f_{\max}$=5Hz, 8Hz, 10Hz and 12Hz. The seismic waves incident from the right.

neighbouring positions, higher strains and stresses are expected for higher resolving frequencies. This behaviour can be realised in Fig. 9.22. The maximum strains and stresses, e.g., for $f_{\max}$=5Hz reach about half of the values of $f_{\max}$=12Hz. For $f_{\max}$=5Hz, 8Hz, and 10Hz, it can be stated that also the maximum strains and stresses increase with an increasing maximum resolving frequency $f_{\max}$.

Comparing the values for $f_{\max}$=10Hz and 12Hz, it can be observed that they range in the same interval. Nevertheless, whereas the values for $f_{\max}$=12Hz are, except at the ends of the pipeline, more or less the same for every section, the values for $f_{\max}$=10Hz increase with increasing coordinate x. In Fig. 9.22, the waves arrive from the right and travel to the left. This is the reason why the maximum values on the right of Fig. 9.22 are greater than on the left for $f_{\max}$=10Hz. Observing the entire distributions of $f_{\max}$=10Hz and 12Hz in Fig. 9.22, it is recognised that the values do not change significantly. It is assumed that the maximum strains and stresses will stay in this range also for higher maximum resolving frequencies. Hence, for the following simulations, performed in the subsequent chapter, the maximum resolving frequency will be set to $f_{\max}$=10Hz.

10 Applications and parameter studies

After the studies of computational aspects and the earthquake simulation, both performed in Chap. 9, extended analyses of the dynamic response behaviour of seismic excited underground lifelines are performed in the present chapter. In order to determine pipeline failures, the strains and stresses of an existing straight lifeline exposed to an earthquake are analysed with the multi-method approach from Sec. 7.5. The seismic excitation of the lifeline is caused by a medium earthquake (Sec. 10.1) and a strong earthquake (Sec. 10.3). The medium earthquake of magnitude M_w=4.25 is the real one from Sec. 9.3, whereas the strong earthquake of magnitude M_w=5.9 is artificially generated by means of the probabilistic treatment from Sec. 10.2. After those analyses, parameter studies are performed to illuminate the influences of the position and the construction details of the pipeline (Sec. 10.4) as well as the pipe design parameters (Sec. 10.5). Apart from the straight pipeline, a tee joint connection is studied, in Sec. 10.6. Thereupon, in Sec. 10.7 the probability of failure of the straight pipeline is examined by means of the probabilistic concept introduced in Sec. 8.4.

10.1 Straight pipeline excited by M_w=4.25 earthquake

In Sec. 9.3, a real earthquake with magnitude M_w=4.25 was simulated and the computational results were compared to records observed at a seismic station in the city of Forlì. In the present section, the dynamic response of an existing underground lifeline in the vicinity of this station is simulated.

The analysed lifeline is a straight steel pipeline which is of major importance for the water maintenance of Forlì. Fig. 10.1 shows a detail of the map of Forlì with the lifeline network and the location of the seismic station where the earthquake was recorded. The analysed straight pipeline is marked by a dashed line. Additionally, a tee joint is signed which will be analysed in Sec. 10.6.

The near-field model of the pipeline analysed here is depicted in Fig. 10.2. The material parameters of

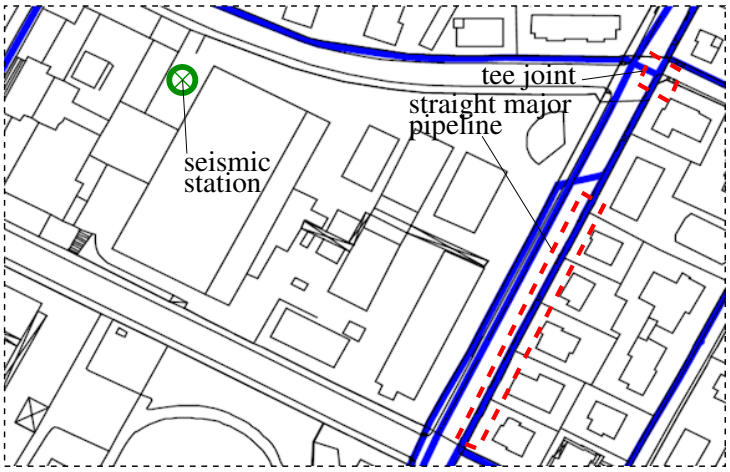

Figure 10.1: Map of Forlì exhibiting the seismic station and the lifeline network (indicated in blue). The analysed parts of the network are marked.

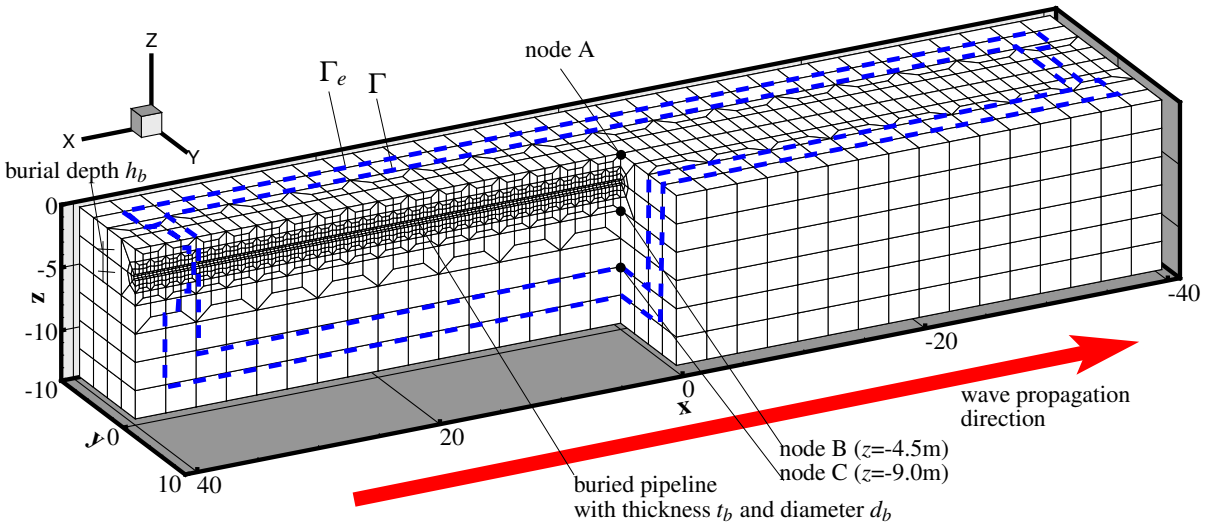

Figure 10.2: FE mesh of the near-field of the straight continuous buried pipeline under consideration. The burial depth h_b is marked as well as the design parameters t_b and d_b. The dashed lines highlight the DRM interfaces Γ and Γ_e. The nodes A, B and C are located at coordinates x=y=0 and different z.

Table 10.1: Material and design parameters.

pipe	$E_p\left[\frac{\text{GN}}{\text{m}^2}\right]$	ν_p[-]	$\rho_p\left[\frac{\text{kg}}{\text{m}^3}\right]$	t_p[m]	d_p[m]	soil	$E_s\left[\frac{\text{MN}}{\text{m}^2}\right]$	ν_s[-]	$\rho_s\left[\frac{\text{kg}}{\text{m}^3}\right]$	h_b[m]
steel	210	0.3	7850	0.01	0.5		272	0.45	1947	2.0

the existing pipeline are listed in Tab. 10.1 where the soil parameters which were derived from down-hole tests (see Sec. 9.3.3) are also specified.

The computational parameters for the analysis of the near-field with the hybrid FE-SBFEM are listed in Tab. 10.2. The HHT-α time-integration parameters are chosen as ($\alpha;\beta;\gamma$)=(-0.3333;0.4444;0.8333) and the computation of SBFEM influence matrices is performed with the tolerances ε_z=1·10^{-4} and ε_t=1·10^{-5}. Those parameters will be constant throughout all simulations performed in this chapter.

Table 10.2: Parameters for hybrid FE-SBFE computation.

FEM			SBFEM			time	
nodes	brick FEs	shell FEs	N_S	nodes	elements	$t_{\max}$ [s]	Δt [s]
12182	8640	1792	4	2 · 212 + 2 · 231	2 · 188 + 2 · 200	11.25	2.5·10^{-4}

In Fig. 10.2, the adjacent interfaces Γ and Γ_e of the DRM are marked by dashed lines. For every FE node on those interfaces, the seismic ground motion for the Forlì earthquake of magnitude M_w=4.25 which was addressed in Sec. 9.3 is simulated. The number of nodes are 447 on Γ and 731 on Γ_e. The equivalent seismic forces are determined by means of Eq. (9.3) an applied to those nodes. In the large scale model, the near-field location and position is similar to the one sketched in Fig. 9.20. So, the pipeline is oriented such, that its longitudinal direction coincidences with the seismic wave propagation direction (see Fig. 10.2).

The aim of the following investigation is to compare the simulated ground motions resulting from different models in order to verify their ability to map the seismic wave propagation in the near-field and to check the effects of the buried lifeline on the ground response. Further, it is controlled whether the strains and stresses in the pipe walls exceed their limit values given in Sec. 8.2.1.

Surface ground motion: The simulated surface ground motions at node A (see Fig. 10.2) is studied. Therefore, three near-field simulations are performed. In the first, the near-field as depicted in Fig. 10.2 is analysed by means of the hybrid FE-SBFEM. In the two other simulations, a free-field domain, i.e., a near-field that consists only of soil, is analysed. The domain has the same dimensions as the one containing the pipeline from Fig. 10.2. The free-field simulations are preformed with the hybrid FE-SBFEM and with the pure FEM, respectively. In latter, static displacement boundary conditions are prescribed at the boundaries of the near-field, i.e., wave transmission to the far-field is disabled. The fixed degrees of freedom are $u = 0$ at the side boundaries parallel to the y-axis, $v = 0$ at the side boundaries parallel to the x-axis and $u = v = w = 0$ at the bottom boundary.

In Fig. 10.3, the resulting displacements at node A of those near-field simulations are compared to the large scale simulation's results from Sec. 9.3. For comparison reasons, the large scale ground motion is transformed to the coordinate system of the near-field (angle=120°).

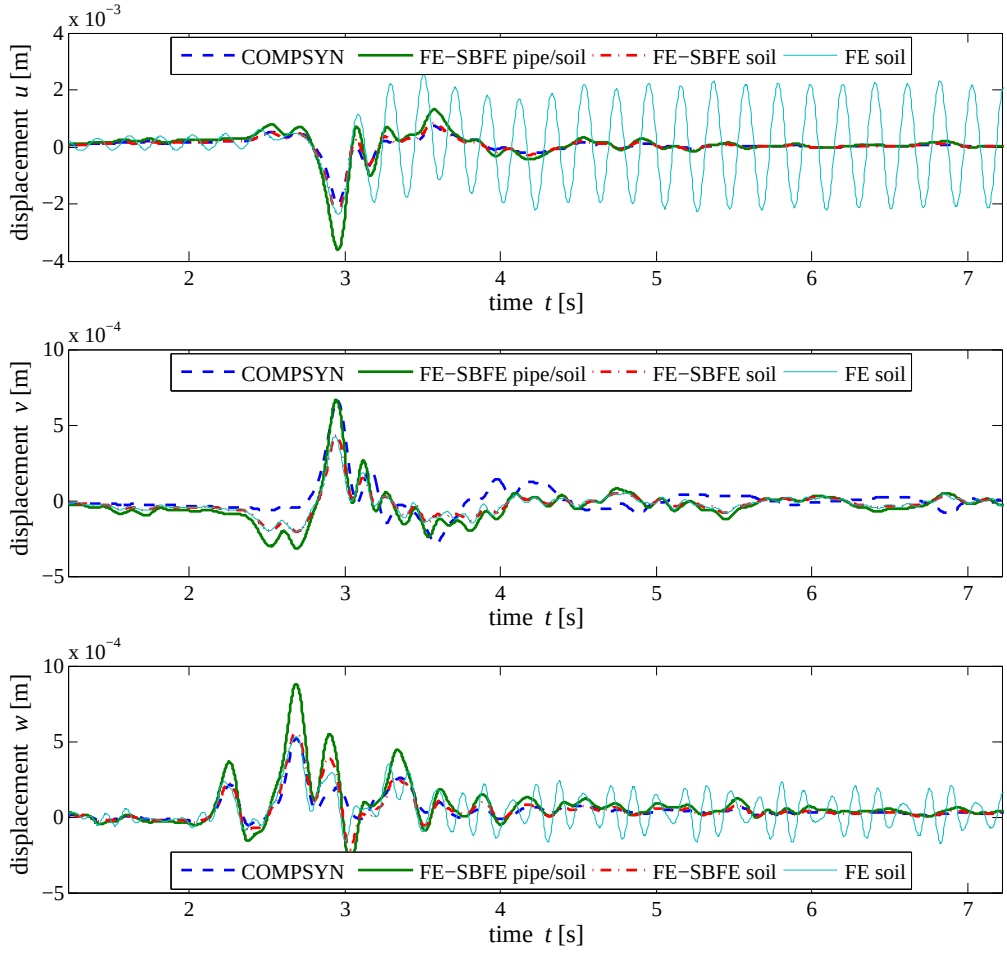

Figure 10.3: Simulated displacements at node A (see Fig. 10.2) excited by the $M_w = 4.25$ Forlì earthquake. Comparison of the large scale simulation results (COMPSYN) with the results of the reduced near-field modelled by the hybrid FE-SBFEM for two cases: with the pipeline (FE-SBFE pipe/soil) and without (FE-SBFE soil). The near-field without pipeline is also modelled by the pure FEM (FE soil) without the SBFEM, which enables the wave radiation.

The displacements u and w of the pure FEM simulation exhibit a strongly oscillating response. As discussed before, this oscillation is due to the wave reflections at the boundaries of the near-field. The oscillation shows that it is necessary to employ absorbing boundary conditions, like the SBFEM, in order to simulate an undisturbed dynamic response in the near-field. The results of the two hybrid FE-SBFE simulations are similar to the results of the large scale simulation. Considering the x- and z-direction, the FE-SBFE free-field simulation matches the large scale simulation almost perfectly, whereas the FE-

SBFE simulation of the pipeline embedded in the soil exhibits larger maximum amplitudes. Looking at the y-direction, the free-field results are slightly smaller than the large scale simulation results, whereas the pipe-soil domain results behave conformable to the ones of the large scale simulation.

The good accordance of the free-field FE-SBFEM results and the large scale simulation shows the effectiveness of the DRM. The quantitative difference of the pipe-soil domain results compared to the large scale simulation results exhibits the influences of the local features, i.e., the buried pipeline, in the reduced domain of the second step of the DRM. In other words, the ground motion is affected by an embedded pipeline.

Wave propagation in the near-field: Due to the location of the near-field at the surface, surface waves, in particular Rayleigh waves, are expected to arise. Since the induced seismic waves propagate along the x-axis, the soil particle's motion induced by Rayleigh waves proceeds in the x-z-plane. Fig. 10.4 shows the x-z-motion for the three nodes A, B and C which are marked in Fig. 10.2 at different depths z. For all three positions, the elliptical motion can be recognised which is characteristic for Rayleigh waves. Further, a decay of amplitudes with increasing depth is obvious which is a property of Rayleigh waves as well (compare Fig. 2.2(a)).

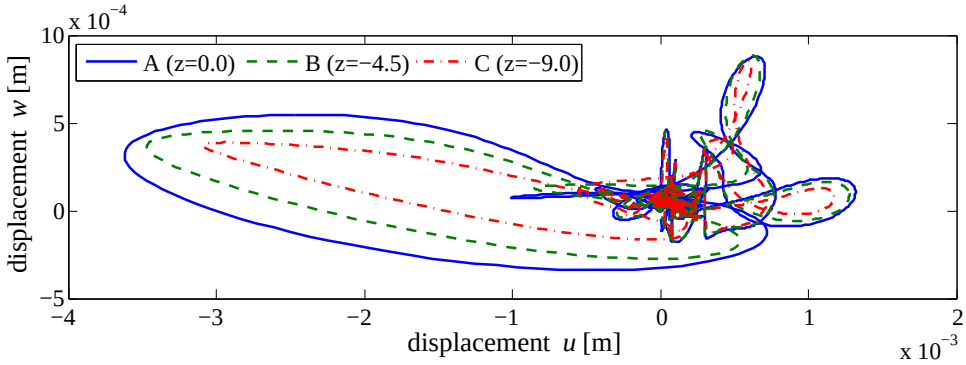

Figure 10.4: Displacements in x-z-plane at nodes A, B and C from Fig. 10.2. The typical elliptical motion of Rayleigh waves is shown. The dissipated energy which is proportional to the encircled area decreases with decreasing z-coordinate.

The Euclidean norm of the displacement vector is defined as the square root of the sum of squared displacement components $|\mathbf{u}| = \sqrt{u^2+v^2+w^2}$. The contour plots for $|\mathbf{u}|$ are depicted in Fig. 10.5 for discrete time-stations. It can be seen that the seismic motion is only introduced into the domain which is located inside of the interface Γ (compare Fig. 10.2). Outside of the interface Γ_e, the motion is nearly at rest. This is due to the derivation of the DRM where only the relative motion $\mathbf{w}_e$ is considered outside of the interface Γ_e (see Sec. 7.2.1). The strongest motion occurs at time t =2.95s where also a relative motion $\mathbf{w}_e$ outside of Γ_e can be detected which is not neglectable. This motion is caused by the localised feature in the near-field, i.e., by the pipeline. To prevent unwanted waves in the region of interest around the pipeline, the relative motion $\mathbf{w}_e$ needs to be permitted to leave the near-field domain. This is achieved by incorporating the SBFEM at the near-field/far-field interface, so that the outgoing waves can be absorbed there. The successful absorption can be seen for later times, e.g., for t =3.35s, where the outer motion $\mathbf{w}_e$ is close to zero. Thus, no waves are trapped inside the near-field. This shows that the SBFEM is able to model the wave-radiation into the far-field and acts successfully as absorbing boundary condition.

Generally, a non-uniform ground motion can be recognised in the inner domain. The motion due to the different waves can be roughly observed. The arrival of the body waves can be noted at time t =2.15s where the near-field performs a nearly uniform motion. At time t =2.75s, surface waves incident in the near-field domain from the left. As was discussed before, these are the Rayleigh waves. They induce a non-uniform motion as it is, e.g., depicted in Fig. 10.5 for the time t =3.35s.

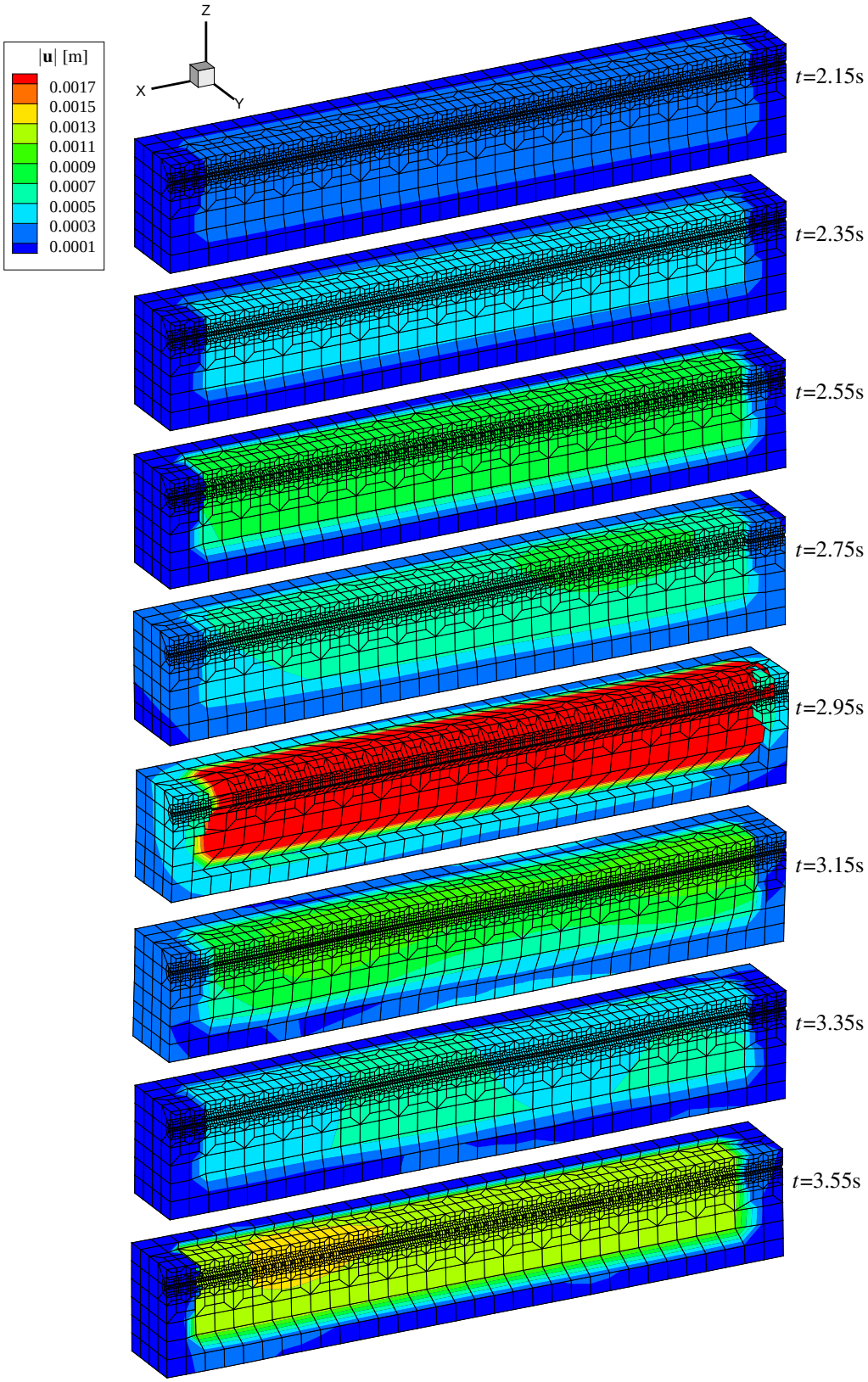

Figure 10.5: Wave propagation in the near-field which is excited by the equivalent seismic forces of the DRM. Those forces introduce the simulated seismic motion of the Forlì earthquake of magnitude M_w =4.25 into the near-field. For representation reasons, the model is bisected along the x-axis and the displacements are magnified by the factor 1000. The contours are plotted for $|\mathbf{u}| = \sqrt{u^2+v^2+w^2}$.

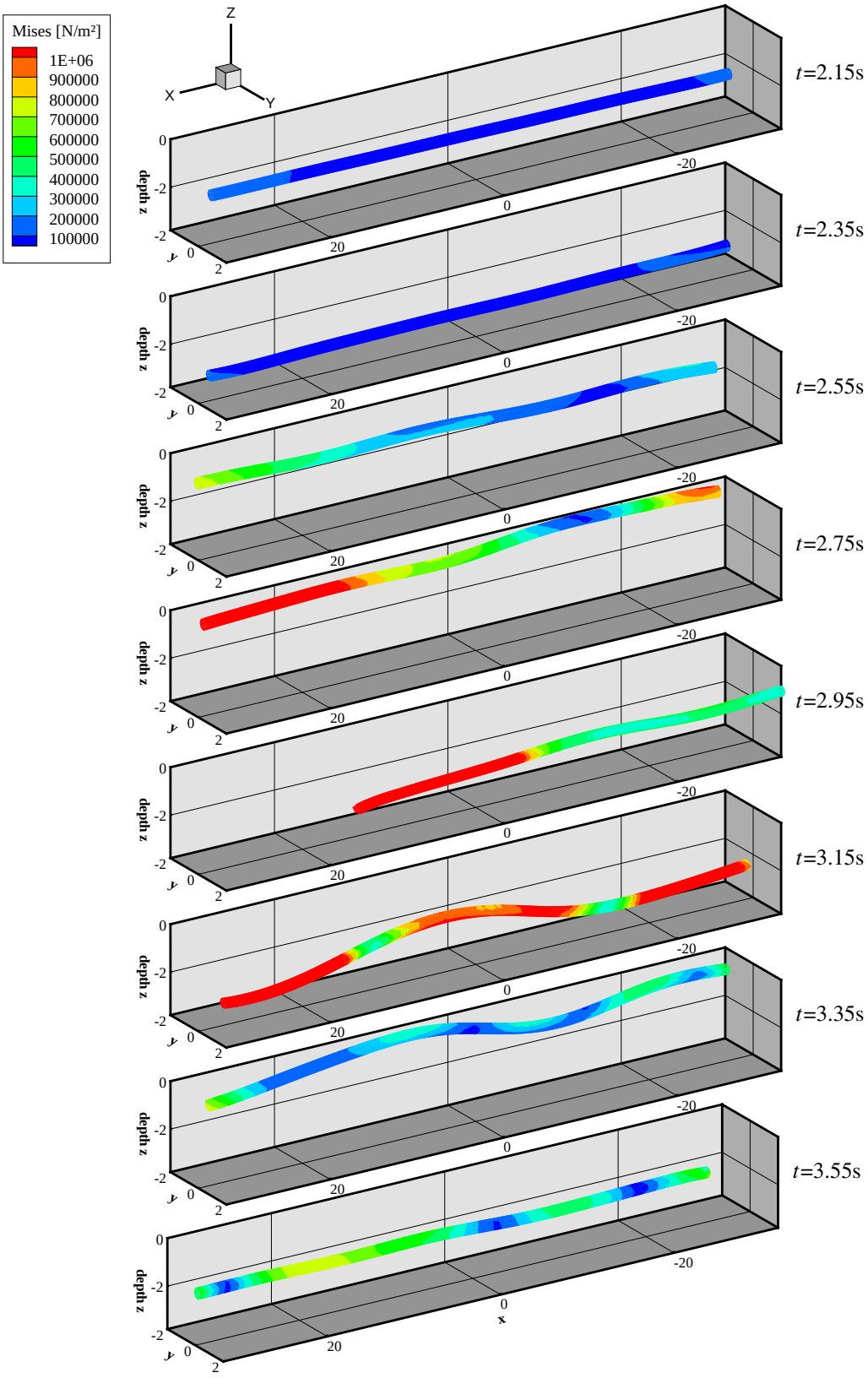

Figure 10.6: Von Mises stresses in the deformed pipeline caused by the M_w=4.25 earthquake. The representation of the displacements is magnified by the factor 5000.

Strains and stresses in the pipeline: The buried pipeline analysed here is continuous. Since the near-field does not cover the entire length of this pipeline, attention has to be paid to the truncation boundaries where the modelling of the pipeline ends, but the actual pipeline does not. As can be seen in Fig. 10.5, the seismic wave propagation is simulated only within the domain which is bordered by the interface Γ (see Fig. 10.2). In order to study the effects on the dynamic response of the pipeline, two cases of truncation of the pipeline model are examined. In the first case, the pipeline model reaches outside of the interface Γ, whereas the pipeline model is truncated at this interface Γ in the second case. The two cases are sketched in Fig. 10.7.

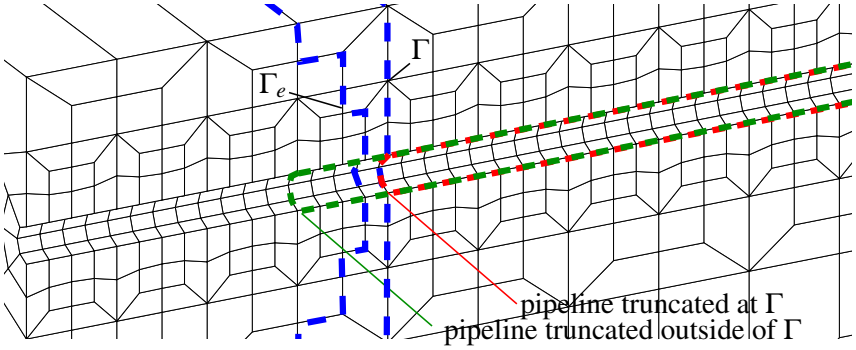

Figure 10.7: Zoom of bisected FE mesh from Fig. 10.2. The boundaries where the two analysed pipeline models are truncated are marked.

For the evaluation of the maximum strains and stresses, the pipeline is divided into sections, as explained in Sec. 9.3.6. For each of those sections, the maximum values of strains and stresses are determined. So, the pipeline which measures 70m in the inner domain bounded by Γ, is subdivided into 70 sections each of 1m length. The resulting maximum strains and stresses are depicted in Fig. 10.8.

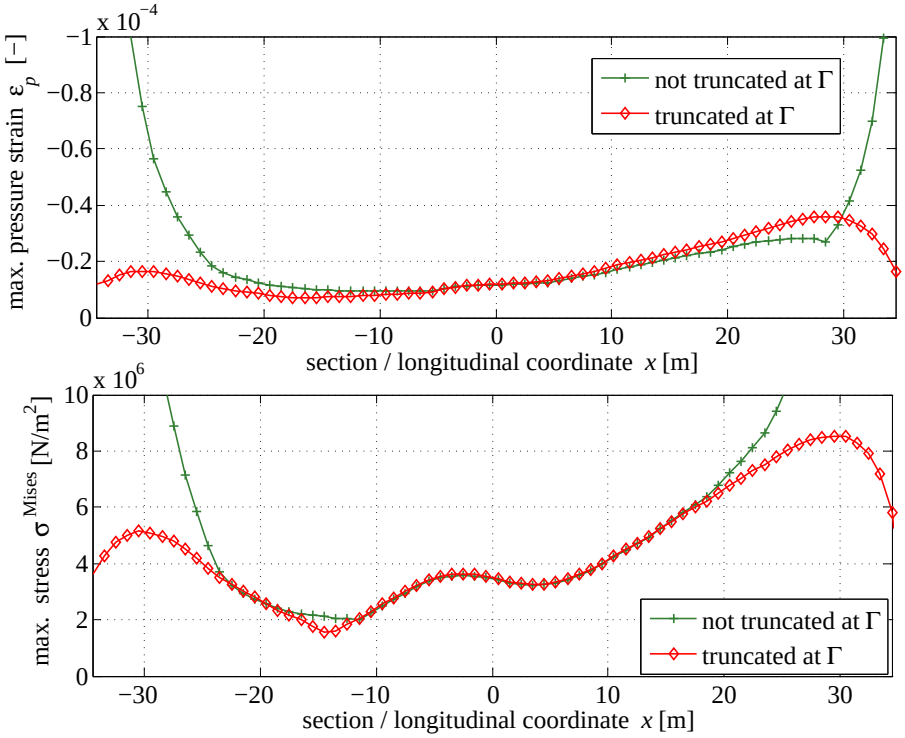

Figure 10.8: Maximum pressure strains ε_p and von Mises stresses σ^{Mises} in the pipeline sections of 1m length. The seismic waves incident from the right.

Comparatively large strains and stresses can be observed for the pipeline model that is not truncated at Γ. This is expected since the pipeline crosses both adjacent DRM interfaces Γ and Γ_e. As discussed in Sec. 7.2.1 and depicted in Fig. 10.5, the domain outside of Γ_e is nearly at rest whereas the domain

inside of Γ is seismically excited. This difference in motion between inner and outer domain induces high strains and stresses in the pipeline, which are partly transferred to the inner domain. In contrast, the strains and stresses in the pipeline model which is truncated at Γ decrease at these truncation boundaries. The realistic strain and stress distribution might be in between of those two extreme cases. Anyway, in the region from about -20m to 20m, the strains and stresses accord well for both cases of truncation. Thus, model-independent, i.e., realistic distributions of the strains and stresses can be assumed in this region. For the subsequent evaluations of the maximum values of strains and stresses, the pipeline is modelled with the truncation boundaries at Γ.

The yield stress of steel is f_y=235.0 MN/m^2 and the maximum allowable strain is derived from Eq. (8.7) as $\varepsilon_p^{\text{lim}}$=0.7%. As can be seen in Fig. 10.8 for the considered pipeline model, those values are not reached and, thus, the pipeline does not fail. Anyhow, as can be seen, the strains and stresses have their highest values in the part of x=20-35m. This is the part where the seismic waves incident (from the right in Fig. 10.8). This distributions exhibit that the high strains and stresses are induced by waves propagating parallel to the surface. These are mainly surface waves and not body waves which incident from below and would move the pipeline uniformly and, thus, would not induce high stresses over the pipeline's length. Thus, it is essential to simulate the excitation by surface waves which cannot be achieved by simpler models as sketched in Figs. 4.7(b) and 7.1(b).

The contour plot of the von Mises stress distribution in the pipeline which is truncated at Γ is depicted in Fig. 10.6. It can be recognised that the largest stress values are not reached at the same time as the largest motion, i.e., at t =2.95s, but at t =3.15s. The bending deformation in the pipeline that lead to those stresses can be clearly realised in Fig. 10.6 at t =3.15s. This bending is due to the motion induced by the Rayleigh waves (see Fig. 10.5 at t =3.15s).

Concluding, it can be stated that the wave propagation is modelled realistically in the near-field. Thereby, the model dimensions of the pipeline are decisive. Nevertheless, since the same distribution of strains and stresses can be observed at a certain distance from the truncation boundaries, the model-dependency vanishes when the near-field domain is modelled adequately large. The distribution of strains and stresses indicates that the seismic excitation requires an advanced modelling as performed here. Simpler models would not be appropriate. Nevertheless, strains and stresses that would lead to a failure of the pipeline are not reached. Thus, the dynamic response due to a stronger seismic excitation should be studied.

10.2 Probabilistic earthquake generation

So far, a real earthquake with a medium magnitude of $M_w = 4.25$ was simulated as seismic excitation to the near-field domain containing the pipeline. This earthquake does not have the potential to lead to a failure of the analysed steel pipeline. Hence, an artificial earthquake is generated by means of a probabilistic treatment in order to generate a seismic input to the near-field that is more likely to damage an underground pipeline.

Procedure: The procedure is based on a probabilistic approach. Initially, an earthquake scenario is established by means of the seismic history of the region of interest. In other words, the parameters of an historical event that is likely to have a certain return period are selected as basis for the procedure. With those parameters, a model of the seismic source and for the earth crust is established as done in Sec. 9.3.

Starting from this earthquake source model, which is up to now deterministic based, a special treatment is performed to incorporate the probabilistic aspects of the seismic excitation. Firstly, a random slip model for the finite seismic fault is generated following the stochastic-deterministic k^2-model from Sec. 7.4.2. The random parameters are the phase angle ϕ in Eq. (7.45) and the position of nucleation point on the fault. With this randomly generated slip distribution, the PGV is computed at the desired location by utilising the large scale earthquake model. The ground motion parameter PGV is chosen since it is commonly connected to the failure of buried pipelines in literature, e.g., in [O'Rourke, 1995; Davis and Bardet, 2000].

The generation of the random slip distribution as well as the simulation of the PGV are executed for a certain number of realisations and the PGVs are assembled by their relative frequency. From this relative frequency, the random moments μ_{Xm} of the random variable X=PGV are computed by means of Eq. (8.21). When the so calculated moments up to order three, i.e., the mean μ_X, the variance σ_X and the skewness ν_X, do not change further in value when evaluating more realisation results to the relative frequency, the generation procedure is stopped. From the random moments, a probability distribution is approximated which is used as the basis for the seismic input. For a deterministic analysis of the near-field, the earthquake which generates the mean μ_X is employed. For a probabilistic analysis, the derived probability distribution of the PGV can be used directly, e.g., when the PEM is incorporated as in Sec. 10.7.

Generation: To exemplify the procedure of the probabilistic treatment and to generate an artificial seismic excitation of high magnitude, an earthquake scenario for Forlì is modelled. Fig. 10.9 from [Gruppo di lavoro CPTI, 2004] shows a compilation of historical earthquakes that stroke Forlì. It can be realised that maximum seismic events from intensities larger than 7 on the MCS-scale frequently occur with an approximate return period of 200 years. From this diagram, the event from April 11th, 1688 was chosen in the following to be the prototype of the artificial seismic excitation.

Whereas the acquisition from [Cinti *et al.*, 2004] gives information about the magnitude of this event ($M_w = 5.9$), the catalogue of [Istituto Nazionale di Geofisica e Vulcanologia, 2007] provides information about the location. These data are listed in Tab. 10.3. Recalling that Forlì is geographically located at

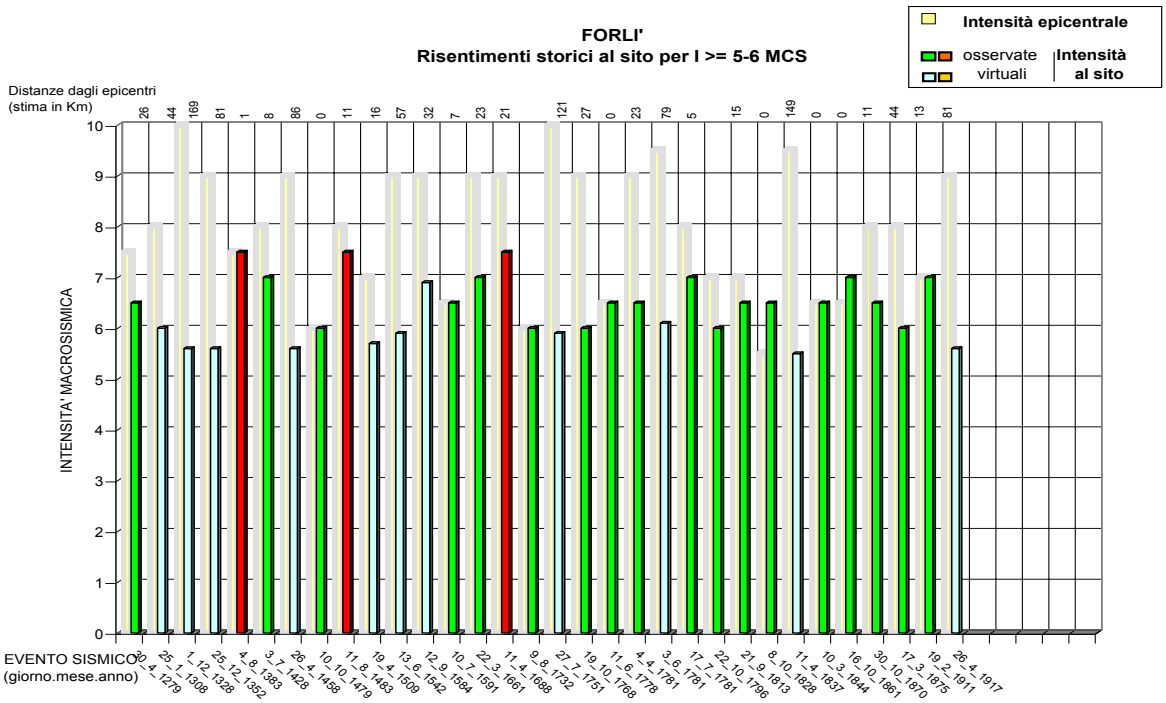

Figure 10.9: Compilation of historical earthquakes in Forlì from [Gruppo di lavoro CPTI, 2004].

Table 10.3: Source parameters of the M_w =5.9 earthquake according to [Cinti *et al.*, 2004] and [Istituto Nazionale di Geofisica e Vulcanologia, 2007].

time (UTC)	M_w	latitude	longitude	hypocentral depth $\hat{h}$	strike $\hat{\phi}$	dip $\hat{\delta}$	rake $\hat{\lambda}$
11/04/1688	5.9	44.38N	011.95E	12.0 km *	114° *	55° *	83° *

* assumed to be the same as for the M_w=4.25 earthquake

Table 10.4: Calculated source parameters following the scaling laws from Sec. 7.4.1.

M_w	M_0 [Nm]	S [km^2]	L [km]	W [km]	v_R [km/s]	τ_R [s]	$[\bar{u}]$ [m]	$[\bar{\sigma}]$ [MN/m^2]
5.9	$8.81 \cdot 10^{17}$	92.90	13.63	6.82	2.8	2.29	3.10	12.16

Table 10.5: Computational input parameters for the M_w=5.9 earthquake simulation.

Earth						Fault points	
f_{max} [Hz]	R_{max} [km]	t_{max} [s]	Δt [s]	k_{max} [1/m]	FE nodes	x	z
10	140.0	32.77	0.002	20000	686	69	35

the latitude 44.22N and the longitude 012.05E, the epicentral distance to the analysed earthquake source is 19.49km and the azimuth is 335°NW. According to Sec. 7.4.1, the source parameters are calculated as listed in Tab. 10.4.

Starting from this earthquake source model, which is up to now deterministic based, the procedure for generating a probabilistic earthquake is performed. So, a random slip model for the finite seismic fault is generated following the k^2-model and the PGV at the location of the seismic station in Forlì is simulated. The simulation is performed by the large scale model which is used in Sec. 9.3. The computational input parameters for the present simulation are listed in Tab. 10.5.

To analyse the probability distribution of the generated seismic input, it is necessary to determine the parameters that characterise this distribution. Those parameters are the moments of the probability distribution. The random moments μ_X, σ_X, and ν_X of the observed relative frequency of the simulated PGV are listed in Tab. 10.6 in dependency of the maximum realised number of large scale simulation runs.

Table 10.6: Random moments for the random variable X=PGV derived from the relative frequencies after the stated number of realisations of the large scale simulation.

number of realisations	μ_X [cm/s]	σ_X [cm/s]	ν_X [-]
1000	83.67	82.41	1.64
2000	82.78	80.95	1.73
3000	82.16	79.69	1.68
4000	81.91	78.37	1.64
5000	82.27	78.22	1.60

It can be recognised that all three moments do not change significantly for the displayed numbers of realisation. Thus, it is assumed that 5000 realisations is a suitable number to derive the moments of the PGV probability distribution from the observed frequencies. The observed relative frequency of the PGV results after 5000 realisations is plotted in Fig. 10.10. Two continuous probability density functions are fitted to this discrete distribution: a log-normal and an exponential function. The exponential function is assumed to project the properties of the observed relative frequency of the PGV at the seismic station in Forlì more realistically.

The seismic input for the subsequent sections is adopted to have the exponential probability distribution shown in Fig. 10.10. The simulated seismic event with the mean PGV of μ_X=82.27cm/s as marked in Fig. 10.10 is used for the deterministic analyses performed in the subsequent Secs. 10.3 to 10.6. In the probabilistic simulations in Sec. 10.7, the seismic input is effectively treated as probabilistic variable by means of the PEM.

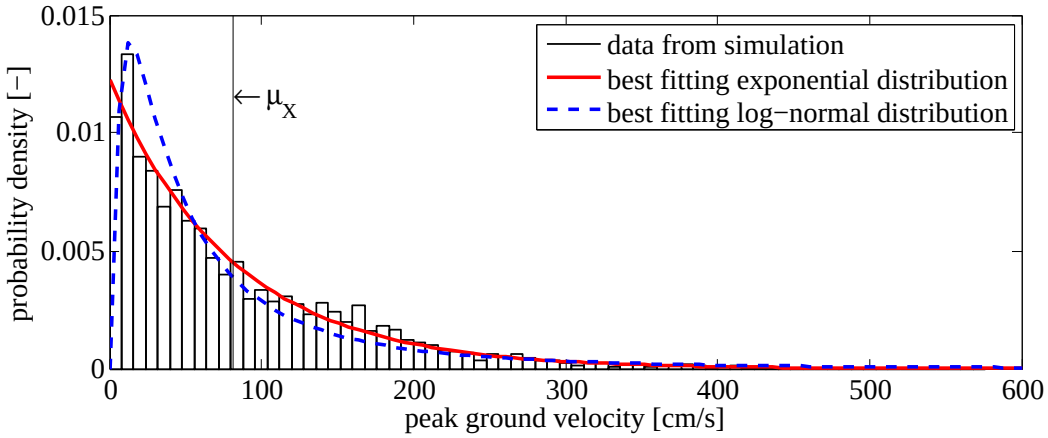

Figure 10.10: Observed relative frequency of the simulated peak ground velocities for an earthquake of magnitude M_w=5.9 with marked mean μ_X=82.27cm/s and two fitted probability density functions. The exponential function is assumed to be best fitting and, thus, is used in the further progress.

10.3 Straight pipeline excited by M_w=5.9 earthquake

In this section, an artificial earthquake of magnitude M_w=5.9 is used as seismic input to the pipeline-soil domain analysed in Sec. 10.1. The performed analysis is deterministic. Therefore, the seismic event that corresponds to the mean μ_X of the exponential probability distribution of the PGV from Fig. 10.10 is incorporated. The input parameters for the large scale earthquake simulation are given in the previous section. The present section follows the same lines as Sec. 10.1. Hence, the same three near-field models are studied and compared to the large scale simulation results. The material and design parameters as well as the parameters for the hybrid FE-SBFE computation equal those of Sec. 10.1. Only the seismic excitation is different.

Surface ground motion: As in Sec. 10.1, the simulated displacements at node A. marked in Fig. 10.2, are analysed. These displacements are derived from the three near-field models described in Sec. 10.1 and are compared to the ones from the large scale simulation which yields the mean of the PGV, i.e., μ_X=82.27cm/s. Those displacement progressions are depicted in Fig. 10.11. Again, wave reflection oscillations can be observed when the displacements are computed with the pure FEM. The other results exhibit a good qualitative accordance. Especially, the amplitudes of the FE-SBFE simulation match the amplitudes of the large scale earthquake simulation very well. The amplitudes of the FE-SBFE model containing pipe and soil are slightly larger than the large scale results. Thus, the phenomenon, that the ground motion is affected by the underground pipeline, can be observed for the M_w=5.9 seismic excitation as well as for the M_w=4.25 earthquake.

Wave propagation in the near-field: The Rayleigh wave motion in the x-z-plane at the three nodes A, B and C from Fig. 10.2 is plotted in Fig. 10.12. As in Sec. 10.1, the characteristic ellipses can be recognised as well as the decay of amplitudes with depth. A difference to the Rayleigh wave motion of the M_w=4.25 earthquake (Fig. 10.4) is the size of the area encircled by the ground motion amplitudes. This area is proportional to the energy which is dissipated by the motion. Roughly, it can be stated that the area encircled by the ground motion of node A in Fig. 10.12 is scaled by the factor $1{\cdot}10^6$ compared to the area in Fig. 10.4. Hence, it is obvious that the M_w=5.9 earthquake is much more hazardous than the M_w=4.25 earthquake.

The seismically deformed near-field containing soil and pipeline is depicted at discrete time-stations in Fig. 10.13. Note that, contrary to Fig. 10.5, the displacements are only magnified by the factor 10. From

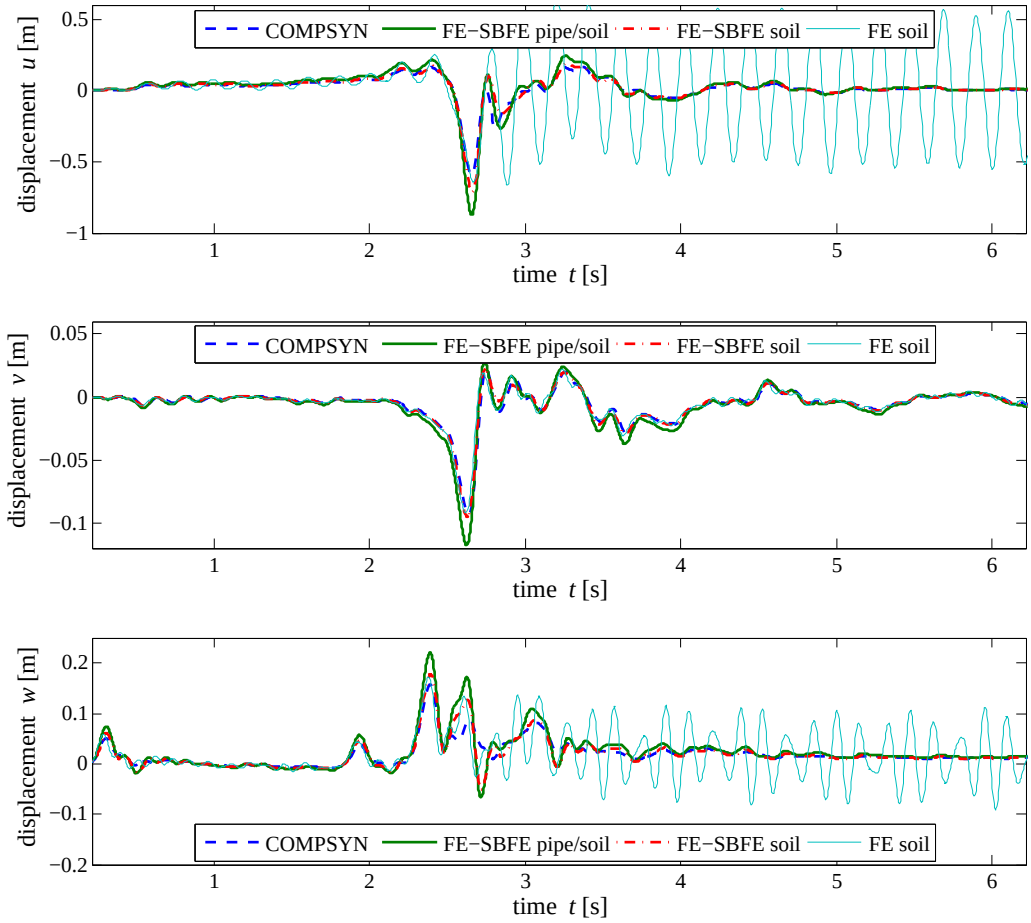

Figure 10.11: Simulated displacements at node A (see Fig. 10.2) excited by the artificial M_w=5.9 Forlì earthquake. Comparison of the large scale simulation results (COMPSYN) with those of the reduced near-field modelled by the pure FEM (FE-soil) and by the hybrid FE-SBFEM with pipeline (FE-SBFE pipe/soil) and without (FE-SBFE soil).

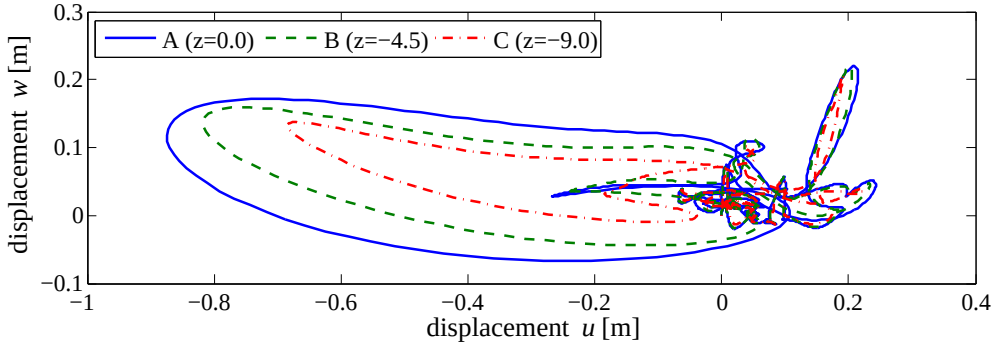

Figure 10.12: Displacements in x-z-plane at nodes A, B and C from Fig. 10.2. The typical elliptical motion of Rayleigh waves is shown. The dissipated energy which is proportional to the encircled area decreases with decreasing z-coordinate.

the seismically deformed near-field in Fig. 10.13, it is easy to recognise that the seismic motion belonging to the M_w=5.9 earthquake is much bigger than the one of the M_w=4.25 earthquake analysed in Sec. 10.1. The characteristics of the DRM that the seismic motion is only introduced inside of the interface Γ and, adversely, the outer domain which contains the relative motion is only marginally moved, are evidenced in Fig. 10.13. This shall be not discussed any closer here, since the topic were addressed before. Again, the initially uniform motion due to the body waves can be observed, e.g., at time t =2.05s whereas later, the non-uniform motion is quite obvious, e.g., at t =2.85s.

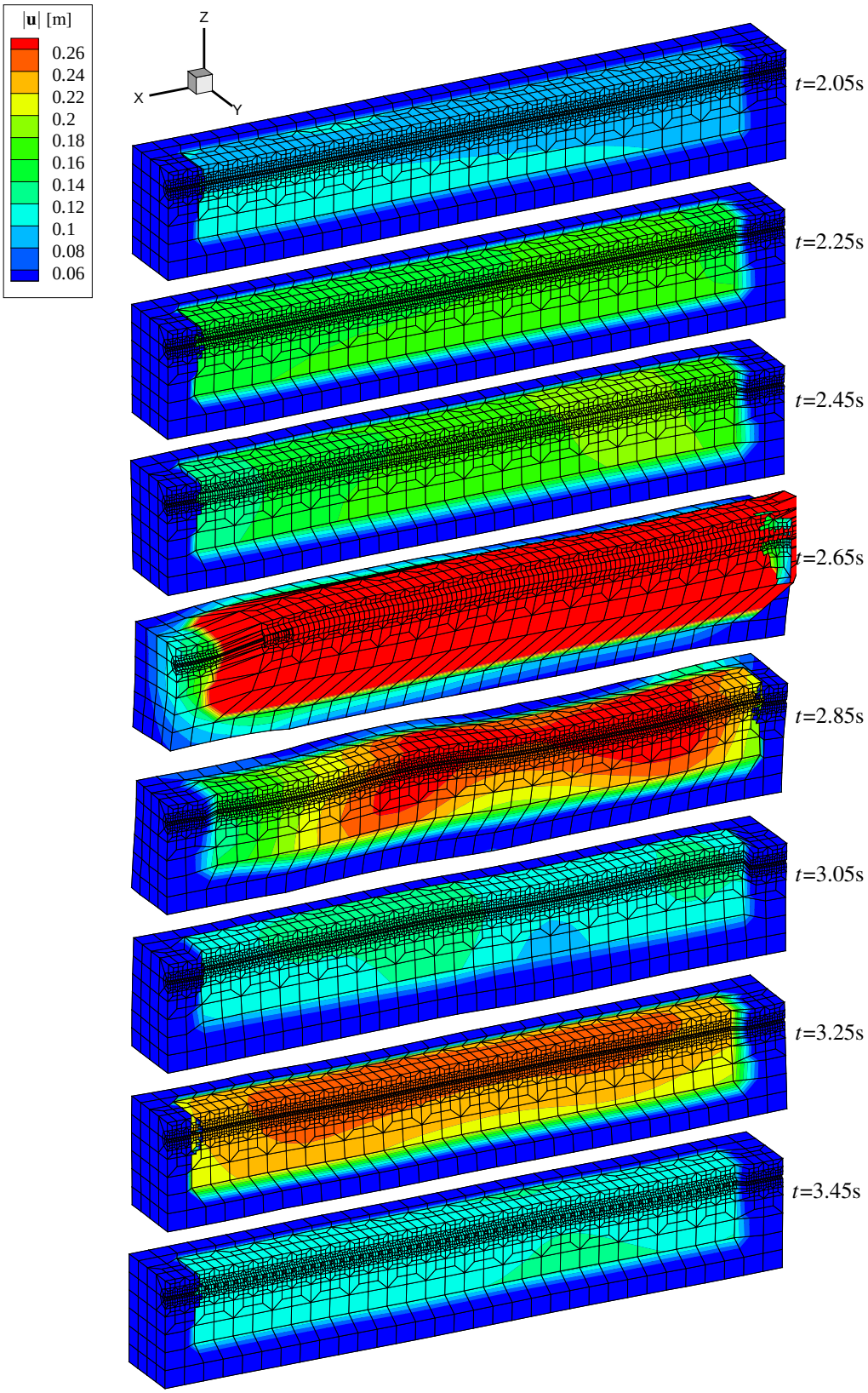

Figure 10.13: Wave propagation in the near-field which is excited by the equivalent seismic forces of the DRM. Those forces introduce the simulated seismic motion of the Forlì earthquake of magnitude M_w =5.9 into the near-field. The model is for representation reasons bisected along the x-axis and the displacements are magnified by the factor 10. The contours are plotted for $|\mathbf{u}| = \sqrt{u^2+v^2+w^2}$.

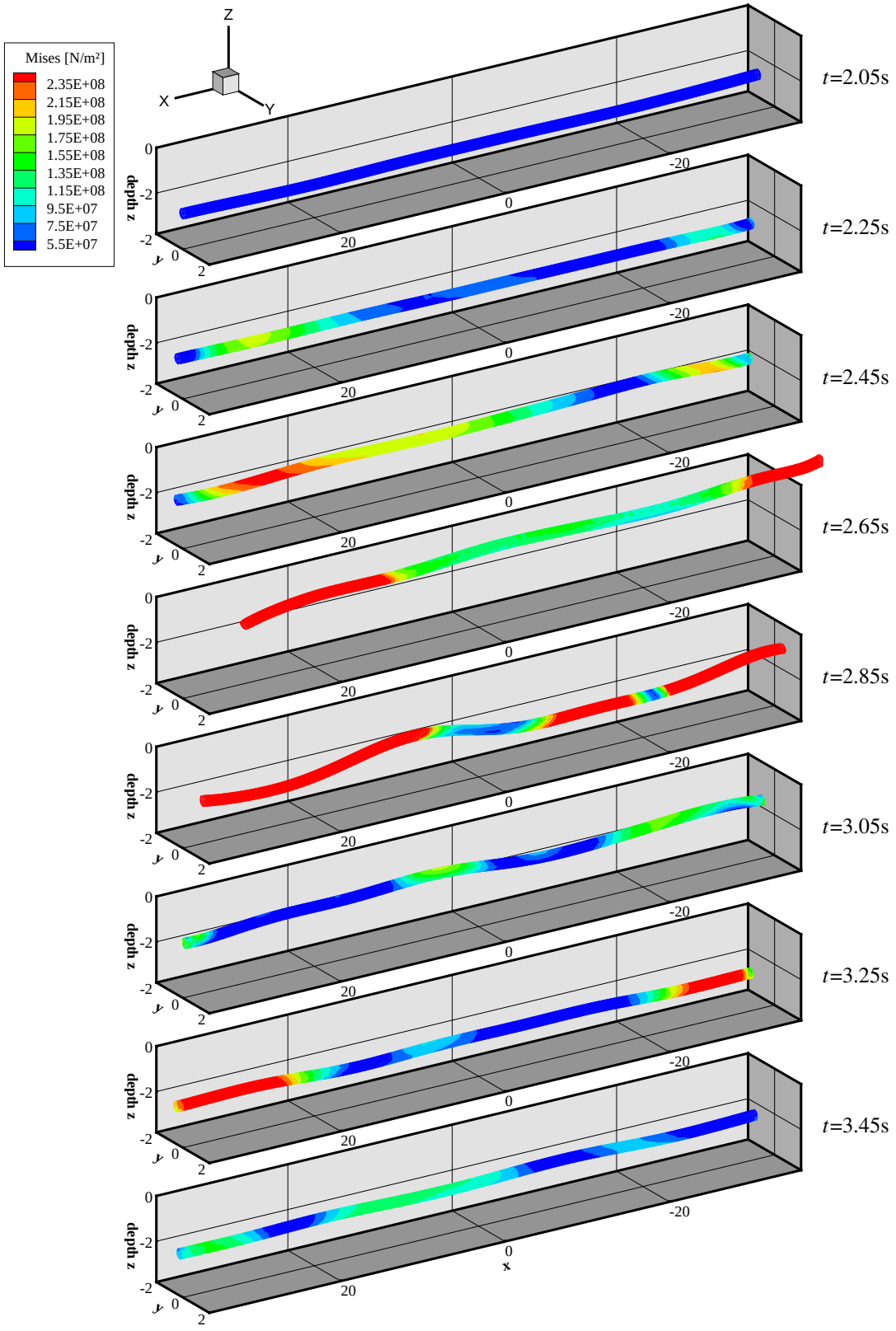

Figure 10.14: Von Mises stresses in the deformed pipeline caused by the M_w=5.9 earthquake. The representation of the displacements is magnified by the factor 10.

Strains and stresses in the pipeline: As for the M_w=4.25 earthquake excitation, the two cases of the truncation of the pipeline model are studied (see Fig. 10.7). Also here, for the evaluation of the strains and stresses in the pipe wall, the pipeline is subdivided into 1m sections. The maximum strains and stresses in these sections are depicted in Fig. 10.15 for the two cases of truncation. In the middle part of the pipeline from about -20m to 20m, a good accordance of the distributions of the two case can be recognised. This behaviour could be observed in Fig. 10.8 as well. The distributions in Fig. 10.15 exhibit also similar qualitative progressions, i.e., they posses high values at the right where the seismic waves incident, lower values in the middle and slightly higher at the left end. Like for Fig. 10.8, it can be assumed that the strains and stresses are model-independent, i.e., reliable in the middle part of the pipeline.

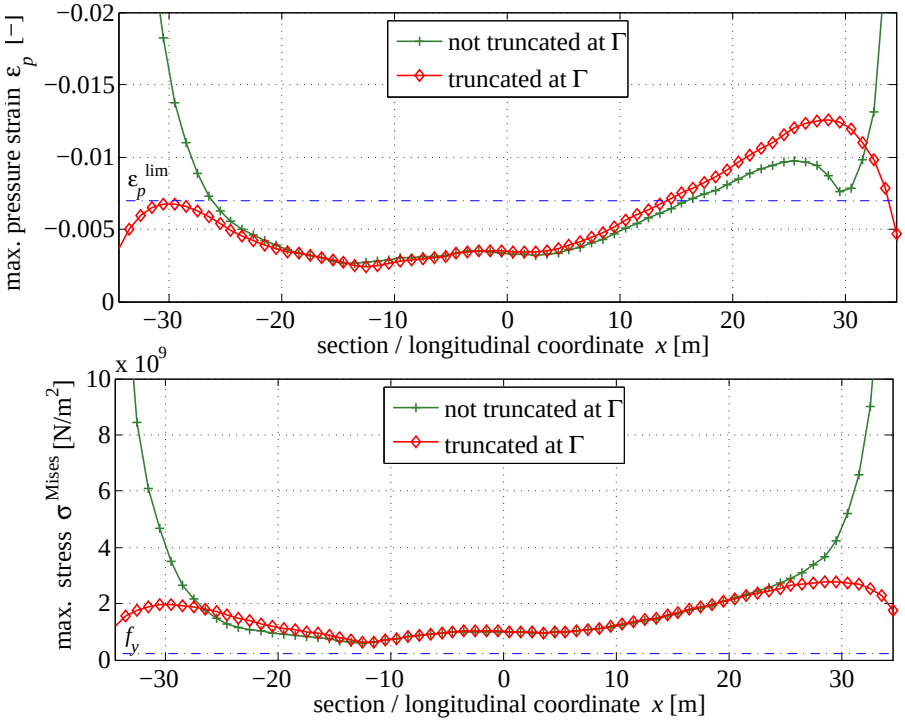

Figure 10.15: Maximum pressure strains ε_p and von Mises stresses σ^{Mises} in the pipeline sections of 1m length. The seismic waves incident from the right. The yield stress f_y is marked in the lower plot.

Considering the failure criteria, it is seen that the strains for the pipe model truncated at Γ exceed the maximum allowable pressure strain $\varepsilon_p^{\text{lim}}$=0.7% (compare Eq. (8.7)) only in the sections at which the seismic waves incident in the near-field, i.e., on the right of Fig. 10.15. In contrast, the maximum von Mises stresses exceed the yield stress f_y=235.0MN/m^2 in every section as it is depicted in the lower plot of Fig. 10.15. Thus, the seismic event of magnitude M_w=5.9 which causes the mean PGV μ_X=82.27cm/s leads to the failure of the entire modelled buried pipeline. The simulation time t_σ^{fail} at which the yield stress f_y is reached the first time in the considered section, i.e., the time at which the section fails, is plotted in Fig. 10.16. Examining the pipeline model, truncated at Γ, exhibits that the pipeline fails mainly in three steps. At first, the ends fail at times around t=2.30s. Then, at the right end where the seismic waves incident the adjacent part fails at t=2.45s and, finally, the remaining sections fail in the interval from t=2.50-2.56s.

The von Mises stress distribution over the pipeline of the model, which is truncated at Γ, is observed closer. Fig. 10.14 shows the contour plot of those stresses induced by the motion depicted in Fig. 10.13. The stresses larger than the yield stress f_y=235.0MN/m^2 are marked by red colour. As for the soil, a uniform motion can be observed, at first. This motion does not induce large stresses. At time t =2.65s, the largest displacements pointing in x-direction occur. Even though, the red marked failure can be observed at the ends of the pipeline, the largest stresses do not appear here. Those stresses are induced

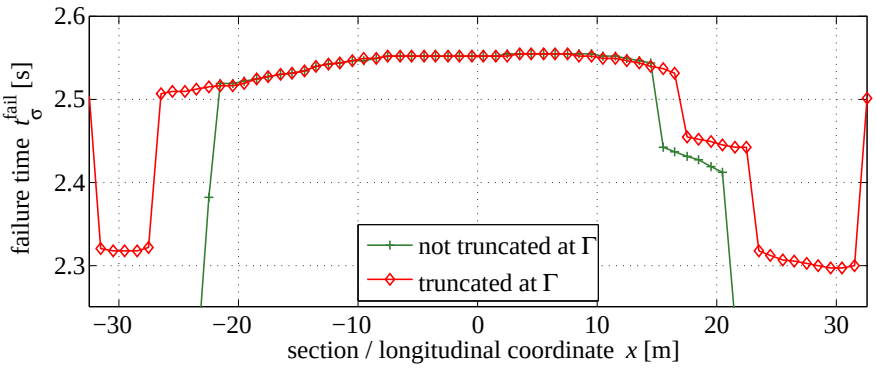

Figure 10.16: Time of failure due to the maximum von Mises stresses σ^{Mises} in the pipeline sections of 1m length.

at time t =2.85s where the Rayleigh motion leads to the bending of the pipeline.

Concluding it can be stated that the deterministic failure of an underground lifeline due to waves, caused by a strong seismic event, can be simulated. Further, the controlling failure for the specific analysed pipeline is due to the exceedance of the maximum stresses from the criterion of Eq. (8.9). In the executed simulation, the progressive failure of the pipeline can be modelled by identifying the times where the yield stress is exceeded. Since the model considers linear material behaviour, the post failure response is not modelled. Nevertheless, the distributions of the dynamic strains and stresses even after the exceedance of a failure limit present a reliable basis for the earthquake-save design. Therefore, parameter studies are performed in the following sections in order to analyse the influences of the parameters on the seismic behaviour of the underground lifeline.

10.4 Position of pipeline and construction details

After the presentation of the multi-method approach procedure and the determination of the deterministic failure of a straight buried pipeline due to a M_w=5.9 earthquake, the influences of parameters of position and construction are studied in this section. Unless otherwise noted, the parameters concerning material and geometry of pipeline and soil are those listed in Tab. 10.1 and the ones concerning the computation are those of Tab. 10.2. The seismic excitation caused by the artificial M_w=5.9 earthquake connected to the mean μ_X (PGV=82.27cm/s).

10.4.1 Angle of incidence of the seismic waves

The local position of the buried pipeline and the near-field is varied in this section. Therefore, the relative angle between pipeline and seismic fault location is changed. This variation can also be interpreted as the rearrangement of the seismic source. Hence, the same pipeline is studied, but the seismic excitation originates from another fault. The study, performed here, can be seen as an example for the analysis of various earthquake scenarios.

Three cases are analysed. In the first case (compare Sec. 10.3) the seismic waves propagate in the longitudinal direction of the pipeline. In the two other cases, two different relative angles between pipeline and wave propagation direction, namely 45° and 90°, are considered. All three cases are sketched in Fig. 10.17. The procedure of analysis as well as the input parameters are the same as referred to in the previous sections of this chapter. Since the stress failure criterion was identified as the controlling one, the maximum von Mises stresses are evaluated for the 1m pipeline sections as done before. This stress distribution is depicted in Fig. 10.18.

It is obvious that the seismic waves that incident at an angle of 90° induce lower stresses in the pipeline than the waves incident from other directions. This is expected since the pipeline is flexible perpendicular

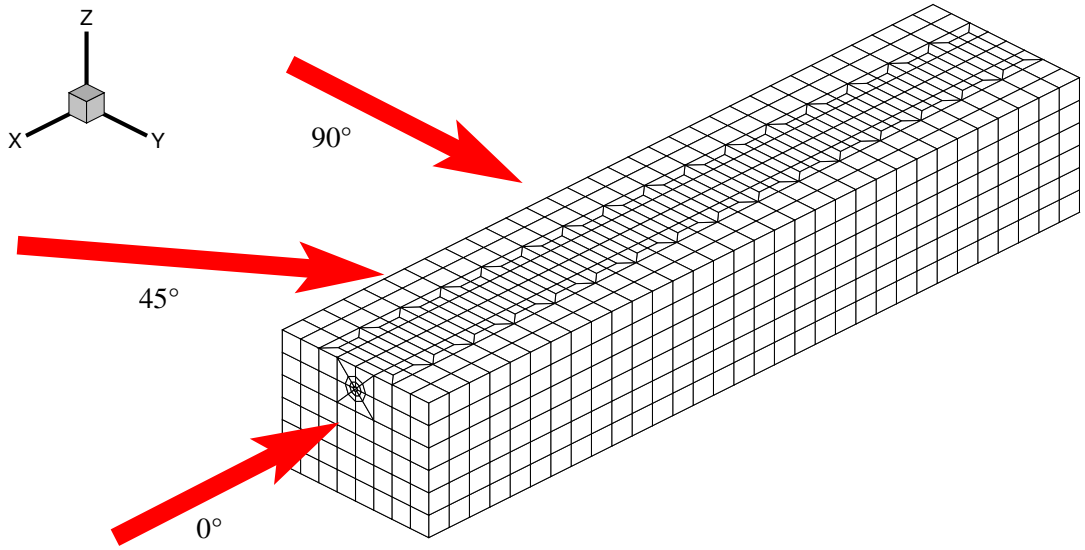

Figure 10.17: FE mesh of the near-field with the three analysed propagation directions of the incident seismic waves. The relative angle between longitudinal pipe direction and seismic wave propagation direction is given.

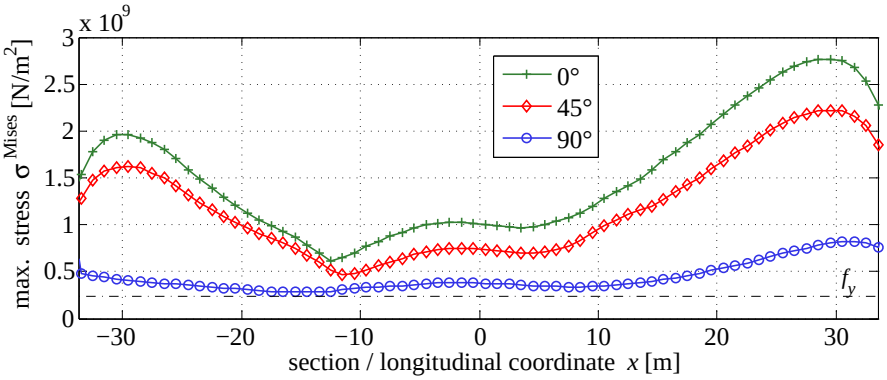

Figure 10.18: Maximum von Mises stresses σ^{Mises} in the pipeline sections of 1m length. The seismic waves incident at varying angles and the yield stress f_y is marked.

to the longitudinal axis and, thus, performs the same motion in this direction as the soil does. The pipeline does not strengthen the entire soil-pipe system in this direction. In contrast, the highest stresses occur due to the wave propagation direction of 0° in which the pipeline strengthens the soil-pipe system most. But also for an angle of incidence of 45°, the resulting maximum stresses are only slightly smaller than for an angle of 0°. This indicates that not only seismic waves that propagate in the longitudinal direction of the buried pipeline endanger it, but even those that incident at angles up to 45°.

10.4.2 Burial depth

The influences of the burial depth of an underground pipeline on the von Mises stress distribution is analysed in this section. The pipeline of Forlì, which was studied in the previous sections, is buried at h_b=2.0m depth. Its stress distribution is compared to a pipeline that has a burial depth of h_b=1.5m. Except of this depth h_b, all parameters of pipeline and soil remain the same as before.

The maximum von Mises stress distribution over the length of the two pipelines with different burial depth h_b is plotted in Fig. 10.19. The maximum stresses are higher for the pipeline buried at h_b=1.5m.

Thus, it can be concluded that the bending deformation which induces the high stresses (compare Fig. 10.14 t =2.85s) is larger at z=1.5m than at z=2.0m. This coincidences with the distribution of the Rayleigh wave amplitudes which are largest close beneath the surface and decline rapidly with depth (see Fig. 2.2(a)).

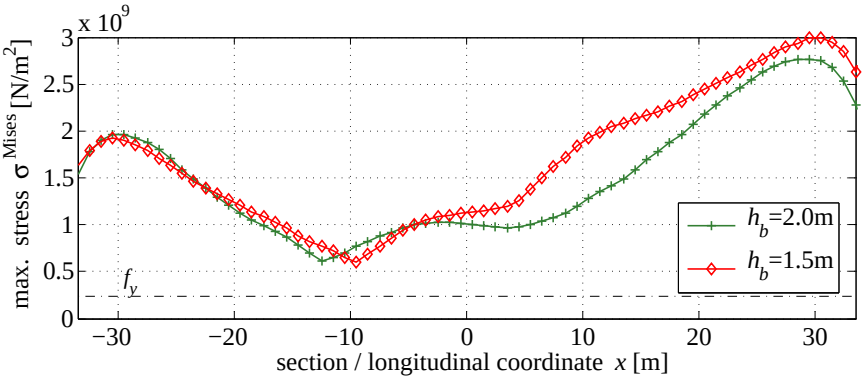

Figure 10.19: Maximum von Mises stresses σ^{Mises} in the pipeline sections of 1m length for different burial depths h_b. The seismic waves incident from the right and the yield stress f_y is marked.

So, it can be stated that, in general, it is safer in terms of seismic resistance to install underground lifelines at greater vertical distance from the surface, e.g., at h_b=2.0m in the examined case. Which depth is best depends on the analysed seismic event which produces the Rayleigh wave and on the soil, since the size of the amplitudes of the Rayleigh waves depend on the wavelength, i.e., on a material parameter.

10.4.3 Backfilled trench

During the construction process of underground pipelines, those structures are usually embedded in a backfilled trench. In this trench, the soil properties are different to those of the ordinary surficial soil. The influence of this backfilled trench under seismic wave excitation on the dynamic stresses in the buried lifeline should be studied. Therefore, a trench, as depicted in Fig. 10.20, is modelled as filled with two different soil types. The first soil type is a sand with the elastic parameters E=50MN/m^2, ν=0.3, and ρ=1750kg/m^2, whereas the second is a gravel with the parameters E=200MN/m^2, ν=0.36, and ρ=1925kg/m^2 [Pichler *et al.*, 2005]. The geometry parameters of the trench are shown in Fig. 10.20.

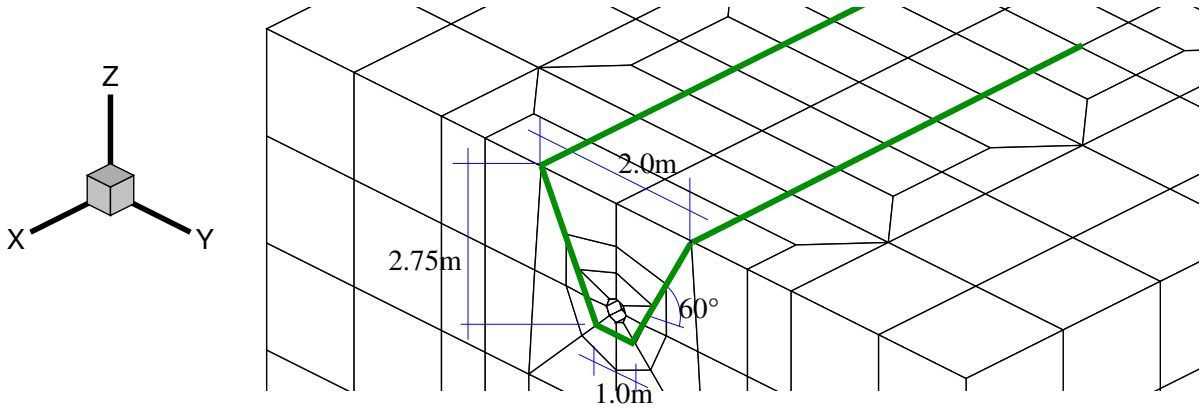

Figure 10.20: Detail of the FE mesh of the near-field domain with the backfilled trench. The dimensions of the trench are indicated.

The maximum von Mises stresses in the pipeline sections resulting from the simulation with trench and from the one without trench (from Sec. 10.3) are plotted in Fig. 10.21.

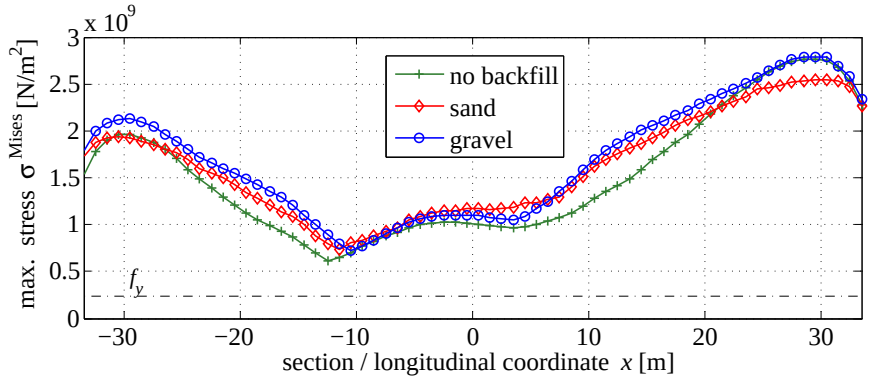

Figure 10.21: Maximum von Mises stresses σ^{Mises} in the pipeline sections of 1m length for different backfill materials. The seismic waves incident from the right and the yield stress f_y is marked.

Compared to the stresses of the model without backfilled trench, the pipeline embedded in the trench filled with sand exhibits a maximum stress distribution that is lower at the right side (where the waves incident). In the remaining sections of the pipeline, the maximum stresses are all higher. For the trench filled with gravel, the maximum stresses are over the entire length higher than for the pipeline buried without trench. Those higher stresses exhibit the influences of the backfill material.

As it was stated before, the Rayleigh wave was identified as the controlling wave type which introduces the highest stresses in the pipe walls. The Rayleigh wave amplitude depends next to the depth also on the material parameters (see Chap. 2). In Fig. 10.21, it can be observed that the stresses increase when the pipeline is embedded in the backfill soil. This increase is related to the Rayleigh wave amplitudes which have their maximum values at a different depth for the backfill material as for the surficial soil. Since the stresses increase for the backfill material in the present application, it can be conclude that the depth of the maximum Rayleigh wave amplitude is close to the burial depth of the pipeline.

Anyhow, the application shows that the backfill does not lead to a stress reduction in the pipeline, although it could. Thus, careful studies have to be performed, before the execution of a backfilling to improve the seismic resistance of a buried lifeline.

10.4.4 Slippage at soil-pipe interface

The strains and stresses in the analysed pipeline are caused by the seismic transient ground deformation. Obviously, this deformation of the ground is transferred to the pipeline via the connecting interface between pipe and soil. In this section, the modelling of this interface is addressed.

So far, the interface nodes of the brick elements of the soil and the nodes of the shell elements of the pipeline are modelled as rigidly bonded to each other. This modelling approach is the same as it was adopted, e.g., by [Newmark, 1971]. It conservatively assumes that the deformation of the soil is the same as the deformation of the pipeline. Nevertheless, this identical motion of the soil and the pipeline should not be confused with the assumption that the motion of the pipeline is the same as the free-field motion. The results of Secs. 10.1 and 10.3 indicate that the dynamic behaviour of the entire soil-pipe system is affected by the pipeline embedded in the soil. Thus, the deformation of the rigidly connected system of pipeline and soil differs from the deformation of the pure soil, i.e., from the free-field motion.

The influences of an elastic connection between the pipeline and the soil should be analysed here. Therefore, the connection between soil and pipeline is modelled by three-dimensional linear elastic spring elements of varying stiffness. With those elements, the phenomenon of slippage between pipe and soil in the longitudinal direction of the pipeline is studied. The stiffness of the springs in the normal as well as in the circumferential direction of the pipeline is kept at a high value (k_s=2·10^{12}N/m) so that the degrees

of freedom in those directions can be considered as tied. In contrast, the stiffness of the springs in the longitudinal direction of the pipeline is studied for several cases in which it is successively reduced from k_s=2·10^{12}N/m to 2·10^{2}N/m.

The elastic springs act at discrete FE nodes on the interface between pipe and soil and represent the elastic resistance to the slippage for a respective slip area. Thus, the stiffness of the elastic springs itself is not a meaningful factor when analysing the occurrence of slippage or grip between pipe and soil, since it is not model-independent. To receive a meaningful factor, the stiffness k_s is divided by the respective slip area on the interface, i.e., the dimensions of a shell element. In the studied near-field model, this area is $A = 0.061\text{m}^2$. The resulting variable is the *bedding factor in slippage direction* $b_s = k_s/A$. The maximum von Mises stress distribution over the pipeline length for the varying bedding factors b_s is plotted in Fig. 10.22.

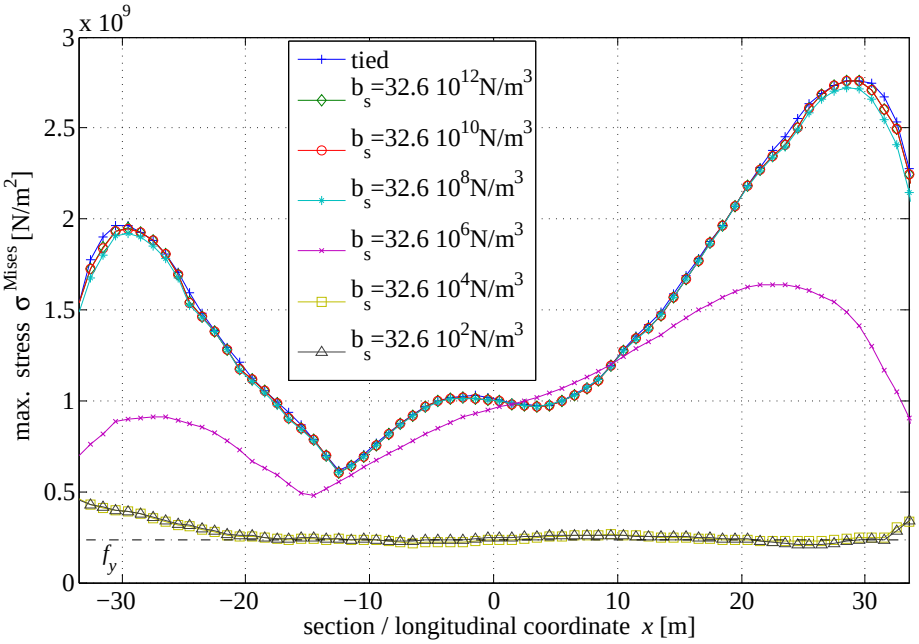

Figure 10.22: Maximum von Mises stresses σ^{Mises} in the pipeline sections of 1m length for varying bedding factors b_s. The seismic waves incident from the right and the yield stress f_y is marked.

Even though, the influences of seven different bedding factors are analysed, only three different distribution of the resulting maximum stresses can be seen. The maximum stress distributions for the tied interface as well as for the bedding factors b_s=32.6·10^{12} to 32.6·10^{8}N/m^3 exhibit an equal progression over the length of the pipeline. The stress distributions belonging to the bedding factors b_s=32.6·10^4 and 32.6·10^{2}N/m^3 are equal to each other as well but with significantly less maximum values. The stress distribution simulated with the bedding factor b_s=32.6·10^{6}N/m^3 is the only result that ranges between those two extreme distributions. So, it can be concluded that slippage between pipe and soil occurs only in a limited range around the bedding factor b_s=32.6·10^{6}N/m^3. The models which imply other bedding factors can be classified into two extreme cases: either the pipe and the soil completely stick or they completely slip on each other.

The other way round, when it can be concluded from the soil and pipe conditions that a slippage is probable to occur in longitudinal pipeline direction, it can be modelled best with a linear spring of a stiffness which is related to a bedding factor of b_s=32.6·10^{6}N/m^3. Anyway, the modelling of the pipe-soil interface with linear elastic spring is only an approximate approach. If the slippage behaviour needs to be studied in more detail, advanced approaches are demanded as, e.g., non-linear springs or contact elements. Nevertheless, the basic approach incorporating linear springs gives a tendency which resistance needs to be overcome so that slippage occurs.

10.5 Pipe design parameters

In the previous studies, parameters were analysed which can be associated to both the soil and the pipeline. In the subsequent studies, the effects of parameters are examined which are solely attributed to the design of the pipeline. As before, parameters which are not accounted other keep the values of Tabs. 10.1 and 10.2, respectively.

10.5.1 Segmented pipelines

The first design characteristic to be studied is the segmentation of the pipeline. Up to now only continuous pipelines have been studied which exhibit failure modes due to seismic events which are different from segmented ones. Thus, the failure modes of segmented pipelines should be studied.

As was discussed previously failure of segmented pipelines occurs mainly at the joints at which the pipeline segments are connected. To enable a relative joint movement in the numerical model, it is necessary to allow also a relative movement between pipe and soil. Therefore, the slippage approach from the previous section is incorporated in which the slip is modelled by a bedding factor b_s=32.6MN/m^3. Hence, the seismic response of a straight pipeline is simulated which is subdivided into segments of 5m length. The joint connections are modelled by three-dimensional linear elastic springs which feature the same stiffness in all three spatial directions. The joint spring stiffnesses k_j of the seven analysed cases are listed in Tab. 10.7. Additionally, the stiffness divided by the represented edge of the joint in circumferential direction, i.e., by the edge of a shell element $l_j = 0.196$m, is given.

Table 10.7: Stiffnesses k_j and k_j/l_j of the springs representing the joints of the seven analysed cases.

case		I	II	III	IV	V	VI	VII
k_j	[N/m]	$2{\cdot}10^{10}$	$2{\cdot}10^{9}$	$2{\cdot}10^{8}$	$2{\cdot}10^{7}$	$2{\cdot}10^{6}$	$2{\cdot}10^{4}$	$2{\cdot}10^{2}$
k_j/l_j	[N/m^2]	$10.2{\cdot}10^{10}$	$10.2{\cdot}10^{9}$	$10.2{\cdot}10^{8}$	$10.2{\cdot}10^{7}$	$10.2{\cdot}10^{6}$	$10.2{\cdot}10^{4}$	$10.2{\cdot}10^{2}$

For the seven analysed cases, the maximum von Mises stress distribution over the pipeline length is depicted in Fig. 10.23. It can be recognised that with decreasing joint stiffness also the maximum stresses decrease. This is plausible since the stresses can only be marginally transferred from one pipe segment

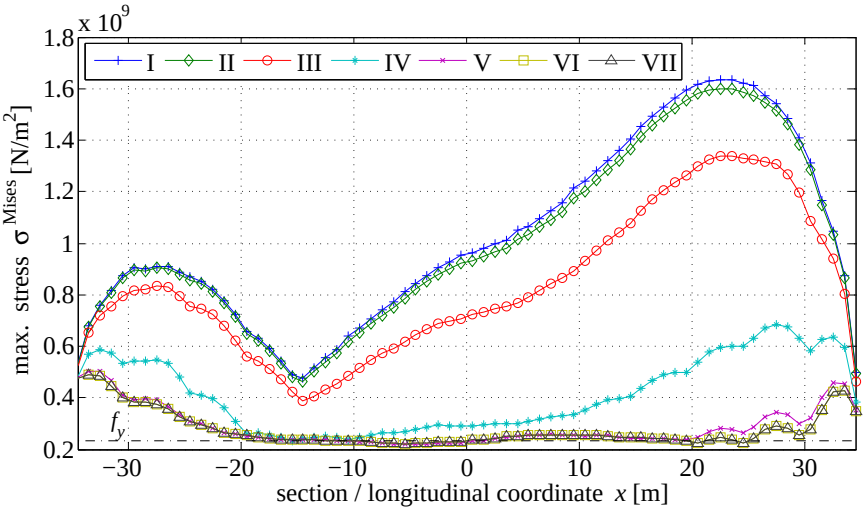

Figure 10.23: Maximum von Mises stresses σ^{Mises} in the segmented pipeline for varying joint stiffnesses. The segments have the length of 5m. Slippage between pipe and soil is modelled with the bedding factor b_s=32.6MN/m^3. The seismic waves incident from the right and the yield stress f_y is marked.

to the other when the joint stiffness is low. Further, in the stress distribution, e.g., of case IV, kinks can be observed every 5m. Since, those kinks occur at the locations of the joints, it is indicated that the joints are the weakest parts in the pipeline.

The contours of the von Mises stress distribution of case IV at time t=2.85s are plotted in Fig. 10.24. Also here, decays of the stresses at the joints can be roughly recognised. Thus, it is expected that the joints fail first before the failure criteria in the segments are exceeded. Therefore, the joint failure criteria according to Sec. 8.2.2 of the 13 marked joints (in Fig. 10.24) are examined for the seven studied cases.

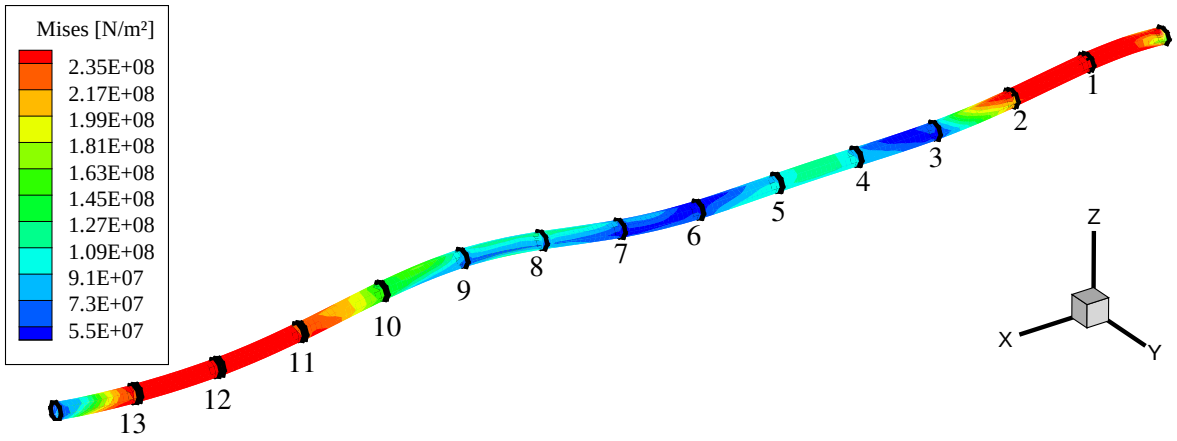

Figure 10.24: Von Mises stress distribution in the deformed segmented pipeline at time t=2.85s for case IV. The joints are marked and numbered.

The failure criteria of the joints are given in Eqs. (8.12) to (8.14). Whereas the requested joint depth d_j for the axial expansion criterion is assumed to be d_j=8cm, the limit compressive displacement Δu^p_{ult} is stated by [O'Rourke and Liu, 1999] to range between 0.32cm and 0.95cm. Here, it is set to Δu^p_{ult}=0.50cm. The allowable angular offset Θ_{lim} for pipe laying purposes which is incorporated in the joint rotation criterion is set to a typical manufacturer's recommended value. Such is denounced by [O'Rourke and Liu, 1999] for pipelines of diameter d_p=0.5m as an allowable angle of Θ_{lim}=3°.

The maximum relative joint displacements for expansion and contraction at the 13 joints are depicted in Figs. 10.25 and 10.26 where also the respective limit values are plotted. It is seen in Fig. 10.25 that a joint failure due to a relative expansional motion only occurs in the outer joints for some cases, namely for the ones with a stiff joint modelling. In contrast, Fig. 10.26 shows that the limit compressive displacement Δu^p_{ult} is exceeded at every joint for all analysed cases. The allowable angular offset Θ_{lim} is not exceeded and, thus, not shown here.

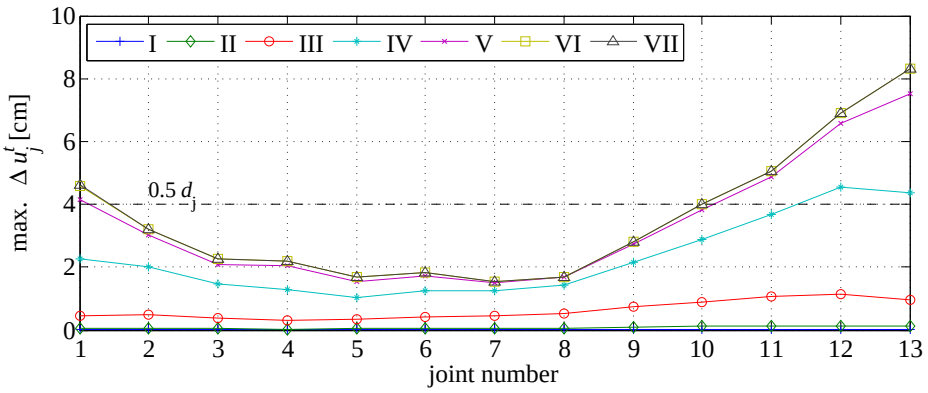

Figure 10.25: Maximum relative expansional joint displacements with failure criterion.

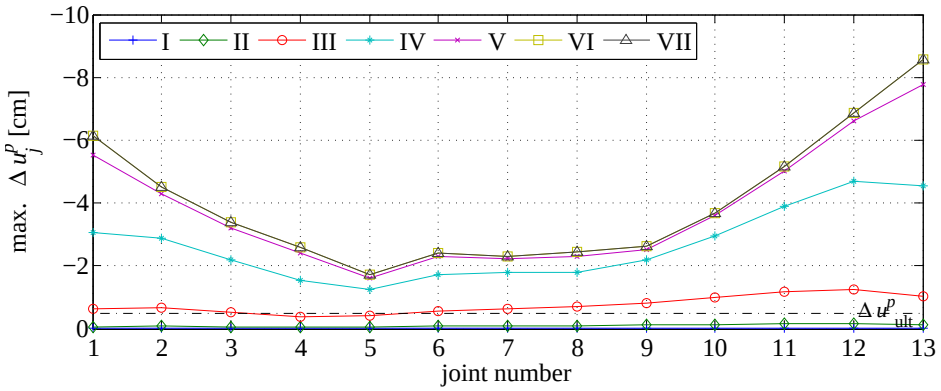

Figure 10.26: Maximum relative contracting joint displacements with failure criterion.

Finally, the time at which the different failures occurs is examined. Analysing case IV, the failures due to joint compressions occur at times between t=2.15s and 2.30s whereas the yield stresses in the segments are exceeded at times from t=2.55s to 2.70s. So, as it was expected, the controlling failure criteria for segmented pipelines are the ones of the joints and not the ones of the segments.

10.5.2 Cross section

After the examination of segmented pipelines, the analyses of the pipe design parameters is from now on again concentrated on continuous pipelines. Here, the influences of the cross sectional parameters, namely diameter d_p and wall thickness t_p, on the resulting stresses are examined.

At first, the thickness of the walls of the straight continuous pipeline of diameter d_p=0.5m is varied. The resulting maximum stresses over the length of the pipeline are plotted in Fig. 10.27. It can be seen that thinner pipe walls attract higher stresses. So, as it is expected, it can be stated that pipelines with thicker walls are more earthquake resistant. Still, even the stress distribution in the thickest pipe wall of t_p=100mm exceeds the yield stress f_y in every section.

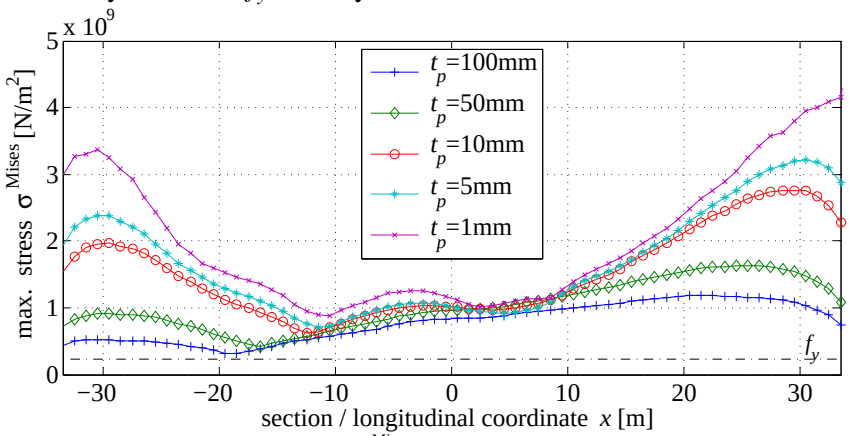

Figure 10.27: Maximum von Mises stresses σ^{Mises} in the pipeline of diameter d_p=0.5m for varying wall thickness t_p. The seismic waves incident from the right and the yield stress f_y is marked.

In a second investigation, the same thicknesses of the pipe wall as before are analysed for a smaller diameter of d_p=0.2m. The results are depicted in Fig. 10.28. Qualitatively, the same stress distributions as for the diameter d_p=0.5m can be observed, i.e., thinner pipe walls attract higher stresses. But the direct comparison between the stresses of the pipelines of the two analysed diameters in Fig. 10.29 where both pipes have a wall thickness of t_p=10mm exhibits quantitative differences. The maximum von Mises stresses in the pipeline of diameter d_p=0.2m exceed the stresses of the pipe with diameter d_p=0.5m at least in the endings of the pipeline. In the middle part from x=-10m to 20m, the maximum stresses are nearly equal. Overall, it can be seen that the pipeline of smaller diameter attracts the higher stresses. Thus, it can be concluded that pipelines with smaller diameter are more endangered by seismic waves.

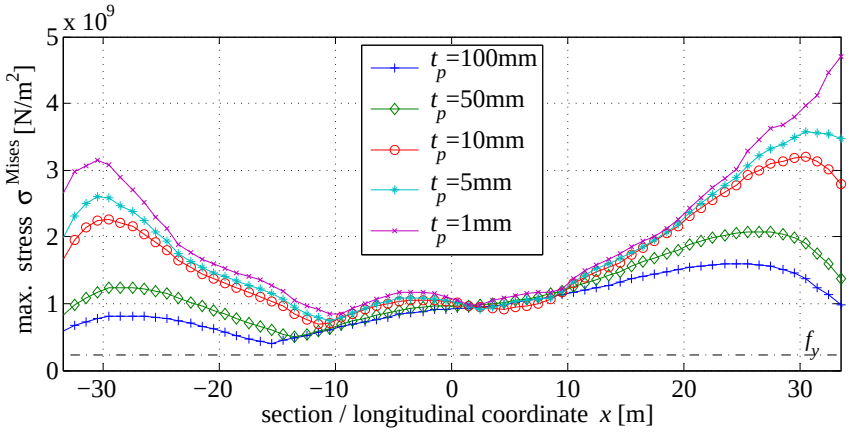

Figure 10.28: Maximum von Mises stresses σ^{Mises} in the pipeline of diameter d_p=0.2m for varying wall thickness t_p. The seismic waves incident from the right and the yield stress f_y is marked.

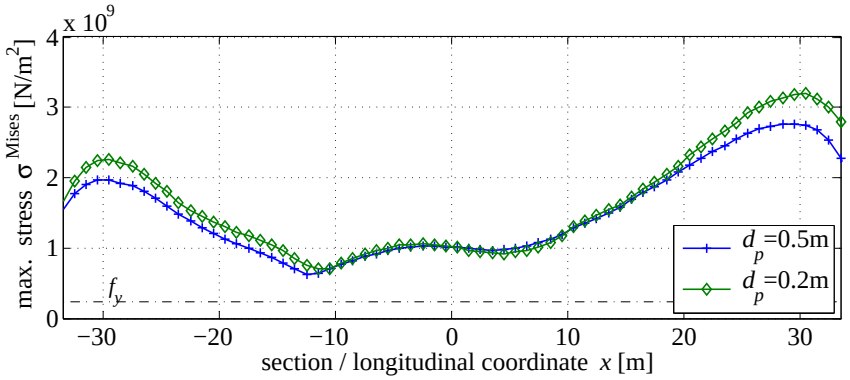

Figure 10.29: Maximum von Mises stresses σ^{Mises} in pipelines of diameter d_p=0.2m and d_p=0.5m for wall thickness t_p=10mm. The seismic waves incident from the right and the yield stress f_y is marked.

10.5.3 Pipe material

As the last examined design parameter, the influences of the pipe material is studied. Therefore, six different materials are analysed which are commonly used for the design of underground pipelines. Their linear elastic material parameters as well as their yield stresses f_y are listed in Tab. 10.8.

Table 10.8: Mechanical properties of common pipe materials. The values in brackets refer to the ranges found in literature.

	steel	grey cast iron (grey CI)	spheroidal cast iron (sphe CI)	concrete	polyvinyl chloride (PVC)	high density polyethylene (HDPE)
E [GN/m^2]	210	100 (90-155)	175 (170-185)	25 (22-45)	2 (1-3.5)	1
ν [-]	0.3	0.23 (0.21-0.26)	0.23 (0.21-0.26)	0.2	0.4 (0.1-0.45)	0.38 (0.3-0.4)
ρ [kg/m^3]	7850	7250	7250	2000 (1800-2450)	1450 (1380-1550)	955 (940-970)
f_y [MN/m^2]	235	200 (150-400)	350 (350-800)	20 (2-30)	45 (35-75)	16 (15-25)

The dynamic response of the straight continuous pipeline is analysed for the different materials. Since the different material parameters range in a large interval, the resulting stresses are expected to behave similarly. Thus, the maximum von Mises stresses along the longitudinal pipe axis are depicted in two figures. Fig 10.30 shows the maximum stress distribution of the stiffer materials. The steel pipeline attracts the highest stresses, whereas the pipelines made of cast iron exhibit a qualitatively similar distribution but with lower maximum stresses. The lowest stresses in Fig 10.30 are induced in the concrete pipeline, since it features the lowest Young's modulus. In all pipelines analysed in Fig 10.30, the yield stress is exceeded.

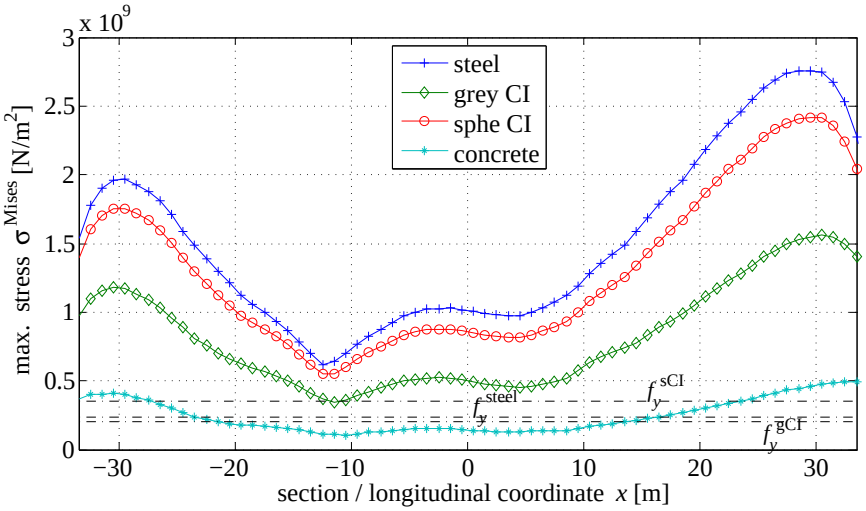

Figure 10.30: Maximum von Mises stresses σ^{Mises} in the pipeline sections of 1m length for stiff pipe materials. The seismic waves incident from the right.

In Fig 10.31, the maximum stress distributions of the softer materials are depicted. A completely different stress distribution as for the stiff materials can be observed. Apart from the peaks at the ends of the pipeline, the maximum values remain relatively constant below the yield stress. Anyway, at the ends, the yield stresses are exceeded for both materials.

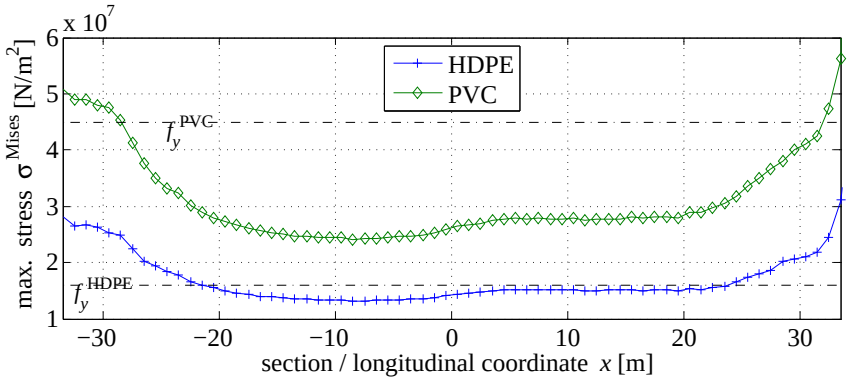

Figure 10.31: Maximum von Mises stresses σ^{Mises} in the pipeline sections of 1m length for soft pipe materials. The seismic waves incident from the right.

This study shows that it is important to consider the material behaviour of the pipeline when analysing its resistance to seismic wave propagation effects. Not the pipes manufactured of stiff materials but the soft pipelines which can adopt nearly the same deformation as the free-field ground are preferable in terms of earthquake resistance.

10.6 Tee joint excited by M_w=5.9 earthquake

So far, straight buried pipelines were analysed. An advantage of the three-dimensional modelling of the seismic excited lifelines is, next to, e.g., the incorporation of three-dimensional wave propagation effects and the dynamic response analysis at every point of the structure, the potential of analysing complex three-dimensional structures.

To demonstrate this potential, the seismic response of a tee joint of the lifeline network of Forlì is simulated in this section. The location of this joint is depicted in Fig. 10.1. The FE mesh of the near-field is shown in Fig. 10.32 where additionally the DRM interface Γ and Γ_e are marked. Like in Sec. 10.4.1, three different angles of incidence of the seismic waves are simulated. The wave propagation directions are sketched in Fig. 10.32. The material parameters of soil and pipeline correspond to the ones given in Tab. 10.1, whereas the computational parameter are listed in Tab. 10.9.

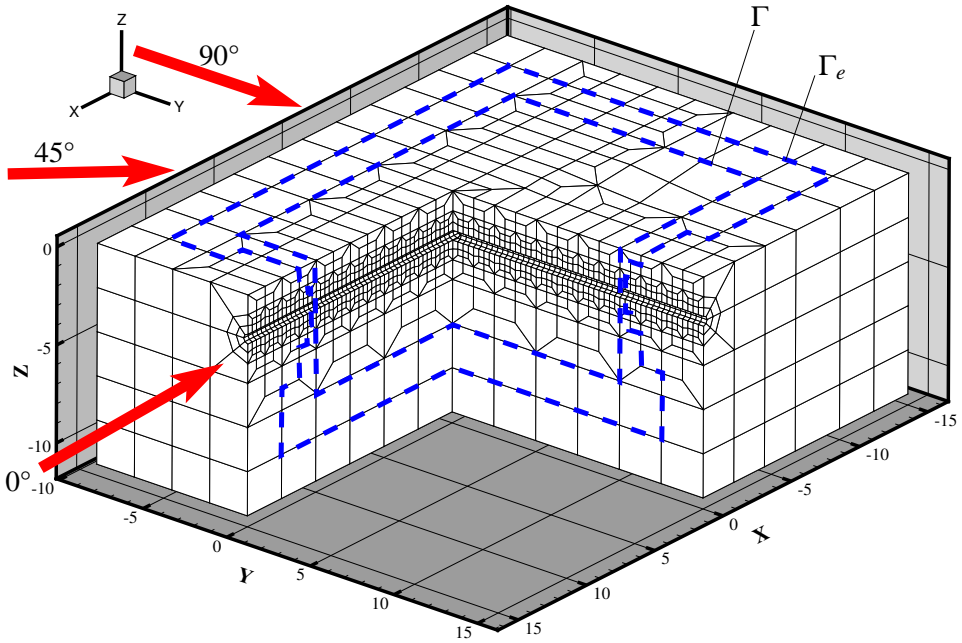

Figure 10.32: Cut FE mesh of the near-field containing the tee joint of two continuous buried pipelines under consideration. For the seismic wave propagation, three different angles of incidence are studied. The dashed lines highlight the DRM interfaces Γ and Γ_e.

Table 10.9: Parameters for the hybrid FE-SBFE computation.

FEM			SBFEM			time	
nodes	brick FEs	shell FEs	N_S	nodes	elements	$t_{\max}$ [s]	Δt [s]
6181	4508	768	3	$2 \cdot 152 + 172$	$2 \cdot 130 + 142$	11.25	$2.5 \cdot 10^{-4}$

For the evaluation of the stresses, the two jointed pipelines (in x- and y-direction) are divided into sections of 1m length. The maximum von Mises stress distributions for all three incident angles are depicted in Fig. 10.33. In Fig. 10.33(a), the stress distributions for the longer pipeline part which runs in x-direction is shown. A peak of the maximum stresses can be recognised at the midpoint at x=0 for all three angles of incidence. This is the point where the second pipeline which is directed along the y-axis is connected to the pipeline in x-direction (x=y=0). The stress distribution for the pipeline in y-direction is depicted Fig. 10.33(b). The stress peak at the left is at y=0 the same as in the plot above for x=0.

As for the applications studied before, the angle of the incident waves can be recognised from the stresses in Fig. 10.33(a). The stresses for the angles 0° and 45° are higher on the right where the waves incident and lower at the left. The stress distribution of the angle 90° does not vary much except at the special locations, i.e., at the ends of the pipeline and at the joint position x=0.

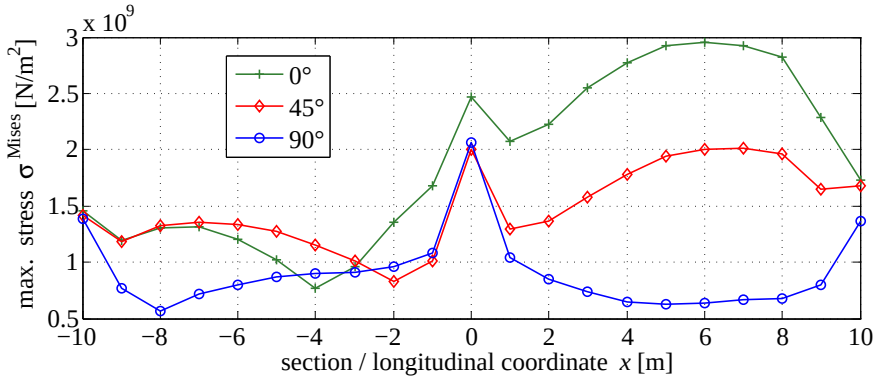

(a) Maximum von Mises stresses σ^{Mises} in the pipeline running along the x-axis.

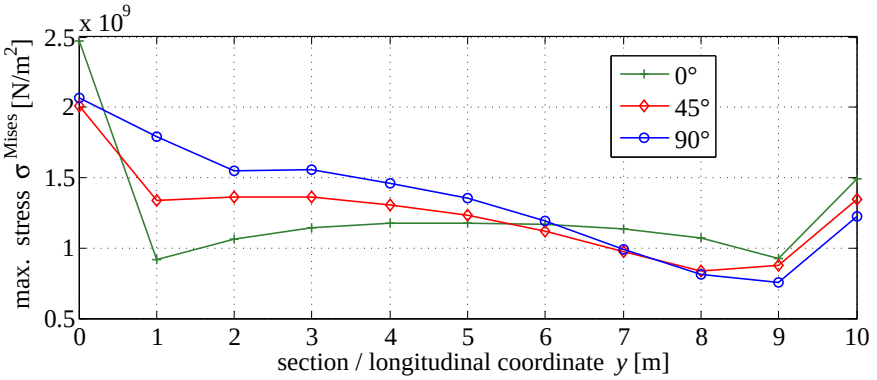

(b) Maximum von Mises stresses σ^{Mises} in the pipeline running along the y-axis.

Figure 10.33: Maximum von Mises stresses σ^{Mises} in the pipeline sections of 1m length.

Looking at Fig. 10.33(b), the maximum stresses due to the three angles of incidence exhibit qualitatively similar distributions, but with quantitative differences. Exceptions are the before mentioned special positions. At the joint (y=0), the waves that incident at an angle of 0° induce the largest stress value. This is caused by the stresses in the pipeline pointing in x-direction. In the remaining part of the pipeline, the stresses are relatively constant. For the cases where the waves incident at angles of 45° and 90°, the largest values occur also at the joint at the left (y=0). With increasing y-coordinate the stresses decrease. The decrease is stronger for the angle of 90°, i.e., for the waves that propagate along the longitudinal direction of this pipe.

The von Mises stresses in the deformed pipeline joint are depicted in Fig. 10.34. They are shown for all three analysed angles of incidence at the time $t = 2.50$s. At this time station, the yield stress is exceeded for the incident angles 45° and 90° for the first time. The highest stresses, indicated in red, occur in the respective wave propagation direction. The location of the high-stress areas depends on the particular wave propagation situation at the observed time station. Next to those areas, local concentrations of high stresses can be observed at the joint. This corresponds to the stress concentrations at this point shown in Fig. 10.33. For the angle of 45°, Fig. 10.34 shows two areas of high stresses, i.e., both parts of the jointed pipeline contribute to the transfer of the dynamic load. Due to that fact, the amplitudes of the stresses are reduced by the factor cos(45°)=0.707 compared to the angle 0°. This relative difference in the stresses can be observed for some points in the stress distribution of Fig. 10.33(a), e.g., at coordinate x =6m.

So, it can be stated that under seismic considerations, the joint connections are important since they attract high stresses as the stress peaks at the joint connections show. Further, it is seen that the angle of incidence of the seismic waves strongly affects the stress distributions in the two jointed pipelines.

Concluding, it is seen that the introduced methodology enables the incorporation of three-dimensional features, as waves that incident at different angles to three-dimensional pipeline constellations. Thus, also larger parts of lifeline networks can be analysed with this methodology.

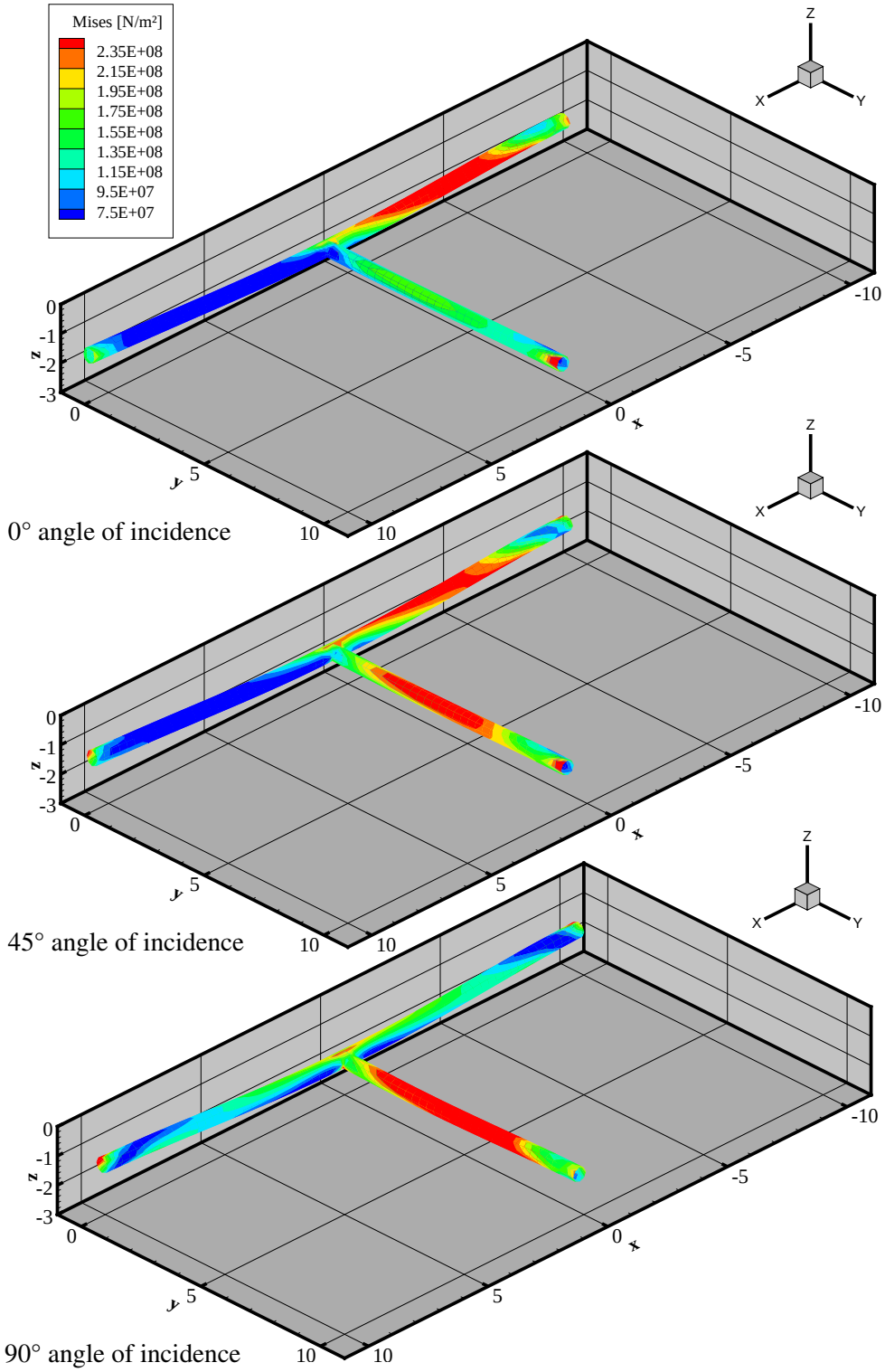

Figure 10.34: Von Mises stresses in the deformed tee joint at time $t = 2.50$s. The stresses are caused by the M_w=5.9 earthquake waves which incident at different angles (0°, 45°, 90°). The representation of the displacements is magnified by the factor 10.

10.7 Consideration of uncertainties

In the previous sections, the applications were restricted to deterministic treatments. In order to perform a risk analysis, the failure probability of the lifeline is needed instead of the deterministic failure. Hence, the procedure based on the PEM from Sec. 8.3 is introduced. To show its details and potentials, this procedure is applied for two random variables in the present section. Of course, the assumption of regarding only two variables as randomly distributed is not very realistic, but it is appropriate to show the procedure of utilising the PEM. The incorporation of more random variables is straight forward.

The two input variables which are considered as randomly distributed are the PGV and the Young's modulus E_s of the near-field soil. In terms of a risk analysis (see Eq. (1.2)), these two parameters can be attributed to the categories of hazard and exposure. Thus, the random distributed PGV contributes to the probability of hazard P_H, whereas the Young's modulus of the near-field soil contributes to the probability of exposure P_{Ex}.

With those two random variables, the probability of failure, i.e., the damage risk, can be determined by the probabilistic procedure described in Sec. 8.3. Therefore, at first, the random moments of the two input variables have to be deduced at their evaluation points. Those points are determined according to the PEM for multiple variables by [Hong, 1998]. Then, four deterministic simulation runs incorporating the multi-method approach from Sec. 7.5 are performed - one for each evaluation point. Those simulations yield the maximum stresses in the examined pipeline sections from which, by means of the PEM weights, their random moments are derived. With those random moments of the maximum stresses, the probability distribution and, finally, by incorporating the yield stress, the probability of failure of the examined pipeline section is achieved.

Following the probabilistic concept from Sec. 8.4, the failure probability of a buried lifeline considering multiple random variables is determined subsequently. As far as deterministic properties are concerned, the large scale model as well as the near-field model accord to the ones from Secs. 10.2 and 10.3. Initially, the characteristics of the two random variables X_1=PGV and X_2=E_s are considered.

First random input variable (PGV): The first variable that is assumed to have a random distribution is the PGV. Strictly speaking, the PGV is not a random variable, since it depends in this model deterministically on the causing slip distribution and the nucleation point on the seismic fault. This slip distribution is the actual random variable. Nevertheless, the PGV depends on the slip distribution and is thus a measure for it. Hence, it can be regarded as random variable.

In the generation of a probabilistic seismic excitation for Forlì with the magnitude $M_w = 5.9$ in Sec. 10.2, a relative frequency of the PGV at the receiver location was found by executing 5000 simulation runs. To this relative frequency, an exponential probability density function was fitted.

The first three random moments of the probability distribution of the input variable X_1=PGV are given in Tab. 10.6 as μ_{X_1}=82.27cm/s, σ_{X_1}=78.22cm/s and v_{X_1}=1.60. To use the PEM, the evaluation points of the random input variable have to be determined by means of Eqs. (8.28) and (8.29). With the number of random variables being $N = 2$, the evaluation points can be determined to x_{11}=17.75cm/s and x_{21}=271.93cm/s. The exponential probability density function of the input variable X_1=PGV, the locations of the mean μ_{X_1} and of the evaluation points x_{11} and x_{21} are shown in Fig. 10.35. Analogously to the evaluation points, the corresponding weights can be derived from Eqs. (8.30) and (8.31) as P_{11}=0.373 and P_{21}=0.127.

Second random input variable (Young's modulus of soil): The second random input variable X_2 is the Young's modulus E_s of the soil which surrounds the pipeline. The value of E_s which was used in all previous analyses was derived from down-hole tests at the examined site. Thus, this value is assigned to be the mean μ_{X_2} of the random distribution. In general, the variability of the Young's modulus is relatively large. According to [Fenton and Griffiths, 2005], the ratio between mean and standard deviation, i.e., $COV = \sigma_{X_2}/\mu_{X_2}$, can range up to COV=4. Since the ground examination tests were performed in

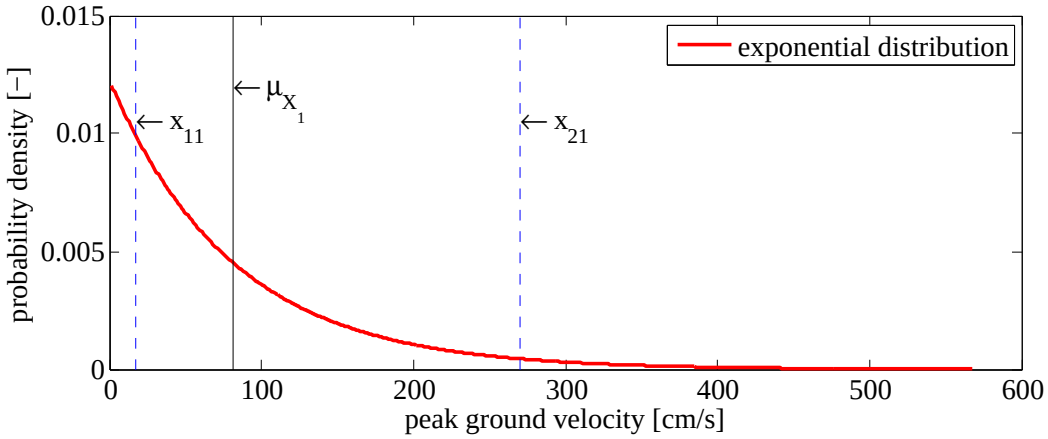

Figure 10.35: Best fitting exponential distribution of the PGV with mean μ_{X_1}=82.27cm/s and evaluation points x_{11}=17.75cm/s and x_{21}=271.93cm/s determined for N=2 random variables.

the analysed site, more confidence is given to the mean value μ_{X_2} so that a ratio of COV=0.1 is assumed for this analysis. Hence, with the mean μ_{X_2}=272MN/m^2, the standard deviation can be determined to σ_{X_2}=27.2MN/m^2. The probabilistic distribution of the Young's modulus is regarded as log-normal distributed ($\mu_{\ln(X_2)}$=5.6MN/m^2, $\sigma_{\ln(X_2)}$=99.8kN/m^2) so that its skewness gives ν_{X_2}=0.30. The so derived probability distribution is depicted in Fig. 10.36.

In order to incorporate also the second random input variable X_2=E_s in the PEM, the evaluation points and the corresponding weights have to be determined. From Eqs. (8.28) to (8.31) the evaluation points x_{12}=236.7MN/m^2 and x_{22}=314.0MN/m^2 as well as their corresponding weights P_{12}=0.272 and P_{22}=0.228 are achieved.

Execution of the deterministic simulations: After the determination of the input variables of the PEM, the next step is to evaluate the deterministic function $Y = g(X_1, X_2)$ from Eq. (8.34) at the four discrete evaluation points x_{11}, x_{21}, x_{12} and x_{22}, respectively. In this analysis, the deterministic function $g(X_1, X_2)$ is the multi-method approach from Sec. 7.5, whereas the output parameter Y is the maximum von Mises stress σ^{Mises} in the respective sections of the pipeline.

Following [Hong, 1998], the evaluation of the deterministic function, i.e., the multi-method approach, needs to be performed four times. In the first two simulation runs, the earthquake excitation X_1 is computed to yield x_{11} and x_{21}, whereas the Young's modulus X_2 is hold to its mean μ_{X_2}. For the last two simulations, the Young's modulus X_2 is varied from x_{12} to x_{22} and the seismic excitation X_1 is kept at

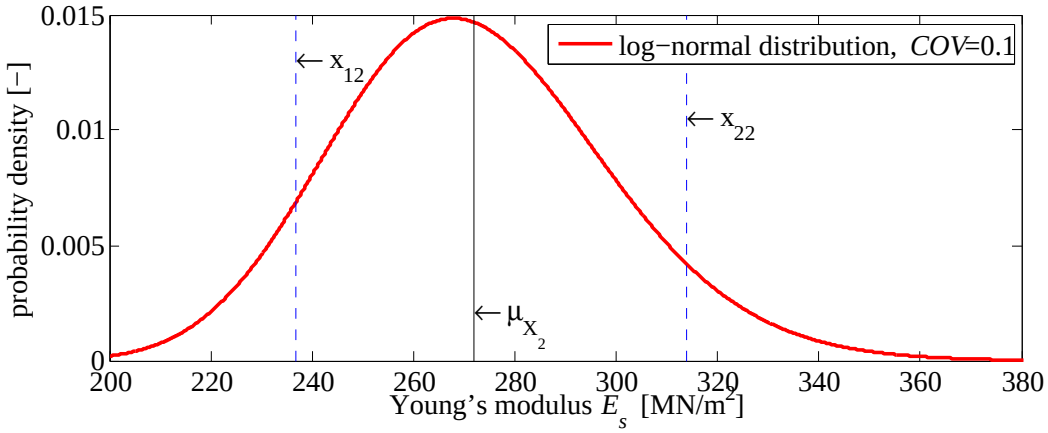

Figure 10.36: Log-normal probabilistic distribution of the Young's modulus E_s of the near-field soil. The mean μ_{X_2}=272MN/m^2 and the PEM evaluation points x_{12}=236.7MN/m^2 and x_{22}=314.0MN/m^2 are marked.

its mean μ_{X_1}. Thus, three deterministic large scale earthquake simulations have to be performed for μ_{X_1}, x_{11} and x_{21} in this application. From those large scale simulations, the equivalent seismic forces for the near-field are determined. With those seismic excitations, four deterministic hybrid FE-SBFE simulations of the near-field containing the pipeline and the soil are executed (for μ_{X_1} and x_{12}, μ_{X_1} and x_{22}, x_{11} and μ_{X_2}, x_{21} and μ_{X_2}). The combinations of the random variables for the four evaluation points are listed in Tab. 10.10.

Table 10.10: Input x_{pn}, output y_{pn} and weights P_{pn} for the four deterministic simulations in the probabilistic analysis using the PEM after [Hong, 1998].

eval. point pn	PGV X_1 $\left[\frac{\text{cm}}{\text{s}}\right]$	E_s X_2 $\left[\frac{\text{MN}}{\text{m}^2}\right]$	P_{pn}	sec. 1 y_{pn} $\left[\frac{\text{GN}}{\text{m}^2}\right]$	sec. 2 y_{pn} $\left[\frac{\text{GN}}{\text{m}^2}\right]$	sec. 3 y_{pn} $\left[\frac{\text{GN}}{\text{m}^2}\right]$	sec. 4 y_{pn} $\left[\frac{\text{GN}}{\text{m}^2}\right]$	sec. 5 y_{pn} $\left[\frac{\text{GN}}{\text{m}^2}\right]$	sec. 6 y_{pn} $\left[\frac{\text{GN}}{\text{m}^2}\right]$
11	x_{11}=17.75	μ_{X_2}=272.0	0.373	0.08	0.06	0.06	0.07	0.10	0.11
21	x_{21}=271.93	μ_{X_2}=272.0	0.127	2.45	1.47	1.27	1.56	2.53	3.49
12	μ_{X_1}=82.27	x_{12}=236.7	0.272	2.35	1.52	1.10	1.42	2.34	3.06
22	μ_{X_1}=82.27	x_{22}=314.0	0.228	1.62	0.97	0.98	1.05	1.84	2.50

From those four near-field simulations, the maximum von Mises stresses $y_{11} = \sigma_{11}^{\text{Mises}}$, $y_{21} = \sigma_{21}^{\text{Mises}}$, $y_{12} = \sigma_{12}^{\text{Mises}}$ and $y_{22} = \sigma_{22}^{\text{Mises}}$ in the pipeline are determined per pipe section. These maximum stresses are the output variables y_{11}, y_{21}, y_{12} and y_{22} which will be used to calculate the random moments μ_{Ym} in Eq. (8.33). From those random moments, probability distributions for the maximum stress can be derived so that finally, the failure probability of the pipeline section is achieved.

The resulting maximum stresses in the pipeline (shown in Fig. 10.2) which are derived from the four deterministic simulations are plotted in Fig. 10.37. For the probabilistic analysis, the pipeline is subdivided into six sections of 10m length. The maximum von Mises stresses in each of those 10m sections are depicted in Fig. 10.37 as thick dashed lines and their values are listed in Tab. 10.10.

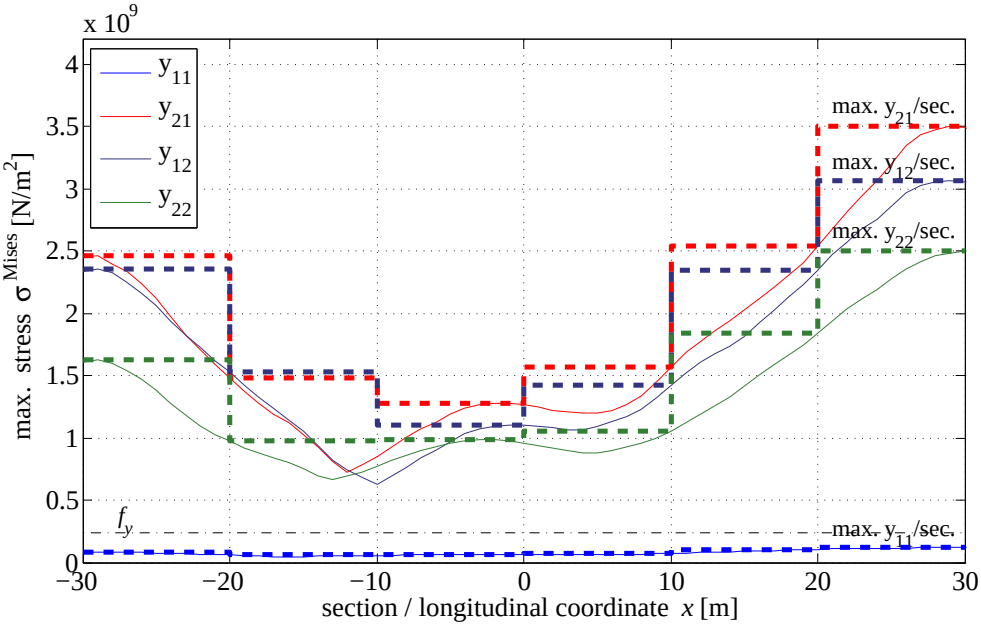

Figure 10.37: Maximum von Mises stress distribution over pipeline (—) for the four evaluation points x_{11}, x_{21}, x_{12} and x_{22}. The maximum stresses $y_{11} = \sigma_{11}^{\text{Mises}}$, $y_{21} = \sigma_{21}^{\text{Mises}}$, $y_{12} = \sigma_{12}^{\text{Mises}}$ and $y_{22} = \sigma_{22}^{\text{Mises}}$ per each 10m section are marked as bold dashed lines.

Probabilistic evaluation of the deterministic simulations: With the results of the four deterministic simulations, i.e., with the maximum stresses per each pipe section, the random moments of this probabilistically distributed output variable can be determined by the PEM. Therefore, the four output values y_{11}, y_{21}, y_{12} and y_{22} as well as the four weights P_{11}, P_{21}, P_{12} and P_{22} which are all given in Tab. 10.10 are inserted in Eq. (8.33) in order to determine the expected values $E(Y^m)$ of order m. With those values, mean μ_Y, standard deviation σ_Y and skewness ν_Y of the probabilistic maximum stress distribution $Y{=}\sigma^{\text{Mises}}$ for each pipeline section is computed by means Eq. (8.23). The so derived moments are listed in Tab. 10.11.

Table 10.11: Resulting random moments for the six sections.

	μ_Y	$E(Y^2)$	σ_Y	$E(Y^3)$	ν_Y
sec. 1	$1.35{\cdot}10^9$	$2.87{\cdot}10^{18}$	$1.02{\cdot}10^9$	$1.88{\cdot}10^{27}$	1.76
sec. 2	$0.84{\cdot}10^9$	$1.12{\cdot}10^{18}$	$0.64{\cdot}10^9$	$0.40{\cdot}10^{27}$	1.55
sec. 3	$0.71{\cdot}10^9$	$0.75{\cdot}10^{18}$	$0.50{\cdot}10^9$	$0.26{\cdot}10^{27}$	2.05
sec. 4	$0.85{\cdot}10^9$	$1.11{\cdot}10^{18}$	$0.62{\cdot}10^9$	$0.48{\cdot}10^{27}$	2.00
sec. 5	$1.41{\cdot}10^9$	$3.08{\cdot}10^{18}$	$1.03{\cdot}10^9$	$2.07{\cdot}10^{27}$	1.85
sec. 6	$1.89{\cdot}10^9$	$5.53{\cdot}10^{18}$	$1.39{\cdot}10^9$	$5.42{\cdot}10^{27}$	1.98

By means of the resulting random moments μ_Y, σ_Y and ν_Y, the probability density distribution of the von Mises stresses $Y{=}\sigma^{\text{Mises}}$ in the concerning pipeline section can be determined (see Eq. (8.21)). Those probability density distributions are depicted in Fig. 10.38 for the sections 1 to 6. The mean μ_Y and the four results of the PEM evaluation $y_{11}{=}\sigma^{\text{Mises}}_{11}$, $y_{21}{=}\sigma^{\text{Mises}}_{21}$, $y_{12}{=}\sigma^{\text{Mises}}_{12}$ and $y_{22}{=}\sigma^{\text{Mises}}_{22}$ are marked as well.

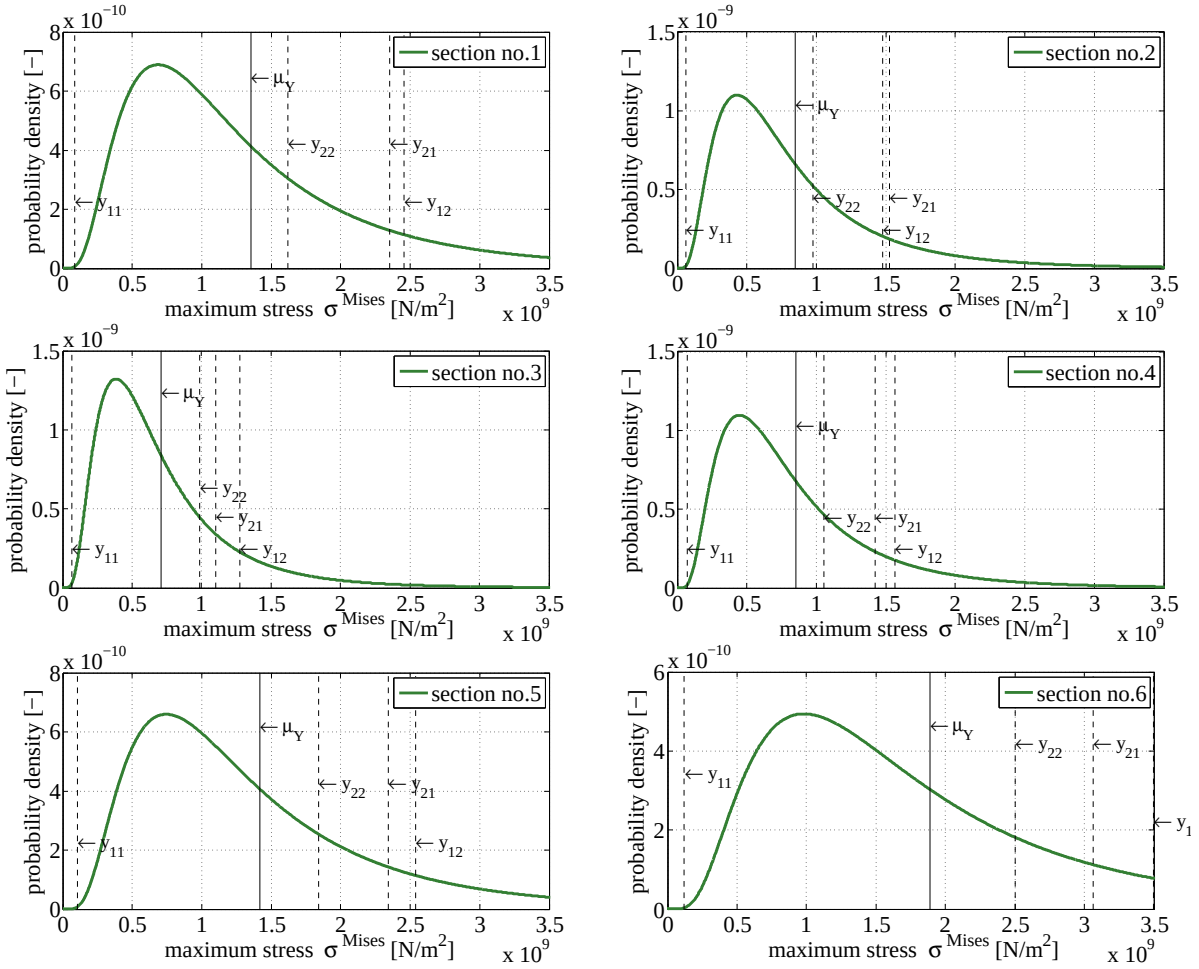

Figure 10.38: Probability density distribution of the maximum von Mises stresses in each of the six analysed sections. The mean μ_Y and the results at the four evaluation points are marked.

Determination of the probability of failure: From the probability distributions of Fig. 10.38, the probability of the exceedance of a certain stress value can be derived. This probability of exceedance can be directly read from the distribution when instead of the density the cumulative probability distribution is plotted in which the densities are summed. This representation is chosen in Fig. 10.39.

As stated in Eq. (8.9), the failure of a pipeline section is expected to occur when the von Mises stress σ^{Mises} exceeds the yield stress f_y. Therewith, the probability of resistance P_r, i.e., the probability that the maximum von Mises stress σ^{Mises} in a pipeline section remains lower than f_y=235MN/m^2, is marked in Fig. 10.39 for the six analysed sections. Thus, the probability of failure P_f can be determined from $P_f = 1 - P_r$. The probability of failure P_f which is equal to the damage risk R_d in Eq. (1.2) is given for the six examined sections of the pipeline in Fig. 10.39.

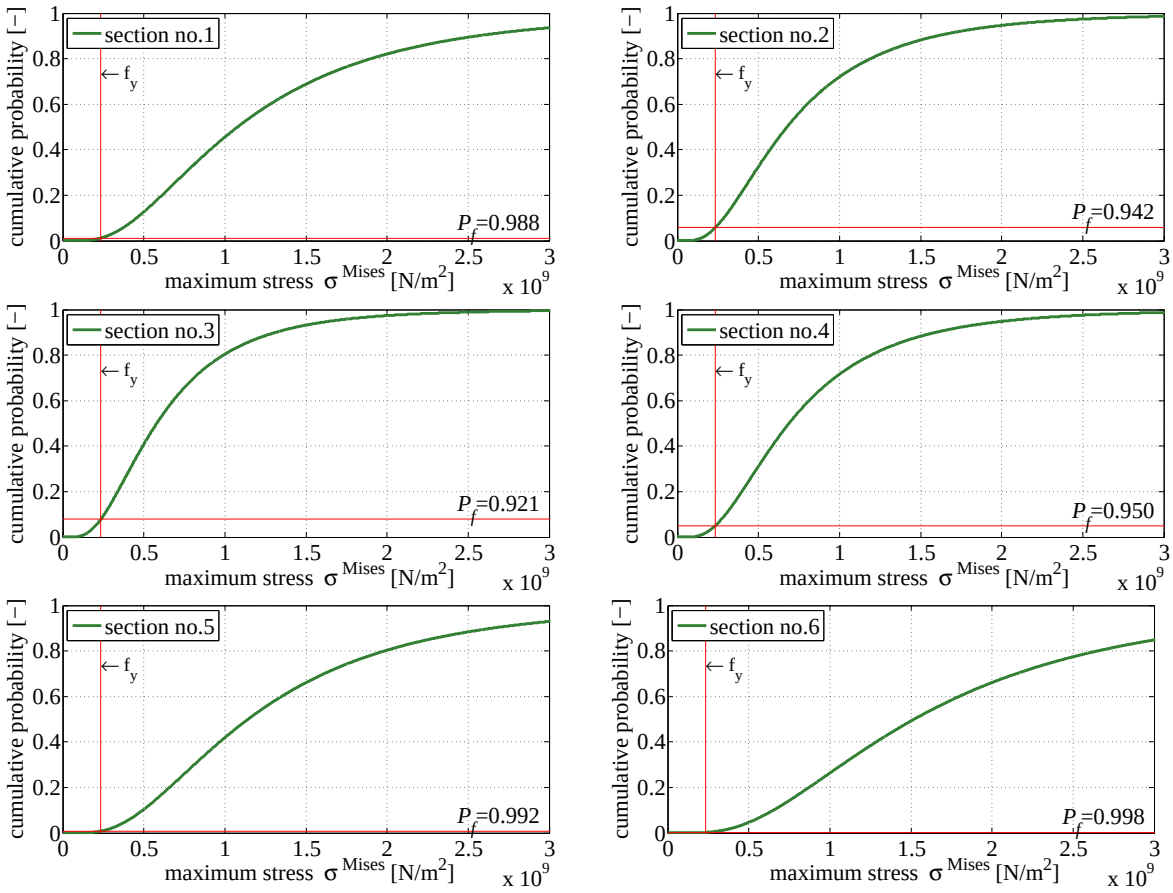

Figure 10.39: Cumulative probability distribution of the maximum von Mises stresses in each of the six analysed sections with marked failure probability P_f.

As could already be expected from the four deterministic simulation results in Fig. 10.37 where three of the maximum von Mises stress distributions exhibit values far above the yield stress, the failure probability of the examined pipeline due to the M_w=5.9 earthquake is very high. Also, it is obvious that the sections at the endings of the pipeline, especially section 6 where the waves incident, are more probable to fail than the sections in the middle (sections 2 to 4). On basis of the results of the probabilistic analysis, it can be stated that the studied buried pipeline is nearly certain to fail (max. P_f=99.8%) under the seismic wave excitation of a M_w=5.9 earthquake.

For a further analysis of the total risk which incorporates also terms of the consequences $E(D)$, the derived failure probabilities P_f can be incorporated. Concluding, it is shown that the entire methodology developed in this work is able to quantify the probability of failure of underground pipelines. Therewith, a detailed damage risk analysis of underground pipelines exposed to transient seismic waves including a reliable seismic excitation and three-dimensional soil-structure interaction can be performed. Moreover, the introduced methodology is not only restricted to underground pipelines but is also applicable to any other structure which is subject to seismic wave propagation effects.

Conclusions and outlook

The earthquake resistance of underground lifelines is particular important for civilisation in seismic-prone areas. Since the seismically caused failure of lifelines can result in disastrous events, the demand for reliable models examining their dynamic response under earthquake excitation is obvious.

In this work, a methodology is developed to analyse the damage risk of buried lifelines exposed to seismic wave propagation effects. This risk analysis covers the probabilities of hazard occurrence, exposure and vulnerability, whereas consequences are excluded. The performance of the analysis is achieved by a methodology that combines multiple numerical methods to an approach that covers deterministic and probabilistic treatments. In this approach, the seismic wave propagation from the causing earthquake source to the near-field of the buried lifeline is regarded. In doing so, the dynamic response of pipelines embedded in soil as well as the probability of their failure due to transient seismic wave propagation, including all types of waves, is realistically simulated.

Conclusions

In the development of the methodology, the emphasis is placed on three topics: incorporation of dynamic soil-structure interaction enabling wave radiation to infinity, advanced and realistic modelling of seismic wave excitation, and over-all consideration of uncertainties.

Dynamic soil-structure interaction is examined by a hybrid finite element-scaled boundary finite element method. Whereas the finite element method (FEM) enables a detailed modelling of the near-field, i.e., of the domain containing pipeline and soil, the scaled boundary finite element method (SBFEM) fulfils the wave radiation condition at infinity.

In latter method, increase of efficiency is achieved by reducing the non-locality in space and time in combination with employing substructuring techniques. It is demonstrated that the incorporation of substructures in the SBFEM leads to a significant reduction of CPU time of about 98% without evanescent losses of accuracy. The successful absorption of waves by the use of the incorporated SBFEM techniques is evidenced.

Commonly, the **seismic wave propagation** in an extended near-field is considered by simplified approaches. For the analysis of the dynamic response of a structure due to transient wave propagation effects, a realistic modelling of those effects is indispensable. Therefore, a novel procedure for modelling seismic wave propagation in the near-field based on the domain reduction method (DRM) is introduced in this work. This procedure includes two steps. In the first step, a large scale simulation of an earthquake is performed by means of numerical Green's functions constructed by the discrete wavenumber finite element method (DWFEM). The earthquake source is regarded as finite fault with a complex slip distribution derived from the deterministic-stochastic k^{-2}-model. In a second step, the dynamic response of a reduced domain containing the structure surrounded by soil is examined with the hybrid method, described above. The reduced domain is excited by forces equivalent to the excitation of the seismic source from the first step.

The competency of the integrated large scale model is approved by comparing simulation results to the recorded ground motion of a real earthquake. Further, the ability of the DRM to introduce the seismic wave field correctly with respect to all kinds of waves into the near-field is demonstrated. Thereby, the necessity of implementing absorbing boundary conditions, like the SBFEM, at the near-field/far-field

interface of the reduced domain is pointed out. Altogether, it is demonstrated that a realistic seismic wave propagation inside the near-field can be modelled.

To consider uncertainties, an integrated **probabilistic concept** is suggested. This analysis includes parameters of the entire seismic wave propagation path, starting from the earthquake source, through the earth crust and the soil and ending up at the buried lifeline. The basis of this concept is a point estimate method (PEM) for multiple random variables. The advantage of this concept is the efficient and reliable determination of the failure probability of a structure by the implicit usage of the deterministic multi-method approach addressed before.

The procedure of the probabilistic concept is demonstrated by the artificial generation of an earthquake which features a probabilistic distribution of its produced ground motion. Further, the probability of failure of pipeline sections due to this earthquake is determined. In this, exemplary two random input variables are considered which cover the fields of hazard and exposure.

The **applicability** of the present methodology is shown by analysing relevant parts of an existing lifeline network of a seismic-exposed municipality in Emilia-Romagna, Italy. Furthermore, studies are executed to exhibit the effects of computational aspects. Hereon, extended parameter studies are performed which analyse aspects of the position of the pipeline with respect to the seismic source, of construction details, like burial depth, backfill, and slippage between pipe and soil, as well as of pipe design properties, like segmentation of the pipeline, cross section, and pipe material. Those studies also approve the utilisability of the presented methodology to problems which are highly three-dimensional, like the examination of effects of seismic waves which incident at varying angles and the dynamic response analysis of a tee joint connection of two pipelines. The results of those parameter studies provide suggestions how to improve the seismic resistance of underground pipelines.

The work in hand introduces a sophisticated tool for an integrated analysis of the seismic damage risk of underground lifelines. Furthermore, the present methodology is not only applicable to buried lifelines but to any other structure or region of interest under seismic wave excitation.

Outlook

The introduced methodology was developed with the emphasis placed on the three mentioned topics addressed above. In order to process those central questions, a secondary status is attributed to some phenomena which, thus, are not regarded. Nevertheless, it could be revealing to study their effects. Some of this further research shall be briefly listed.

In the large scale model, the attenuation effects of earthquakes are not included. Thus, the realistic simulation is restricted to epicentral distances of about 30km. Models, which posses the same efficiency as the used model and which are able to simulate attenuated seismic ground response need to be incorporated to study lifelines at large epicentral distances.

Linear behaviour of material and geometry is considered in the examination of the near-field containing pipeline and soil. The effects of non-linear material of the soil as well as of the pipeline, e.g., for concrete, could be studied. The slippage between pipe and soil as well as the effects at the joints between two pipeline segments are modelled by linear springs. A more detailed analysis concerning the effects of the phenomena occurring at those points of connection could be performed, e.g., by means of non-linear contact elements.

The influences of the material transported in the pipeline on the dynamic response are believed not to be significant and, thus, are not considered. Nevertheless, the examination of the interaction effects of the pipeline surrounded by the soil with the conveyed material could be interesting.

Finally, the results obtained from the present methodology should be compared to measurements gained from observations and experimental results.

Concluding, the present work provides a good basis for future research on the seismic resistance of buried lifelines. This research is crucial considering the disastrous consequences of their failure.

Appendices

A Mathematical notation

Notation

Cartesian coordinates $\mathbf{x}$ are denoted as

$$\mathbf{x} = \begin{bmatrix} x & y & z \end{bmatrix}^T = \begin{bmatrix} x_1 & x_2 & x_3 \end{bmatrix}^T , \tag{A.1}$$

displacements $\mathbf{u}$ as

$$\mathbf{u} = \begin{bmatrix} u & v & w \end{bmatrix}^T = \begin{bmatrix} u_1 & u_2 & u_3 \end{bmatrix}^T , \tag{A.2}$$

stresses $\boldsymbol{\sigma}$ as

$$\boldsymbol{\sigma} = \begin{bmatrix} \sigma_{11} & \sigma_{22} & \sigma_{33} & \sigma_{23} & \sigma_{31} & \sigma_{12} \end{bmatrix}^T , \tag{A.3}$$

and strains $\boldsymbol{\varepsilon}$ in pseudo-vector notation as

$$\boldsymbol{\varepsilon} = \begin{bmatrix} \varepsilon_{11} & \varepsilon_{22} & \varepsilon_{33} & 2\varepsilon_{23} & 2\varepsilon_{31} & 2\varepsilon_{12} \end{bmatrix}^T . \tag{A.4}$$

Conventions

Where it is more concise, the indical notation is used instead of the more common symbolic notation, to represent tensors and matrices. In this notation partial differentiation may be abbreviated using the comma convention

$$\frac{\partial a_i}{\partial x_j} = a_{i,j} . \tag{A.5}$$

Further on, the *Einstein summation convention* is utilised which states that a subscript that is appearing twice is summed from 1 to 3:

$$a_i b_i = \sum_{i=1}^{3} a_i b_i . \tag{A.6}$$

Additionally, *Kronecker delta* is used which is defined as

$$\delta_{ij} = \begin{cases} 0 & \text{for} \quad i \neq j \\ 1 & \text{for} \quad i = j \end{cases} \tag{A.7}$$

providing under an integral the filter property

$$\int_{t_0}^{t_1} f(t)\delta(t-a)dt = \begin{cases} f(a) & \text{for} \quad t_0 < a < t_1 \\ 0 & \text{for} \quad a < t_0 \text{ and } a > t_1 \end{cases} \tag{A.8}$$

called *Dirac distribution*.

Assuming two scalar functions $u_i(\mathbf{x},t)$ and $t_i(\mathbf{x},t)$ which are continuous in their defined domain and in the time-interval $t \in [0,\infty[$. The operator $*$ symbolises the *convolution* in time which is defined as

$$t_i(\mathbf{x},t) * u_i(\mathbf{x},t) = \begin{cases} \int_0^t t_i(\mathbf{x},t-\tau)u_i(\mathbf{x},\tau)d\tau & \forall\,(\mathbf{x},t>0) \\ 0 & \forall\,(\mathbf{x},t<0) . \end{cases} \tag{A.9}$$

Differential operators

- Nabla Operator

$$\nabla = \frac{\partial}{\partial x_1}\mathbf{e}_1 + \frac{\partial}{\partial x_2}\mathbf{e}_2 + \frac{\partial}{\partial x_3}\mathbf{e}_3 \tag{A.10}$$

- Gradient of vector

$$\begin{aligned}\nabla\mathbf{a} = \frac{\partial a_1}{\partial x_1}\mathbf{e}_1\mathbf{e}_1 + \frac{\partial a_2}{\partial x_1}\mathbf{e}_1\mathbf{e}_2 + \frac{\partial a_3}{\partial x_1}\mathbf{e}_1\mathbf{e}_3 + \frac{\partial a_1}{\partial x_2}\mathbf{e}_2\mathbf{e}_1 + \frac{\partial a_2}{\partial x_2}\mathbf{e}_2\mathbf{e}_2 + \frac{\partial a_3}{\partial x_2}\mathbf{e}_2\mathbf{e}_3 \\ + \frac{\partial a_1}{\partial x_3}\mathbf{e}_3\mathbf{e}_1 + \frac{\partial a_2}{\partial x_3}\mathbf{e}_3\mathbf{e}_2 + \frac{\partial a_3}{\partial x_3}\mathbf{e}_3\mathbf{e}_3\end{aligned} \tag{A.11}$$

- Divergence

$$\nabla\cdot\mathbf{a} = \frac{\partial a_1}{\partial x_1} + \frac{\partial a_2}{\partial x_2} + \frac{\partial a_3}{\partial x_3} = \frac{\partial a_i}{\partial x_i} = a_{i,i} \tag{A.12}$$

- Curl

$$\nabla\times\mathbf{a} = \begin{vmatrix} \mathbf{e}_1 & \mathbf{e}_2 & \mathbf{e}_3 \\ \frac{\partial()}{\partial x_1} & \frac{\partial()}{\partial x_2} & \frac{\partial()}{\partial x_3} \\ a_1 & a_2 & a_3 \end{vmatrix} = \left(\frac{\partial a_3}{\partial x_2} - \frac{\partial a_2}{\partial x_3}\right)\mathbf{e}_1 + \left(\frac{\partial a_1}{\partial x_3} - \frac{\partial a_3}{\partial x_1}\right)\mathbf{e}_2 + \left(\frac{\partial a_2}{\partial x_1} - \frac{\partial a_1}{\partial x_2}\right)\mathbf{e}_3 \tag{A.13}$$

- Curl of curl

$$\nabla\times\nabla\mathbf{a} = \nabla\nabla\cdot\mathbf{a} - \nabla\cdot\nabla\mathbf{a} \tag{A.14}$$

-

$$\begin{aligned}\nabla\nabla\cdot\mathbf{a} = \left[\frac{\partial^2 a_1}{\partial x_1^2} + \frac{\partial^2 a_2}{\partial x_2\partial x_3} + \frac{\partial^2 a_3}{\partial x_1\partial x_3}\right]\mathbf{e}_1 + \left[\frac{\partial^2 a_1}{\partial x_2\partial x_1} + \frac{\partial^2 a_2}{\partial x_2^2} + \frac{\partial^2 a_3}{\partial x_2\partial x_3}\right]\mathbf{e}_2 \\ + \left[\frac{\partial^2 a_1}{\partial x_3\partial x_1} + \frac{\partial^2 a_2}{\partial x_3\partial x_2} + \frac{\partial^2 a_3}{\partial x_3^2}\right]\mathbf{e}_3\end{aligned} \tag{A.15}$$

- Laplacian

$$\nabla^2\mathbf{a} = \nabla\cdot\nabla\mathbf{a} = \nabla^2 a_1\mathbf{e}_1 + \nabla^2 a_2\mathbf{e}_2 + \nabla^2 a_3\mathbf{e}_3 = \left(\frac{\partial^2}{\partial x_1^2} + \frac{\partial^2}{\partial x_2^2} + \frac{\partial^2}{\partial x_3^2}\right)\mathbf{a} \tag{A.16}$$

B Earthquake simulation results

The results of earthquake simulation described in Sec 9.3 of the frequency-pair $f_{\max}$ =20Hz and f_{lp} =20Hz are depicted.

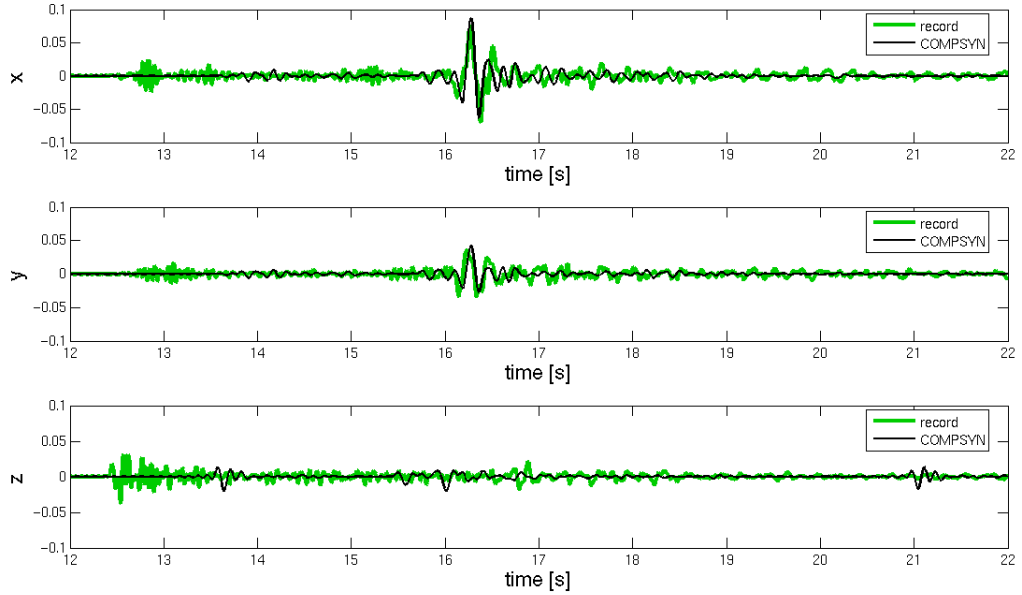

Figure B.1: Acceleration [g] (f_{max}= 20Hz, f_{lp}= 20Hz)

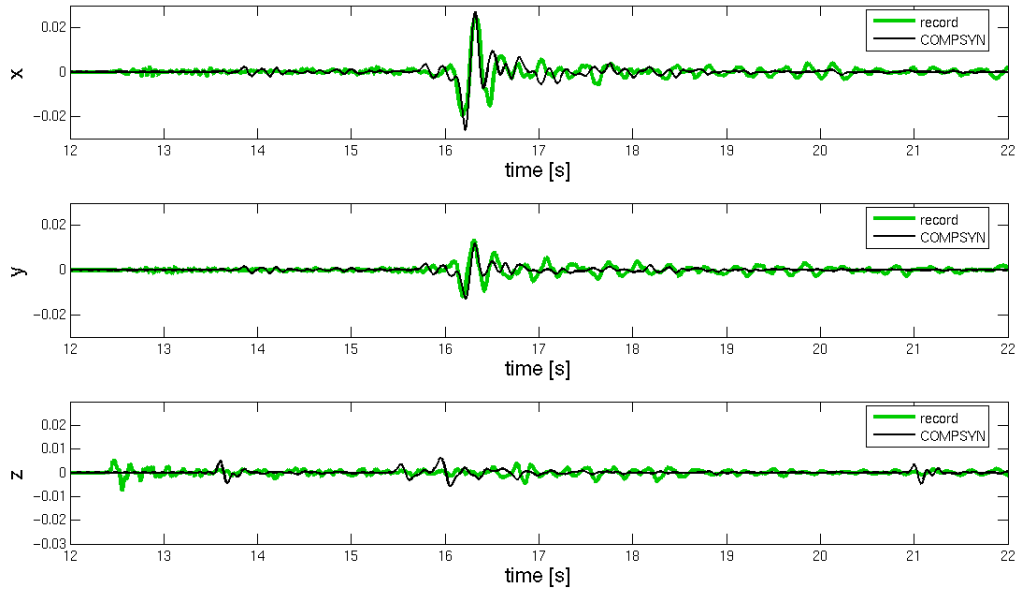

Figure B.2: Velocity [m/s] (f_{max}= 20Hz, f_{lp}= 20Hz)

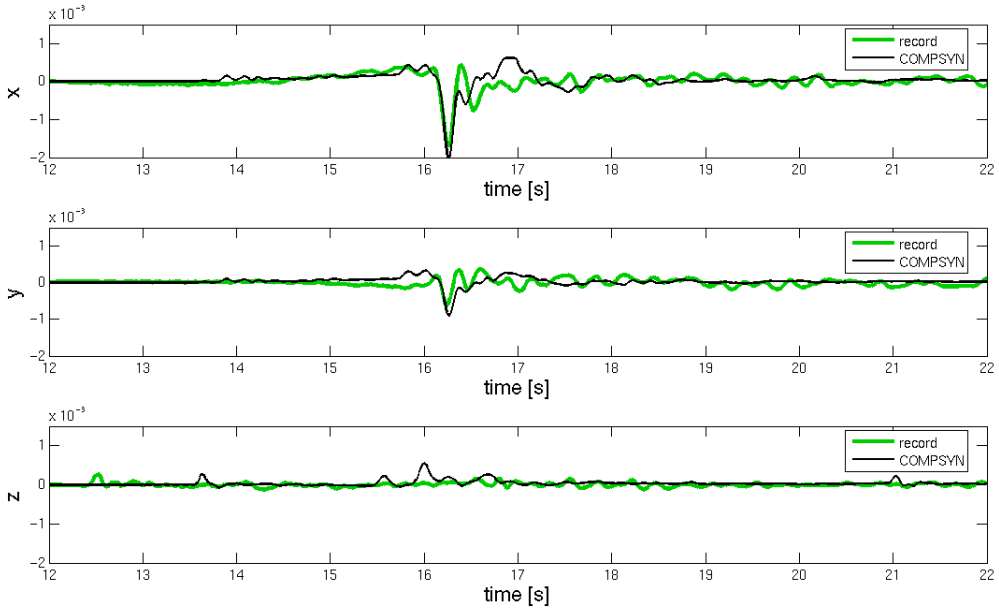

Figure B.3: Displacement [m] (f_{max}= 20Hz, f_{lp}= 20Hz)

		x	y	z
PGA [g]	record	$7.39 \cdot 10^{-2}$	$3.52 \cdot 10^{-2}$	$3.74 \cdot 10^{-2}$
	simulation	$8.69 \cdot 10^{-2}$	$4.14 \cdot 10^{-2}$	$2.02 \cdot 10^{-2}$
	error [%]	17.63	17.60	-46.01
PGV [$\frac{mm}{s}$]	record	24.63	13.32	7.51
	simulation	27.13	12.95	6.19
	error [%]	10.14	-2.78	-17.68
PGD [mm]	record	1.70	0.61	0.27
	simulation	2.03	0.90	0.55
	error [%]	19.59	47.62	105.35
I_A [$\frac{mm}{s}$]	record	13.00	6.65	4.56
	simulation	13.41	3.22	1.68
	error [%]	3.14	-51.62	-63.11
D_s [s]	record	8.04	10.95	8.34
	simulation	13.35	11.34	12.19
	error [%]	65.99	3.59	46.27
error mean [%]		23.30	24.64	55.68
Q_{GM}		19.80	11.39	20.50

Table B.1: Ground motion parameters (f_{max}= 20Hz, f_{lp}= 20Hz)

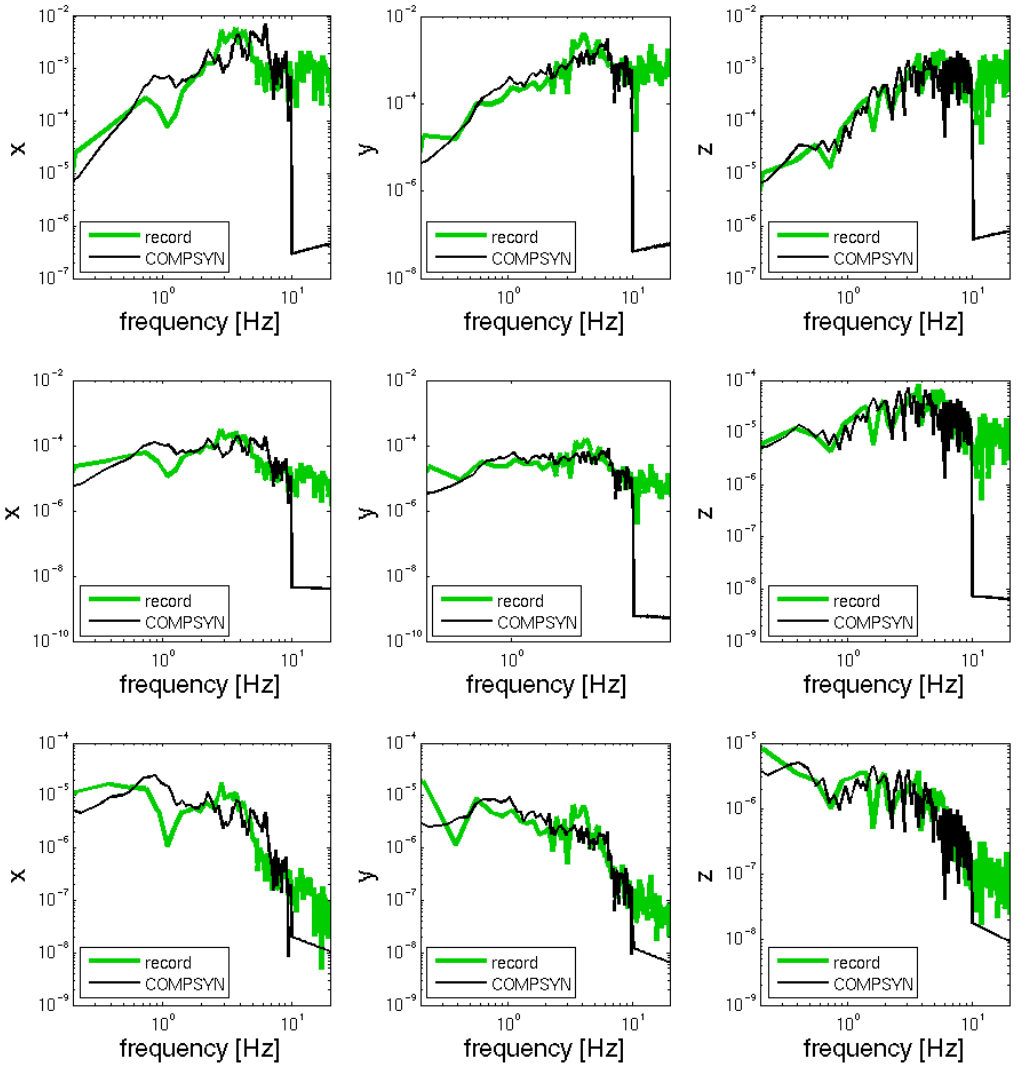

Figure B.4: From top to bottom: frequency-spectra of acceleration, velocity, and displacement (f_{max}= 20Hz, f_{lp}= 20Hz)

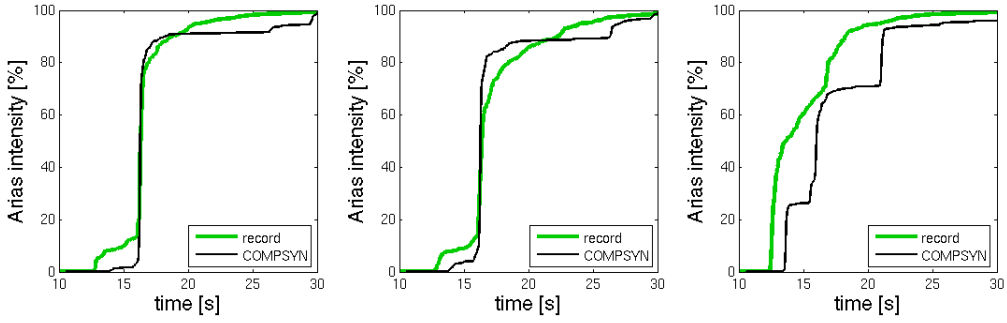

Figure B.5: Arias intensity (f_{max}= 20Hz, f_{lp}= 20Hz)

Nomenclature

Roman symbols

A, B	amplitudes
$B^m_{zk}, B^m_{rk}, B^m_{\phi k}$	complex scalar body force coefficients
$\mathbf{b}$	body force vector
$b_j^{[u]}$	body force equivalent to displacement discontinuity
b_s	bedding factor in slippage direction
$\mathbf{C}$	damping matrix
C_{ikjl}	elastic stiffness tensor
c_{ij}	boundary matrix
c_L	Love wave velocity
c_P	P-wave velocity
c_R	Rayleigh wave velocity
c_S	S-wave velocity
$\mathbf{D}$	gradient operator
D	final offset after rupture
D_s	strong motion duration after [Trifunac and Brady, 1975]
d_j	joint depth
d_p	pipe diameter
$\mathbf{E}$	elasticity matrix
E	Young's modulus
$E()$	expected value
E_p, ν_p, ρ_p	material parameter of pipeline
E_s, ν_s, ρ_s	material parameter of soil
$\mathbf{f}$	force vector
$\mathbf{f}^{\text{eff}}$	equivalent seismic forces (DRM)
$\mathbf{f}_r$	interaction force
$\mathbf{f}_{seis}$	body force vector of original seismic excitation (DRM)
f	frequency
$f()$	function
$f_{\max}$	maximum resolving frequency of DWFEM
f_{lp}	low-pass frequency
f_0	corner frequency
f_c	cutoff frequency
$f_X(x)$, $f_Y(y)$	probability distribution function
f_y	yield stress
$\mathbf{G}^*$	Green's function
G	shear modulus
g	gravity of earth
$\hat{h}$	hypocentral depth
h_b	burial depth of pipeline
$\mathbf{I}$	unit matrix
I_0	total intensity
I_A	Arias intensity
$\mathbf{J}$	Jacobian matrix
J_m	first kind Bessel function
$\mathbf{K}$	stiffness matrix
K	bulk modulus
k	wavenumber
k_j	joint spring stiffnesses
k_s	slip spring stiffness
$k_{\max}$	maximum wavenumber (DWFEM)
L	length of seismic fault

$L(D)$	linear differential operator
$\mathbf{M}$	mass matrix
$\mathbf{M}^{\infty}$	acceleration unit-impulse response matrix (SBFEM)
M_0	seismic moment
M_L	Richter local magnitude
M_s	surface wave magnitude
M_w	moment magnitude
m_b	body wave magnitude
$\mathbf{N}$	shape function vector
N_S	number of SBFEM substructures
$\mathbf{n}$	normal vector
$\mathbf{P}$	stress divergence matrix
$\mathbf{p}_i$	vector of a ground motion parameter
P_r	probability of resistance
P_{Ex}	probability of exposure
P_f	probability of failure
P_H	probability of hazard
P_{pn}	PEM weight of variable X_n
P_V	probability of vulnerability
p	horizontal slowness
p	load per unit area
Q_{GM}	ground motion index
$\mathbf{R}_k^m$, $\mathbf{S}_k^m$, $\mathbf{T}_k^m$	surface vector harmonics
R	total risk
R_d	damage risk
r_p	pipe radius
$\mathbf{S}$	stress tensor
$\mathbf{S}^{\infty}$	displacement unit-impulse response matrix (SBFEM)
S	rupture area
$\grave{S}_1, \acute{S}_1, \grave{S}_2, \acute{S}_2$	amplitudes
$\mathbf{t}$	traction vector
$\mathbf{t}^*$	fundamental traction solution
T	period
$[t_j]$	traction discontinuity on fault
Δt	time-step
t	time
$t_{\max}$	simulation time
$\bar{t}_i$	Neumann boundary condition
t_p	thickness of pipe wall
t_r	rise time
$U_{zk}^m, U_{rk}^m, U_{\phi k}^m$	complex scalar displacement coefficients
$\mathbf{u}$	displacement vector
$\dot{\mathbf{u}}$	velocity vector
$\ddot{\mathbf{u}}$	acceleration vector
$\mathbf{u}^*$	fundamental displacement solution
$\lvert\mathbf{u}\rvert$	length of displacement vector (Euclidean norm)
Δu_j^p	relative axial contacting joint displacement
Δu_j^t	relative axial extensional joint displacement
Δu_{ult}^p	ultimate relative axial joint displacement
$[u_j]$	displacement discontinuity on fault
u_{0i}	initial displacement condition
$\bar{u}_i$	Dirichlet boundary condition
v_{0i}	initial velocity condition
v_R	rupture velocity
$\mathbf{w}_e$	residual motion in outer domain Ω^+ (DRM)
W	strain-energy density
W	width of seismic fault
$\mathbf{x}$	coordinate vector
$\mathbf{x}$	field point

X, Y	random variable
x_{pn}	PEM evaluation point of variable X_n
Y_k^m	second kind Bessel function
(z, r, ϕ)	cylindrical coordinates

Greek symbols

α	HHT-α time-integration parameter
β	HHT-α time-integration parameter
Δ	angle of epicentral distance
$\hat{\delta}$	dip angle
δ_{ij}	Dirac delta-function
$\boldsymbol{\varepsilon}$	strain tensor
ε	radius of spherical extension around singular point
ε_p	pressure strain
ε_t	tolerance threshold for reduction of non-locality in time (SBFEM)
$\varepsilon_{t,\mathrm{lim}}$	limit tensile strain
ε_z	zero-element threshold for reduction of non-locality in space (SBFEM)
$\hat{\phi}$	strike angle
φ	scalar potential
Γ	boundary
Γ	interface between Ω and Ω^+ (DRM)
Γ_e	external interface adjacent to Γ (DRM)
Γ_t	Neumann boundary
Γ_u	Dirichlet boundary
γ	HHT-α time-integration parameter
$\boldsymbol{\eta}$	point on internal surface Σ
η	vertical slowness
λ	Lamé's constant
$\hat{\lambda}$	rake angle
λ_{min}	minimum resolving wavelength (DWFEM)
λ_R	Rayleigh wave length
μ	Lamé's constant
μ	shear modulus
μ_X, μ_Y	mean of random variable
μ_{Xm}, μ_{Ym}	random moment of order m
ν	Poisson's ratio
ν_X, ν_Y	skewness of random variable
Θ_j	relative joint rotation
Θ_{lim}	limited relative joint rotation
ρ	mass density
Σ	internal surface
$\boldsymbol{\sigma}$	stress tensor
$\boldsymbol{\sigma}^P$	vector of principal stresses
$\sigma_n^{\mathrm{Mises}}$	von Mises stress
$\sigma_n^{\mathrm{Tresca}}$	Tresca stress
σ_p	pressure stress
$\sigma_{p,\mathrm{lim}}$	limit pressure stress
σ_t	tensile stress
σ_X, σ_Y	standard deviation of random variable
Ω	domain
Ω^+	outer domain (DRM)
Ω_0	region of interest (DRM)
ω	angular frequency
$\boldsymbol{\xi}$	source point
$\boldsymbol{\Psi}$	vector potential

Abbreviations

BEM	boundary element method
CI	cast iron
CPU	central processing unit
DRM	domain reduction method
DWFEM	discrete wavenumber finite element method

FDM	finite difference method
FEM	finite element method
HDPE	high density polyethylene
PGA	peak ground acceleration
PGD	peak ground displacement
PGV	peak ground velocity
PVC	polyvinyl chloride
P-wave	primary wave
S-wave	secondary wave
SBFEM	scaled boundary finite element method
SH-wave	horizontal secondary wave
SSI	soil-structure interaction
SV-wave	vertical secondary wave
UTC	coordinated universal time

Bibliography

Aki, K. (1967). Scaling law of seismic spectrum. *Journal of Geophysical Research*, **72**, 1217–1231.

Aki, K. and Richards, P. G. (2002). *Quantitative seismology*. University Science Books, Sausalito, Calif., 2 edition.

Akiyoshi, T. (1978). Compatible viscous boundary for discrete models. *Journal of Engineering Mechanics*, **104**, 1253–1265.

American Lifelines Alliance (2001a). *Guideline for the Design of Buried Steel Pipe*. American Society of Civil Engineers, New York, NY.

American Lifelines Alliance (2001b). *Seismic Fragility Formulations for Water Systems - Part 1 - Guideline*. American Society of Civil Engineers, New York, NY.

American Lifelines Alliance (2001c). *Seismic Fragility Formulations for Water Systems - Part 2 - Appendices*. American Society of Civil Engineers, New York, NY.

Anderson, J. G. (2003). Strong-motion seismology. In W. H. K. Lee, H. Kanamori, P. C. Jennings, and C. Kisslinger, editors, *International Handbook of Earthquake and Engineering Seismology*, chapter 57, pages 937–966. Academic Press, New York.

Andrews, D. J. (1981). A stochastic fault model, 2, time-dependent case. *Journal of Geophysical Research*, **86**, 10821–10834.

Ang, A. H. S. and Newmark, N. M. (1963). Computation of underground structural response - DASA Report No. 1386. Technical report, Urbana.

Antes, H. (1985). A boundary element procedure for transient wave propagations in two-dimensional isotropic elastic media. *Finite Elements in Analysis and Design*, **1**, 313–322.

Antes, H. (1989). Dynamic interaction analysis in wave propagation problems by a time-dependent boundary element method. In G. Kuhn and H. Mang, editors, *Proc. of IUTAM/IACM-Symp. on Discretization Methods in Structural Mechanics, Juni 89*, Wien. Springer Verlag Berlin,Wien, New York.

Antes, H. (2002). *Boundary Element Methods for Wave Propagation Problems - Lecture Notes*. Institute of Applied Mechanics, TU Braunschweig, Braunschweig.

Antes, H. (2005). *A Short Course on Boundary Element Methods - Lecture Notes*. Institute of Applied Mechanics, TU Braunschweig, Braunschweig.

Antes, H. and Spyrakos, C. (1997). Soil-structure interaction. In D. E. Beskos and S. A. Anagnotopoulos, editors, *Computer Analysis and Design of Earthquake Resistant Structures*, chapter 7, pages 271–332. Computational Mechanics Publications.

Antes, H. and Tröndle, G. (1992). Experience with multigrid in three-dimensional acoustic boundary element method. In *Proc. 14th Aeroacoustics Conference, Springer*, Aachen.

Antes, H., Capuani, D., Klein, R., and Tralli, A. (1995). Dynamic soil-structure interaction of coupled shear walls by boundary element method. *Earthquake Engineering and Structural Dynamics*, **24**, 861–879.

Aoki, Y. and Hayashi, S. (1973). Spectra for earthquake resistive design of underground structures. In *Proc. 5th World Conf. Earthquake Eng.*, Rome.

Apsel, R. and Luco, J. (1983). On the green's functions for a layered half-space. part ii. *Bulletin of the Seismological Society of America*, **73**(4), 931–951.

Arias, A. (1970). A Measure of Earthquake Intensity. In R. Hansen, editor, *Seismic Design for Nuclear Power Plants*, pages 438–469. MIT Press, Cambridge (MA).

Astley, R. J. (2000). Infinite elements for wave problems: a review of current formulations and an assessment of accuracy. *International Journal for Numerical Methods in Engineering*, **49**(7), 951–976.

Augusti, G. (2006). What do we mean by "risk"? In *Sokrates/Erasmus Intensive Post-Graduate Programme "Stochastic Dynamics in Risk Management Procedures"*, Florence.

Augusti, G., Borri, C., and Niemann, H.-J. (2001). Is Aeolian risk as significant as other environmental risks? *Reliability engineering system safety . - London : Elsevier*, **74**, 227–238.

Axelsson, O. (1996). *Iterative solution methods*. Cambridge Univ. Press, Cambridge, UK.

Ayala, A. G., O'Rourke, M. J., and Escobar, J. A. (1990). Evaluation of the effects of the 1985 michoacan earthquake on the water systems in metropolitan mexico city. *Earthquake Spectra*, **6**(3), 473–496.

Aydinoglu, M. N. (1980). Unified formulations for soil-structure interaction. In *Proceedings of the 7th World Conference in Earthquake Engineering*, volume 7, pages 121–128, Istanbul, Turkey.

Baecher, G. B. and Christian, J. T. (2003). *Reliability and statistics in geotechnical engineering*. Wiley, Chichester.

Ballantyne, D. (1995). Issues and recommendations in water and wastewater lifeline earthquake engineering. In A. J. Schiff and I. G. Buckle, editors, *Critical Issues and State-of-the-Art in Lifeline Earthquake Engineering*, pages 41–56, New York, NY. American Society of Civil Engineers.

Baron, M. L. and Matthews, A. T. (1961). Diffraction of a pressure wave by a cylindrical cavity in an elastic medium. *Journal of applied mechanics . - New York*, **28**, 345–354.

Bartels, R. H. and Stewart, G. W. (1972). Algorithm 432: Solution of the matrix equation ax + xb = c. *Communications of the ACM*, **15**, 820–826.

Basu, U. and Chopra, A. K. (2004). Perfectly matched layers for transient elastodynamics of unbounded domains. *International Journal for Numerical Methods in Engineering*, **59**, 1039–1074.

Bathe, K.-J. (1996). *Finite element procedures*. Prentice Hall, Englewood Cliffs, NJ.

Bazyar, M. H. and Song, C. (2006a). Time-harmonic response of non-homogeneous elastic unbounded domains using the scaled boundary finite-element method. *Earthquake engineering structural dynamics . - London : Wiley*, **35**, 357–384.

Bazyar, M. H. and Song, C. (2006b). Transient analysis of wave propagation in non-homogeneous elastic unbounded domains by using the scaled boundary finite-element method. *Earthquake engineering structural dynamics . - London : Wiley*, **35**, 1787–1806.

Beer, G. (2001). *Programming the Boundary Element Method*. Wiley and Sons, Chichester, UK.

Benjamin, J. R. and Cornell, C. A. (1970). *Probability, Statistics, and Decision for Civil Engineers*. McGraw-Hill, New York.

Berenger, J. P. (1996). Three-dimensional perfectly matched layer for the absorption of electromagnetic waves. *Journal of Computational Physics*, **127**, 363–379.

Bettess, P. (1992). *Infinite Elements*. Penshaw Press.

Betti, E. (1872). Teoria della elasticità. *Il Nuovo Cimento*, **2**, 6–10.

Bielak, J. and Christiano, P. (1984). On the effective seismic input for non-linear soil-structure interaction systems. *Earthquake Engineering and Structural Dynamics*, **12**, 107–119.

Bielak, J., Loukakis, K., Hisada, Y., and Yoshimura, C. (2003). Domain reduction method for three-dimensional earthquake modeling in localized regions, part i: Theory. *Bulletin of the Seismological Society of America*, **93**(2), 817–824.

Bolt, B. A. (1969). Duration of strong motion. In *Proceedings of the 4th World Conference on Earthquake Engineering*, pages 1304–1315, Santiago, Chile.

Bonnet, M. (1995). *Boundary integral equation methods for solids and fluids*. Wiley and Sons, Chichester, UK.

Bonnet, M., Maier, G., and Polizzotto, C. (1998). Symmetric galerkin boundary element methods. **51**(11), 669–704.

Boore, D. (2003). Simulation of Ground Motion Using the Stochastic Method. *Pure and applied geophysics . - Basel : Birkhäuser*, **160**, 635–676.

Borsutzky, R. (2006). Seismic risk analysis of buried lifelines: simulation of seismic ground motion. Technical report, International Graduate College "Risk Management of Natural and Civilization Hazards on Buildings and Infrastructure". Periodical report, July 2006.

Borsutzky, R. and Lehmann, L. (2005). Numerische Simulation unterirdischer Versorgungsleitungen unter Erdbebeneinwirkung. In K. Meskouris, C. Butenweg, and K. G. Hinzen, editors, *D-A-CH Tagung 2005 in Köln: Aktuelle Themen des Erdbebeningenieurwesens und der Baudynamik*, pages 89–94, Aachen. Deutsche Gesellschaft für Erdbebeningenieurwesen und Baudynamik (DGEB).

Borsutzky, R. and Lehmann, L. (2006a). Numerical analysis of buried lifelines exposed to earthquake motion. In *First European Conference on Earthquake Engineering and Seismology*, Geneva.

Borsutzky, R. and Lehmann, L. (2006b). Simulation of traffic induced vibrations with a three-dimensional soil structure interaction model. Vienna, Austria. The Thirteenth International Congress on Sound and Vibration.

Brune, J. N. (1971). Tectonic stress and the spectra of seismic shear waves from earthquakes: Correction. *Journal of Geophysical Research*, **76**, 5002.

Chen, Y. and Krauthammer, T. (1992). Seismic effects on large reinforced concrete lifelines - Parts I/II. *Comput. Struct.*, **32**, 129–135.

Chin, Y. F., Rajapakse, R. K., Shah, A. H., and Datta, S. K. (1987). Dynamics of buried pipes in a backfill trench. *Soil dynamics and earthquake engineering*, **6**, 158–163.

Christian, J. T. (2004). Geotechnical engineering reliability: How well do we know what we are doing? *Journal of Geotechnical and Environmental Engineering*, **130**(10), 985–1003.

Christian, J. T. and Baecher, G. B. (1999). Point-estimate method as numerical quadrature. *Journal of Geotechnical and Geoenvironmental Engineering*, pages 779–786.

Christian, J. T. and Baecher, G. B. (2002). The point-estimate method with large numbers of variables. *International journal for numerical and analytical methods in geomechanics*, **26**(15), 1515–1530.

Cinti, F. R., Faenza, L., Marzocchi, W., and P., M. (2004). Probability map of the next M >= 5.5 earthquakes in Italy. *Geochemistry Geophysics Geosystems*, **5**.

Clough, R. W. and Penzien, J. (1975). *Dynamics of structures*. McGraw-Hill, New York.

Coifman, R., Rokhlin, V., and Wandzura, S. (1993). The fast mulitpole method for the wave equation – a pedestrian prescritption. *IEEE Antennas and Propagation Magazine*, **35**(3), 7–12.

COMET (2007). *http://comet.nerc.ac.uk*. Centre for the Observation and Modelling of Earthquakes and Tectonics.

Constantopoulos, I. V., Motherwell, J. T., and Hall, J. R. (1979). Dynamic analysis of tunnels. In W. Wittke, editor, *Numerical Methods in Geomechanics*, pages 841–848. A. A. Balkema, Rotterdam.

Cremonini, M. G., P., C., and Bielak, J. (1988). Implementation of effective seismic input for soil-structure interaction systems. *Earthquake engineering structural dynamics*, **16**, 615–625.

Crespellani, T., Vannucchi, G., and Zeng, X. (1992). Seismic hazard analysis in the florence area. In *European Earthquake Engineering*, volume 3.

Crespellani, T., Madiai, C., Marcellini, A., Maugeri, M., and Vannucchi, G. (1997). *Seismic Behaviour of Ground and Geotechnical Structures*, chapter Zonation of geotechnical seismic hazards in Tuscany, Italy. A. A. Balkema, Rotterdam.

Crespellani, T., Facciorusso, J., and Renzi, S. (2006). Seismic risk analysis of a lifeline system subjected to permanent ground deformations. In *First European Conference on Earthquake Engineering and Seismology*, Geneva, Switzerland.

Crouch, R. S. and Bennet, T. (2000). Efficient ebe treatment of the dynamic far-field in non-linear fe soil-structure interaction analyses. In *European Congress on Computational Methods in Applied Sciences and Engineering 2000*, Barcelona. ECCOMAS.

Cuthill, E. and McKee, J. (1969). Reducing the bandwidth of sparse symmetric matrices. In *24th Nat. Conf.*, pages 157–172. ACM.

Dasgupta, G. (1982). A finite element formulation for unbounded homogeneous continua. *Journal of Applied Mechanics, ASME*, **49**, 136–140.

Datta, S. K., Shah, A. H., and El-Akily, N. (1982). Dynamic behaviour of a buried pipe in a seismic environment. *Journal of applied mechanics . - New York*, **49**, 141–148.

Datta, S. K., Wong, K. C., and Shah, A. H. (1984a). Dynamic stresses and displacements around cylindrical cavities of arbitrary shape. *Journal of applied mechanics . - New York*, **51**, 798–803.

Datta, S. K., Shah, A. H., and Wong, K. C. (1984b). Dynamic stresses and displacements in buried pipe. *Journal of engineering mechanics*, **110**, 1451–1466.

Datta, S. K., O'Leary, P. M., and Shah, A. H. (1985). Three-dimensional dynamic response of buried pipelines to incident longitudinal and shear waves. *Journal of applied mechanics . - New York*, **52**, 919–926.

Davis, C. A. and Bardet, J. (2000). Responses of buried corrugated metal pipes to earthquakes. *Journal of Geotechnical and Geoenvironmental Engineering*, pages 28–39.

Davis, C. A. and Bardet, J. P. (1998). Seismic Analysis of Large-Diameter Flexible Underground Pipes. *Journal of geotechnical and geoenvironmental engineering*, **124**(10), 1005–1015.

Dawkins, W. P. (1969). Analysis of tunnel liner-paching systems. *Journal of the Engineering Mechanics Division*, **95**, 679–693.

Deans, J. J. and Tang, J. H. K. (1979). Seismic stresses in buried piping of arbitrary configuration. In *Transactions 5th International Conference on Structural Mechanics in Reactor Technology*, Amsterdam.

Deeks, A. and Wolf, J. (2002). An h-hierarchical adaptive procedure for the scaled boundary finite-element method. *International Journal for Numerical Methods in Engineering*, **54**, 585–605.

Department of Earth Science (2007). *http://www.geo.uib.no*. University of Bergen.

Deutsches Institut für Normung (1999). *DIN 4150-3, Einwirkungen auf bauliche Anlagen 3*, volume DIN 4150-3 of *Deutsche Normen*. Normenausschuss Bauwesen, Normenausschuss Akustik, Lärmminderung und Schwingungstechnik, Berlin.

Doherty, J. and Deeks, A. (2003a). Elastic response of circular footings embedded in a non-homogeneous half-space. *Géotechnique . - London : Inst.*, **53**, 703–714.

Doherty, J. P. and Deeks, A. J. (2003b). Scaled boundary finite-element analysis of a non-homogeneous elastic half-space. *International journal for numerical methods in engineering . - Chichester : Wiley*, **57**, 955–974.

Dominguez, J. (1993). *Boundary Elements in Dynamics*. Computational Mechanics Publications, Southampton, UK.

Duffy, D. G. (2001). *Green's functions with applications*. Studies in advanced mathematics. Chapman Hall/CRC, Boca Raton, Fla.

Eguchi, R. T. (2003). Lifeline seismic risk. In W. Chen and C. Scawthorn, editors, *Earthquake Engineering Handbook*, chapter 22. CRC Press, Boca Raton.

Eidinger, J. M. and Avila, E. A. (1999). *Guidelines for the seismic evaluation and upgrade of water transmission facilities*, volume 15 of *Technical Council on Lifeline Earthquake Engineering monograph*. American Soc. of Civil Engineers, Reston, Va.

Eidinger, J. M. *et al.* (2001). *Seismic Fragility Formulations for Water Systems, Part 1 - Guideline*. American Lifelines Alliance.

El-Akily, N. and Datta, S. K. (1981). Response of a circular cylindrical shell to disturbances in a half-space - Parts I/II. *Earthquake engineering structural dynamics*, **8/9**, 469–477,477–489.

Elhmadi, K. and O'Rourke, M. J. (1988). Soil springs for buried pipeline axial motion. *Journal of Geotechnical Engineering*, **114**, 1335–1339.

Elhmadi, K. and O'Rourke, M. J. (1989). *Seismic Wave Propagation Effects on Straight Jointed Buried Pipelines*. National Center for Earthquake Engineering Research, Buffalo, NY.

Elhmadi, K. and O'Rourke, M. J. (1990). Seismic Damage to Segmented Buried Pipelines. *Earthquake Engineering and Structural Dynamics*, **19**(4), 529–539.

Emolo, A., Innaccone, G., Zollo, A., and Gorini, A. (2004). Inferences on the source mechanisms of the 1930 Irpinia (Southern Italy) earthquake from simulations of the kinematic rupture process. *Annals of geophysics . - Bologna : Editrice Compositori*, **47**, 1743–1754.

Engquist, B. and Majda, A. (1977). Absorbing boundary conditions for the numerical simulation of waves. *Math. of Computation*, **31**, 629–651.

Eringen, A. C. and Suhubi, E. S. (1975). *Elastodynamics, Volume II, Linear Theory*. Academic Press, New York, San Francisco, London.

European Committee for Standarization (CEN) (1998). *Eurocode 8: Design of structures for earthquake resistance - Part 4: Silos, tanks and pipelines - CEN ENV 1998-1-1*. Brussels.

Ewing, M., Jardetzky, W. S., and Press, F. (1957). *Elastic waves in layered media*. McGraw-Hill, New York.

Facciorusso, J., Crespellani, T., and Madiai, C. (2006). Investigation of the seismic soil structure interaction on a concrete instrumented building. In *First European Conference on Earthquake Engineering and Seismology*, Geneva, Switzerland.

Fahmi, K. J. and Malkawi, A. I. H. (1998). Dynamic site response evaluation of the port city of aqaba (jordan) employing the equivalent linear method. *Canadian Geotechnical Journal*, **35**(6), 961–975.

Fenton, G. A. and Griffiths, D. (2005). Three-Dimensional Probabilistic Foundation Settlement. *Journal of geotechnical and geoenvironmental engineering*, **131**(2), 232–239.

Flores-Berrones, R. and Liu, X. L. (2003). Seismic vulnerability of buried pipelines. *Geofisia International*, **42**, 237–246.

Frankel, A. (1991). High-frequency spectral falloff of earthquakes, fractal dimension of complex rupture, *b* value, and the scaling of strength on fault. *Journal of Geophysical Research*, **96**, 6291–6302.

Gallovic, F. and Brokesová, J. (2004). On strong ground motion synthesis with k-2 slip distributions. *Journal of seismology . - Dordrecht: Kluwer*, **8**, 211–224.

Gardien, W. and Stuit, H. G. (2003). Modelling of soil vibrations from railway tunnels. *Journal of Sound and Vibration*, (267), 605–619.

Gaul, L., Kögel, M., and Wagner, M. (2003). *Boundary Element Methods of Engineers and Scientists*. Springer, Berlin, GER.

Genes, M. and Kocak, S. (2005). Dynamic soil-structure interaction analysis of layered unbounded media via a coupled finite element-boundary element-scaled boundary finite element model. *International journal for numerical methods in engineering . - Chichester : Wiley*, **62**, 798–823.

Givoli, D. (1992). *Numerical methods for problems in infinite domains*, volume 33 of *Studies in applied mechanics*. Elsevier, Amsterdam.

Givoli, D. (2004). High-order local non-reflecting boundary conditions: a review. *Wave Motion*, **39**(4), 319–326.

Google earth (2006). *http://earth.google.de*. Google.

Gould, P. (1994). *Introduction to Linear Elasticity*. Springer Verlag, Berlin, Wien, New York.

Green, G. (1828). *An Essay on the application of mathematical analysis to the theories of electricity and magnetism*. Wheelhouse, Nottingham.

Grote, M. and Keller, J. (1995). Exact non-reflection boundary conditions for the time-dependent wave equation. *SIAM Journal of Applied Mathematics*, **55**, 280–297.

Gruppo di lavoro CPTI (2004). *Catalogo Parametrico dei Terremoti Italiani, versione 2004 (CPTI04)*. INGV, Bologna.

Guddati, M. and Lim, K. (2006). Continued fraction absorbing boundary conditions for convex polygonal domains. *International Journal for Numerical Methods in Engineering*, **66**, 949–977.

Gutenberg, B. (1945). Magnitude determination for deep-focus earthquakes. *Bulletin of the Seismological Society of America*, **35**, 117–130.

Gutenberg, B. and Richter, C. F. (1936). On seismic waves (third paper). *Gerlands Beiträge zur Geophysik*, **47**, 73–131.

Hahn, G. and Sritharan, S. (1994). Lateral response of underground pipelines to earthquakes. *Computers structures . - Oxford : Pergamon Press*, **53**, 601–612.

Hall, W. J. and Newmark, N. M. (1978). Seismic Design Criteria for Pipelines and Facilities. *Journal of the Technical Councils of ASCE*, **104**(1), 91–107.

Halldórsson, B. (1999). *On Modeling of Earthquake Wave Motion and its Effects on Multi-Support Pipelines*. Acta Polytechnica Scandinavica No. 115. Finnish Academy of Technology, Espoo.

Hanks, T. C. (1982). $f_{\max}$. *Bulletin of the Seismological Society of America*, **72**(6A), 1867–1879.

Hanks, T. C. and Kanamori, H. (1979). A moment-magnitude scale. *Journal of Geophysical Research*, **84**, 2348–2350.

Hartmann, F. (1981). Computing the c–matrix in non–smooth boundary points. In C. Brebbia, editor, *New Developments in Boundary Element Methods*, pages 367–379. Butterworths, London.

Hartmann, H. G. and Waas, G. (1986). Seismic response of pile foundations and pile forces caused by kinematic and inertial interaction. In *8th International Conference on Structural Mechanics in Reactor Technology*, Brussels.

Hashash, Y. M., Hook, J. J., Schmidt, B., and I-Chiang Yao, J. (2001). Seismic design and analysis of underground structures. *Tunnelling and underground space technology*, **16**(4), 247–294.

Haskell, N. A. (1964). Radiation pattern of surface waves from point sources in a multi-layered medium. *Bulletin of the Seismological Society of America*, **54**(1), 377–393.

Heaton, T. H. (1990). Evidence for and implication of self-healing pulses of slip in earthquake rupture. *Physics of the earth and planetary interiors*, **64**, 1–20.

Herrero, A. and Bernard, P. (1994). A Kinematic Self-Similar Rupture Process for Earthquakes. *Seismological Society of America: Bulletin of the Seismological Society of America*, **84**(4), 1216–1228.

Higdon, R. L. (1986). Absorbing boundary conditions for difference approximations to the multi-dimensional wave equation. *Mathematics of Computation*, **176**, 437–459.

Hilber, H., Hughes, T., and Taylor, R. (1977). Improved numerical dissipation for time integration algorithms in strucutral dynamics. *Earthquake Engng. and Struct. Dyn.*, **5**, 283–292.

Hindy, A. and Novak, M. (1979). Earthquake response of underground pipelines. *Earthquake engineering structural dynamics*, **7**, 451–476.

Hong, H. P. (1998). An efficient point estimate method for probabilistic analysis. *Reliability Engineering and System Safety*, **59**, 261–267.

Hoshiya, M., Yamamoto, K., and Ohno, H. (2004). Redundancy index of lifelines for mitigation measures against seismic risk. *Probabilistic engineering mechanics*, **19**(3), 205–210.

Hughes, T. (1983). *Analysis of transient algorithms with particular reference to stability behaviour*, pages 67–155. North-Holland.

Hughes, T. (1987). *The Finite Element Method: Linear Static and Dynamic Finite Element Analysis*. Prentice-Hall, Englewood Cliffs, USA.

Hutchings, L. (2007). *www.llnl.gov/hmc*. Lawrence Livermore National Laboratory.

ISO (2002). *ISO/IEC Guide 73: Risk management - Vocabulary - Guidelines for use in standards*. International Organization for Standardization.

Israeli, M. and Orszag, S. (1981). Approximation of radiation boundary conditions. *Journal of Computational Physics*, **41**, 115–135.

Istituto Nazionale di Geofisica e Vulcanologia (2007). *Catalogo Parametrico dei Terremoti Italiani - Appendici - http://www.mi.ingv.it*.

Kanamori, H. and Anderson, D. L. (1975). Theoretical basis of some empirical relations in seismology. *Bulletin of the Seismological Society of America*, **65**, 1073–1095.

Kane, J., Al-Moqbel, A., Rodi, W., and Toksöz, M. N. (2002). Geostatistically constrained seismic deconvolution. Technical report, Earth Resource Laboratory, Dept. of Earth, Atmospheric, and Planetary Sciences, M.I.T., Cambridge, MA.

Karabalis, D. and Rizos, D. (1993). Dynamic analysis of 3-d foundations. In G. Manolis and T. Davies, editors, *Boundary Element Techniques in Geomechanics*. Elsevier, London, UK.

Kausel, E. (1994). Thin-layer method: Formulation in time domain. *International Journal for Numerical Methods in Engineering*, **37**, 927–941.

Kausel, E. (1999). Dynamic point sources in laminated media via the thin-layer method. *International journal of solids and structures . - New York*, pages 4725–4742.

Kausel, E. (2006). *Fundamental solutions in elastodynamics: a compendium*. Cambridge Univ. Press, Cambridge.

Kausel, E. and Peek, R. (1982). Dynamic loads in the interior of a layered stratum: An explicit solution. *Bulletin of the Seismological Society of America*, **72**(5), 1459–1481.

Kausel, E., Whitman, R. V., Morray, J. P., and Elsabee, F. (1978). The spring method for embedded foundations. *Nuclear Engineering Design*, **48**, 377–392.

Keller, J. B. and Givoli, D. (1989). Exact non-reflecting boundary conditions. *J. Comput. Phys.*, **82**(1), 172–192.

Kim, E. J., Bielak, J., and Ghattas, O. (2003). Large-scale northridge earthquake simulation using octree-based multiresolution mesh method. In G. Turkiyyah *et al.*, editors, *16th ASCE Engineering Mechanics Conference, July 16-18- 2003*. University of Washington, Seattle.

Kisliakov, D. (1990). Investigation of the Dynamic Interaction Between a High-pressure Pipeline and the Moving Liquid Inside under Seismic Loading. *Earthquake Engineering and Structural Dynamics*, **19**(8), 1143–1152.

Klin, P. and Priolo, E. (2006). Technique to avoid sharp slip transitions and negative values in k^{-2}-model. Istituto Nazionale di Oceanografia e di Geofisica Sperimentale (INOGS), unpublished.

Klinc, P., Priolo, E., Mirabella, F., and Barchi, M. (2004). 3D model and ground motion simulation for the Colfiorito area. Technical report, Istituto Nazionale di Geofisica e Vulcanologia, Gruppo Nazional per la Difesa dai Terremoti.

Kobayashi, S. and Nishimura, N. (1983). Analysis of soil-structure interaction by boundary integral equation method. In P. Lascaux, editor, *Numerical Methods in Engineering*. Pluralis, Paris.

Koike, T., Maruyama, O., and Garciano, L. E. (2007). Ground strain estimation for lifeline earthquake engineering. *Structural engineering and mechanics . - Taejon : Techno-Pr.*, **25**, 291–310.

Kontoni, D. P. N., Beskos, D. E., and Manolis, G. D. (1987). Uniform halfplane elastodynamic problems by an approximate BEM. *Soil dynamics and earthquake engineering*, **6**, 227–238.

Kramer, S. L. (1996). *Geotechnical Earthquake Engineering*. Prentice Hall, Inc., N.J.

Krauthammer, T. and Chen, Y. (1986). Dynamic response of RC conduits under earthquake conditions. In *Proc. 8th European Conference on Earthquake Engineering*, Lisbon.

Krauthammer, T. and Chen, Y. (1988). Free field earthquake ground motions: effects of various numerical simulation approaches on soil-structure interaction results. *Engineering structures . - Oxford : Elsevier*, **10**, 85–94.

Krenk, S. (2002). Unified formulation of radiation conditions for the wave equations. *International Journal for Numerical Methods in Engineering*, **53**, 275–295.

Kubala, B. and Rao, M. (1996). Earth's core temperature. *Byrdand Black*.

Kuhlmann, W. (2004). *Gesamtkonzept zur Ermittlung der seismischen Vulnerabilität von Bauwerken am Beispiel unterirdischer Rohrleitungen*. Aachen, Techn. Hochsch., Diss.

Kuribayashi, E. and Iwasaki, T. (1974). Effects of soil deposits on seismic behaviour of prefabricated highwax tunnels. In *Proc. 5th World Conf. Earthquake Eng.*, pages 2614–2623.

Lane, H., Ekevid, T., Kettil, P., Ching, C. Y., and Wiberg, N.-E. (2007). Vehicle-track-underground modeling of rail induced wave propagation. *Computers structures . - Oxford : Pergamon Press*, **85**, 1215–1229.

Lee, V. W. and Trifunac, M. D. (1979). Response of tunnels to incident SH waves. *Journal of the Engineering Mechanics Division*, **105**, 643–659.

Lehmann, L. (2005a). Application of a coupled finite element/scaled boundary element procedure to acoustics. In O. E. Papadrakakis, M. and B. Schrefler, editors, *Computational Methods for Coupled Problems in Science and Engineering*, page 142, Santorini Island, Greece. ECCOM, International Center for Numerical Methods in Engineering (CIMNE).

Lehmann, L. (2005b). An effective finite element approach for soil-structure analysis in the time-domain. *Structural Engineering and Mechanics*, **21**(4), 437–450.

Lehmann, L. (2005c). Simulating sound propagation in infinite domains with an efficient finite element approach. In *Twelfth International Congress on Sound and Vibration*, pages 160–161, Lisbon, Portugal.

Lehmann, L. (2007). *Wave Propagation in Infinite Domains - With Applications to Structure Interaction*, volume 31 of *Lecture Notes in Applied and Computational Mechanics*. Springer Verlag, Berlin, Wien, New York.

Lehmann, L. and Antes, H. (2001). Dynamic structure - soil - structure interaction applying the symmetric galerkin boundary element method (sgbem). *Mechanics Research Communications*, **28**(3), 297–304.

Lehmann, L. and Borsutzky, R. (2006). Seismic analysis of structures: Influence of the soil. Geneva, Switzerland. First Conference on Earthquake Engineering and Seismology.

Lehmann, L. and Borsutzky, R. (2007). Fast three-dimensional seismic simulation in the time-domain with consideration of soil-structure interaction. In *COMPDYN*, Rethymno, Crete, Greece.

Lehmann, L., Antes, H., and Schanz, M. (2004). Transient analysis of soil-structure interaction problems: An effective fem/sbfem approach. In G. A. Holzapfel, W. Moser, and G. Rechard, editors, *Advanced Numerical Analyses of Solids and Structures, and Beyond*, pages 99–116, Graz, A. Institute for Structural Analysis, Verlag der Technischen Universität Graz.

Lehmann, L., Clasen, D., and Borsutzky, R. (2007). A new coupled solution strategy for soil-structure interaction analysis in the time-domain. In M. P. E. Onate and B. Schrefler, editors, *Computational Methods for Coupled Problems in Science and Engineering II*, page 333, St. Eulalia, Spain. International Center for Numerical Methods in Engineering.

Liao, Z. and Wong, H. (1984). A transmitting boundary for the numerical simulation of elastic wave propagation. *Soil Dyn. and Earthquake Eng.*, **3**, 174–183.

Lin, Y. K., Zhang, R., and Yong, Y. (1990). Multiply supported pipeline under seismic wave excitation. *Journal of engineering mechanics*, **116**, 1094–1108.

Lindemann, J. and Becker, W. (2002). Free-Edge Stresses around Holes in Laminates by the Boundary Finite-Element Method. *Mechanics of composite materials . - New York*, **38**, 407–416.

Lindman, E. L. (1975). "Free-Space" boundary conditions for the time dependent wave equation. *Journal of Computational Physics*, **18**, 66–78.

Liolios, A. *et al.* (2002). A computational approach to the dynamic soil-pipeline interaction induced by high-speed railway traffic. In E. Lund *et al.*, editors, *15th Nordic Seminar on Computational Mechanics*, pages 259–262, Aalborg.

Liu, S. W., Datta, S. K., Kahir, K. R., and Shah, A. H. (1991). Three-dimensional dynamics of pipelines buried in backfilled trenches due to oblique incidence of body waves. *Soil dynamics and earthquake engineering*, **10**, 182–191.

Love, A. E. H. (1927). *A treatise on the mathematical theory of Elasticity*. Univ. Press, Cambridge, 4 edition.

Luco, J. and Apsel, R. (1983). On the green's functions for a layered half-space. part i. *Bulletin of the Seismological Society of America*, **73**(4), 909–929.

Lysmer, J. and Kuhlmeyer, R. (1969). Finite dynamic model for infinite media. *J. of Eng. Mech. Division, ASCE*, **95**, 859–875.

Lysmer, J. and Waas, G. (1972). Shear Waves in Plane Infinite Structures. *Journal of the Engineering Mechanics Division*, **98**(1), 85–105.

Mahran, E. (2004). *Finite-Infinite-Elemente-Modellierung zur Simulation der Boden-Bauwerk-Flüssigkeit-Interaktion unter dynamischer Anregung*. Wuppertal, Univ., Diss.

Manolis, G. D. and Beskos, D. E. (1983). Dynamic response of lined tunnels by an isoparametric boundary element method. *Comput, Methods Appl. Mech. Eng.*, **36**, 291–307.

Manolis, G. D. and Beskos, D. E. (1997). *Underground and lifeline structures*, chapter 16, pages 775–837. Computational Mechanics Publications, Southampton.

Manolis, G. D. *et al.* (1995). A hierarchy of numerical models for ssi analysis of buried pipelines. In A. S. Cakmak and C. A. Brebbia, editors, *Soil Dynamics and Earthquake Engineering VII*, pages 643–650, Southampton. Computational Mechanics Publications.

Manolis, G. D., Talaslides, D. G., Tetepoulidis, P. I., and Apostolidis, G. (1994). Soil structure interaction analyses for integrated pipeline design. In M. Papadrakakis and B. H. V. Topping, editors, *Advances in Simulation and Interaction Techniques*, pages 51–59, Edinburgh. Civil-Comp Press.

Mansur, W. (1983). *A Time Stepping Technique to solve Wave Propagation Problems Using the Boundary Element Method*. dissertation, University of Southampton.

Mansur, W. and Brebbia, C. (1983). Transient elastodynamics using a time-stepping technique. In C. Brebbia, T. Futagami, and M. Tanaka, editors, *Boundary Elements*, pages 677–698. Springer, Berlin, GER.

Mantic, V. (1993). A new formula for the c-matrix in the somigliana identity. *Journal of Elasticity*, **33**, 191–201.

Mashaly, E. A. and Datta, T. K. (1987). Parametric studies on seismic response of buried pipelines. In J. L. Humar, editor, *5th Canadian Conference in Earthquake Engineering*, pages 625–635, Rotterdam. A. A. Balkema.

Mathews, I. C. and Geers, T. (1987). A doubly asymptotic, nonreflecting boundary for ground-shock analysis. *Journal of applied mechanics . - New York*, **54**, 489–497.

Mathews, I. C. and Geers, T. L. (1985). A doubly asymptotic, non-reflecting boundary for ground shock analysis. In T. A. Cruse, A. B. Pifko, and H. Armen, editors, *Advanced Topics in Boundary Element Analysis*, volume 72. American Society of Mechanical Engineers, New York.

Mavridis, G. A. and Pitilakis, K. D. (1995). Transverse seismic analysis of buried pipelines. In M. J. O'Rourke, editor, *Lifeline Earthquake Engineering, Proceedings of the Fourth U.S. Conference*, pages 144–151, New York, NY. American Society of Civil Engineers.

Mercalli, G. (1883). *Vulcani e Fenomeni Vulcanici in Italia*. Arnaldo Forni, Bologna.

Mitchell, A. R. and Griffiths, D. F. (1980). *The finite difference method in partial differential equations*. A Wiley-Interscience Publication, Chichester: Wiley, 1980.

Moser, A. P. (2001). *Buried pipe design*. McGraw-Hill professional engineering. McGraw-Hill, New York, NY [u.a.], 2 edition.

Muleski, G. E. and Ariman, T. A. (1985). A shell model for buried pipes in earthquakes. *Soil dynamics and earthquake engineering*, **4**, 43–51.

Muleski, G. E., Ariman, T., and Aumen, C. E. (1979). A shell model of buried pipe in a seismic environment. *Journal of Pressure Vessels Technology*, **101**, 44–50.

Naggar, M. H. E. (2003). *Seismic Response of Structures with Underground Storeys*. Institute for Catastrophic Loss Reduction, Toronto.

Nash, P. T., McGuire, R. L., and Wenzel, A. B. (1984). Blast damage of underground piping. In S. K. Datta, editor, *Earthquake Source Modelling, Ground Motion and Strutural Response*, pages 163–173.

Navarro, C. (1992). Seismic analysis of underground structures. In *Proc. 10th World Conf. Earthquake Eng.*, Madrid.

Navarro, C. and Samartin, A. (1988). Simplified longitudinal seismic analysis of buried tunnels. *Software Eng. Workstations*, **4**, 3–10.

Nedjar, D., Hamane, M., Bensafi, M., Elachachi, S., and Breysse, D. (2007). Seismic response analysis of pipes by a probabilistic approach. *Soil dynamics and earthquake engineering . - Amsterdam : Elsevier Science*, **27**, 111–115.

Nelson, I. and Isenberg, J. (1976). Soil island approach to structure/media interaction. In C. S. Desai, editor, *Numerical Methods in Geomechanics*, pages 41–57.

Newmark, N. M. (1971). Earthquake response analysis of reactor structures. In *Proc. 1st Int. Conf. on Structural Mechanics in Reactor Technology*, Berlin.

Newmark, N. M. and Hall, W. J. (1975). Pipeline Design to Resist Large Fault Displacement. *Proceedings U.S. National Conference on Earthquake Engineering, University of Michigan, Ann Arbor, MI*, pages 416–425.

Nishimura, N. (2002). Fast multipole accelerated boundary integral equation methods. *Applied Mechanics Reviews*, **55**, 299–324.

O'Leary, P. M. and Datta, S. K. (1985). Dynamic of buried pipelines. *Soil dynamics and earthquake engineering*, **4**, 151–159.

Olson, A. H., Orcutt, J. A., and Frazier, G. A. (1984). The discrete wavenumber/finite element method for synthetic seismograms. *The geophysical journal of the RAS, DGG and EGS*, **77**, 421–460.

Oprsal, I. and Zahradník, J. (2002). Three-dimensional finite difference method and hybrid modeling of earthquake ground motion. *Journal of Geophysical Research*, **8**(107), 2161.

O'Rourke, M. and Shinozuka, M. (1995). Mitigation of seismic damage to lifelines gas and liquid fuel systems. In A. J. Schiff and I. G. Buckle, editors, *Critical Issues and State-of-the-Art in Lifeline Earthquake Engineering*, pages 30–40. American Society of Civil Engineers, New York, NY.

O'Rourke, M. J. (1995). Seismic behaviour of buried pipeline components: A state-of-the-art review. In G. Duma, editor, *Proceedings of the 10th European Conference on Earthquake Engineering*, volume 3, pages 2153–2162, Rotterdam. A. A. Balkema.

O'Rourke, M. J. and Elhmadi, K. (1988). Analysis of continuous buried pipelines for seismic wave effects. *Earthquake engineering structural dynamics*, **16**, 917–929.

O'Rourke, M. J. and Liu, X. (1999). *Response of Buried Pipelines Subject to Earthquake Effects*. Multidisciplinary Center for Earthquake Engineering Research, Buffalo, NY.

O'Rourke, T. D. and Jeon, S.-S. (2000). Seismic zonation for lifelines and utilities. In A. J. Schiff and A. K. Tang, editors, *Proceedings of the Sixth International Conference on Seismic Zonation*, Palm Springs, CA. Earthquake Engineering Research Institute.

O'Rourke, T. D., Grigoriu, M. D., and Khater, M. M. (1985). A State of the Art Review: Seismic Response of Buried Pipelines. In C. Sundarrarajan, editor, *Decade of Progress in Pressure Vessels*. ASME.

Osservatorio Sismico delle Strutture (2003). I.T.I. G.Marconi - Ampliamento - Registrazione del 07-12-2003 ora UTC 10:20. Technical report, Forlì.

Pan, E. (2003). Three-Dimensional Green's Functions in an Anisotropic Half-Space With General Boundary Conditions. *Journal of applied mechanics . - New York*, **70**, 101–110.

Papageorgiou, A. S. and Aki, K. (1983). A specific barrier model for the quantitative description of inhomogeneous faulting and the prediction of strong ground motion. Part II. Applications of the model. *Bulletin of the Seismological Society of America*, **73**(4), 953–978.

Paris, F. and Canas, J. (1997). *Boundary Element Method: Fundamentals and Applications*. Oxford University Press, Oxford, UK.

Park, J. and Kausel, E. (2004). Impulse Response of Elastic Half-Space in the Wave Number-Time Domain. *Journal of engineering mechanics*, **130**(10), 1211–1222.

PEER (2003). *PEER Strong Motion Database*. Pacific Earthquake Engineering Research Center. http://peer.berkeley.edu/smcat.

Penzien, J., Chen, C. H., Lee, Y. L., and Jean, W. Y. (1992). Seismic analysis of rectangular tunnels in soft ground. In *Proc. 10th World Conf. on Earthquake Eng.*, Madrid.

Pichler, B., Hellmich, C., Eberhardsteiner, J., and Mang, H. A. (2005). Assessment of Protection Systems for Buried Steel Pipelines Endangered by Rockfall - . *Computer-aided civil and infrastructure engineering . - Boston*, **20**(5), 331–342.

Pickett, J. P. *et al.*, editors (2000). *The American Heritage® Dictionary of the English Language, www.bartleby.com/61/*. Houghton Mifflin Company, Boston, 4 edition.

Ponziani, F. (1994). *Digitalizzatione e reinterpretazione di dati di sismica crostale: ipotesi su un modello geodinamico per l'Italia Centrale - Tirreno Settentrionale*. Ph.D. thesis, University of Perugia, Italy.

Priolo, E., Vuan, A., Klinc, P., and Laurenzano, G. (2002). Estimation of the ground motion upper limit in Switzerland: EXWIM numerical simulations - PEGASOS Project -Final report. Technical report, Istituto Nazional di Oceanografia e di Geofisica Sperimentale, Trieste.

Ramberg, W. and Osgood, W. R. (1943). *Description of stress-strain curves by three parameters*, volume 902 of *Technical note / National Advisory Committee for Aeronautics*. National Advisory Committee for Aeronautics, Washington D.C.

Rayleigh, L. (1885). On waves propagated along the plane surface of an elastic solid. *Proceedings of the London Mathematical Society*, **17**, 4–11.

Richart, F. E., Woods, R. D., and Hall, J. R. (1970). *Vibrations of soils and foundations*. Civil engineering and engineering mechanics seriesPrentice-Hall international series in theoretical and applied mechanics. Prentice-Hall, Englewood Cliffs/N.J.

Richter, C. F. (1935). An instrumental earthquake scale. *Bulletin of the Seismological Society of America*, **25**, 1–32.

Richter, C. F. (1958). *Elementary Seismology*. W. H. Freeman, San Francisco.

Roach, G. F. (1995). *Green's functions*. Univ. Press, Cambridge, 2. ed edition.

Roesset, J. M. and Ettouney, M. M. (1977). Transmitting boundaries: A comparison. *International journal for numerical and analytical methods in geomechanics*, **1**, 151–176.

Romanel, C. and Kundu, T. (1993). A Hybrid Modelling of Soil-Structure Interaction Problems for Deeply Embedded Structures in a Multilayered Medium. *Earthquake engineering structural dynamics*, **22**(7), 557–572.

Rosenblueth, E. (1975). Point estimates for probability moments. *Proceedings of the National Academy of Sciences of the USA*, **72**(10), 3812–3814.

Rucker, M. L. and Dowding, C. D. (2000). Segmented (buried utilities) pipeline damage rates from dynamic loadings. In J. L. Tassoulas *et al.*, editors, *Fourteenth Engineering Mechanics Conference*, Austin, Texas.

Ruge, P., Trinks, C., and Witte, S. (2001). Time-domain analysis of unbounded media using mixed-variable. *Earthquake Engineering and Structural Dynamics*, **30**, 899–925.

Sakurai, A. and Takahasi, S. (1969). Dynamic stresses of underground pipelines during earthquakes. In *Proc. 4th World. Conf. Earthquake Eng.*, pages 81–96, Santiago de Chile.

Schanz, M. (2001). *Wave Propagation in Viscoelastic and Poroelastic Continua*. Springer Verlag, Berlin, GER.

Schwartz, C. W. (1980). Numerical analysis of underground structures. In D. R. Schelling, editor, *Proc. 2nd Conf. on Computing in Civil Engineering*, New York.

Schweiger, H. F., Thurner, R., and Pöttler, R. (2001). Reliability analysis in geotechnics with deterministic finite elements. *The International Journal of Geomechanics*, **1**(4), 389–413.

Selcuk, A. S. and Yücemen, M. S. (2000). Reliability of Lifeline Networks with Multiple Sources under Seismic Hazard. *Natural Hazards*, **21**(21), 1–18.

Selvadurai, A. P. S., Au, M. C., and Shinde, S. B. (1990). Soil-pipeline interaction in a pipeline with prescribed displacements. In S. M. Sargand, G. F. Mitchell, and J. O. Owen, editors, *Structural Performance of Flexible Pipes*. A. A. Balkema, Rotterdam.

Shah, H. H. and Chu, S. L. (1974). Seismic analysis of underground structural elements. *Journal of the Power Division*, **100**, 53–62.

Shearer, P. M. (1999). *Introduction to seismology*. Cambridge Univ. Press, Cambridge.

Shen, J. and Wang, H. (1994). Seismic analysis of 3d lifeline underground structures. In S. A. Savidis, editor, *Earthquake Resistant Construction and Design*, volume 1, pages 429–436, Rotterdam. A. A. Balkema.

Silvester, P. P., Lowther, D. A., Carpenter, C. J., and Wyatt, E. A. (1977). Exterior finite elements for 2-dimensional field problems with open boundaries. *Proceedings of the Institution of Electrical Engineers*, **124**, 1267–1270.

Simonis, J. C. and Nash, P. T. (1984). Sesimic testing of modelled buried pipelines. In S. K. Datta, editor, *Earthquake Source Modelling, Ground Motion and Strutural Response*, pages 175–190. ASME, New York.

Sivakumar Babu, G. and Rao, R. S. (2005). Reliability measures for buried flexible pipes. *Canadian geotechnical journal*, **42**(2), 541–549.

Smith, W. D. (1974). A nonreflecting plane boundary for wave propagation problems. *Journal of Computational Physics*, **15**, 492–503.

Sommerfeld, A. (1949). *Lectures on theoretical physics Vol.6: Partial differential equations in physics*. Pure and applied mathematics. Academic Press, New York.

Song, C. (2004). A matrix function solution for the scaled boundary finite-element equation in statics. *Computer methods in applied mechanics and engineering . - Amsterdam : Elsevier*, **193**, 2325–2356.

Song, C. and Wolf, J. (1995). Consistent infinitesimal finite-element cell method: out-of-plane motion. *Journal of Engineering Mechanics ASCE*, **121**, 613–619.

Song, C. and Wolf, J. (1996a). consistent infinitesimal finite-element cell method for diffusion equation in unbounded medium. *Computer Methods in Applied Mechanics and Engineering*, **132**, 319–334.

Song, C. and Wolf, J. (1996b). Consistent infinitesimal finite-element cell method: three-dimensional vector wave equation. *International Journal for Numerical Methods in Engineering*, **39**, 2189–2208.

Song, C. and Wolf, J. (1997). Consistent infinitesimal finite-element cell method for incompressible unbounded medium. *Communications in Numerical Methods in Engineering*, **13**, 21–32.

Spudich, P. and Archuleta, R. J. (1987). Techniques for Earthquake Ground-Motion Calculation with Applications to Source Parameterization of Finite Faults. In B. A. Bolt, editor, *Seismic Strong Motion Synthetics*, pages 205–265. Academic Press, Inc., Orlando.

Spudich, P. and Xu, L. (2003). Documentation of software package compsyn: Programs for earthquake ground motion calculations using complete 1-d green's functions. In *CD accompanying IASPEI Handbook of Earthquake and Engineering Seismology*, page 56 pp. International Association of Seismology and Physics of the Earth's Interior Academic Press.

Stamos, A. A. and Beskos, D. E. (1992). Dynamic soil-structure interaction in 3-D underground structures. In C. A. Brebbia, J. Dominguez, and F. Paris, editors, *Boundary Elements XIV, Vol. 2*. Elsevier Applied Science, London.

Stamos, A. A. and Beskos, D. E. (1995). Dynamic analysis of large 3-d underground structures by the bem. *Earthquake Engineering and Structural Dynamics*, **24**, 917–934.

Stokes, G. (1849). On the dynamical theory of diffraction. *Transaction of the Cambridge Philosophical Society*, **9**, 1–62.

Takada, S. and Tanabe, K. (1987). Three dimensional seismic response of buried continuous or jointed pipelines. *Transactions ASME, Pressure Vessels and Piping Division*, **109**, 80–87.

Takada, S., Hassani, N., and Fukuda, K. (2002). Damage Directivity in Buried Pipelines of Kobe City During the 1995 Earthquake. *Journal of earthquake engineering . - Singapore : World Scientific*, **6**, 1–16.

Takeuchi, H. and Saito, M. (1972). Seismic surface waves. In B. A. Bolt, editor, *Seismology: Surface Waves and Earth Oscillations*, volume 11 of *Methods in Computational Physics*. Academic Press, New York, San Francisco, London.

Thatcher, R. W. (1978). On the finite element method for unbounded media. *SIAM Journal of Numerical Analysis*, **15**, 466–477.

Toprak, S. and Taskin, F. (2007). Estimation of Earthquake Damage to Buried Lifelines Caused by Ground Shaking. *Natural Hazards*, (40), 1–24.

Triantafyllidis, T. (1984). *Analytische Lösung des Problems der dynamischen Untergrundkopplung starrer Fundamente*, volume 97 of *Veröffentlichungen des Institutes für Bodenmechanik und Felsmechanik der Universität Fridericiana in Karlsruhe*. Zugl.: Karlsruhe, Univ., Diss.

Triantafyllidis, T. (1991). 3-d time domain bem using a half-space green‘s functions. *eabem*, **8**, 115–124.

Trifunac, M. D. and Brady, A. G. (1975). A Study on the Duration of Strong Earthquake Ground Motion. *Bulletin of the Seismological Society of America*, **65**(3), 581–626.

Tsai, J.-S., Jou, L.-D., and Lin, S. H. (2000). Damage to buried water supply pipelines in the chi-chi (taiwan) earthquake and a preliminary evaluation of seismic resistance of pipe joints. *J. Chin. Inst. Eng.*, **23**(4), 395–408.

Tsynkov, S. V. (1998). Numerical solution of problems on unbounded domains. A review. *Applied Numerical Mathematics: Transactions of IMACS*, **27**(4), 465–532.

Underwood, P. and Geers, T. L. (1981). Doubly asymptotic boundary-element analysis of dynamic soil-structure interaction. *International Journal of Solid Structures*, **17**, 687–697.

Valliappan, S., Chandrasekaran, V., and Lee, I. K. (1979). Interaction between tunnel openings due to vibration effects. In W. Wittke, editor, *Numerical Methods in Geomechanics*. A. A. Balkema, Rotterdam.

Vannucci, G. and Gasperini, P. (2003). A database of revised fault plane solutions for Italy and surrounding regions A database of revised fault plane solutions for Italy and surrounding regions. *Computer and Geosciences*, **29**, 903–909.

Varandega, C. and Luciani, A. (1986). Seismic analysis of lifelines: Methods for stiffness changes and local effects. In *Proc. 8th European Conf. Earthquake Eng.*, Lisbon.

Venkatesan, S., Nelson, L., and Wilson, J. (2006). Simple model accounting for the soil resonance phenomenon. In *Earthquake Engineering in Australia*, Canberra.

von Estorff, O. and Antes, H. (1991). Dynamic response of tunnel structures. In W. Krätzig *et al.*, editors, *Structural Dynamics 2*, pages 803–810. A. A. Balkema, Rotterdam.

von Estorff, O. and Firuziaan, M. (2000). Coupled bem/fem approach for nonlinear soil/structure interaction. *Engineering analysis with boundary elements*, **24**, 715 – 725.

von Estorff, O. and Kausel, E. (1989). Coupling of boundary and finite elements for soil-structure interaction problems. *Earthquake Engineering and Structural Dynamics*, (18), 1065–1075.

von Estorff, O., Stamos, A. A., Beskos, D. E., and Antes, H. (1991). Dynamic interaction effects in underground traffic systems. *Eng. Anal. Bound. Elem.*, **8**, 167–175.

Vougiouskas, E. A. and Carydis, P. G. (1995). A model for analysis of the performance of segmented pipelines crossing a normal fault. In G. Dumas, editor, *Proceedings 10th European Conference in Earthquake Engineering*, pages 2173–2178, Rotterdam. A. A. Balkema.

Waas, G. (1972). *Linear two-dimensional analysis of soil dynamics problems in semi-infinite layered media*. Ph.D. thesis, University of California, Berkley, CA.

Wang, H. (1995). Seismic analysis of 3-d subway tunnels. In A. S. Cakmak and C. A. Brebbia, editors, *Soil Dynamics and Earthquake Engineering VII*, pages 433–440, Southampton. Computational Mechanics Publications.

Wang, H. and Takemiya, H. (1994). Dynamic responses of tunnels to incident in plane seismic waves in layered half space by hybrid method. In S. A. Savidis, editor, *Earthquake Resistant Construction and Design*, volume 1, pages 421–428, Rotterdam. A. A. Balkema.

Warner, R. F. and Kabaila, A. P. (1968). *A Monte-Carlo techniques for the study of structural safety*, volume 27 of *Uniciv-report*. Univ. of New South Wales, Sydney.

Watkins, R. K. and Anderson, L. R. (2000). *Structural Mechanics of Buried Pipes*. CRC Press, Boca Raton, London, New York, Washington, D.C.

Wells, D. L. and Coppersmith, K. J. (1994). New Empirical Relationships among Magnitude, Rupture Length, Rupture Width, Rupture Area, and Surface Displacement. *Seismological Society of America: Bulletin of the Seismological Society of America*, **84**(4), 974–1002.

Wheeler, L. and Sternberg, E. (1968). Some theorems in classical elastodynamics. *Archive for Rational Mechanics and Analysis*, **31**(1), 51–90.

White, W., Valliappan, S., and Lee, I. K. (1977). Unified boundary for finite dynamic models. *Journal of Engineering Mechanics*, **103**, 949–964.

Wolf, J. (2002). Response of unbounded soil in scaled boundary finite-element method. *Earthquake engineering structural dynamics . - London : Wiley*, **31**, 15–32.

Wolf, J. P. (1985). *Dynamic Soil-Structure Interaction*. Prentice Hall, Inc., Englewood Cliffs, N.Y.

Wolf, J. P. (1988). *Soil-structure interaction analysis in time domain*. Prentice-Hall International series in civil engineering and engineering mechanics. Prentice-Hall, Englewood Cliffs, NJ.

Wolf, J. P. (2003). *The Scaled Boundary Finite Element Method*. John Wiley & Sons Ltd, Chichester.

Wolf, J. P. and Song, C. (1995). Doubly asymptotic multi-directional transmitting boundary for dynamic unbounded medium-structure-interaction analysis. *Earthquake Engineering and Structural Dynamics*, **24**, 175–188.

Wolf, J. P. and Song, C. (1996). *Finite-Element Modelling of Unbounded Media*. John Wiley & Sons Ltd, Chichester.

Wong, K. C., Shah, A. H., and Datta, S. K. (1985). Diffraction of elastic waves in a halfspace - II Analytical and numerical results. *Bulletin of the Seismological Society of America*, **75**, 69–92.

Wong, K. C., Datta, S. K., and Shah, A. H. (1986). Three-dimensional motion of buried pipeline - Parts I/II. *Journal of engineering mechanics*, **112**, 1319–1337,1338–1345.

Woodward-Clyde Consultants, Walnut Creek, C. P. i. W. S. (1988). *Soil Response to Earthquake Ground Motion*. Electric Power Research Institute, Palo Alto, CA.

Wrobel, L. and Aliabadi, M. (2002). *The Boundary Element Method*. Wiley and Sons, Chichester, UK.

Yang, Z., He, L., Bielak, J., Zhang, Y., Elgamal, A., and Conte, J. (2003). Nonlinear seismic response of a bridge site subject to spatially varying ground motion. In G. Turkiyyah *et al.*, editors, *16th ASCE Engineering Mechanics Conference, July 16-18- 2003*. University of Washington, Seattle.

Yoshimura, C., Bielak, J., Hisada, Y., and Fernández, A. (2003). Domain reduction method for three-dimensional earthquake modeling in localized regions, part ii: Verification and applications. *Bulletin of the Seismological Society of America*, **93**(2), 825–840.

Yuan, H. R. and Walker, R. E. (1970). The investigations of a simple soil-structure interaction model. In D. A. Howells, I. P. Haigh, and C. Taylor, editors, *Dynamic Waves in Civil Engineering*. John Wiley Sons Ltd, New York.

Zhang, C., Chen, X., and Wang, G. (1999a). A Coupling Model of FE-BE-IE-IBE for Non-linear Layered Soil-Structure Interactions. *Earthquake engineering structural dynamics . - London : Wiley*, **28**, 421–442.

Zhang, X., Wegner, J., and Haddow, J. (1999b). Three-dimensional Dynamic Soil-Structure Interaction Analysis in the Time Domain. *Earthquake engineering structural dynamics*, **28**(12), 1501–1524.

Zhang, Y., Yang, Z., Bielak, J., Conte, J. P., and Elgamal, A. (2003). Treatment of seismic input and boundary conditions in nonlinear seismic analysis of a bridge ground system. In G. Turkiyyah *et al.*, editors, *16th ASCE Engineering Mechanics Conference, July 16-18- 2003*. University of Washington, Seattle.

Zhao, C. and Liu, T. (2003). Non-reflecting artificial boundaries for transient scalar wave propagation in a two-dimensional infinite homogeneous layer. *International journal for numerical methods in engineering . - Chichester : Wiley*, **58**, 1435–1456.

Zienkiewicz, O. C. and Taylor, R. L. (2005). *The finite element method [Vol. 2]: For solid and structural mechanics*. Elsevier Butterworth-Heinemann, Amsterdam, 6 edition.

Zienkiewicz, O. C., Taylor, R. L., and Zhu, J. Z. (2005). *The finite element method [Vol. 1]: Its basis and fundamentals*. Elsevier Butterworth-Heinemann, Amsterdam, 6 edition.

Zollo, A., Bobbio, A., Emolo, A., Herrero, A., and Natale, G. (1997). Modelling of ground acceleration in the near source range: The case of 1976, Friuli earthquake (M = 6.5), northern Italy. *Journal of seismology*, **1**(4), 305–320.

Braunschweiger Schriften zur Mechanik – BSM

Bisher erschienene Berichte in dieser Reihe

1–1990 Plonski, Thomas:
Dynamische Analyse von schnelldrehenden Kreiszylinderschalen

2–1991 Wegener, Konrad:
Zur Berechnung großer plastischer Deformationen mit einem Stoffgesetz vom Überspannungstyp

3–1992 Gröhlich, Hubert:
Finite-Element-Formulierung für vereinheitlichte inelastische Werkstoffmodelle ohne explizite Fließflächenformulierung

4–1992 Hesselbarth, Hanfried:
Simulation von Versetzungsstrukturbildung, Rekristallisation und Kriechschädigung mit dem Prinzip der zellulären Automaten

5–1992 Schlums, Hartmut:
Ein stochastisches Werkstoffmodell zur Beschreibung von Kriechen und zyklischem Verhalten metallischer Werkstoffe

6–1992 Kublik, Frithjof:
Vergleich zweier Werkstoffmodelle bei ein- und mehrachsigen Versuchsführungen im Hochtemperaturbereich

7–1992 Bechtloff, Jürgen:
Interpolationsverfahren höheren Grades für Robotersteuerungen

8–1993 Müller, Michael:
Dreidimensionale elastodynamische Analyse von Tanks mit fluidbenetzten Einbauten

9–1993 Senker, Peter:
Stabilitätsanalyse elastischer Rotorsysteme

10–1993 Cheng, Weimin:
Schallabstrahlung einer schwingenden Reisner/Mindlin Platte

11–1993 Wiebe, Thomas:
Wellenausbreitung in poroelastischen Medien: Untersuchung mit Randintegralgleichungen

12–1993 Hahne, Matthias:
Beschreibung der plastischen Längsdehnung bei Torsion mit einem makroskopischen Stoffgesetz

13–1993 Heisig, Gerald:
Zum statischen und dynamischen Verhalten von Tiefbohrsträngen in räumlich gekrümmten Bohrlöchern

14–1994 de Araújo, Francisco Célio:
Zeitbereichslösung linearer dreidimensionaler Probleme der Elastodynamik mit einer gekoppelten BE/FE-Methode

15–1994 Kristen, Martin:
Untersuchungen zur elektrischen Ansteuerung von Formgedächtnis-Antrieben in der Handhabungstechnik

16–1994 Latz, Kersten:
Dynamische Interaktion von Flüssigkeitsbehältern und Baugrund

17–1994 Jäger, Monika:
Entwicklung eines effizienten Randelementverfahrens für bewegte Schallquellen

18–1994 August, Martin:
Schwingungen und Stabilität eines elastischen Rades, das auf einer nachgiebigen Schiene rollt

19–1995 Erbe, Matthias:
Zur Simulation von Risswachstum in dreidimensionalen, elastisch-plastischen Strukturen mit der Methode der Finiten Elemente

20–1995 Gerdes, Ralf:
Ein stochastisches Werkstoffmodell für das inelastische Materialverhalten metallischer Werkstoffe im Hoch- und Tieftemperaturbereich

21–1995 Tröndle, Georg:
Effiziente Schallberechnung mit einem adaptiven Mehrgitterverfahren für die 3-D Randelementmethode

22–1996 Degenhardt, Richard:
Nichtlineare dynamische Bauwerksprobleme und Interaktion mit dem Baugrund

23–1996 Feise, Hermann Josef:
Modellierung des mechanischen Verhaltens von Schüttgütern

24–1996 Haubrok, Dietmar:
Reibungsfreie Kontaktprobleme der 2-D Elastostatik und -dynamik als Optimierungsaufgabe mit REM-Matrizen

25–1996 Lehmann, Lutz:
Numerische Simulation der Spannungs- und Geschwindigkeitsfelder in Silos mit Einbauten

26–1996 Klein, Ralf:
Dynamische Interaktion von dünnwandigen Tragwerken und Boden mit Abschirmschlitzen

27–1996 Kopp, Thilo:
Simulation großer inelastischer Deformationen bei Torsionsversuchen

28–1997 Harder, Jörn:
Simulation lokaler Fließvorgänge in Polykristallen

29–1997 Lewerenz, Malte Christian:
Zur numerischen Behandlung von Werkstoffmodellen für zeitabhängig plastisches Materialverhalten

30–1997 Meywerk, Martin:
Stabilität und Verschleiß bei auf Schienen laufenden Eisenbahnradsätzen

31–1997 Plagge, Frank:
Nichtlineares, inelastisches Verhalten von Spiralseilen

32–1997 Neubert, Michael:
Richtungsregelung beim Tiefbohren

33–1998 Sangi, Daryoush:
Die Versetzungsstrukturbildung in Metallen

34–1998 Thielecke, Frank:
Parameteridentifizierung von Simulationsmodellen für das viskoplastische Verhalten von Metallen - Theorie, Numerik, Anwendung -

35–1998 Vietgen, Jürgen:
Numerische Simulation duktilen Risswachstums unter Berücksichtigung von Schädigung

36–1998 Läer, Bernard:
Einfluß transienter Anregungen auf die Zylinderkopf-Akustik

37–1998 Scheld, Christian:
Auswirkungen dynamischer Interaktionen auf das Schwingungsverhalten von Tanks

38–1999 Baaran, Jens:
Schallfeldanalyse bei sich bewegenden schallerzeugenden Körpern

39–1999 Daros, Carlos:
Wellenausbreitung in unendlich ausgedehnten piezoelektrischen Medien mit transversal isotroper Symmetrie

40–2000 Nils, Wagner:
Untersuchung der Boden-Fahrzeug-Interaktion mit gekoppelten Rand- und Finite-Element-Methoden

41–2001 Langer, Sabine:
Schalltransmission durch Isolierverglasung

42–2001 Schacht, T.:
Orientierungsabhängige Rissbildung in duktilen Metallen

43–2002 Ackerman, Lutz:
Simulation der Schalltransmission durch Wände

44–2002 Barthold, Franz-Joseph:
Zur Kontinuummechanik inverser Geometrieprobleme

45–2002 Böhrnsen, Jens-Uwe:
Dynamisches Verhalten von Schüttgütern beim Entleeren aus Silos

46–2002 Zorn, C.:
Plastisch instabile Verformung aufgrund dynamischer Reckalterung und korrelierten Versetzungsgleitens

47–2002 Küsel, M.:
Wellige Verschleißmuster auf Laufflächen von Eisenbahnrädern

48–2002 Bross, S.:
Versetzungsdynamik und Reckalterung als Ursache instabilen Materialverhaltens beim Portevin-Le Chatelier-Effekt

49–2002 Vesper, Matthias:
Modellierung von Korn und Korngrenze in polykristallinen Gefügen

50–2003 Steindorf, Jan:
Partitionierte Verfahren für Probleme der Fluid-Struktur Wechselwirkung

51–2003 Meyer, Marcus:
Reduktionsmethoden zur Simulation des aeroelastischen Verhaltens von Windkraftanlagen

52–2003 Wittich, Hauke:
Inhomogene Gleitung bei nahgeordneten CuAl-Legierungen

53–2003 Hupfer, Knut:
Einfluß der Mikrostruktur auf die Festigkeitseigenschaften von Metallschäumen

54–2004 Schmelzer, Martin:
Identifikation der Parameter von Zeitbereichsmodellen linear-viskoelastischer Werkstoffe

55–2004 Ostendorf, Michael:
Geschwindigkeitsmessungen in Silos mit der Particle Image Velocimetry

56–2004 Engelhardt, Marek:
Numerische Verfahren zur Identifizierung von Fehlstellen aus Randdaten

57–2005 Keese, Andreas:
Numerische Lösung von Systemen mit stochastischen Unsicherheiten - Ein allgemeiner Rahmen für Stochastische Finite Elemente

58–2005 Pryl, Dobromil:
Einfluß der Poroelastizität auf die Wellenausbreitung: Eine zeitabhängige Randelementformulierung

59–2005 Fries, Thomas-Peter:
Ein stabilisiertes und gekoppeltes netzfreies/netzbasiertes Verfahren für Fluid-Struktur Interaktionsprobleme

60–2006 Kayser-Herold, Oliver:
Least-Squares Methoden zur Lösung von Fluid-Struktur-Interaktionsproblemen

61–2006 Hampel, Sebastian:
Numerische Simulation der Schallausbreitung unter Berücksichtigung meteorologischer Einflüsse

62–2007 Struckmeier, Vera:
Ein numerisches Modell für seismisch induzierte Bodenverflüssigung